UNIVERSITÀ DEGLI STUDI DI TRIESTE

UNIVERSITÀ DEGLI STUDI DI TRIESTE

XXXVIII CICLO DEL DOTTORATO DI RICERCA IN

Scienze della Terra, Fluidodinamica e Matematica. Interazioni e Metodiche

Finanziato dall'Unione europea - NextGenerationEU

Rapid Assessment of Seismic Moment and Radiated Energy for Northeastern Italy

Settore scientifico-disciplinare: GEOS04/A (ex GEO10)

GEOFISICA DELLA TERRA SOLIDA

DOTTORANDO

SEYEDMOHAMMADSADEGH JAFARI

COORDINATORE

PROF. STEFANO MASET

SUPERVISORE DI TESI

PROFESSA VERONICA PAZZI

CO-SUPERVISORI DI TESI

PROF. GIOVANNI COSTA

DR. DENIZ ERTUNCAY

ANNO ACCADEMICO 2024/2025

Finanziato dall'Unione europea NextGenerationEU | Ministero dell'Università e della Ricerca | Italiadomani | Università degli Studi di Trieste

Acknowledgments

In the name of Him, the source of every name,
who set heaven's dance, earth's gentle frame.

I owe a debt of gratitude beyond words to my supervisors, Prof. Veronica Pazzi, Prof. Giovanni Costa, and Dr. Deniz Ertuncay, whose guidance offered not only knowledge but also enduring inspiration. Beyond being my supervisors, they stood by me as genuine friends.

I warmly thank the current and former members of the SeisRaM working group at the University of Trieste, Dr. Simone Francesco Fornasari, Dr. Laura Cataldi (now at OGS), Dr. Arianna Cuius (now at INGV), Mr. Federico Parentelli (Ph.D. candidate), and Ms. Chantal Beltrame (Ph.D. candidate), whose support and collaboration have been essential to the realization of this work.

My sincere appreciation also goes to the professors of the University of Trieste and ICTP for their support in courses, academic and official matters: Prof. Stefano Parolai, Prof. Fabio Romanelli, Prof. Abdelkrim Aoudia (in cherished memory), and Prof. Stefano Maset.

Special thanks to European Union resources, NextGeneration EU - National Recovery and Resilience Plan (PNRR) for co-financing this doctoral scholarship under Monitoring Earth's Evolution and Tectonics (MEET) program.

Finally, my deepest and infinite thanks belong to my beloved parents and brother, whose unwavering support and love have sustained me throughout this journey.

Contents

List of Figures

List of Tables

Abstract

This study investigates the use of the Generalized Inversion Technique (GIT) to decompose earthquake waveforms and retrieve seismic source, path, and site properties through spectral analysis in Northeastern Italy. The GIT is applied in a non-parametric form, allowing direct use of observational data without predefined particular assumptions. The primary objectives are: (i) to obtain reliable source spectra and estimate key source parameters, and (ii) to develop empirical, region-specific models for their rapid estimation. After obtaining source spectra by GIT, key source parameters including Seismic Moment (M_0) and Seismic Radiated Energy (E_R) calculated. Specifically for M_0, the calculation is being done by fitting an ω^2 Brune source model to the obtained source spectra. The next step was to develop empirical models for the region by linking M_0 to Peak Displacement of S waves (PD_S) and E_R to the Integral of Squared S-wave velocity ($IV2_S$). The calibration of the models consists of finding some coefficients related to hypocentral distances and consequently local attenuation characteristics with the aim to rapid estimates of M_0 and E_R. The study also evaluates several methodological aspects of the GIT, including reference station selection, using H/V spectral ratio in the GIT, station correction and weighting strategies. Overall, the non-parametric GIT showed efficiency and flexibility, producing results consistent with previous studies and offering practical, regionally calibrated tools for real-time seismic applications.

1 Introduction

Earthquakes are the result of sudden slip along fault planes, which occurs when the accumulated elastic strain energy, which was built up through long-term tectonic loading, exceeds the friction on the fault surface [Scholz, 2002, Aki and Richards, 2002]. This sudden release of energy initiates a rupture process that propagates through the Earth's crust, generating seismic waves that travel outward from the fault area. The physical representation of this rupture is referred to as the seismic source, which can be modeled as a point source or as a finite fault [Scholz, 2002, Lay and Wallace, 1995].

The seismic source radiates energy in the form of body waves (P and S waves) and surface waves, and its characteristics are quantified through a set of parameters known as source parameters [Lay and Wallace, 1995]. These include the seismic moment, which reflects the size of an earthquake [Aki and Richards, 2002]; the radiated energy, which accounts for the portion of energy converted into seismic waves [Kostrov, 1974]; the corner frequency, which is related to the rupture duration and fault dimensions [Stein and Wysession, 2003, Lay and Wallace, 1995]; and the stress drop, which measures the change in shear stress across the fault during rupture [Kanamori, 1975]. Accurate estimation of these parameters is essential for understanding the physics of earthquake generation, evaluating rupture dynamics, and improving ground motion prediction models. Moreover, source parameter analysis contributes to broader geophysical objectives such as seismic hazard assessment and imaging of Earth's internal structure [Aki and Richards, 2002].

Quantitative seismology provides the theoretical and observational framework for analyzing earthquake processes by interpreting ground motion recordings obtained from seismic instruments [Udías and Buforn, 2017]. These recordings capture the propagation of seismic waves through the Earth and are typically expressed as the convolution of three distinct components: the source term, which describes the initial rupture; the path term, which accounts for wave attenuation and scattering during propagation; and the site term, which reflects local amplification effects due to near-surface geology or instrument response [Stein and Wysession, 2003]. Each of these components plays a critical role in shaping the observed ground motion and must be carefully separated to retrieve reliable physical insights.

Among these, the source component is of particular interest in seismological studies, as it contains the fundamental mechanisms of fault rupture, energy release, and stress redistribution [Lay and Wallace, 1995]. Investigating the source allows researchers to infer fault geometry, rupture velocity, and scaling relationships between magnitude and stress drop, which are important for both theoretical modeling and practical applications in seismic hazard mitigation.

Two fundamental earthquake source parameters are **Seismic Moment (M_0)** and **Seismic Radiated Energy (E_R)**. From these, two widely used magnitude scales, **Moment Magnitude (M_W)** and **Energy Magnitude (M_E)**, are derived. These parameters are essential not only for characterizing individual seismic events but also for making regional seismic models and infrastructure reinforcement strategies.

Despite their importance, reliable estimation of M_0, E_R, and related source parameters remains challenging, particularly in regions with heterogeneous attenuation such as Northeastern Italy. This study is motivated by the need to (i) evaluate whether a Generalized Inversion Technique (GIT) can robustly separate source, path, and site effects in this region, (ii) determine how methodological choices, such as reference-station selection, H/V constraints, and weighting strategies, affect the stability of the inversion, and (iii) establish empirical relationships that allow rapid estimation of source parameters from ground-motion observables. These questions guide the structure of the thesis and define its main scientific objectives.

This thesis is organized into six main chapters. Chapter 1 has introduced the key source parameters, seismic moment and radiated energy, and provided a comprehensive view over previous studies as well as a general overview of the geological and tectonic framework of Northeastern Italy. Chapter 2 outlines the data which are used in this study and Chapter 3 talks about methodology, including spectral decomposition using the generalized inversion technique, empirical attenuation modeling, and evaluation of inversion quality. Chapter 4 presents the results, covering source spectra, site effects, attenuation characteristics, and energy estimates, along with a discussion of methodological limitations and uncertainties. Chapter 5 offers a discussion of the findings, including implications for magnitude scaling and methodological choices. Finally, Chapter 6 provides a general conclusion and a short talk about future directions.

1.1 Source Parameters

1.1.1 Seismic Moment

Seismic moment is a fundamental source parameter that quantitatively characterizes the size of an earthquake. It plays a central role in both kinematic and dynamic modeling of fault slip distributions

and rupture processes. In its simplest physical interpretation, M_0 represents the moment of force couples that constitute a dipolar seismic source [Lay and Wallace, 1995, Udías and Buforn, 2017, Madariaga, 2011]. More generally, it is expressed as a second-order symmetric tensor (3×3), containing the distribution of elementary force couples acting within the source volume [Lay and Wallace, 1995, Udías and Buforn, 2017, Madariaga, 2011].

For planar fault geometries, seismic moment is defined as the product of shear modulus (rock rigidity), average slip, and rupture area [Aki, 1966, Lay and Wallace, 1995, Stein and Wysession, 2003]:

$$M_0\ (N\,m) = \mu \cdot A \cdot D \tag{1}$$

where μ(Pa or N/m^2) is the shear modulus of the source area, A (m^2) is the fault area, and D (m) is the average slip. This scalar quantity is widely regarded as the most robust and physically meaningful metric for describing earthquake size, showing more ability than other magnitude scales in capturing the energy release and fault mechanics.

Seismic moment exhibits a direct relationship with strong ground motion characteristics, particularly influencing the amplitude of low-frequency spectral components. Its accurate estimation is essential for seismic hazard assessment, ground motion prediction, and the development of scaling laws in seismology [Abercrombie, 2021, James, 1989, Madariaga, 2011].

The relationship between seismic moment and different magnitude scales is fundamentally related to the spectral characteristics of radiated seismic waves. These waves are governed by the product of the scalar seismic moment and the source time function, which shows the temporal evolution of fault rupture during an earthquake [Stein and Wysession, 2003].

A simplified source model assumes that the time function is the convolution of two rectangular (boxcar) functions [Lay and Wallace, 1995, Aki and Richards, 2002, Stein and Wysession, 2003]: one representing the finite fault length and the other representing the finite rise time of slip at any point on the fault. This convolution captures the combined effects of rupture propagation and slip initiation. In the frequency domain, the Fourier transform [Fourier, 1822] of the resulting time function is equivalent to the product of the individual transforms of the boxcar functions.

The Fourier transform of a boxcar of height $1/T$ and length T is based on the following equation which produces sinc function (Figure 1) [Aki and Richards, 2002, Shearer, 2009, Stein and Wysession, 2003]:

$$F(\omega) = \int_{-T/2}^{T/2} \frac{1}{T} e^{i\omega t} dt = \frac{1}{Ti\omega}(e^{i\omega T/2} - e^{-i\omega T/2}) = \frac{\sin(\omega T/2)}{\omega T/2} \tag{2}$$

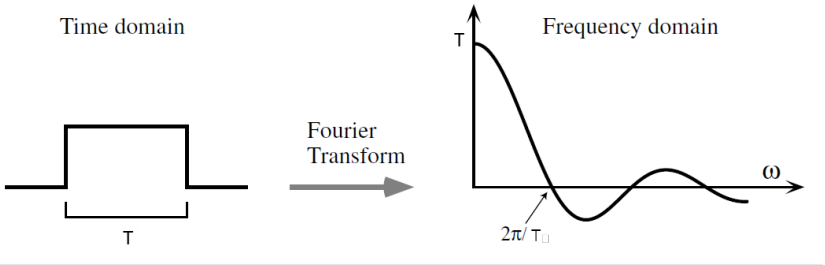

Figure 1: A boxcar pulse in the time domain and its product in the frequency domain which is a sinc function (the figure is published by Shearer 2009)

The sinc function, defined as "sinc $x = (\sin x)/x$", contains the finite duration of the source pulse in the frequency domain. As shown in Equation 3, the spectral amplitude of the radiated seismic signal is modeled as the product of the seismic moment and two sinc terms, which are corresponding to the rupture time (T_R) and rise time (T_D) of the faulting process. This formulation captures the band-limited nature of the source spectrum, with high-frequency attenuation is governed by the temporal characteristics of the rupture [Aki and Richards, 2002, Shearer, 2009, Stein and Wysession, 2003].

$$|A(\omega)| = M_0 \left| \frac{\sin(\omega T_R/2)}{\omega T_R/2} \right| \left| \frac{\sin(\omega T_D/2)}{\omega T_D/2} \right| \tag{3}$$

Taking the logarithm, the Equation 3 yields a linearized expression (Equation 4) that facilitates inversion and spectral fitting:

$$\log A(\omega) = \log M_0 + \log[\mathrm{sinc}(\omega T_R/2)] + \log[\mathrm{sinc}(\omega T_D/2)] \tag{4}$$

A practical approximation for the sinc function is often employed to simplify analysis: sinc x as 1 for $x < 1$, and $1/x$ for $x > 1$. This behavior is illustrated in Figure 2 (Top), where the transition from flat spectral response to high-frequency decay is evident. Such approximations are particularly useful in estimating corner frequencies and interpreting spectral behavior in observed ground motion data.

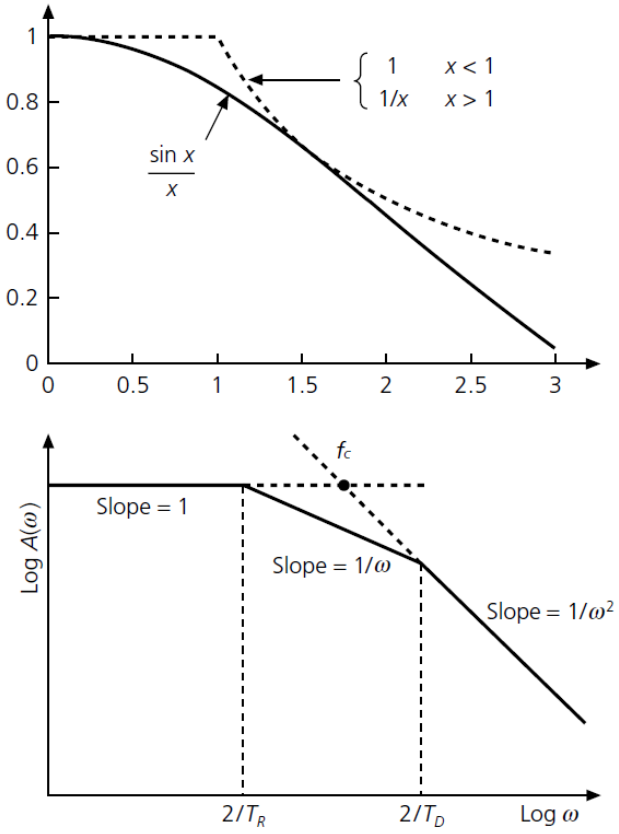

Figure 2: Top: Simplified representation of the $\sin x/x$ function, commonly applied in modeling the finite duration of the seismic source pulse. Bottom: Theoretical earthquake source spectrum, segmented into three frequency-dependent regions with slopes of 1, ω^{-1}, and ω^{-2}, delineated by angular frequencies associated with rupture and rise times, T_R and T_D. A widely used approximation replaces this dual-transition model with a single corner frequency, f_c (or f_0), marking the boundary between the low- and high-frequency spectral domains. The low-frequency plateau, extending toward zero frequency, corresponds to M_0. [Aki, 1967, Brune, 1970, Stein and Wysession, 2003] (the figure is published by Stein and Wysession 2003)

Under this approximation, as shown in Figure 2 by plotting the $\log A(\omega)$ versus $\log \omega$, the curve simplifies into three linear segments, each corresponding to a distinct frequency band (Figure 2, Bottom). Assuming $T_R > T_D$, the spectral behavior can be described as follows:

$$\log|A(\omega)| = \begin{Bmatrix} \log M_0, & \omega < 2/T_R \\ \log M_0 - \log(T_R/2) - \log\omega, & 2/T_R < \omega < 2/T_D \\ \log M_0 - \log(T_R T_D/4) - 2\log\omega, & 2/T_D < \omega \end{Bmatrix} \tag{5}$$

This spectral function as plotted in Figure 2, Bottom, is segmented into three distinct frequency domains, delineated by the frequency points $2/T_R$ and $2/T_D$, which are called corner frequencies. The spectrum remains flat for frequencies less than the first corner frequency, decays proportional to ω^{-1} between the two corner frequencies, and exhibits a steeper decay following ω^{-2} for the high frequencies. Consequently, the source spectrum is effectively parameterized by three key factors: seismic moment, rupture time, and rise time [Lay and Wallace, 1995, Aki and Richards, 2002, Stein and Wysession, 2003, Shearer, 2009].

As previously discussed, M_0 is particularly sensitive to the low-frequency portion of the source spectrum and represents a static, physical property of an earthquake [Choy and Boatwright, 1995, Picozzi et al., 2017]. Leveraging M_0, the moment magnitude (Equation 6) computed using a logarithmic scaling relation [Kanamori, 1977, Hanks and Kanamori, 1979, Bormann, 2012].

$$M_W = \frac{2}{3}(\log M_0 - 9.1) \tag{6}$$

where M_0 is in N.m.

Unlike traditional magnitude scales, M_W offers a consistent and reliable measure of earthquake size across a broad range of magnitudes, which is effectively avoiding saturation that limit the accuracy of scales such as M_L [Kanamori, 1977, Hanks and Kanamori, 1979]. This makes M_W the preferred metric for quantifying the size of seismic events (energy release) in both regional and global seismological studies.

1.1.2 Seismic Radiated Energy

Radiated energy represents the portion of an earthquake's total energy that is emitted as seismic waves and ultimately propagates through the Earth's interior and surface [Kostrov, 1974, Dahlen, 1977, Rivera and Kanamori, 2005]. While seismic moment and static stress drop are fundamental parameters describing the geometry and amount of fault slip, they do not directly capture the dynamic aspects of rupture, such as rupture velocity or slip rate [Shearer, 2009]. In contrast, the total radiated energy is a dynamic measure that reflects the actual energy released as seismic waves during rupture [Shearer, 2009]. It provides insight into the efficiency of energy radiation and the intensity of ground shaking. Theoretically, it corresponds to the seismic energy that would reach the far field in an idealized, homogeneous medium without attenuation [Shearer, 2009]. Therefore, it serves as a fundamental metric for

evaluating earthquake dynamics and complements static parameters in characterizing the full energy budget of seismic events.

Radiated energy plays a significant role in earthquake characterization, as it directly quantifies the portion of energy emitted as seismic waves which can be serving as a representative for the destructive potential of an event. It complements Seismic Moment by offering dynamic insight into rupture behavior, stress release, and the overall energy budget of the earthquake source [Choy and Boatwright, 1995, Boatwright and Fletcher, 1984].

Unlike Seismic Moment which reflects static fault displacement and is primarily sensitive to low-frequency spectral content, radiated energy is more responsive to high-frequency source details. This sensitivity makes it a critical parameter for evaluating rupture velocity, slip heterogeneity, and the efficiency of energy radiation [Choy and Boatwright, 1995, Picozzi et al., 2017]. Together, these metrics provide a comprehensive framework for understanding both the mechanical and energetic aspects of earthquake processes.

By using the E_R, the energy magnitude (Equation 7) calculated [Choy and Boatwright, 1995, Choy et al., 2001, 2006, Bormann and Giacomo, 2011, Bormann, 2012].

$$M_E = \frac{2}{3}\log E_R - 2.9 \tag{7}$$

where E_R is in J.

While M_E captures destructive energy, M_W illustrates tectonic significance. Understanding both is fundamental for seismic hazard assessment and seismic events characterization [Bormann, 2012].

1.2 Study Background

The estimation of earthquake source parameters has traditionally relied on spectral fitting techniques, wherein observed Fourier Amplitude Spectra (FAS) of seismic recordings are matched to theoretical models that describe the frequency-dependent radiation from a fault rupture. One of the most widely adopted models is the Brune's model [Brune, 1970], which assumes a flat spectral plateau up to a characteristic corner frequency, beyond which the amplitude decays proportional to ω^2. This model provides a simplified yet effective framework for estimating key source parameters such as seismic moment, stress drop, and rupture duration from spectral shapes.

To find the source spectrum, there are two most popular methods: one is the use of Empirical Green's Function (EGF), and the other method is GIT [Abercrombie et al., 2025]. There are also some other methods but they are usually overlapping or combining the mentioned methods [Abercrombie et al., 2025]. However, the EGF method is strongly constrained by the availability of suitable EGF i.e. an event which must be close in space, large enough for good signal, yet small enough relative to the target event. Therefore, this is limiting the number of events that can be used in this method [Abercrombie, 2021, Abercrombie et al., 2025].

On the other hand, GIT was introduced as a robust method for decomposing observed spectral amplitudes into their components: *source*, *path*, and *site* [Andrews, 1986, Castro et al., 1990]. GIT operates within an inversion framework that treats the logarithm of spectral amplitudes as a linear combination of these three terms, allowing for their simultaneous estimation, sometimes with imposing rigid parametric constraints. This approach is particularly advantageous in regional studies where large datasets cover diverse site conditions and propagation paths.

The distinction between forward and inverse problems is central to this methodology. While forward modeling involves predicting spectral data from known physical parameters, inverse modeling is trying to infer those parameters from observed data, which is a process complicated by issues of nonuniqueness, and parameter trade-offs [Stein and Wysession, 2003]. GIT mitigates these challenges by leveraging statistical regularization such as different constraints, and network-wide averaging, enabling stable solutions even in the presence of data heterogeneity [Castro et al., 1996, Boatwright et al., 1991, Klin et al., 2017].

Over the past years, GIT has been successfully applied to lots of regional datasets across various tectonic regimes, including stable continental plates, active fault zones, and induced seismicity environments. Its application has yielded consistent estimates of seismic moment, corner frequency, and stress drop, while also providing insights into regional attenuation properties and site-specific amplification functions. These results have significantly advanced the understanding of earthquake source and site scaling and have contributed to the refinement of ground motion prediction models used in seismic hazard assessment.

In their study on regional seismicity in Mexico, Castro et al. [1990] conducted a comparative analysis of parametric and nonparametric spectral inversion techniques to estimate earthquake source parameters and characterize attenuation and site effects. Both inversion approaches yielded broadly consistent results in terms of seismic moment and corner frequency, confirming the reliability of spectral methods for source characterization across different modeling frameworks. However, the authors noted that

nonparametric inversion was particularly advantageous for capturing complex attenuation behavior, especially in regions with heterogeneous crustal properties and frequency-dependent propagation effects.

They mentioned the statement by Baker [1988] that the nonparametric approach, which avoids imposing rigid functional forms on the attenuation term, allowed for more flexible modeling of the frequency-dependent quality factor and geometrical spreading. This flexibility is critical in tectonically active regions like central Mexico, where lateral variations in lithology and crustal structure can significantly influence wave propagation. By allowing the data to affect the shape of the attenuation curves, nonparametric inversion revealed spectral features that would likely be ignored under parametric constraints.

Importantly, the study also highlighted the influence of site response, even at stations classified as rock sites. Contrary to the assumption that rock sites provide flat, reference-level amplification, Castro et al. [1990] observed significant deviations in spectral amplitudes attributable to local site effects. These amplifications can change the shape of the apparent source spectra and introduce variability in the inversion results, underscoring the necessity of incorporating site-specific corrections even for hard-rock stations.

In the context of a seismic microzonation project conducted in central Italy, Parolai et al. [2000] performed a comparative assessment of three widely used techniques for estimating site response: the GIT, the Reference Site Method (RSM) [Borcherdt, 1970], and the horizontal-to-vertical spectral ratio, also known as the receiver function approach [Langston, 1977, Lermo and Chávez-García, 1993].

The results demonstrated that both GIT and RSM yielded broadly consistent estimates of site amplification across the studied stations. These methods effectively captured the frequency-dependent amplification characteristics of local soil and rock conditions. In contrast, the HVSR technique tended to systematically underestimate amplification levels. This underestimation was attributed to the method's sensitivity to the selected time window and the presence of transient noise, which can have negative effects on the spectral ratio and true site effects.

Furthermore, the study explored the performance of various inversion algorithms used within the GIT framework, including Singular Value Decomposition (SVD) [Press et al., 1994], Simultaneous Iterative Reconstruction Technique (SIRT) [van der Sluis and van der Vorst, 1987], and Least Squares (LSQ) [Menke, 1984]. All three algorithms produced comparable results in terms of spectral decomposition and site term retrieval, suggesting that the choice of inversion solver has limited impact on the final estimates.

However, the authors emphasized that successful application of GIT requires careful selection of refer-

ence sites. These reference stations serve as baseline conditions against which relative site effects are measured. Additionally, prior knowledge of the regional quality factor is essential for accurate separation of source and path contributions.

In a detailed investigation of weak-motion seismicity across the United Kingdom, Edwards et al. [2008] applied spectral inversion techniques to a dataset consisting of earthquakes with local magnitudes ranging from 2.0 to 4.7. The study aimed to extract reliable source and site parameters and characterize regional attenuation properties by analyzing the behavior of S-wave Fourier amplitude spectra.

The inversion framework employed in the study allowed for the estimation of seismic moment, corner frequency, site response functions and stress drop, while also isolating the effects of attenuation and geometrical spreading. One of the key outcomes was the derivation of frequency-independent depth-dependent quality factor models, which describe the attenuation of seismic waves in the crustal volume beneath the U.K.

The study demonstrated that even weak-motion events, when recorded by a sufficiently dense and well-calibrated seismic network, can yield meaningful insights into all source, site and propagation parameters. Moreover, it is possible to calibrate the attenuation relations.

In an investigation of seismic wave attenuation in Romania, Oth et al. [2008] applied the GIT to a dataset of S-wave Fourier amplitude spectra recorded across different of stations. The primary objective was to characterize the frequency-dependent attenuation properties of the crust and upper mantle, with particular emphasis on deriving reliable quality factor models. The study focused on a region exhibiting clustered seismicity, which presents unique challenges for spectral decomposition due to overlapping source effects and limited ray paths coverage.

The inversion framework enabled the simultaneous estimation of source, path, and site contributions, revealing that attenuation behavior in the Romanian crust is both frequency-dependent and spatially heterogeneous. The derived $Q(f)$ models exhibited significant lateral variability, reflecting the complex tectonic and lithological structure of the region. These findings underscore the necessity of region-specific calibration in spectral inversion studies.

Moreover, the study highlighted the importance of adapting GIT configurations to the characteristics of the seismic dataset. It also emphasized on the importance of the azimuthal dependence of ground motion.

In a comprehensive study of the 2009 L'Aquila earthquake sequence in central Italy, Bindi et al. [2009] conducted a joint spectral analysis of strong-motion acceleration records to estimate key seismological

parameters, including source characteristics, seismic wave attenuation, and site amplification effects. The dataset consisted of recordings from the mainshock, an event of moment magnitude 6.3, as well as 12 aftershocks, providing a robust basis for spectral decomposition across a range of magnitudes and source-receiver geometries.

The analytical framework employed by the authors involved simultaneous inversion of acceleration spectra to isolate the contributions of source, path, and site effects. The inversion results yielded consistent estimates of seismic moment and stress drop across the event sequence, while also revealing spatial variability in attenuation and amplification patterns.

A particularly important outcome of the study was the identification of distinct features in the attenuation curves at source-receiver distances of approximately 50 km and 150 km. These anomalies were interpreted as manifestations of crustal-scale structural effects, specifically reflections and refractions of seismic waves at major velocity discontinuities within the crust and upper mantle. Such features are indicative of complex wave propagation phenomena, including energy trapping and scattering, which can significantly influence the amplitude and frequency content of ground motion at regional distances.

In a comprehensive study aimed at characterizing regional attenuation, source spectra and site response across Japan, Oth et al. [2011] applied the GIT to a large dataset of S-wave Fourier amplitude spectra recorded by both surface and borehole seismic stations. The study leveraged the advantages of nonparametric inversion, which avoids imposing rigid functional forms on spectral components, thereby allowing for flexible and data-driven decomposition of observed ground motion into source, path, and site contributions. They proved this approach to be particularly effective in resolving frequency-dependent attenuation and spatially variable site effects in a tectonically complex region.

One of the key findings of the study was the contrast in site amplification behavior between surface and borehole sensors. Surface stations exhibited strong amplification effects, often with high variability across frequencies and locations, reflecting the influence of near-surface layers and local geological heterogeneities. In contrast, borehole sensors, which were installed at depth, showed significantly reduced variability in site response, offering a more stable and reliable basis for spectral inversion. These results underscore the critical role of borehole data in minimizing uncertainties associated with site amplification and improving the accuracy of source and attenuation estimates.

The inversion also revealed that the attenuation characteristics in Japan are highly region-specific and exhibit strong frequency dependence. The derived quality factor models varied significantly across different tectonic domains, highlighting the need for localized calibration.

Regarding source characterization, the study found that the inverted source spectra generally conformed to the standard ω^2 model, which assumes a flat spectral plateau up to a corner frequency, followed by a decay. However, notable differences were shown between crustal and subcrustal earthquakes. Crustal events were associated with lower corner frequencies and stress drops on the order of 1 MPa. In contrast, subcrustal earthquakes exhibited higher corner frequencies and stress drops on the order of 10 MPa.

In an investigation of the 2016 Amatrice–Norcia earthquake sequence in central Italy, Picozzi et al. [2018a] focused on the empirical scaling relationships for seismic moment and radiated energy, two fundamental parameters that describe the size and dynamic properties of earthquake rupture. The study aimed to rapidly estimate these quantities for a series of events with M_W ranging from 2.5 to 6.5, enabling characterization of source properties during an active seismic crisis.

The authors employed a robust inversion methodology to extract source spectra from strong-motion recordings, allowing for the calculation of both M_0 and E_R directly from observed ground motion.

A key outcome of the study was the observed consistency between the derived scaling relationships and those obtained from previous studies in similar tectonic settings. The comparison confirmed that the estimated seismic moments and radiated energies aligned well with established trends, confirming the reliability of the adopted methodology.

In a study of the Irpinia fault system in southern Italy, Picozzi et al. [2019] employed analyses to estimate key earthquake source parameters, specifically seismic moment and radiated energy, with the aim of tracking the mechanical evolution of the fault network over time. By analyzing a sequence of seismic events, the authors aimed to characterize the temporal and spatial variations in stress release and rupture process, thereby gaining insight into the ongoing deformation processes within this tectonically active region.

In a global-scale investigation of tectonic and induced seismicity, Picozzi et al. [2018b] analyzed the scaling behavior between seismic moment and radiated energy across four distinct datasets: global earthquakes, regional events in Japan and Central Italy, and induced seismicity at The Geysers geothermal field in California. The study aimed to evaluate the performance and physical interpretability of energy magnitude relative to moment magnitude.

Both M_E and M_W are derived from physically meaningful quantities and are considered non-saturating magnitude scales. This distinguishes them from empirical scales such as local magnitude (M_L) and body-wave magnitude (m_b), which tend to saturate for moderate-to-large events and are less reliable

for characterizing rupture dynamics. The authors proposed that M_E, being directly linked to the high-frequency content of seismic radiation, may offer a more sensitive and robust metric for developing ground motion prediction equations, especially in regions where stress drop and rupture velocity vary significantly.

A key discussing point of the study was the systematic deviation between M_E and M_W observed in individual events. When $M_E > M_W$, the event typically exhibits a high stress drop and enhanced high-frequency radiation, indicative of sudden rupture and stronger ground shaking. Conversely, when $M_E < M_W$, the event is characterized by low stress drop and reduced high-frequency energy, often associated with slow rupture processes such as tsunami-generating subduction earthquakes. These deviations reflect the dynamic efficiency of the rupture and provide insight into the energy partitioning during seismic events.

The study further demonstrated that the scaling relationship between M_E and M_W is strongly modulated by stress drop. For events with $\Delta\sigma \geq 1$ MPa, the two magnitude scales exhibit near-linear correspondence, with a slope close to unity, suggesting consistent energy-to-moment ratios across these events. In contrast, for events with $\Delta\sigma < 1$ MPa, the scaling diverges, highlighting the limitations of using M_W alone to capture the full spectrum of rupture behavior in low-stress-drop scenarios.

These findings underscore the potential of M_E as a complementary magnitude scale for seismic hazard modeling, particularly in applications that require accurate representation of high-frequency ground motion.

In a comprehensive evaluation of multiple scenarios of the GIT, Shible et al. [2022] emphasized that no single inversion strategy universally applies to all seismic datasets. The selection of an appropriate GIT configuration, whether parametric, nonparametric, or semi-parametric, must be based on the specific characteristics of the dataset. This context-dependent nature of inversion modeling reflects the inherent complexity of decomposing source, path, and site effects from observed spectral amplitudes. However, they mentioned that in case of no limitation about data availability, nonparametric approaches have more ability to provide information about sources and attenuation than parametric approaches.

One of the key findings of the study is the relative stability of site response estimates across different inversion schemes. Regardless of the methodological framework employed, site amplification functions tend to exhibit consistent spectral shapes and amplitudes, suggesting that site terms are the most robust and least sensitive to inversion strategy. This consistency is likely due to the averaging effect across multiple events and the relatively stationary nature of near-surface geological conditions at recording stations.

In contrast, the source and attenuation components of the inversion show significantly greater variability. Even when unified constraints are imposed, such as fixed geometrical spreading models or shared reference site conditions, the retrieved source spectra and attenuation functions can diverge depending on the inversion architecture and regularization choices. This variability underscores the challenges in accurately resolving source parameters and attenuation properties, particularly in regions with complex crustal heterogeneity or sparse station coverage.

Despite these differences, the moment magnitude estimates derived from various GIT configurations remain remarkably stable, with inter-method variability typically within a factor of 0.1. This suggests that seismic moment, and by extension moment magnitude, is a relatively well-constrained parameter in spectral inversion, owing to its dependence on low-frequency spectral amplitude.

In an investigation of the 2019 Ridgecrest earthquake sequence in Southern California, Bindi et al. [2023a] employed a spectral decomposition framework to isolate and analyze the source spectra of seismic events associated with these complex rupture events. The Ridgecrest sequence, which consists of an M_W 6.4 foreshock followed by an M_W 7.1 mainshock and numerous aftershocks, provided a rich dataset for examining rupture dynamics, stress release, and regional attenuation behavior.

The study utilized the GIT to decompose the observed Fourier amplitude spectra into their constituent components. The analysis introduced different choices, such as window duration and attenuation modeling, leading to estimates of seismic moment and corner frequency under different scenarios.

In further detailed investigation of spectral inversion practices, Bindi et al. [2023b] examined how methodological choices, particularly the duration of the S-wave time window used for Fourier amplitude spectra computation, affect the estimation of corner frequency and, by extension, stress drop. The study utilized a dataset spanning a wide magnitude range and demonstrated that the selected time window applies a systematic influence on the retrieved source parameters, with implications for both small and moderate-to-large events.

The analysis revealed a magnitude-dependent sensitivity of f_c to window length. For smaller earthquakes ($M_W < 3$), the average ratio of f_c values computed using a 20-second window versus a 5-second window was approximately 1.1, indicating relatively minor differences. However, for larger events ($M_W > 4.5$), this ratio dropped significantly to around 0.66, suggesting that longer windows tend to yield lower corner frequency estimates.

In addition to windowing effects, the study evaluated the influence of attenuation modeling on source parameter retrieval. Specifically, the application of the epicentral distance (instead of hypocentral dis-

tance) was found to increase f_c estimates by approximately 10 percent for shallow events (depths < 6 km).

The findings underscore the high sensitivity of spectral inversion results to modeling assumptions, particularly in relation to attenuation structure and time window selection. These factors can introduce systematic biases that exceed the statistical uncertainties typically reported in inversion studies.

In a regional-scale investigation of earthquake source properties across central and southern Europe, Yen et al. [2024] conducted a systematic analysis of seismic events with the primary objective of estimating moment-based stress drop and evaluating the conformity of observed source spectra to theoretical models. The study leveraged a dataset of broadband seismic recordings and applied spectral inversion techniques to retrieve key source parameters, including seismic moment and corner frequency from S-wave Fourier amplitude spectra.

The analysis revealed that the source spectra followed the classical ω^2 model. This spectral shape is consistent with self-similar rupture dynamics and supports the use of simplified scaling relationships for stress drop estimation.

Robust and stable stress drop estimates were obtained for events with moment magnitudes > 3, where the spectral signal is sufficiently strong and the inversion results are less sensitive different factors. For smaller events, the limited bandwidth posed challenges for accurate spectral decomposition, often resulting in greater uncertainty in the retrieved source parameters.

In a comprehensive spectral inversion study focused on seismicity in New Zealand, Zhu et al. [2024] performed spectral decomposition of S-wave FAS to investigate the relation between source characteristics, attenuation behavior, and ground motion variability.

One of the key findings of the study was the observation that deeper earthquakes exhibit more attenuation, particularly at high frequencies. This depth-dependent attenuation may be attributed to increased energy loss through anelastic mechanisms and scattering as seismic waves traverse longer and in more heterogeneous paths. Additionally, deeper events show higher source spectral amplitudes at high frequencies, and as a result, higher corner frequency and higher Brune's stress parameter ($\Delta\sigma$).

The study also mentioned the point that ($\Delta\sigma$) plays a critical role in explaining between-event variability in ground motion predictions. However, the study found that $\Delta\sigma$ is practically independent of earthquake magnitude.

Recent improvements in computational tools have made the GIT easier to use and more widely available for both research and practical applications. These advances have many advantages like reproducibility,

user interface design, and scalability, making it faster and clearer to apply spectral decomposition to different seismic datasets.

Klin et al. [2017] introduced GITANES, a MATLAB-based graphical user interface (GUI) specifically designed for site amplification analysis using GIT-derived spectral components. The tool provides an intuitive environment for users to visualize and interpret site response functions, making it particularly valuable for microzonation studies and regional ground motion modeling. By changing the complexity of inversion routines into a user-friendly interface, GITANES made GIT easier for practitioners and enhances the reproducibility of site effect assessments.

Building on the need for open-source and scalable solutions, Morasca et al. [2025] developed GITpy, a Python-based software package capable of performing spectral decomposition, including the estimation of source, path, and site terms. GITpy integrates with modern scientific computing systems and supports batch processing of large datasets, making it well-suited for regional hazard studies, earthquake engineering and seismic monitoring. Its modular architecture and transparent code promote community-driven development and methodological standardization. Moreover, it can provide an environment for practices in computational seismology.

In parallel, Spallarossa et al. [2021] launched RAMONES, a web-based operational service calibrated using GIT-derived spectral parameters. RAMONES enables rapid estimation of earthquake source parameters, specifically seismic moment and radiated energy, for events occurring in central Italy. The platform connects scientific research with civil protection needs, helping people make quick decisions during earthquakes and improving public safety by sharing real-time information. Its link to regional seismic networks and automated data processing shows how GIT-based tools can be useful in everyday earthquake monitoring.

Collectively, these software innovations show a shift in how GIT is applied and used. They enhance computational efficiency, improve methodological ability, and facilitate the achievement of spectral inversion results into both academic research and emergency response frameworks. Since seismology-related studies need reliable source characterization and site amplification data, the role of accessible, well-calibrated GIT tools will continue to grow in importance.

In the present work, both theoretical approaches and empirical attenuation models are employed to estimate M_0 and E_R as two of the very important source parameters in Northeastern Italy. The theoretical framework is based on spectral analysis and inversion techniques, while the empirical models are based on the specific attenuation characteristics of the study area. This dual approach allows for a balance between computational accuracy and practical efficiency, enabling reliable and scalable calculations

across a large dataset of seismic events.

To talk about the motivation for this study, apart from stemming from a research purpose, it is definitely remarkable that earthquake source characterization is not only an academic subject, but also has direct implications for public safety, engineering design, and regional planning. The main objective is to verify the robustness of GIT by reapplying the method to the data used in previous studies and testing different processing manipulations. By working on the accuracy and efficiency of seismic moment and energy estimation, this study supports the development of more robust ground motion models and contributes to the long-term goal of seismic risk reduction in Northeastern Italy as a tectonically active region.

Moreover, Northeastern Italy has a complex seismic history and remains vulnerable to moderate-to-strong earthquakes. Enhancing the regional seismic database with updated source parameters helps ensure that future hazard assessments are based on the most reliable and representative data. This work provides the first specific models for the study area through a methodological framework that can also be adapted to other regions, making it a valuable contribution to the broader field of seismology.

The study area is Northeastern part of Italy, with a particular focus on the regions of Friuli Venezia Giulia and Veneto. These areas are covered by different seismic monitoring networks. One of the central objectives of this research is to contribute to the update and refinement of the databases of these networks, enhancing the quality and completeness of seismic source information available for future studies.

Additionally, another objective and innovative contribution, of this study is the development of empirical attenuation models based on the seismotectonic context of Northeastern Italy. These functions are designed to enable rapid estimation of seismic moment and radiated energy directly from observable waveform metrics.

The mentioned empirical functions derived herein reflect the attenuation behavior specific to the geological and tectonic features of Northeastern Italy, incorporating both source–site distance and waveform metrics. As such, they represent a regionally optimized toolset for the broader future goals of seismic hazard assessment, enhancing ground motion prediction capabilities in complex tectonic environments, real-time seismic monitoring, early warning systems, and rapid post-event characterization.

Based on prior investigations in Northeastern Italy, Castro et al. [1996] conducted a detailed study of seismic attenuation and site response in the Friuli region, leveraging strong-motion recordings and digital seismic network data from the 1976 earthquake sequence. This sequence, which included several damaging events, provided a valuable dataset for characterizing regional wave propagation and near-

surface amplification effects in a tectonically active portion of the southern Alpine margin.

The study employed a nonparametric spectral decomposition approach to estimate the S-wave quality factor across epicentral distances ranging from 10 to 190 km. This method allowed for the empirical derivation of attenuation functions without imposing predefined parametric forms, thereby capturing the frequency-dependent behavior of seismic energy loss. Attenuation was analyzed at discrete frequencies spanning the range of 0.4 to 25 Hz, resulting in two frequency-dependent relations of the form $Q(f) = 20.4f$ for strong motion recordings and $Q(f) = 16.1f^{0.92}$ for digital seismographic data, in both of which anelastic attenuation will be more at higher frequencies, a characteristic feature of the heterogeneous crustal structure in the region.

In addition to attenuation modeling, the study derived site amplification functions from spectral residuals and validated these estimates using Nakamura's horizontal-to-vertical spectral ratio technique [Nakamura, 1989]. The comparison revealed a high degree of consistency between the GIT-derived site terms and the H/V ratios, showing the robustness of the spectral decomposition framework.

In a focused investigation of seismic source characteristics in Northeastern Italy, Franceschina et al. [2006] analyzed a dataset of local earthquakes with magnitudes ranging from $M_L = 2.0$ to $M_L = 5.7$, recorded by the short-period local seismic network of the Istituto Nazionale di Oceanografia e Geofisica Sperimentale (OGS), [Zivcic et al., 2000]. The study aimed to derive robust estimates of source parameters, i.e. seismic moment, radiated energy, and corner frequency.

To ensure the reliability of spectral decomposition, the authors selected only those seismic stations exhibiting low horizontal-to-vertical spectral ratios ($H/V \leq 2$), a criterion showing minimal site amplification and stable near-surface conditions. This filtering strategy allowed for cleaner isolation of source and path effects, enhancing the robustness of the retrieved source spectra.

The corrected displacement spectra were found to follow closely Brune's classical ω^2 source model. The derived source parameters spanned a wide range:

- M_0: from 1.5×10^{12} Nm to 1.1×10^{17} Nm
- E_R: from 2.6×10^{6} J to 9.9×10^{12} J
- f_c: from 0.5 Hz to 9.9 Hz

In a regional study focused on seismic site response across Northeastern Italy, Klin et al. [2021] conducted a detailed assessment of site amplification effects using spectral inversion techniques. The analysis aimed to explore the relationship between spectral amplification and time-domain ground motion

metrics, such as peak ground velocity (PGV) and peak ground acceleration (PGA), which are critical inputs for engineering design and seismic hazard modeling.

The study revealed that for stations on rock sites, PGV has a negative bias while PGA shows both negative and positive bias. However, for stations on soil, bot PGA and PGV have dominant positive bias. The findings of the study also suggests that in spite of GIT, H/V is not always reliable because it can either overestimate or underestimate the amplification function which is emphasizing on the superiority of GIT.

In an investigation of seismic ground motion behavior in the Northeastern border region of Italy, adjacent to Slovenia and Austria, Cataldi et al. [2022] employed a parametric spectral modeling framework to analyze the full frequency-dependent characteristics of earthquake ground motion. This approach is grounded in the parametrization of seismic source properties, attenuation, and site amplification effects, offering a physically consistent method for reconstructing ground motion spectra across the frequency range of 0.5 to 25 Hz.

The model assumes a Brune-type source representation, characterized by a single corner frequency. This relation, which is used for the inversion of source spectra, enables the estimation of seismic moment, stress drop, and by extension, attenuation parameters from observed ground motion recordings. Although site effects are not explicitly modeled, they emerge as a by-product of the spectral residuals, allowing for indirect estimation of amplification behavior.

Applied to a regional dataset from Northeastern Italy, the spectral inversion yielded source and attenuation parameters that are consistent with values reported in prior studies across the Southern Alps tectonic domains. Site amplification estimates were validated, confirming the accurate recovery of frequency-dependent amplification peaks.

However, the study also talk about key limitations of the modeling approach. The challenge of ground motion prediction in low-to-moderate seismicity regions like Northeastern Italy is more due to the scarcity of strong-motion recordings. This data gap make it difficult to directly calibrate the empirical ground motion prediction equations for large magnitude events based on local conditions. As a result, practitioners often rely on two alternative strategies:

- **Calibration based on other regions**: Adopting GMPEs developed for other tectonically active regions (e.g., Scherbaum et al. [2005], Cotton et al. [2006]), with adjustments for local attenuation and site effects.
- **Stochastic simulation**: Generating synthetic accelerograms based on weak-motion spectral mod-

els and statistical scaling laws (e.g., Atkinson and Boore [1995], Boore [2003]), which can be extrapolated to larger magnitudes.

Cataldi et al. [2022]'s work contributes to the refinement of these approaches by offering a regionally calibrated spectral modeling framework that captures the essential physics of ground motion generation and propagation.

To talk about the recent studies in the region, Tarchini et al. [2025] provided a comprehensive catalog of events in Northeastern Italy from 2016 to 2023. Not only they provided M_W estimates for the region, they also established an empirical relation between M_W and M_L.

More recently, Moratto et al. [2026] did a comprehensive analysis of earthquake source parameters including seismic moment, corner frequency, static stress drop, apparent stress, radiated energy, and seismic efficiency in the Southeastern Alps between the years 2016 and 2023. They performed single station spectral inversion using SourceSpec software [Satriano, 2024].

They mentioned that radiated energy shows a weak magnitude trend, suggesting that smaller events may release energy less efficiently. They also claimed that events in Western Prealpine and the Eastern Dinaric Margin show higher stress drops and Central Alpine Foreland has lower stress drops.

1.2.1 Main Validation Reference

Since in this study, different and diverse methodological approaches were used, there was a strong need to a reference material in order to check and validate the achieved results through it. Thanks to the comprehensive study by Cataldi et al. [2025] that contains the computation of all key source parameters as well as site an attenuation properties, the best validating reference was found to fulfill this desire.

In their study, they have investigated stress drop and seismic efficiency distributions for Southeastern Alps through non-parametric GIT by using GITpy software [Morasca et al., 2025]. They found that the source parameters are widely dependent on spatial characteristics, specifically on the mechanical properties of the faults. As an example of their findings was the increase of the stress drop with depth.

They claimed about using reasonable assumptions during their procedures. For instance, they talked about taking advantage of multiple reference stations in their work. Although they mentioned that in inverse problems, it is challenging to retrieve a unique solution, they were able to find consistent results. According to which, the complexity of the seismicity in the study region was completely confirmed.

Considering energy computation, by using integral of source spectra with an extrapolation to omega-square model, they have reached the linear regression of the form $E = -8.738 + 1.266(M_0)$ to calculate

energy directly through using seismic moment.

1.3 General Seismotectonic Setting of the Study Area

Northeastern Italy lies at the meeting point of several major tectonic regions, making it a geologically complex and seismically active area. It includes the Eastern Southern Alps, shaped by the long-term collision between the Adriatic microplate and the Eurasian plate (Figure 3), as well as the Dinaric orogenic belt and the Adriatic foreland. These zones have evolved over millions of years through continuous tectonic interaction and deformation [Anderlini et al., 2020, Guidarelli et al., 2017, Cuffaro et al., 2010].

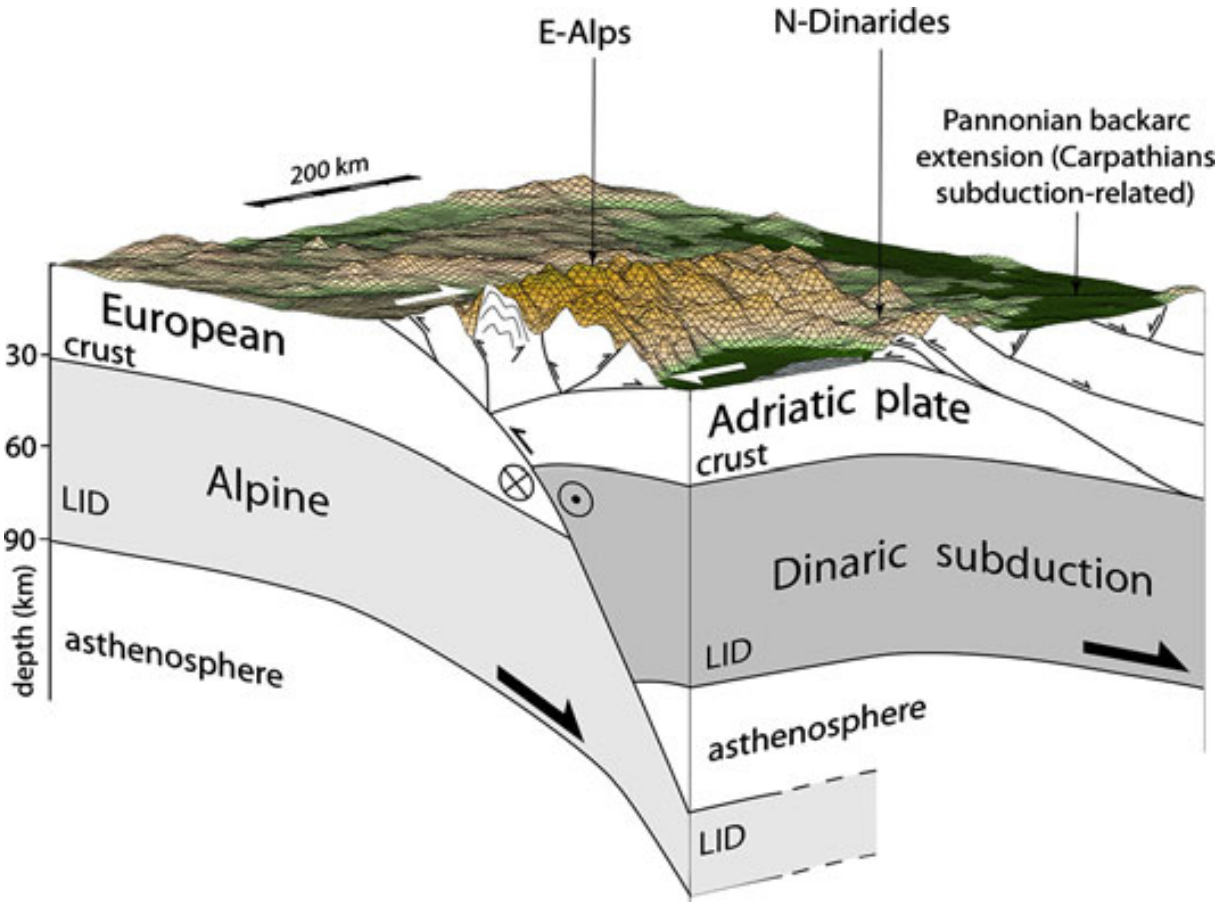

Figure 3: 3D reconstruction at the interference between the Alpine and Dinaric subductions in Northeastern Italy by Cuffaro et al. [2010]

The study area spans the regions of Friuli-Venezia Giulia, Veneto, and extends into western Slovenia, all of which exhibit ongoing faulting, significant crustal strain, and history of destructive seismic events [Cheloni et al., 2014, Rovida et al., 2011, Gasperini et al., 1999, Burrato et al., 2008, Aoudia et al., 2000, Sirovich and Pettenati, 2004, Hammerl, 1994, Galadini et al., 2005, Fitzko et al., 2005, Camassi et al., 2011, Rovida et al., 2017].

The tectonic activity in Northeastern Italy which is primarily driven by the convergence between the Adriatic and Eurasian plates is expressed through continental collision within the South-Eastern Alps, which mark the Northeastern edge of the active collisional zone [Brückl et al., 2010].

This area exhibits an important record of seismic activity, shaped by its complex tectonic setting. However, within the Eastern Southern Alps, the Venetian part generally demonstrates a lower cumulative seismic moment release compared to the more active Friuli area [Anderlini et al., 2020].

From a historical perspective, several significant seismic events—summarized in Table 1, are particularly worth mentioning for their impact and geotectonic relevance [Cheloni et al., 2014, Rovida et al., 2011, Gasperini et al., 1999, Burrato et al., 2008, Aoudia et al., 2000, Sirovich and Pettenati, 2004, Hammerl, 1994, Galadini et al., 2005, Fitzko et al., 2005, Camassi et al., 2011, Rovida et al., 2017]. These events provide valuable insights into the recurrence intervals, rupture mechanisms, and spatial distribution of seismic hazards across Northeastern Italy.

Year	**Location**	**Magnitude**
1348	Carinzia (Austrian border)	M_W 6.63
1403	Cividale del Friuli	M_W 5.56
1511	Slovenian Border	M_W 6.32
1690	Villach (Austrian border)	M_W 6.16
1695	Asolo	M_e 6.5
1700	Raveo	M_W 5.8
1776	Tramonti	M_W 5.8
1788	Tolmezzo	M_W 5.7
1794	Tramonti	M_W 5.6
1812	Pordenonese	M_W 5.6
1836	Bassano	M_W 5.5
1873	Bellunese	M_e 6.3
1891	Valle d'Illasi	M_W 5.87
1928	Carnia	M_W 6.0
1936	Bosco del Cansiglio	Me 6.1
1976	Friuli	M_W 6.4
1976	Friuli	M_W 5.6
1976	Friuli	M_W 5.9
1976	Friuli	M_L 6.1
1998	Slovenian Border	M_W 5.6

Table 1: Significant events in the study area.

2 Data

This section provides an overview of the two distinct datasets employed in the present study, each serving a specific role within the modeling framework. The first dataset, referred to as training dataset, consists of a selected collection of seismic events that are utilized to build, calibrate and optimize the empirical model. This dataset forms the empirical foundation upon which the model learns the relationships between input parameters and target variables, enabling the derivation of scaling laws.

The second dataset, called the validation dataset, is created separately and not used during training. This helps ensure an unbiased evaluation of the model's performance. It tests how well the model works on new data by comparing its predictions to actual results. This allows the study to measure how accurate and reliable the model is, and to spot any weaknesses or biases.

The whole dataset is divided into these two datasets and they are selected to ensure representative coverage of the regional seismicity, with attention to temporal completeness, magnitude distribution, and station-event geometry. Therefore, the magnitude, depth and distance ranges for both are consistent with each other without any significant bias.

2.1 Training Dataset

To initiate the development of a preliminary source parameter model and to assess its accuracy and performance, a selected dataset consisting of 35 seismic events was employed in this study. These events correspond to a subset of those previously analyzed by Cataldi et al. [2025] using GIT, thereby ensuring methodological consistency and enabling performance comparison.

A detailed summary of the event characteristics, including origin time, location, magnitude, and radiated energy, is presented in Table 2. Magnitude and energy estimates are adopted from Cataldi et al. [2025], while the other information, such as coordinates and time, are sourced from the Italian National Institute of Oceanography and Applied Geophysics (OGS) [Saraò et al., 2009].

Date (dd/mm/yyyy)	**Time** (HH:MM:SS)	**Latitude** (°)	**Longitude** (°)	**Depth** (km)	**Magnitude** (M_W)	**log Energy** (J)	**Number of Stations**
25/02/2018	08:16:29	46.37	12.59	9.5	3.6	9.69	103
25/02/2018	08:47:29	46.37	12.59	8.1	2.5	6.75	60
25/02/2018	14:36:25	46.36	12.58	9.4	2.9	7.64	75
25/02/2018	14:40:46	46.38	12.59	8.4	2.5	7.28	73
25/02/2018	15:53:05	46.38	12.59	10.6	3.4	9.56	101
25/02/2018	17:19:58	46.37	12.59	9.1	2.4	6.82	56
25/02/2018	17:40:14	46.37	12.60	9.6	2.9	7.83	80
25/02/2018	20:33:28	46.37	12.60	8.1	2.0	6.24	39
11/08/2018	03:26:59	46.33	13.03	10.7	2.8	8.00	96
11/08/2018	03:30:39	46.33	13.03	11.1	3.7	9.66	110
11/08/2018	03:38:03	46.33	13.03	10.9	2.2	7.02	73
11/08/2018	03:54:57	46.33	13.03	13.0	2.8	7.83	95
11/08/2018	04:52:10	46.33	13.03	11.5	2.4	7.45	83
14/06/2019	13:57:24	46.39	12.99	7.0	3.6	9.58	122
14/06/2019	16:13:10	46.39	12.99	6.7	2.1	6.36	61
15/06/2019	04:12:46	46.40	12.99	4.1	3.3	8.75	113
16/06/2019	13:40:55	46.39	12.99	6.4	2.8	8.15	106
03/07/2019	07:18:50	46.48	13.12	8.0	2.4	6.95	28
07/07/2019	21:09:33	46.40	13.00	6.2	2.8	8.14	51
28/07/2019	15:56:01	46.21	12.74	13.9	2.7	7.72	45
28/07/2019	18:33:26	46.47	13.15	6.8	2.0	5.87	25
28/07/2019	19:19:14	46.16	13.06	10.1	3.3	8.20	58
13/08/2019	19:58:44	46.34	12.76	11.4	2.4	7.40	32
29/08/2019	08:54:25	46.30	13.10	7.0	2.4	6.97	35
22/09/2019	12:58:43	46.44	13.02	10.9	3.6	9.65	62
27/03/2024	21:19:37	46.36	12.81	10.2	4.2	10.81	166
27/03/2024	21:45:45	46.35	12.82	8.7	2.2	7.01	116
28/03/2024	02:36:15	46.36	12.81	9.8	2.6	7.46	134
28/03/2024	20:11:21	46.36	12.82	7.2	1.9	6.34	61
29/03/2024	03:46:38	46.36	12.82	8.3	1.9	6.16	74
31/03/2024	01:56:34	46.36	12.80	7.5	1.8	6.13	56
01/04/2024	15:07:56	46.35	12.81	7.3	1.8	6.17	45
02/04/2024	03:36:09	46.36	12.82	9.6	2.1	6.51	86
05/04/2024	12:28:32	46.35	12.82	9.3	3.0	8.78	162
07/04/2024	03:27:54	46.35	12.80	10.1	2.3	7.01	93

Table 2: List of the events used in this study.

The dataset includes a total of 8325 waveforms of three components (two horizontal and one vertical), providing a robust basis for spectral analysis and inversion. The waveform data were retrieved from multiple seismic networks operating in the region, including:

- Friuli Venezia Giulia Accelerometric Network (**RF**) [University of Trieste, 1993]
- North-East Italy Seismic Network (**OX**) [Istituto Nazionale di Oceanografia e di Geofisica Sperimentale - OGS, 2016]
- Italian Strong Motion Network (**IT**) [Presidency of Council of Ministers - Civil Protection Department, 1972]
- Italian National Seismic Network (**IV**) [Istituto Nazionale di Geofisica e Vulcanologia (INGV),

2005]

- North-East Italy Broadband Network (**NI**) [Istituto Nazionale di Oceanografia e di Geofisica Sperimentale and University of Trieste, 2002]
- Mediterranean Very Broadband Seismographic Network (**MN**) [MedNet Project Partner Institutions, 1990]
- Trentino Seismic Network (**ST**) [Geological Survey-Provincia Autonoma di Trento, 1981]
- Austrian Seismic Network (**OE**) [GeoSphere (former ZAMG), 1987]
- Seismic Network of the Republic of Slovenia (**SL**) [Slovenian Environment Agency, 1990]
- Province Südtirol Network (**SI**) [Province Südtirol, 2006]
- Dynamic Planet (PD) multiparametric Northern Italy seismic network (**ZO**) [Massa et al., 2021]

Figure 4 maps the study area, emphasizing the locations of earthquakes and stations. Epicenters of the analyzed events are indicated by stars, and triangles represent the positions of the used stations which are colored based on their recording network.

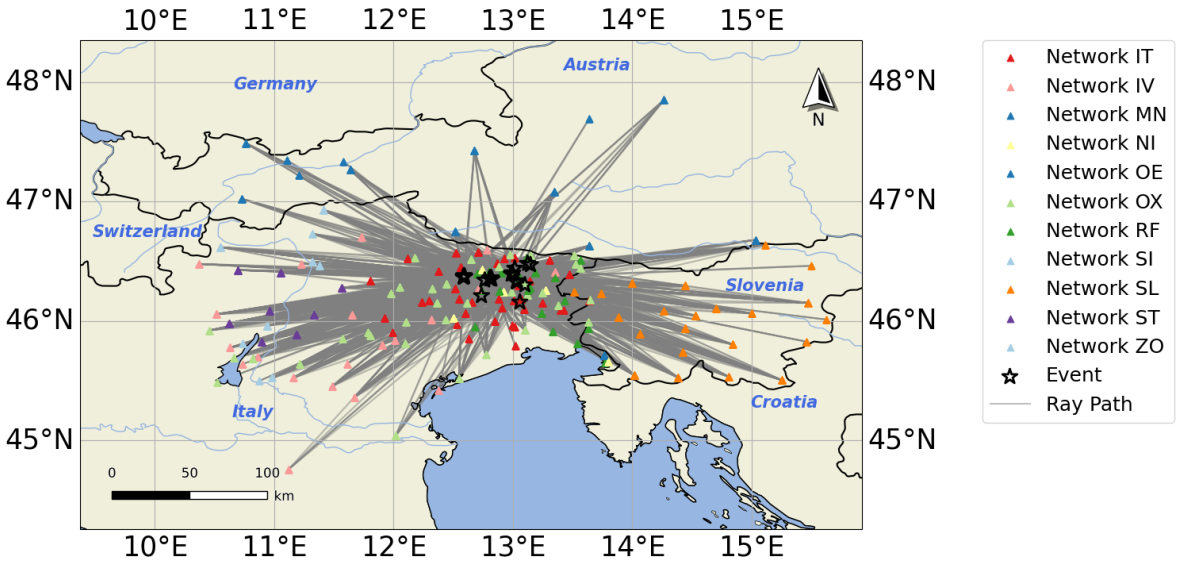

Figure 4: Map of the study area. Black stars show seismic events. Triangles indicate seismic stations color coded based on the seismic network. Network names appear in the legend.

Figure 5 offers a detailed overview of the dataset distribution across key seismological parameters. The central panel features a scatter plot of individual recordings, organized by event magnitude and hypocentral distance. Data points are color-coded by focal depth, enabling simultaneous evaluation of

depth-dependent variations in source-receiver geometry. This visualization helps in identifying clustering patterns and potential depth-related biases.

The top panel displays a histogram of recording counts as a function of hypocentral distance, illustrating the network's spatial coverage and number of observations across varying source-receiver pairs, which is essential for analyzing attenuation and distance-scaling behavior.

The right panel presents a histogram of event counts per magnitude bin, providing insight into the magnitude distribution of the dataset and supporting an assessment of its completeness across the magnitude range.

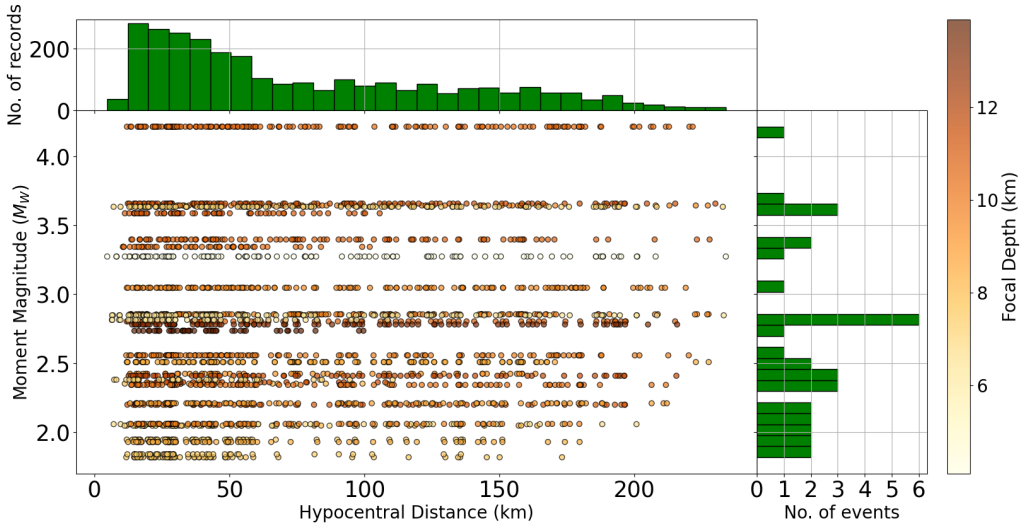

Figure 5: Magnitude-Distance distribution of data recordings, color coded based on hypocentral depth. The number of events per magnitude and the number of recordings per hypocentral distance are shown in histograms.

To enhance the stability and reliability of the inversion results, specific selection criteria were applied to the dataset. Each seismic event was required to be recorded by a minimum of three stations, and conversely, each station had to record at least three distinct events. Additionally, adequate azimuthal coverage, no less than 180° for all events, reduces potential bias arising from sparse or uneven station-event pairings. Similar to these constraints are also considered by other studies [e.g., Yen et al., 2024, Cataldi et al., 2022].

The general characteristics of the seismic stations utilized in this study are summarized in Figure 6 based on information from the ITACA database [Felicetta et al., 2023]. This figure presents a multi-panel classification of the stations according to several key criteria, allowing for a comprehensive overview of

the network configuration and instrumentation. In particular, panel (a) of Figure 6 categorizes the recordings using two-letter station codes, following the nomenclature defined by the FDSN standards [FDSN, 2007]. Within this coding scheme, the first letter denotes the sampling rate and response bandwidth of the instrument, while the second letter specifies the sensor type. A detailed explanation of these instrument classifications, including their operational characteristics and deployment contexts, is provided in Table 3. This classification framework facilitates a clearer understanding of the data quality and spectral coverage associated with each station, which is essential for evaluating the reliability of inversion results and source parameter estimates.

Code	Meaning	Description
HH	High Gain, High Sampling	Broadband seismometer with high sensitivity and ≥ 80 Hz sampling rate
SH	Short Period, High Gain	Short-period sensor, typically with 1–10 Hz natural frequency
EH	Extremely Short Period, High Gain	High-frequency sensor with ≥ 250 Hz sampling, used for strong motion or local events
HG	High Gain, Accelerometer	Accelerometer channel with high gain, often used in strong motion networks
HN	High Gain, Accelerometer	Similar to HG, but typically digitized at lower resolution or used in older networks

Table 3: Explanation of different instrument types used in this study.

Panel (b) of Figure 6 presents a classification of the seismic stations based on topographic characteristics, offering insight into the geomorphological context of each recording site. The categorization scheme, detailed in Table 4, is derived from established morphological parameters, including the average ground inclination (i), the type of the relief, and the relative position of the site with respect to nearby ridges [Di Capua et al., 2010, 2011]. These criteria provide a framework for assessing potential topographic effects which can affect site-specific variations in seismic wave propagation. By incorporating such terrain-based characteristics, the study enhances its capacity to interpret spectral variability and inversion stability in relation to local geological and geomorphological conditions.

Code	Description
T1	flat surfaces, isolated slopes or reliefs with $i \leq 15°$
T2	Slopes with $i > 15°$
T3	Reliefs with ridge top width much smaller than the base, and $15° \leq i \leq 30°$
T4	Reliefs with ridge top width much smaller than the base, and $i > 30°$

Table 4: Explanation of different topography types for the stations used in this study.

Panels (c) and (d) of Figure 6 present the classification of seismic stations according to the Eurocode 8 (EC8) [Aucun et al., 2012] framework, which establishes standardized soil categories for seismic design

applications across Europe. This classification is primarily based on the time-averaged shear wave velocity in the upper 30 meters of the subsurface (V_{S30}), complemented by geological profiling and estimates of the depth to the bedrock [Comité Européen de Normalisation, 2004, Di Capua et al., 2010]. These parameters are critical for assessing site response characteristics and are widely used in engineering seismology and seismic hazard modeling. The specific definitions and thresholds associated with each EC8 soil classes are summarized in Table 5, providing a consistent basis for evaluating site amplification effects and integrating station data into the inversion and modeling framework employed in this study.

Subsoil Class	**Description**	V_{S30} **(m/s)**
A	Rock or other rock-like geological formation, including at most 5 m of weaker material at the surface	> 800
B	Deposits of very dense sand, gravel, or very stiff clay, at least several tens of m in thickness, characterised by a gradual increase of mechanical properties with depth	360 - 800
C	Deep deposits of dense or medium-dense sand, gravel or stiff clay with thickness from several tens to many hundreds of meters	180 - 360
D	Deposits of loose-to-medium cohesionless soil (with or without some soft cohesive layers), or of predominantly soft-to-firm cohesive soil	< 180
E	A soil profile consisting of a surface alluvium layer with V_S values of type C or D and thickness varying between about 5 m and 20 m, underlain by stiffer material with V_S > 800 m/s	—-

Table 5: Explanation of different EC8 and V_{S30} types for the stations used in this study.

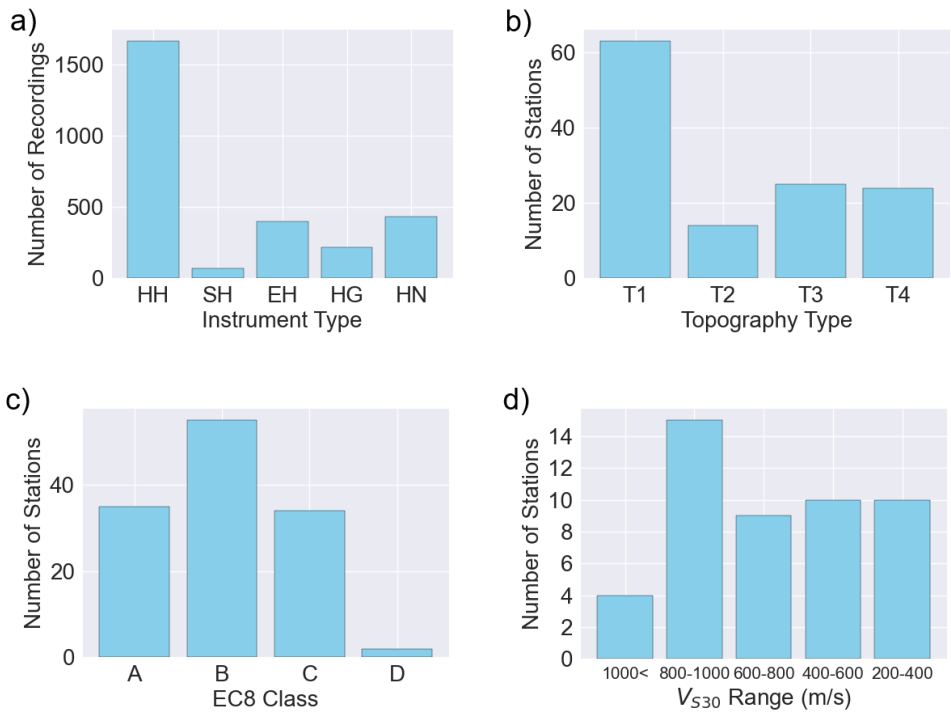

Figure 6: Histograms of a) the distribution of seismic recordings by instrument type, b) distribution of seismic stations across topographic categories, c) number of seismic stations categorized by EC8 soil class, and d) number of seismic stations grouped by V_{S30} ranges.

2.2 Validation Dataset

To assess the reliability of the coefficients obtained from the model, derived via the GIT applied to the training dataset, an independent analysis was conducted using an additional set of 56 seismic events from the same geographical region. These events are also included in the GIT study by Cataldi et al. [2025]. The dataset consists of accelerometric recordings collected by the strong motion network operated by the SeisRaM group at the University of Trieste [University of Trieste, 1993, Costa et al., 2014, 2022], with total of 4874 three components waveform records.

A detailed summary of these events is provided in Table 6, where magnitude and radiated energy values are taken from Cataldi et al. [2025], while the other information are obtained from the National Accelerometric Network of Italy (RAN) [Presidenza del Consiglio dei Ministri, Dipartimento della Protezione Civile, 2014].

Date (dd/mm/yyyy)	**Time** (HH:MM:SS)	**Latitude** (°)	**Longitude** (°)	**Depth** (km)	**Magnitude** (M_W)	**log Energy** (J)	**Number of Stations**
10/08/2016	02:38:05	46.40	12.97	6	2.8	7.90	7
10/08/2016	04:52:47	46.39	12.94	11	3.0	8.54	10
09/02/2017	08:14:08	45.78	11.16	11	3.3	9.43	14
06/09/2017	12:22:29	46.27	11.98	9	3.4	9.35	22
06/09/2017	12:30:32	46.27	11.99	10	3.0	8.17	16
31/10/2017	04:59:03	45.84	10.91	11	2.9	8.44	5
17/01/2018	10:22:20	46.31	13.57	5	3.6	9.47	25
19/01/2018	17:39:43	46.42	13.03	9	3.6	9.58	29
28/03/2018	07:36:52	45.88	11.84	10	2.8	8.90	10
09/05/2018	21:48:01	46.32	13.11	7	3.3	9.14	29
10/11/2018	07:59:36	46.30	13.23	4	2.7	8.19	15
19/11/2018	14:23:45	46.16	13.45	10	2.7	7.65	10
08/01/2019	04:03:11	45.72	13.83	3	2.5	7.16	6
08/08/2019	05:36:35	45.78	11.07	12	3.2	9.28	26
23/10/2019	17:15:20	46.30	13.08	10	2.4	6.79	8
27/10/2019	17:52:55	46.20	12.78	13	3.0	8.46	23
03/01/2020	12:53:40	46.40	12.61	10	2.8	7.87	10
13/07/2020	12:06:53	46.33	12.64	9	3.5	9.04	44
17/07/2020	02:50:57	46.32	13.54	7	4.0	10.54	46
16/01/2021	23:54:55	46.40	12.98	8	3.1	8.64	38
30/01/2021	09:56:28	46.13	12.18	1	2.8	8.01	4
22/02/2021	12:04:06	45.78	10.98	12	3.3	9.34	26
10/08/2021	15:21:30	46.11	13.41	7	2.6	7.52	6
10/08/2021	15:23:01	46.09	13.40	12	2.4	7.03	5
06/09/2021	09:18:02	46.35	13.21	10	3.1	8.84	39
28/09/2021	00:45:55	45.95	12.02	12	3.4	9.27	64
29/09/2021	14:20:38	45.94	12.02	11	3.3	9.21	49
21/10/2021	00:28:54	46.43	13.07	13	3.6	9.42	66
22/10/2021	03:17:17	46.43	13.04	11	2.9	8.21	23
15/11/2021	18:54:11	46.39	13.28	11	2.3	7.30	9
30/11/2021	08:21:35	46.37	13.04	8	2.4	6.91	26
15/02/2022	02:12:49	46.45	13.25	10	3.1	8.72	55
20/02/2022	21:05:02	46.12	13.36	10	2.4	7.25	24
24/02/2022	18:34:53	46.33	12.61	10	2.3	7.23	11
03/05/2022	08:33:59	46.36	12.87	9	2.6	7.75	41
17/06/2022	08:03:28	46.44	13.02	10	2.4	7.41	15
16/07/2022	13:30:40	46.32	12.75	9	3.0	8.12	58
25/08/2022	00:34:36	46.24	12.72	9	3.1	9.10	66
17/09/2022	23:32:17	46.41	12.63	8	2.5	7.28	20
01/11/2022	20:17:22	46.15	13.45	11	2.8	8.31	44
10/11/2022	21:22:12	46.44	11.67	12	2.6	8.15	5
28/11/2022	01:42:17	46.33	12.63	11	2.7	7.96	45
17/12/2022	04:59:18	46.26	12.54	10	2.6	7.85	34
19/12/2022	03:41:53	46.31	12.61	10	2.7	7.94	42
23/12/2022	20:46:12	46.32	12.59	11	2.6	7.76	39
03/02/2023	23:10:48	46.29	12.71	8	2.5	7.86	44
11/03/2023	02:56:31	46.36	12.91	11	3.0	9.03	60
23/06/2023	05:21:47	46.05	12.34	8	2.8	7.45	29
11/09/2023	13:21:26	46.09	13.70	14	3.3	8.85	46
16/10/2023	20:13:03	46.41	13.04	9	2.7	7.85	47
05/11/2023	23:01:00	46.34	13.57	7	2.8	7.24	37
11/11/2023	08:28:29	46.31	13.29	8	2.3	7.53	16
30/12/2023	05:47:10	45.74	11.03	4	2.6	7.99	6
07/01/2024	12:01:33	46.19	12.42	11	2.5	7.70	22
18/07/2024	10:21:39	46.34	13.27	9	2.9	8.41	49
04/09/2024	22:25:09	46.35	12.82	10	2.9	8.40	58

Table 6: List of events used to check the coefficients achieved by the model.

Figure 7 presents the geographical distribution of the study area, highlighting the validating seismic events and recording stations. The epicentral locations of the analyzed earthquakes are marked by red stars, while the blue triangles denote the positions of the used stations. All stations included in this dataset are equipped with accelerometers.

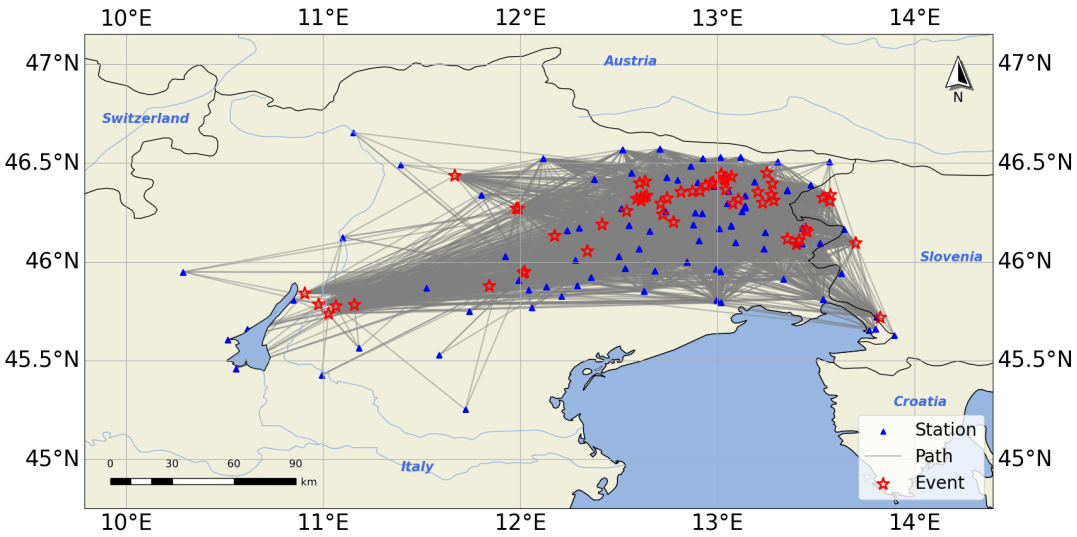

Figure 7: Events used to check the coefficients achieved by the model. Red stars showing seismic events. Blue triangles indicating seismic stations.

Figure 8 provides a comprehensive visualization of the dataset distribution regarding different key seismological parameters. The central panel displays a scatter plot of individual recordings, organized by event magnitude and hypocentral distance. Each data point is color-coded according to the focal depth of the corresponding earthquake, allowing for the assessment of depth-dependent variability in source-receiver pairs. This panel helps the identification of potential biases in the dataset related to depth and distance.

The top panel presents a histogram illustrating the number of available recordings as a function of hypocentral distance. This distribution highlights the spatial coverage of the network and the number of observations for different source-receiver pairs, which is critical for evaluating distance-dependent scaling.

The right panel shows a histogram of event counts per magnitude bin, which is showing the magnitude distribution of the analyzed events. This helps assess the completeness of the dataset across the magnitude range.

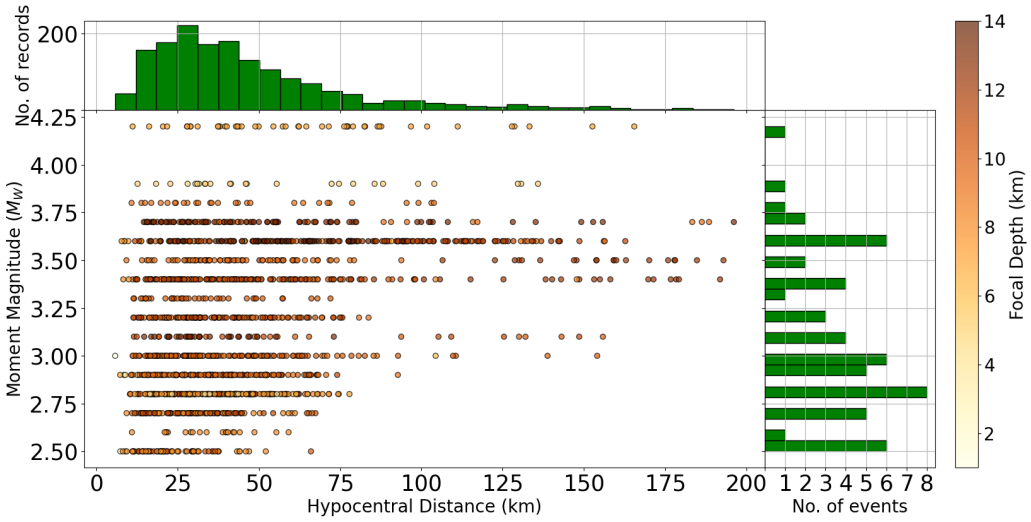

Figure 8: Magnitude-Distance distribution of data recordings to check the coefficients of the model, color coded based on hypocentral depth. The number of events per magnitude and the number of recordings per hypocentral distance are shown in histograms.

3 Methodology

This chapter talks about the methodological framework used to address the research objectives and ensure the reliability of the results. It describes the analytical procedures and computational tools used throughout the study. Each step, from data selection and preprocessing to model calibration and validation, is attempted to be completely documented to support transparency and facilitate comparative evaluation.

3.1 Data Processing and Analysis

In this part, the framework used for seismic data processing and parameter extraction is explained. The initial phase involved the acquisition of waveform data in both MSEED [FDSN Working Group II on Data Exchange, 2000] and SAC [Goldstein et al., 2003] formats, ensuring compatibility with standard seismological analysis tools and preserving metadata integrity.

Following data retrieval, instrumental response functions were removed from the raw data to obtain physical ground motion quantities, either acceleration or velocity, depending on the sensor type. This correction step is critical for ensuring that subsequent spectral analyses will provide true ground motion characteristics.

Subsequently, a dynamic band-pass filter was applied to the corrected waveforms to isolate the frequency range of interest and remove the noise from the usable bandwidth. The corner frequencies of this filter were determined using the method proposed by Gallo et al. [2014], which accounts for spectral content and optimizes the filter parameters accordingly. An example of the corner frequency selection process is presented in Figure 9, highlighting the criteria used to define the passband and demonstrating the effectiveness of the filtering strategy in enhancing signal quality for spectral inversion.

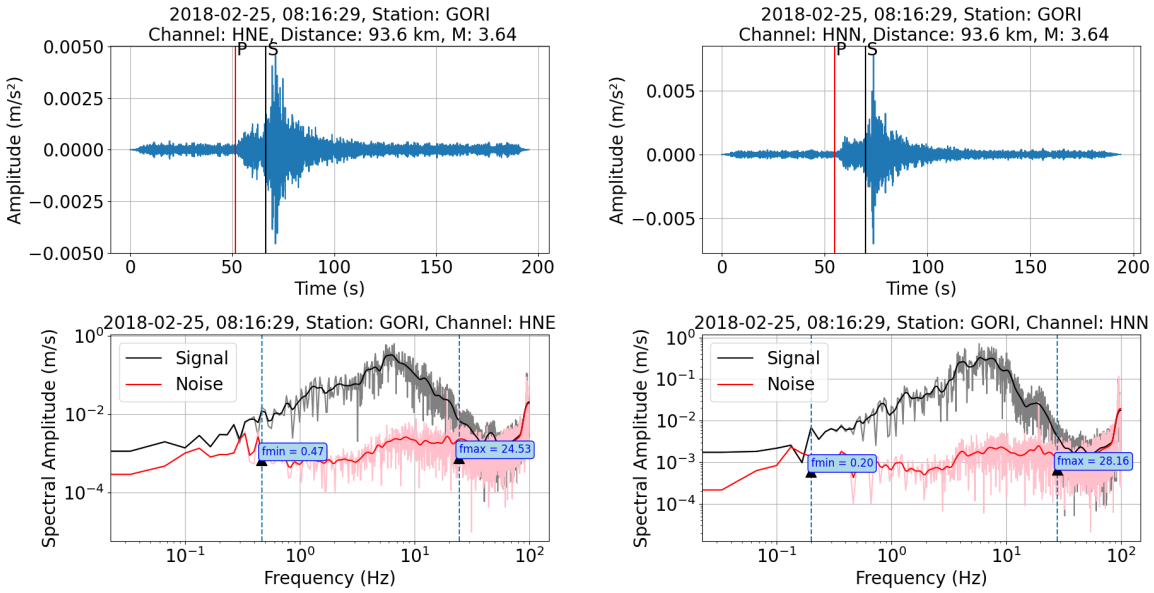

Figure 9: Example of finding corner frequencies of the filter using the method proposed by Gallo et al. [2014]. (Top: the red line is P-wave onset and the black line is S-wave onset. Bottom: fmin and fmax are indicating high-pass and low-pass corner frequencies respectively.)

Subsequent to instrumental correction and filtering, the waveform data were subjected to double integration, first to obtain velocity time series, and then to derive displacement records. This step is essential for analyses requiring displacement spectral parameters, such as seismic moment estimation and corner frequency.

Following integration, the S-wave window was selected to isolate the portion of the waveform containing the highest energy content, which is critical for accurate spectral decomposition and source parameter retrieval. As emphasized by Cruz Hernández and Castro [2025], approximately 91% of the total radiated energy is attributed to S-wave arrivals, underscoring their fundamental role in seismic energy release. This observation is strongly supported by earlier foundational studies. Haskell [1964] and Izutani and Kanamori [2001] demonstrated that most of radiated seismic energy originates from S-wave components, particularly under far-field conditions where shear-wave radiation dominates the energy budget. Moreover, Spallarossa et al. [2021], Picozzi et al. [2018a] and many other studies performed their analyses on S-waves as well. Accordingly, precise selection of the S-wave window is essential for reliable energy computation, as it directly influences the spectral content and amplitude estimates used in the inversion procedures.

Consequently, the window is initiated 0.1 seconds prior to the S-wave arrival time to ensure full capture of the shear-wave onset. The end of the window is determined dynamically based on thresholds

of accumulated energy, which are scaled according to the source-to-site distance (R), following the empirical criteria proposed by Picozzi et al. [2019] and Spallarossa et al. [2021]. This distance-dependent approach ensures that the selected window will cover the complete S-wave packet while minimizing contamination from coda and scattered phases, thereby enhancing the reliability of spectral fitting and inversion results.

- 90% of the total energy when ($R < 25$ km)
- 80% for (25km $< R <$ 50 km)
- 70% when ($R > 50$ km)

For both seismic moment and radiated energy estimations, the waveform analysis was conducted within a constrained time window. Under this constrain, in any case, the minimum length of the window should not be less than 4 seconds and not more than 30 seconds. This temporal range was selected to ensure consistent treatment across all events and capturing the dominant energy-carrying portion of the signal.

To quantify the spectral characteristics of each event–station pair, the Fourier amplitude spectrum ($FAS_{ij}(f)$) was computed at each frequency (f) for the ith event recorded at station j. In order to obtain a single representative spectrum per station per event, the vectorial sum of the two horizontal components was calculated following the approach of Bindi et al. [2009, 2018], Drouet et al. [2008]:

$$FAS = \sqrt{EW^2 + NS^2} \tag{8}$$

This formulation preserves the amplitude of the horizontal components and for doing this calculation, the components were not rotated. An illustrative example of the resulting spectra is presented in Figure 10, showing the frequency-dependent behavior.

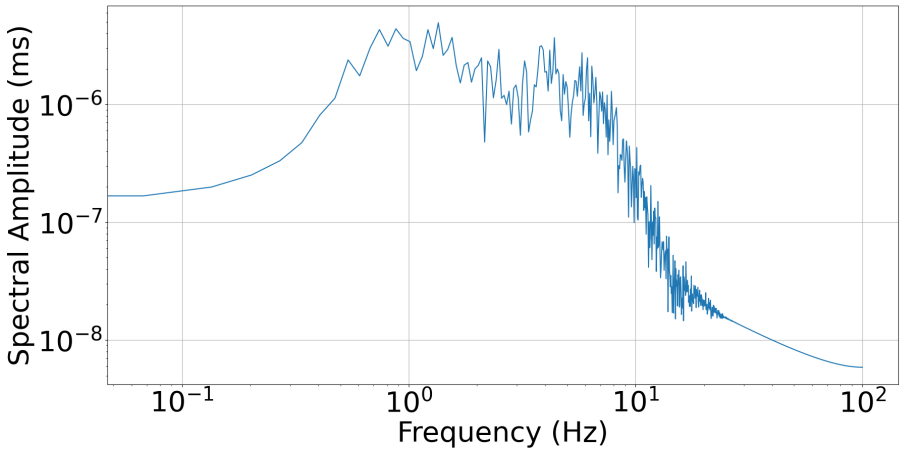

Figure 10: Example of Fourier Amplitude Spectrum (filtered between 0..47 Hz and 24.53 Hz).

The GIT was applied across a frequency range spanning from 0.5 Hz to 20 Hz. This interval was selected to ensure adequate spectral resolution while maintaining compatibility with the signal characteristics and time window constraints of the dataset. A key requirement for performing GIT at each frequency is the availability of a minimum of three valid samples, which ensures statistical robustness and prevents instability in the inversion process.

The lower bound of 0.5 Hz was chosen based on the minimum time window length, which allows for the inclusion of at least two complete cycles of the signal. Given that one cycle at 0.25 Hz corresponds to 4 seconds (the minimum window duration), frequencies below 0.5 Hz would not satisfy the cycle completeness criterion and were therefore excluded from the analysis.

To extract the source spectrum, all computations were performed independently for each frequency point. This frequency-by-frequency approach allows for precise characterization of spectral features and avoids particular assumptions about the functional form of the source spectrum. Importantly, each frequency point used in the inversion must lie within both the predefined GIT frequency range and the usable spectral bandwidth determined by the corner frequencies of the applied band-pass filter. These frequencies, which vary depending on event-specific characteristics, are illustrated in Figure 11 and serve as a constraint to ensure that only reliable spectral content is included in the inversion.

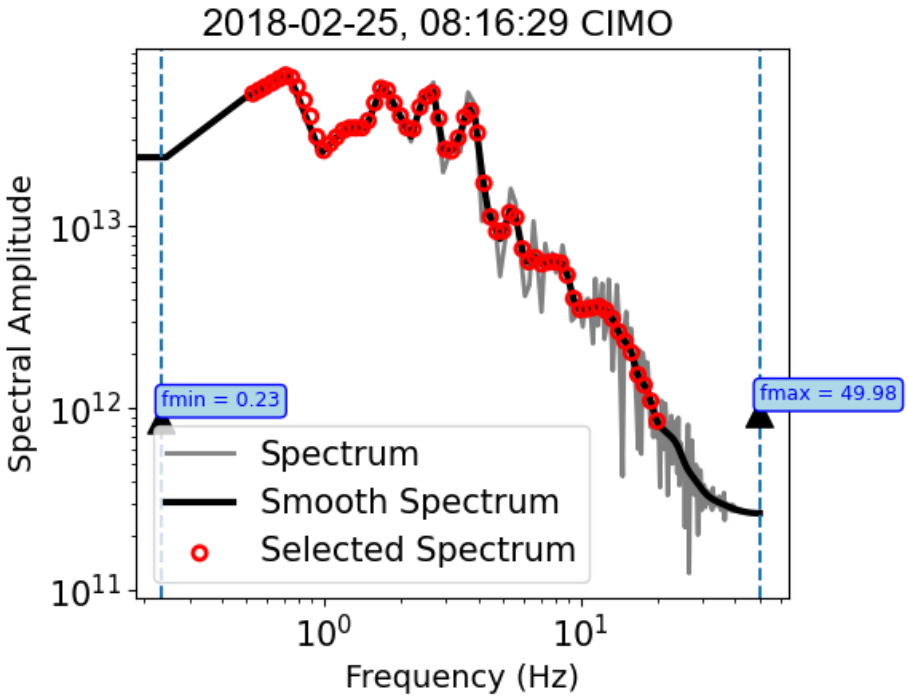

Figure 11: Example of selected frequency points of a spectrum to perform GIT. fmin and fmax are indicating high-pass and low-pass corner frequencies respectively.

3.2 The Generalized Inverse of a Matrix

When dealing with square matrices, computing the inverse is a direct procedure. However, in the case of non-square matrices, a generalized inverse must be employed to obtain meaningful solutions. The Generalized Inverse Technique is commonly utilized to solve linearized systems of the form:

$$\mathbf{Gm} = \mathbf{d} \tag{9}$$

In this formulation, $\mathbf{m} = (m_1, m_2, \ldots, m_M)^T$ denotes an M-component column vector consisting of the unknown model parameters, while $\mathbf{d} = (d_1, d_2, \ldots, d_N)^T$ is an N-component column vector of known parameters obtained from measured data. The system matrix $\mathbf{G} = (G_{ij})$ serves as the forward operator, containing the relationship between the model space and the data space.

Classical linear algebra dictates that a strict inverse $\mathbf{G}^{-1}$ only exists under specific conditions, typically when the matrix is square and non-singular. In general, an exact solution to Equation 9 may be unattainable, instead, an approximate solution can be derived using the generalized inverse $\mathbf{G}^{\dagger}$ [Penrose, 1955, Menke, 1984], which is optimized according to certain criteria. Specifically, when $N > M$

(an overdetermined system) and **G** has full column rank, the generalized inverse is uniquely defined as:

$$\mathbf{G}^{\dagger} = (\mathbf{G}^T\mathbf{G})^{-1}\mathbf{G}^T \tag{10}$$

This formulation yields the least-squares estimate of the model parameters, providing a robust solution that minimizes the discrepancy between predicted and observed data.

This study addresses a linearized inverse problem formulated in the least-squares framework. The model is trying to resolve a set of unknown parameters (that include the earthquake source spectra, propagation path effects, and site spectral responses). The methodological foundation was originally proposed by Andrews [1986] for the characterization of earthquake source spectra, subsequently refined by Castro et al. [1990], and from that time on has been widely adopted and adapted by numerous researchers [e.g., Parolai et al., 2000, Oth et al., 2008]. This approach enables the decomposition of source, path, and site contributions of the observed ground motion, thereby facilitating a more accurate interpretation of seismic waveforms and regional attenuation characteristics.

3.3 Linearizing the Problem and Spectral Decomposition using GIT

The GIT approach is based on the assumption that the logarithm of the amplitude spectrum of the seismogram $U_{ij}(f)$ recorded at the jth site for the ith event can be expressed as the sum of three contributing terms [Andrews, 1986, Castro et al., 1990, Klin et al., 2017, Oth et al., 2008, Zollo et al., 2014]:

$$\log U_{ij}(f) = \log S_i(f) + \log Z_j(f) + \log A(r_{ij}, f) \tag{11}$$

where f represents frequency, $S_i(f)$ is the source term for the ith event, $Z_j(f)$ corresponds to the seismic response at the jth site, and $A(r_{ij}, f)$ accounts for attenuation or propagation effects, describing the impact on seismic waves as they travel a distance r_{ij} through the Earth's crust from the event source to the site location.

To resolve the earthquake source characteristics, site spectral response, and propagation effects, a least-squares inversion framework is employed. This can be implemented using two principal methodologies [Shible et al., 2022]:

- *Parametric Approach*: Assumes that seismic properties, specially attenuation along the propagation path conform to predefined functional forms. The inversion is executed in a single step to simul-

taneously estimate the source and site spectra, along with a parameterized attenuation model. This approach explicitly solves for model parameters embedded within the assumed functional relationships [Shible et al., 2022, Oth et al., 2008, Bindi and Kotha, 2020, Cataldi et al., 2022].

- *Non-parametric Approach*: Avoids imposing any predefined functional form on the source, site or path terms. Only the attenuation component is constrained to follow a smoothly decaying trend with respect to hypocentral distance. This method offers greater flexibility in capturing complex spectral variations without model bias [Shible et al., 2022, Oth et al., 2008, Bindi and Kotha, 2020].

The logarithmic formulation of the parametric model used for inversion at a given frequency index k is given by the following equation [Cataldi et al., 2022]:

$$\begin{aligned} \log U_{ijk}(r_{ij}, f_k) = \log(2\pi f_k) + \log\left(\frac{\Theta_{\lambda\varphi} F \xi}{4\pi\rho v_s^3 R_0}\right) + \log M_{0i} \\ - \log\left(1 + \left(\frac{f_k}{f_{ci}}\right)^2\right) + \log G(r_{ij}, f_k) \\ - \frac{\pi f_k r_{ij}}{v_s Q_0} + \log A_j - \pi f_k \kappa_{0j} + \varepsilon_i^{SO} + \varepsilon^P \end{aligned} \tag{12}$$

This functional representation is derived from a standard spectral decomposition model, improved by uncertainty collector terms ε^{SO} and ε^P, which account for residual variability associated with the source and propagation components, respectively. The source term is modeled using a simplified far-field Brune spectrum [Brune, 1970], wherein the corner frequency serves as a key parameter controlling the spectral shape. The primary parameters influencing the source spectrum include:

- Seismic moment, M_0 (Nm)
- Average radiation pattern, $\Theta_{\lambda\varphi}$
- Free surface amplification factor, F
- Partition factor for shear-wave energy into two horizontal components, ξ
- Reference distance for normalization, R_0 (m)
- Average density near the source, ρ (kg/m^3)
- Shear wave velocity near the source, v_s (m/s)

According to Cataldi et al. [2022], the model parameter vector is structured as follows:

$$\mathbf{p} = \begin{bmatrix} \left[\log M_{01}, \ldots, \log M_{0N_i}\right], \left[f_{c1}, \ldots, f_{cN_i}\right], Q_0, \\ \left[\log A_1, \ldots, \log A_{N_j}\right], \left[\kappa_1, \ldots, \kappa_{N_j}\right], \left[\varepsilon_1^{SO}, \ldots, \varepsilon_{N_i}^{SO}\right], \varepsilon^P \end{bmatrix} \tag{13}$$

It consists of N_i elements representing source spectra, corner frequency, and source uncertainty vectors, along with one term each for the attenuation factor and propagation uncertainty. Additionally, it includes N_j elements corresponding to frequency-independent site amplification and site-related attenuation vectors.

On the other hand, the non-parametric approach directly derived from data without assuming functional forms [Oth et al., 2008, Bindi and Kotha, 2020]. According to Oth et al. [2008], using the parametric approach often leads to the issue of obtaining negative values for Q which can stem from assumptions made about geometrical spreading, as noted by Castro et al. [1990], or from the fact that very simple parametrizations cannot explain attenuation in a certain region. As a result, the nonparametric approach was chosen to use in this study. This approach can be applied in two ways [Shible et al., 2022]:

- *One-Step non-parametric GIT*
- *Two-Step non-parametric GIT*

The one-step GIT method (to obtain source and site) can be executed in two variations [Shible et al., 2022]:

- *Using a predefined propagation term*
- *Without a predefined propagation term*

Although a predefined propagation term is used as input, the inversion remains non-parametric because no functional forms are imposed on the source or site terms. In this case, the known propagation term allows the separation of source and site contributions, enabling their direct estimation from the observed spectra using Equation 11, which can be rewritten as:

$$\log U_{ij}(f) - A(r_{ij}, f) = \log S_i(f) + \log Z_j(f) \tag{14}$$

To describe the propagation term, which represents the attenuation of seismic waves as they travel from

the source to the site, the following equation is used [Klin et al., 2017]:

$$A(r_{ij}, f) = -\gamma \log(r_{ij}) - \frac{\pi f r_{ij}}{v_s Q_s(f)} \tag{15}$$

where f is the frequency, γ is the geometrical spreading factor (ranges between 1 for spherical waves and 0.5 for cylindrical ones), v_s is the S-wave average velocity, Q_s is the quality factor for which the equation which was proposed by [Console and Rovelli, 1981] and used by many other studies like Gallo et al. [2014] was chosen to use as $Q(f) = 80f^{1.1}$, and r is hypocentral distance between the event i and station j.

Finally, determining source properties and site effects requires solving the following equation of the form $\mathbf{Gm} = \mathbf{d}$ for each frequency [Klin et al., 2017]:

$$\begin{pmatrix} \log U_{11} - A(r_{11}) \\ \log U_{12} - A(r_{12}) \\ \vdots \\ \log U_{21} - A(r_{21}) \\ \vdots \\ \log U_{ij} - A(r_{ij}) \end{pmatrix} = \begin{pmatrix} \underbrace{\begin{matrix} 1 & 0 & 0 & . & \dots \\ 0 & 1 & 0 & . & \dots \\ . & . & . & . & \dots \\ 1 & 0 & 0 & . & \dots \\ \vdots & \vdots & \vdots & \vdots & \vdots \end{matrix}}_{\text{stations}} & \underbrace{\begin{matrix} 1 & 0 & 0 & . & \dots \\ 1 & 0 & 0 & . & \dots \\ . & . & . & . & \dots \\ 0 & 1 & 0 & . & \dots \\ \vdots & \vdots & \vdots & \vdots & \vdots \end{matrix}}_{\text{sources}} \end{pmatrix} \begin{pmatrix} \log Z_1 \\ \vdots \\ \log Z_j \\ \log S_1 \\ \vdots \\ \log S_i \end{pmatrix} \tag{16}$$

Considering Equation 16, all U_{ij} values correspond to the Fourier amplitude spectra of each event recorded at each station. The left side of the system matrix reflects elements linked to site parameters, whereas the right side corresponds to components tied to source terms. Each row represents a spectrum. On the left-hand side of the matrix, the column related to the station receives a value of 1, while on the right-hand side, the column corresponding to the event associated with the spectrum is assigned a value of 1.

On the other hand, when a predefined propagation term is not used, Equation 11 can be solved in a single step. In this case, the attenuation, site, and source terms are determined independently for each frequency [Oth et al., 2011]:

$$\begin{pmatrix} \log U_{11} \\ \vdots \\ \log U_{ij} \\ \vdots \\ 0 \\ \vdots \\ 0 \end{pmatrix} = \begin{pmatrix} \underbrace{\begin{matrix} 1 & 0 & 0 & . & \dots \\ 0 & 1 & 0 & . & \dots \\ . & . & . & . & \dots \\ 1 & 0 & 0 & . & \dots \\ \vdots & \vdots & \vdots & \vdots & \vdots \\ w_1 & 0 & 0 & . & \dots \\ -w_2/2 & w_2 & -w_2/2 & . & \dots \\ 0 & -w_2/2 & w_2 & -w_2/2 & \dots \end{matrix}}_{\text{attenuation parameters}} & \underbrace{\begin{matrix} 1 & 0 & 0 & . & \dots \\ 0 & 1 & 0 & . & \dots \\ . & . & . & . & \dots \\ 1 & 0 & 0 & . & \dots \\ \vdots & \vdots & \vdots & \vdots & \vdots \\ . & . & . & . & \dots \\ . & . & . & . & \dots \\ \vdots & \vdots & \vdots & \vdots & \vdots \end{matrix}}_{\text{stations}} & \underbrace{\begin{matrix} 1 & 0 & 0 & . & \dots \\ 1 & 0 & 0 & . & \dots \\ . & . & . & . & \dots \\ 0 & 1 & 0 & . & \dots \\ \vdots & \vdots & \vdots & \vdots & \vdots \\ . & . & . & . & \dots \\ . & . & . & . & \dots \\ \vdots & \vdots & \vdots & \vdots & \vdots \end{matrix}}_{\text{sources}} \end{pmatrix} \begin{pmatrix} \log A_1 \\ \vdots \\ \log A_{N_D} \\ \log Z_1 \\ \vdots \\ \log Z_j \\ \log S_1 \\ \vdots \\ \log S_i \end{pmatrix} \tag{17}$$

Factors linked to attenuation parameters are embedded in the left segment of the system matrix, while the middle segment belongs to site terms and the right segment belongs to source-related components. The weighting factor w_1 ensures that $A(r_0, f) = 1$ at the reference distance, whereas w_2 governs the smoothness of the solution [Castro et al., 1990]. Each row, apart from those incorporating weighting factors, is for each of the spectra. The column related to the distance bin between event and station on the left side of the system matrix is receiving a value of 1 and the column representing the station is set to 1 on the middle segment of the matrix, while the column linked to the spectrum-related event is marked with a value of 1 on the right side.

In the two-step GIT method, the spectral amplitudes $U(r, f)$ at frequency f are initially expressed as a function of distance, following the formulation [Castro et al., 1990, 1996, Oth et al., 2008]:

$$U_{ij}(r_{ij}, f) = A(r_{ij}, f)\hat{S}_i(f) \tag{18}$$

where $\hat{S}_i(f)$ serves as a scaling factor that depends on the size of the ith event. Next, residuals are obtained as the product of the source spectra and the site response:

$$R_{ij}(f) = \frac{U_{ij}(r_{ij}, f)}{A(r_{ij}, f)} = S_i(f)Z_j(f) \tag{19}$$

To facilitate linearization, the logarithm is taken for Equations 18 and 19:

$$\log U_{ij}(r_{ij}, f) = \log A(r_{ij}, f) + \log \hat{S}_i(f) \tag{20}$$

Equation 20 then transforms into a linear system of the form $\mathbf{Gm} = \mathbf{d}$, where $\mathbf{d}$ represents the data vector containing the logarithmic spectral amplitudes, $\mathbf{m}$ is the model parameter vector, and $\mathbf{G}$ is the system matrix. The dataset is divided into N_D bins based on hypocentral distance. In this study, the dataset is divided into 50 bins that are equally spaced on a logarithmic scale with respect to hypocentral distance. This binning strategy reflects the physical nature of seismic wave attenuation, which typically follows a logarithmic decay pattern due to geometrical spreading and anelastic attenuation. Logarithmic spacing allows finer resolution at shorter distances—where spectral amplitudes vary more rapidly, and coarser resolution at greater distances, where changes are smoother. This approach ensures a balanced representation of near and far-field data, improves the conditioning of the system matrix, and enhances the stability and interpretability of the inversion. The choice of 50 bins offers a practical relation between resolution and statistical robustness, ensuring that each bin contains a sufficient number of observations for reliable parameter estimation. In matrix notation, Equation 20 is formulated as:

$$\begin{pmatrix} \log U_{11} \\ \vdots \\ \log U_{ij} \\ \vdots \\ 0 \\ \vdots \\ 0 \end{pmatrix} = \begin{pmatrix} \underbrace{\begin{matrix} 1 & 0 & 0 & . & \dots \\ 0 & 1 & 0 & . & \dots \\ . & . & . & . & \dots \\ 1 & 0 & 0 & . & \dots \\ \vdots & \vdots & \vdots & \vdots & \vdots \\ w_1 & 0 & 0 & . & \dots \\ -w_2/2 & w_2 & -w_2/2 & . & \dots \\ 0 & -w_2/2 & w_2 & -w_2/2 & \dots \end{matrix}}_{\text{attenuation parameters}} & \underbrace{\begin{matrix} 1 & 0 & 0 & . & \dots \\ 1 & 0 & 0 & . & \dots \\ . & . & . & . & \dots \\ 0 & 1 & 0 & . & \dots \\ . & . & . & . & \dots \\ . & . & . & . & \dots \\ . & . & . & . & \dots \\ \vdots & \vdots & \vdots & \vdots & \vdots \end{matrix}}_{\text{sources}} \end{pmatrix} \begin{pmatrix} \log A_1 \\ \vdots \\ \log A_{N_D} \\ \log \hat{S}_1 \\ \vdots \\ \log \hat{S}_{N_E} \end{pmatrix} \tag{21}$$

The left portion of the system matrix incorporates factors associated with attenuation parameters, while

the right-hand side represents those related to source terms. The weighting factor w_1 ensures that $A(r_0, f) = 1$ at the reference distance, whereas w_2 governs the smoothness of the solution [Castro et al., 1990]. Each row, apart from those incorporating weighting factors, represents a spectrum and a value of 1 is assigned to the distance bin column on the matrix's left side, the column on the right that corresponds to the spectrum's associated event also receives a value of 1.

This procedure must be executed twice: first, to determine $\hat{S}$ based on Equation 18, and then again to compute S and Z using Equation 19 for each frequency point.

After performing least-squares inversion for each frequency, attenuation factors (A) corresponding to the number of distance bins, each representing the attenuation characteristics within its respective bin obtained. Likewise, for each event, the scaling factors ($\hat{S}$) achieved.

In the final step, Equation 19 is used to compute the residuals from the first inversion, which are then utilized in the second inversion. The matrix formulation employed in the second inversion is shown as Equation 22, where solutions are determined for each frequency:

$$\begin{pmatrix} \log R_{11} \\ \log R_{12} \\ \vdots \\ \log R_{21} \\ \vdots \\ \log R_{ij} \end{pmatrix} = \begin{pmatrix} 1 & 0 & 0 & . & \dots & 1 & 0 & 0 & . & \dots \\ 0 & 1 & 0 & . & \dots & 1 & 0 & 0 & . & \dots \\ . & . & . & . & \dots & . & . & . & . & \dots \\ 1 & 0 & 0 & . & \dots & 0 & 1 & 0 & . & \dots \\ \vdots & \vdots & \vdots & \vdots & \vdots & \vdots & \vdots & \vdots & \vdots & \vdots \\ \underbrace{\qquad\qquad\qquad\qquad\qquad}_{\text{stations}} & & & & & \underbrace{\qquad\qquad\qquad\qquad\qquad}_{\text{sources}} & & & & \end{pmatrix} \begin{pmatrix} \log Z_1 \\ \vdots \\ \log Z_j \\ \log S_1 \\ \vdots \\ \log S_i \end{pmatrix} \tag{22}$$

The structure and solution of this system is similar to Equation 16. The only difference here is that the data vector contains the residuals of the first step of the inversion (Equation 21).

The inversion methods introduced are the tools for spectral decomposition of seismic waves leading to having source, path and site properties separately. Therefore, spectral decomposition is central to isolating earthquake source radiation from recorded ground motion and it is widely used to estimate source parameters from large datasets of earthquakes and stations. The inversion methods can rely on Brune omega-squared source model [Brune, 1970], assumed homogeneous attenuation (Q) and simplified or empirical site response corrections. However, there are some challenges. For example, Abercrombie [2021] mentioned the following items:

- Trade-offs between quality factor and corner frequency make it hard to decompose source charac-

teristics from individual recordings.

- Limited frequency bandwidth restricts reliability, especially for small earthquakes ($M < 3$).
- Complex rupture behavior (e.g. double corner frequency) can affect the fall-off rate of source spectra.
- Azimuthal variation and directivity are often ignored, though they affect frequency-dependent radiation.

However, to ensure stability and consistency in the inversion, an additional constraint is introduced which is the use of a *Reference Station*. This station serves as a spectral baseline, allowing relative site effects to be normalized across the network.

Using the Reference Station modifies Equation 9 into the following form [Klin et al., 2017, Hartzell, 1992]:

$$\begin{pmatrix} \mathbf{G} \\ \mathbf{F} \end{pmatrix} \mathbf{m} = \begin{pmatrix} \mathbf{d} \\ \mathbf{c} \end{pmatrix} \tag{23}$$

In the simplest case, $\mathbf{F}$ would be a row vector with a unique nonzero term in the position of the station chosen as the reference station [Klin et al., 2017, Oth et al., 2009, Abercrombie, 2021]. While the standard GIT formulation constrains the reference site to have zero amplification ($\log Z_j = 0$), this assumption may not hold for stations with measurable site effects. Following the flexible constraint structure of GIT, the site term can instead be anchored to a known amplification value, such as horizontal-to-vertical spectral ratio $\log(H/V)$, thereby normalizing the inversion to a physically meaningful baseline.

The horizontal-to-vertical spectral ratio (HVSR) method is a widely used passive seismic technique for site characterization, particularly effective in estimating subsurface resonance frequencies and shear-wave velocity profiles.

The HVSR technique was first introduced by Nakamura [1989], who proposed that the ratio of horizontal to vertical components of ambient seismic noise could reveal the fundamental resonance frequency of soft sediment layers overlying bedrock. This resonance frequency is linked to the thickness and shear-wave velocity of the sedimentary layer. The method assumes that vertical components are less affected by site amplification, while horizontal components are more sensitive to impedance contrasts. As a result, the spectral ratio highlights peaks corresponding to resonance effects. It usually relies

on ambient seismic noise rather than active sources, making it cost-effective and suitable for urban or low-seismicity regions. Applications of HVSR include seismic microzonation, site effect studies, and preliminary geotechnical investigations.

To test and improve the physical realism of the site response estimates, H/V spectral ratios derived from the recordings of the events were used in the data vector for the reference station. This approach anchors the inversion to a known frequency-dependent amplification even though it is not the absolute value of site effect. Conversly, by not considering the H/V value, the site response is assuming to show a flat (zero) value for all frequencies. While the GIT is traditionally non-parametric, which means relying solely on empirical decomposition of observed spectra, the inclusion of prior site information introduces a constraint that guides the solution. This approach does not impose a full physical model (e.g., layered velocity structure), but rather uses empirical H/V ratios as soft constraints. Therefore, it retains the flexibility of non-parametric inversion while correcting for potential bias introduced by assuming a zero site term at the reference station.

To assess the performance of various GIT methodologies and to identify the most suitable reference station, a preliminary selection of candidate stations was undertaken. This selection was guided by two basic criteria designed to ensure both spectral fidelity and minimal site-induced bias in the inversion process:

- **Broadband Stations:** Only stations equipped with broadband seismometers were considered eligible. These instruments are capable of capturing a wide frequency spectrum, including the low-frequency components that are critical for accurate seismic moment estimation. Their extended dynamic range enhances the reliability of spectral measurements across diverse magnitudes and source characteristics.
- **EC8 Class A:** Candidate stations were further filtered based on their site classification under the European seismic code EC8 [Comité Européen de Normalisation, 2004]. Specifically, only those categorized as Class A, which are representing rock or very stiff soil conditions, were selected. This classification is associated with minimal site amplification effects, thereby reducing the distortion of spectral amplitudes and improving the robustness of source parameter retrieval.

Based on these criteria, 16 stations were chosen as the potential candidates for being the reference station and the calculations were done considering to choose one of these stations accordingly. These stations are *ACOM*, *BALD*, *CADS*, *CLUD*, *CRNS*, *DOBS*, *GAGG*, *GBAS*, *GEPF*, *GORS*, *JAVS*, *MOZS*, *PRED*, *VARN*, *VNDS*, *VOJS* which can affect the inversion process regarding their site characteristics. In order to test the effect of each station to the final results, for each of which the calculations performed sepa-

rately and the final results of each one compared to the others.

In addition to the reference station constraint, an optional constraint can be incorporated to further stabilize the inversion and reduce trade-offs among model parameters. To mitigate the influence of noisy records and account for missing data, weighting factors can be introduced into the inversion framework. These weights serve a dual purpose: they downweight unreliable observations and provide a practical mechanism for handling incomplete datasets. Specifically, assigning a zero weight to site-event pairs with missing data is computationally more efficient than restructuring the design matrix **G** to accommodate uneven data coverage.

Following the approach introduced by Menke [1989] and used by Klin et al. [2017], the estimate of the model parameters is obtained by pre-multiplying both the data vector d and the system matrix **G** by a diagonal weight matrix:

$$\mathbf{W} = (\mathbf{cov}\ \mathbf{d})^{-1} \tag{24}$$

where **cov d** is the data covariance matrix. By neglecting possible correlations among the data terms, the following equation could be achieved:

$$\mathbf{W} = \mathbf{diag}\{w_1, w_2, \ldots, w_n\} = \mathbf{diag}\{\sigma_1^{-2}, \sigma_2^{-2}, \ldots, \sigma_n^{-2}\} \tag{25}$$

where **diag** means diagonal matrix and σ is the standard deviations of each data term (d). To calculate σ, the ratio of spectral signal (S_{ij}) on the S-wave window to pre-event noise (N_{ij}) of event i recorded at station j is considered as follows:

$$\sigma_n = \frac{N_{ij}}{S_{ij}} = \frac{1}{\sqrt{U_{ij}}} \tag{26}$$

in other words

$$U_{ij} = (\frac{S_{ij}}{N_{ij}})^2 \tag{27}$$

which is defined in terms of the power spectra of the signal and noise components. Hence, the weight terms would be:

$$w_n = U_{ij} \tag{28}$$

To prevent numerical instability during inversion, an upper bound could be imposed on the weighting values, typically denoted as w^{max} with a recommended value such as 100. This limit ensures that no single data point influences the solution in a not proportional way [Klin et al., 2017]. By using the wights, the final equation to solve would be:

$$\begin{bmatrix} \mathbf{WG} \\ w^{max}\mathbf{F} \end{bmatrix} \mathbf{m} = \begin{bmatrix} \mathbf{Wd} \\ w^{max}\mathbf{c} \end{bmatrix} \tag{29}$$

3.3.1 Calculating Seismic Moment

Once the GIT is applied to isolate the source spectra from path and site effects, the resulted source spectrum can be analyzed to estimate key earthquake source parameters, namely seismic moment and corner frequency using the best-fitting omega-squared Brune source model (Equation 30) which was first introduced by Brune [1970] and then used in many studies [e.g., Aki, 1967, Andrews, 1986, Bindi et al., 2018, Franceschina et al., 2006, Gallo et al., 2014, Cataldi et al., 2022]. The model is defined as:

$$\text{Source Spectrum}(f) = \frac{M_0\ \Theta_{\lambda\varphi}\ F\xi}{R_0 4\pi\rho v_s^3} \left[1 + \left(\frac{f}{f_c}\right)^2\right]^{-1} \tag{30}$$

The parameter assumptions adopted in this study remain consistent with those previously defined under the parametric GIT framework in which $\Theta_{\lambda\varphi}$ (average radiation pattern) is 0.55 for S-waves, F (free surface amplification factor) is 2 for both SH and SV waves and ξ (partition factor for shear-wave energy

into two horizontal components) is 1 for vectorial composition of the horizontal components [Cataldi et al., 2022, 2025].

Once the source spectral values are retrieved for all frequency points using any type of the GIT, the complete source spectrum becomes available for analysis. To extract key source parameters, the omega-squared Brune model (Equation 30) is fitted to the spectrum, allowing for the estimation of the corner frequency and seismic moment. For the velocity and density parameters related to the Equation 30, the velocity model of Magrin and Rossi [2020a,b] (Table 7) were used.

Number of Layer	Depth (km)	V_P (km/s)	V_S (km/s)	ρ (kg/m^3)	Number of Layer	Depth (km)	V_P (km/s)	V_S (km/s)	ρ (kg/m^3)
1	0.00	5.13	2.81	2.65	31	30.00	6.90	3.90	2.95
2	1.00	5.15	2.83	2.66	32	31.00	6.99	3.92	2.98
3	2.00	5.54	3.07	2.68	33	32.00	7.06	3.94	3.00
4	3.00	5.76	3.20	2.70	34	33.00	7.11	3.96	3.02
5	4.00	5.90	3.28	2.71	35	34.00	7.15	3.97	3.03
6	5.00	5.98	3.34	2.71	36	35.00	7.19	3.98	3.04
7	6.00	6.04	3.38	2.72	37	36.00	7.23	3.99	3.06
8	7.00	6.09	3.41	2.73	38	37.00	7.27	4.00	3.07
9	8.00	6.10	3.42	2.73	39	38.00	7.31	4.01	3.08
10	9.00	6.12	3.44	2.73	40	39.00	7.35	4.02	3.09
11	10.00	6.13	3.45	2.73	41	40.00	7.40	4.04	3.11
12	11.00	6.14	3.48	2.74	42	41.00	7.46	4.05	3.13
13	12.00	6.16	3.51	2.75	43	42.00	7.54	4.07	3.16
14	13.00	6.18	3.54	2.77	44	43.00	7.57	4.08	3.17
15	14.00	6.21	3.56	2.78	45	44.00	7.59	4.09	3.17
16	15.00	6.23	3.60	2.78	46	45.00	7.61	4.09	3.18
17	16.00	6.25	3.62	2.79	47	46.00	7.64	4.10	3.19
18	17.00	6.28	3.64	2.79	48	47.00	7.69	4.11	3.21
19	18.00	6.31	3.67	2.80	49	48.00	7.74	4.13	3.22
20	19.00	6.34	3.69	2.81	50	49.00	7.80	4.14	3.24
21	20.00	6.37	3.70	2.81	51	50.00	7.84	4.15	3.25
22	21.00	6.40	3.72	2.82	52	51.00	7.88	4.17	3.26
23	22.00	6.44	3.74	2.82	53	52.00	7.93	4.18	3.28
24	23.00	6.46	3.75	2.83	54	53.00	7.97	4.19	3.29
25	24.00	6.49	3.77	2.83	55	54.00	7.99	4.20	3.30
26	25.00	6.53	3.78	2.84	56	55.00	8.00	4.20	3.30
27	26.00	6.57	3.80	2.85	57	56.00	8.00	4.20	3.30
28	27.00	6.62	3.82	2.86	58	57.00	8.00	4.20	3.30
29	28.00	6.70	3.84	2.88	59	58.00	8.00	4.20	3.30
30	29.00	6.80	3.87	2.91	60	59.00	8.00	4.20	3.30

Table 7: 1D Velocity model for Northeastern Italy by Magrin and Rossi [2020a,b].

This fitting procedure provides a physical characterization of the earthquake source. An illustrative example of the derived source spectrum, along with its corresponding Brune model fit, is presented in Figure 12.

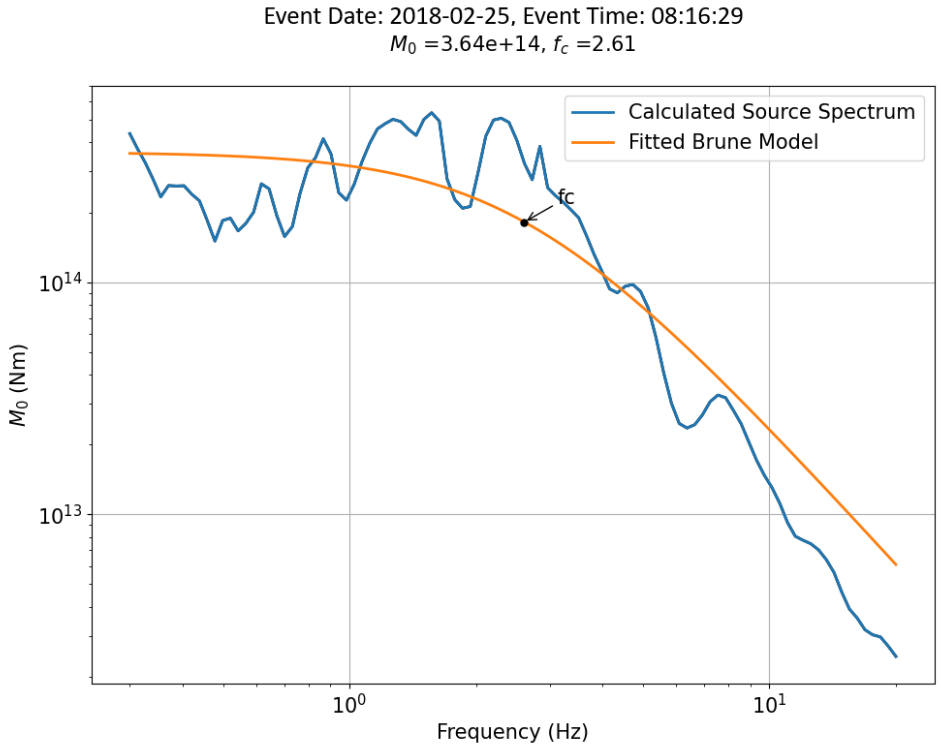

Figure 12: An example of a calculated source spectrum and the Brune model fit.

3.3.2 Calculating Seismic Radiated Energy

In this study, two distinct formulations are employed to all three components of each station to estimate the seismic radiated energy. The components were not rotated. The first approach uses the parameters derived from the GIT, specifically the M_0 and f_c, based on the model used by Izutani and Kanamori [2001] and Picozzi et al. [2018b]:

$$E_R = \frac{4\pi}{5\rho v_s^5} \int_0^\infty |fM(f)|^2 df \tag{31}$$

with the frequency-dependent source model defined as:

$$M(f) = \frac{M_0}{1 + (\frac{f}{f_c})^\gamma} \tag{32}$$

Here, ρ represents the medium's density, v_s is the shear-wave velocity, and γ controls the spectral decay

at high frequencies, set to a value of 2 for Italian datasets as specified by Picozzi et al. [2018b].

The second method, as proposed by Boatwright and Fletcher [1984] derives radiated energy from the integration of S-wave velocity or its spectra:

$$\begin{aligned} E_R &= 4\pi C^2 r^2 \rho_r \beta_r \int_0^\infty \dot{u}_c(\omega)^2 d\omega \\ &= 4\pi C^2 r^2 \rho_r \beta_r \int_0^\infty \dot{u}_c(t)^2 dt \end{aligned} \tag{33}$$

In this formulation, the velocity corrected for anelastic attenuation effects, ensuring that the observed signal reflects energy loss along the propagation path. The coefficient C accounts for variations due to the radiation pattern of the seismic source and local surface amplification effects. The variable r represents the hypocentral distance between the earthquake source and the recording station, while ρ_r and β_r denote the density and shear wave velocity at the receiver site, respectively. Attenuation is modeled through an exponential decay term, typically expressed as exp = $(\frac{\omega r}{\beta Q})$, where Q is the quality factor representing whole-path attenuation [Boatwright and Fletcher, 1984, Boatwright et al., 2002, Choy and Boatwright, 2012].

According to Parseval's theorem [des Chênes, 1799], the total energy of a signal remains invariant under Fourier transformation; that means, the energy computed in the time domain is mathematically equivalent to the energy computed in the frequency domain. This principle provides a theoretical foundation for estimating radiated seismic energy from the squared amplitude spectrum, as it ensures that energy-related quantities derived from frequency-domain equivalently reflect the physical energy content of the original time-domain waveform.

Based on this theorem, the integral of squared velocity, used in Equation 33, can be equivalently performed in either the time domain or the frequency domain [Choy and Boatwright, 2012]. This duality offers flexibility in computational implementation and allows for cross-validation of energy estimates derived from different analytical approaches.

3.4 Empirical Attenuation Models

Following the determination of source parameters, the next analytical step involves deriving empirical coefficients that link observable waveform metrics to fundamental seismic quantities. Specifically, it becomes feasible to estimate both the seismic energy and seismic moment using two robust metrics extracted from the S-wave portion of the signal: the Integral of the Squared Velocity of the S-wave

($IV2_S$) and the Peak Displacement of S-wave (PD_S). These parameters represent essential aspects of the radiated energy and static deformation, respectively, and offer a practical way for magnitude scaling without requiring waveform inversion. Figure 13 illustrates the distribution of $IV2_s$ and PD_s values as a function of hypocentral distance colored rgarding their magnitude. They are used as the inputs to create the empirical attenuation models.

The figure is providing insight into the attenuation behavior of the parameters and potential for regression-based calibration. The observed behavior of both $IV2_s$ and PD_s exhibits a strong dependence on hypocentral distance, reflecting systematic attenuation patterns consistent with theoretical expectations. This spatial variability underscores their suitability as empirical representatives for source energy, enabling the derivation of regression-based relationships that capture the scaling of seismic energy and moment with distance. This approach enables the formulation of empirical relationships that are both computationally efficient and physically meaningful, facilitating rapid estimation of source properties across diverse seismic datasets.

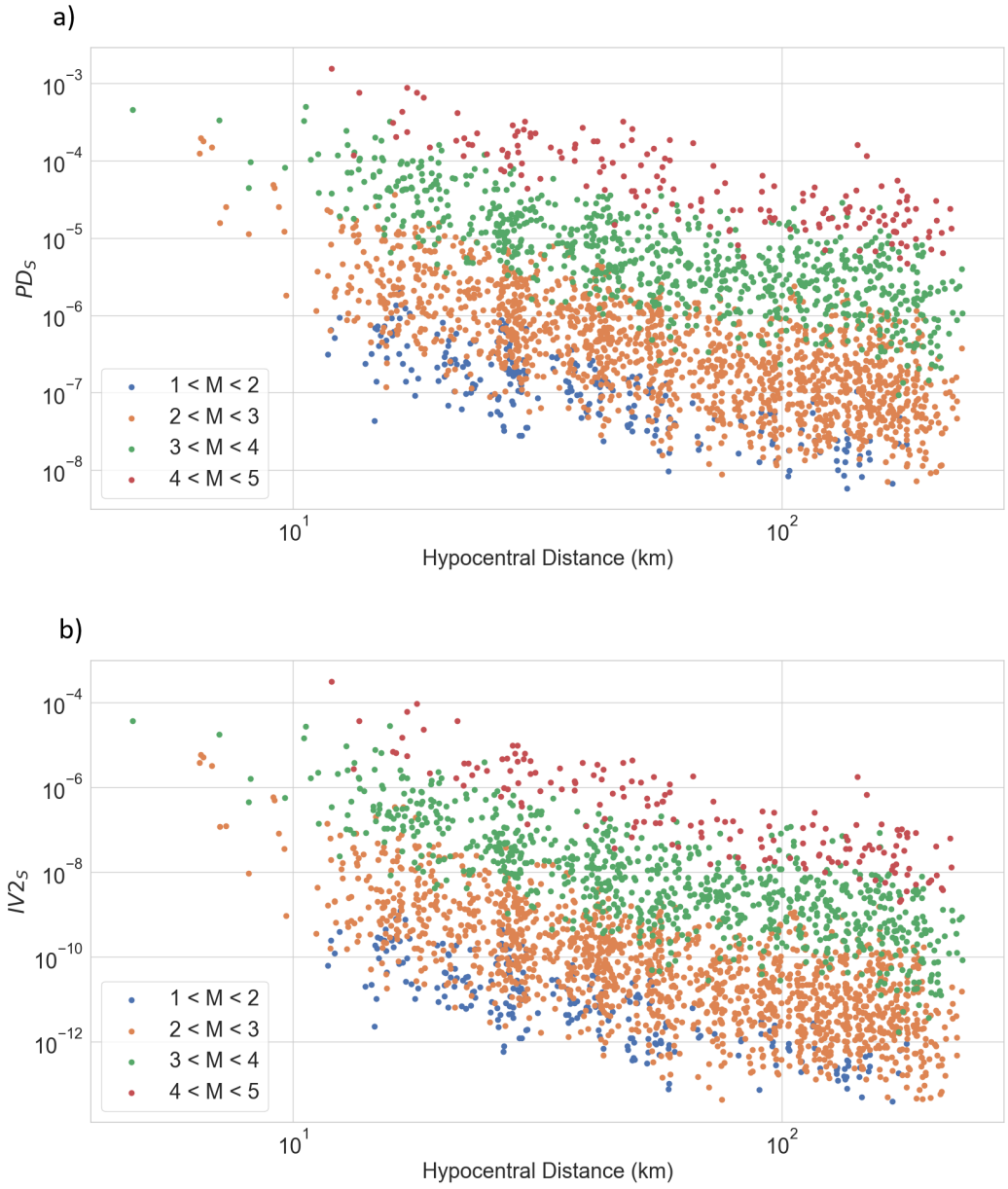

Figure 13: a) Distribution of peak displacement of the data over S-wave with hypocentral distance considering different magnitude ranges. b) Distribution of Integral of Squared Velocity of the data over S-wave with hypocentral distance considering different magnitude ranges.

In this step, the $IV2_S$ and PD_S values for the kth earthquake recorded at the lth station are empirically related to E_R and M_0 using the following attenuation models, i.e. Equations 34 and 35 [Picozzi et al., 2018a]. To calibrate the empirical model that describes how PD_S scales with hypocentral distance and seismic moment, the PD_S values from the North–South and East–West horizontal components are combined using their geometric mean [Spallarossa et al., 2021] to balance the influence of both components. In contrast, when modeling the scaling of $IV2_S$ with hypocentral distance and energy release,

the $IV2_S$ values from all three ground motion components, i.e. North–South, East–West, and vertical, are summed [Spallarossa et al., 2021]. This additive approach reflects the total energy content across all directions, making it suitable for characterizing cumulative measures like $IV2_S$. For all of the calculations, the used components were not rotated.

$$\log[IV2_s(R_H)]_{kl} = A + B\log(E_R)_k + w_j C_j + (1 - w_j)C_{j+1} \tag{34}$$

$$\log[PD_s(R_H)]_{kl} = D + F\log(M_0)_k + w_j G_j + (1 - w_j)G_{j+1} \tag{35}$$

Here, the hypocentral distance (R_H) is divided into N_{bin} discrete intervals. In this study, the number of bins is 50 which are equally space in a logarithmic scale. The index $j = 1,\dots,N_{bin}$ represents a specific node chosen such that the distance R_H falls within the range $r_j \leq R_H \leq r_{j+1}$. The attenuation function is linearly interpolated between nodes r_j and r_{j+1} using the weight factor w, given by:

$$w_j = \frac{r_{j+1} - R_H}{r_{j+1} - r_j} \tag{36}$$

To estimate the coefficients in Equations 34 and 35, which empirically describe the attenuation characteristics of the study region, a dedicated inversion procedure is carried out. This inversion establishes regression relationships between key ground motion metrics and source parameters. Specifically, it links the $IV2_S$ and E_R as well as the PD_S and M_0. The matrix formulation of these empirical models is expressed in Equations 37 and 38, which enable the simultaneous estimation of attenuation coefficients across the network.

$$\begin{pmatrix} \log(IV2_s)_{11} \\ \log(IV2_s)_{12} \\ \vdots \\ \log(IV2_s)_{kl} \end{pmatrix} = \begin{pmatrix} 1 & \log(E_R)_1 & w_1 & 1-w_1 & 0 & \dots \\ 1 & \log(E_R)_1 & 0 & w_2 & 1-w_2 & \dots \\ \vdots & \vdots & \vdots & \vdots & \dots & \dots \\ 1 & \log(E_R)_k & . & . & \dots & \dots \end{pmatrix} \begin{pmatrix} A \\ B \\ C_1 \\ C_2 \\ \vdots \\ C_j \end{pmatrix} \tag{37}$$

$$\begin{pmatrix} \log(PD_s)_{11} \\ \log(PD_s)_{12} \\ \vdots \\ \log(PD_s)_{kl} \end{pmatrix} = \begin{pmatrix} 1 & \log(M_0)_1 & w_1 & 1-w_1 & 0 & \dots \\ 1 & \log(M_0)_1 & 0 & w_2 & 1-w_2 & \dots \\ \vdots & \vdots & \vdots & \vdots & \dots & \dots \\ 1 & \log(M_0)_k & . & . & \dots & \dots \end{pmatrix} \begin{pmatrix} D \\ F \\ G_1 \\ G_2 \\ \vdots \\ G_j \end{pmatrix} \tag{38}$$

The coefficients A, B, and C_j as well as D, F, and G_j are estimated by solving overdetermined linear systems in a least-squares sense. The coefficients C_j and G_j are related to each source-to-receiver distance bin. By using this method, it is possible to have a simpler, and at the same time reliable, estimate of earthquake properties which avoids delays and heavy calculations which could be very beneficial and effective.

In general terms, the schematic representation of the methodological workflow adopted in this study is illustrated in Figure 14. This diagram summarizes the sequential structure and interdependencies among the key analytical stages, including data preprocessing, spectral decomposition, inversion procedure, and source parameter estimation. It serves as a visual summary of the integrated approach employed to derive physically consistent and regionally calibrated seismic source properties.

To explain the workflow illustrated in Figure 14, the initial phase involves data acquisition and preprocessing for the first dataset, which serves as the training set for model development. Following instrumental correction and filtering, source parameters are estimated by solving Equation 11, which can be approached through one of several formulations, namely, Equations 16, 17, or 21 and 22, depending on the spectral characteristics and inversion strategy.

Once the source parameter is obtained, the seismic moment is computed using Equation 30. Seismic energy is then derived using either Equation 31, which requires the moment and corner frequency as inputs, or Equation 33, which offers an alternative formulation. These calculations provide the foundation for establishing empirical relationships between source parameters and observable waveform metrics.

Specifically, Equation 35 is used to derive the empirical relation between seismic moment and the peak displacement of the S-wave, while Equation 34 links radiated energy to the integral of squared S-wave velocity. These attenuation functions show the scaling behavior of source parameters with respect to measurable ground motion features and form the predictive core of the model.

For subsequent datasets, such as the second dataset used in this study for model validation, the established empirical relations enable the estimation of seismic moment and energy directly from waveform observables. By relying solely on peak displacement and integrated squared velocity of the S-wave, the model facilitates efficient and robust source parameter estimation without requiring full spectral inversion, thereby providing easier analysis for broader applications in seismic hazard assessment and rapid event characterization.

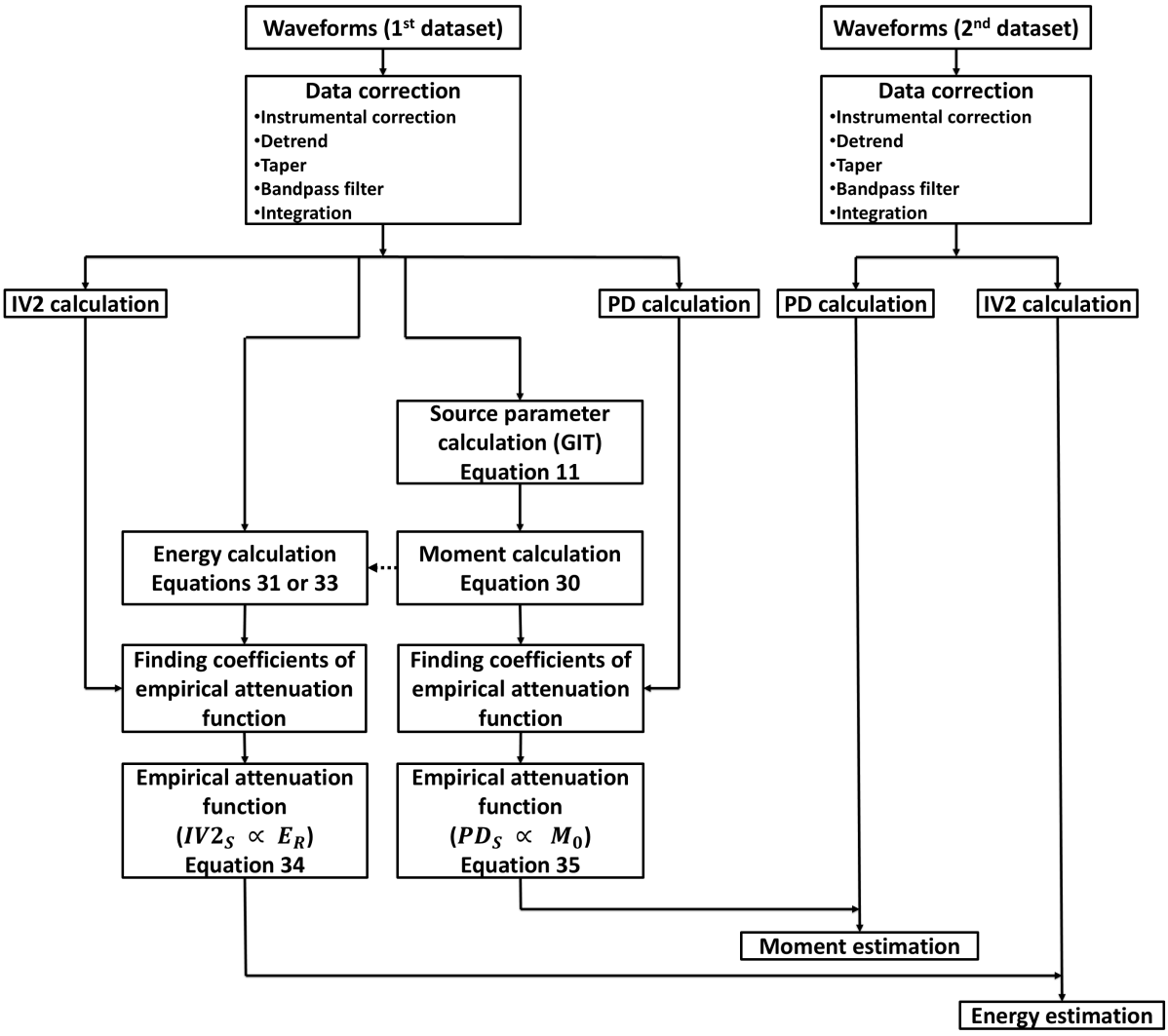

Figure 14: Workflow of this study.

3.5 Measure of Goodness

To evaluate the performance of the derived coefficients, particularly in comparison to the findings of Cataldi et al. [2025], two primary metrics were employed in this study:

- The first is the Root Mean Square Error (RMSE), calculated between the estimated moment and energy properties such as moment magnitude, which provides a direct measure of the average deviation between the two scales.

- The second is the Euclidean Distance (ED), a composite metric that captures the overall discrepancy across multiple dimensions of the parameter space [Samantaray et al., 2024]. This metric was employed to assess the degree of similarity between the source spectra derived in this study and those reported by Cataldi et al. [2025]. This distance metric (Equation 39) contains three statistical measures to evaluate the quality of the comparison. The measures are Correlation Coefficient (CC), Standard Deviation (σ) Ratio and RMSE. In the ideal scenario, the values of CC, σ Ratio and RMSE would be 1, 1 and 0 which makes ED to be 0.

$$ED = \sqrt{(1 - CC)^2 + (1 - \sigma Ratio)^2 + (0 - RMSE)^2} \tag{39}$$

The RMSE is particularly effective for quantifying differences, as it emphasizes larger deviations through squaring, making it a sensitive indicator for large errors [Chai and Draxler, 2014]. The correlation coefficient, on the other hand, captures the strength of linear similarity between two datasets, making it well-suited for evaluating the similarity in spectral shape or trend, rather than absolute amplitude differences [Bluman, 2017, Zhelezniak et al., 2019]. Additionally, the σ ratio offers a normalized measure of variability relative to the mean, enabling meaningful comparisons across datasets [Dodge, 2008, Bluman, 2017].

4 Results

This section presents the outcomes of the spectral inversion and scaling analyses performed on the seismic dataset from Northeastern Italy. The inversion framework was applied to logarithmic spectral amplitudes derived from local earthquake recordings, with the aim of estimating key source parameters and characterizing their dependence on hypocentral distance and magnitude. The released energy was calculated according to the provided formulations as well. The empirical models were calibrated using binned data representations and component-wise spectral and time-domain measures, ensuring consistency with theoretical expectations and observational constraints.

The results are organized to highlight both the reliability of the inversion outputs and the physical interpretability of the scaling relations. Particular attention is given to the behavior of PD_S and $IV2_S$ across varying distances and magnitudes. Regression fits, uncertainty bounds, and visual characteristics are provided to support the robustness of the derived parameters and to facilitate the comparison with existing literature.

4.1 GIT Results

In order to evaluate and contrast the outcomes derived from Equations 23 and 29, two methodological variables were systematically examined:

- The inclusion or exclusion of weighting factors in the analysis.
- The application or omission of the H/V spectral ratio from the reference station

These considerations were essential for assessing the sensitivity and reliability of the resulting estimates under varying input configurations.

Based on the objectives of this study, non-parametric GIT were applied in three configurations, namely, the 2-step method, the 1-step method, and the 1-step method with a predefined attenuation model, across all selected stations. The results were compared to those reported by Cataldi et al. [2025] using the ED metric as a measure of deviation. Figure 15 illustrates the ED outcomes under four distinct input configurations: (a) without weights and without H/V, (b) without weights and with H/V, (c) with

weights and without H/V, and (d) with weights and with H/V.

The figure reveals that the 1-step method with a predefined attenuation model produces noticeably higher variability across reference stations, indicating reduced stability which could depend on the utilized attenuation model. In contrast, both the standard 1-step and 2-step methods yield more consistent ED values, suggesting better robustness under varying input conditions. Furthermore, the inclusion of the H/V spectral ratio in the data vector leads to a clear improvement in performance, as evidenced by lower ED values in panels (b) and (d). This highlights the importance of incorporating site response indicators to enhance the reliability of non-parametric inversion results.

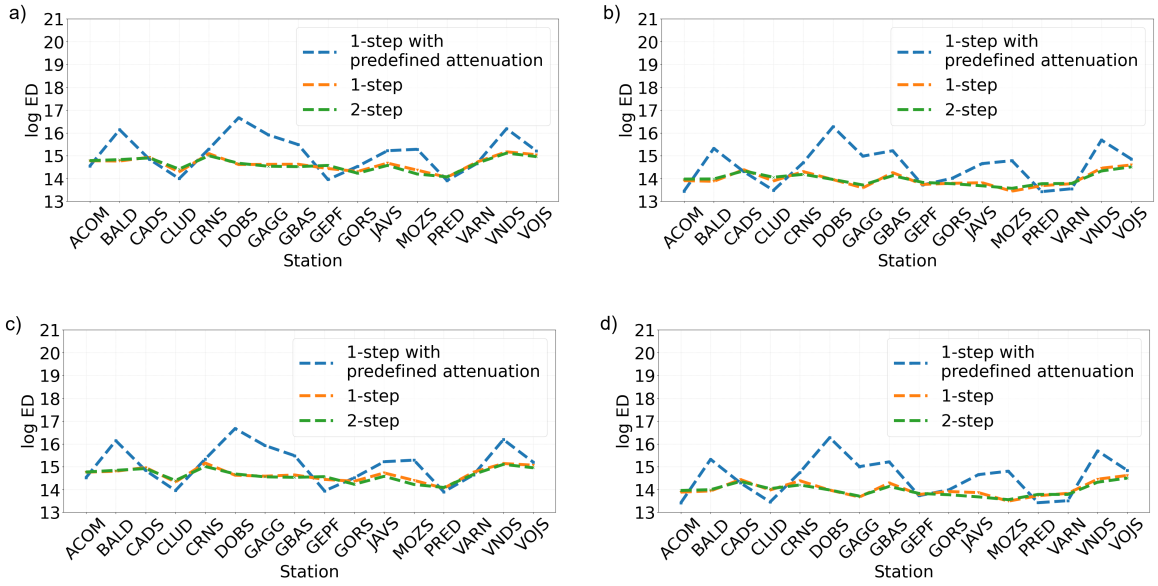

Figure 15: a) ED metric results for different reference stations without using weights and without using H/V. b) ED metric results for different reference stations without using weights and with using H/V. c) ED metric results for different reference stations with using weights and without using H/V. d) ED metric results for different reference stations with using weights and with using H/V.

Moreover, when evaluating the RMSE of magnitude estimates, the corresponding results are presented in Figure 16. The patterns observed are broadly consistent with those shown in the ED metric analysis (Figure 15). Specifically, the 1-step method with a predefined attenuation model exhibits greater variability across reference stations, resulting in elevated RMSE values. In contrast, the standard 1-step and 2-step methods yield more stable and generally lower errors, particularly when combined with H/V spectral ratios. Panels (b) and (d) of Figure 16 clearly demonstrate that incorporating H/V into the data vector improves magnitude estimation accuracy.

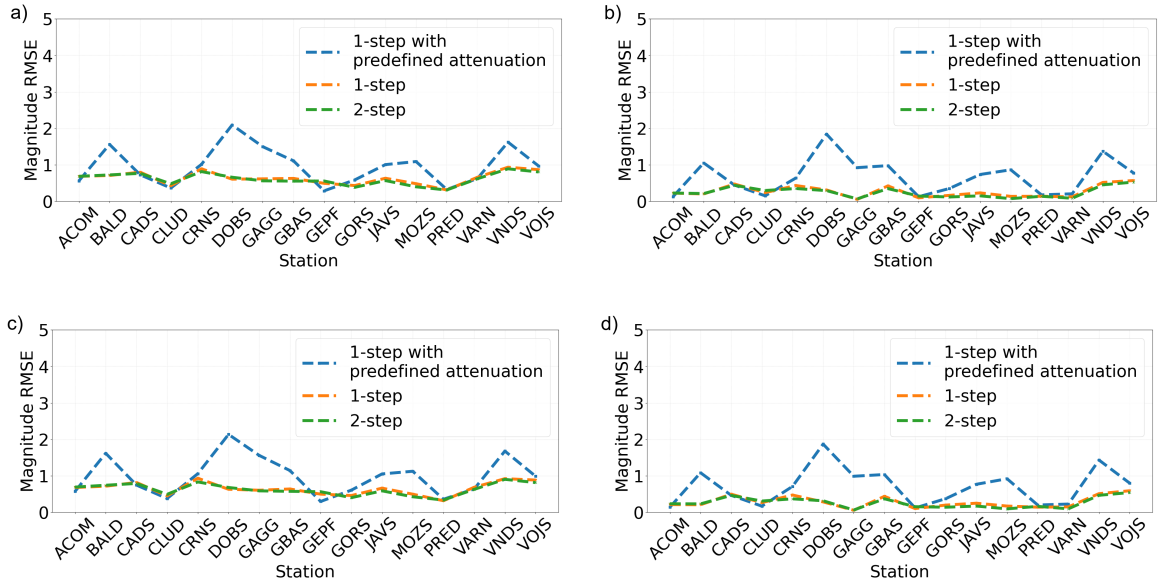

Figure 16: a) Magnitude RMSE results for different reference stations without using weights and without using H/V. b) Magnitude RMSE results for different reference stations without using weights and with using H/V. c) Magnitude RMSE results for different reference stations with using weights and without using H/V. d) Magnitude RMSE results for different reference stations with using weights and with using H/V.

Significantly, by considering the average performance of each method across all selected stations, the outcomes of the two-step GIT demonstrated lower diversity but higher consistency, as illustrated in Figure 17. In both panels,showing average ED and magnitude RMSE, the two-step method consistently yields tighter error ranges across different reference station configurations. This suggests that the two-step approach is more robust to site variability, offering stable performance. While the one-step method with predefined attenuation shows greater fluctuation and sensitivity to station choice, the two-step method maintains uniformity, reinforcing its suitability for regional-scale applications where consistency is critical.

Moreover, the inclusion of the H/V spectral ratio in the data vector consistently improved both ED and magnitude RMSE results where the error metrics show reduced scatter and less errors. The improved performance underscores the value of incorporating site response indicators like H/V, which help to stabilize inversion outputs and mitigate the influence of local amplification effects. Together, these findings highlight the robustness of the two-step method and the critical role of H/V in achieving reliable and regionally consistent magnitude estimates.

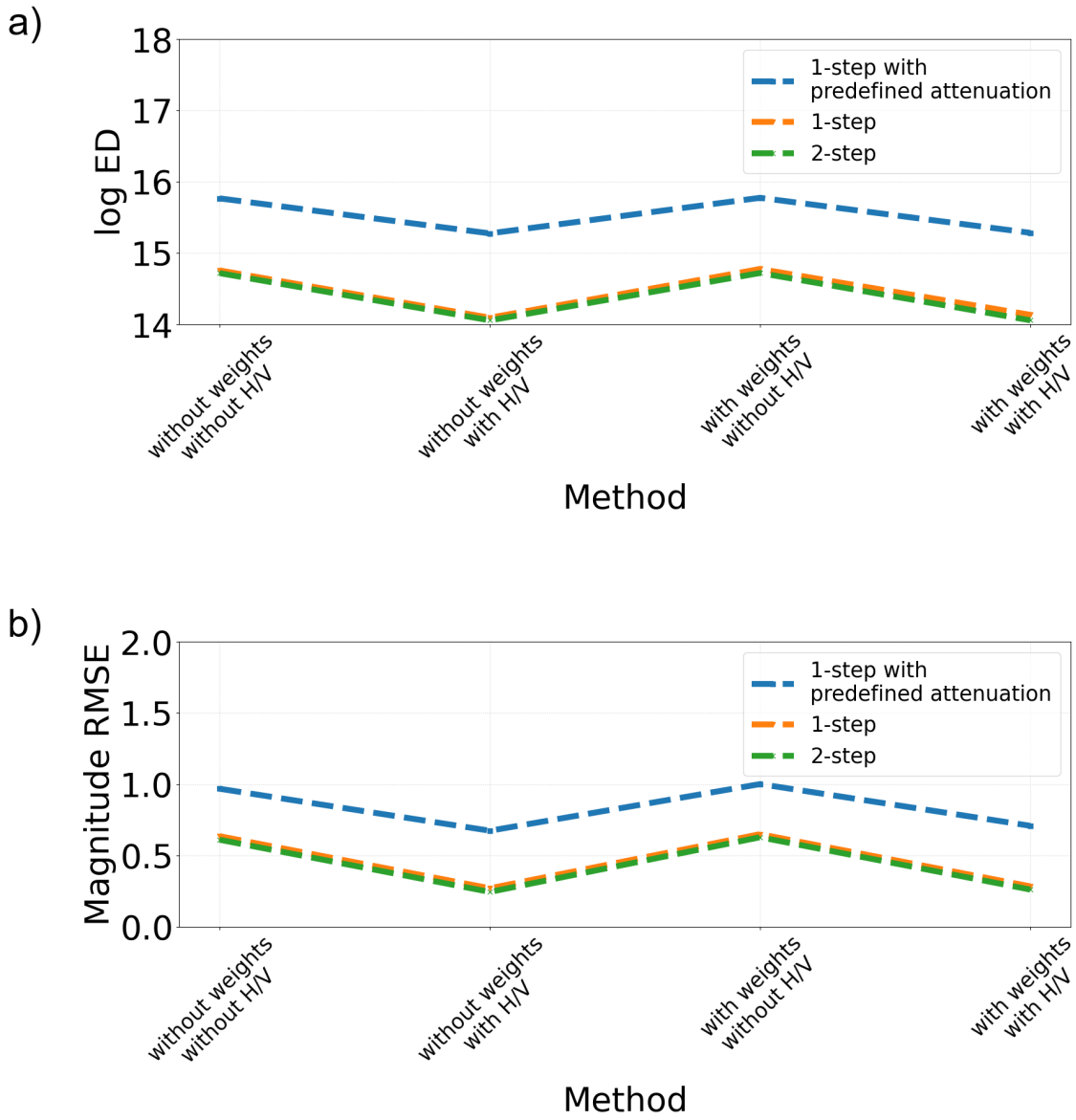

Figure 17: a) Average of ED results for all selected stations. b) Average of Magnitude RMSE results for all selected stations.

As illustrated in Figures 15, 16 and 17, the results of 1-step method with predefined attenuation model is really different in comparison to the results of the methods that are not using predefined model. This observation emphasizes that the attenuation model must be defined very carefully. However, by focusing on the other two methods (Figures 18 and 19), it is noticeable that their results are really similar. This similarity could be due to the fact that they are resolving the same problem with the same parameters and the same data. The constraints are also the same. Therefore, the small differences in the

results could be addressed to the difference in methods which shows a really small and tiny priority of the 2-step method.

For example, regarding the ED metric, in panel (a) of Figure 18, the average ED value of 1-step method is 14.66 and for 2-step method is 14.63. In panel (b) the average ED value of 1-step method is 13.97 and for 2-step method is 13.97. In panel (c) the average ED value of 1-step method is 14.68 and for 2-step method is 14.63. In panel (d) the average ED value of 1-step method is 14.02 and for 2-step method is 13.98.

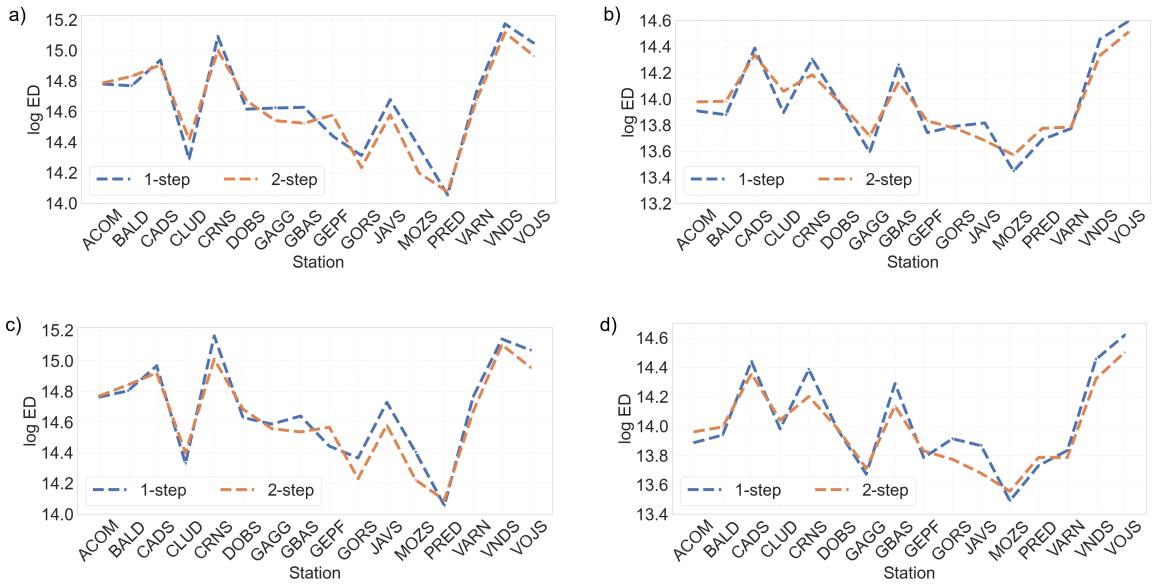

Figure 18: Similar to Figure 15 but only for 1-step and 2-step methods. a) ED metric results for different reference stations without using weights and without using H/V. b) ED metric results for different reference stations without using weights and with using H/V. c) ED metric results for different reference stations with using weights and without using H/V. d) ED metric results for different reference stations with using weights and with using H/V.

Similarly, regarding the magnitude RMSE, in panel (a) of Figure 19, the average RMSE value of 1-step method is 0.64 and for 2-step method is 0.61. In panel (b) the average RMSE value of 1-step method is 0.27 and for 2-step method is 0.25. In panel (c) the average RMSE value of 1-step method is 0.65 and for 2-step method is 0.63. In panel (d) the average RMSE value of 1-step method is 0.29 and for 2-step method is 0.26.

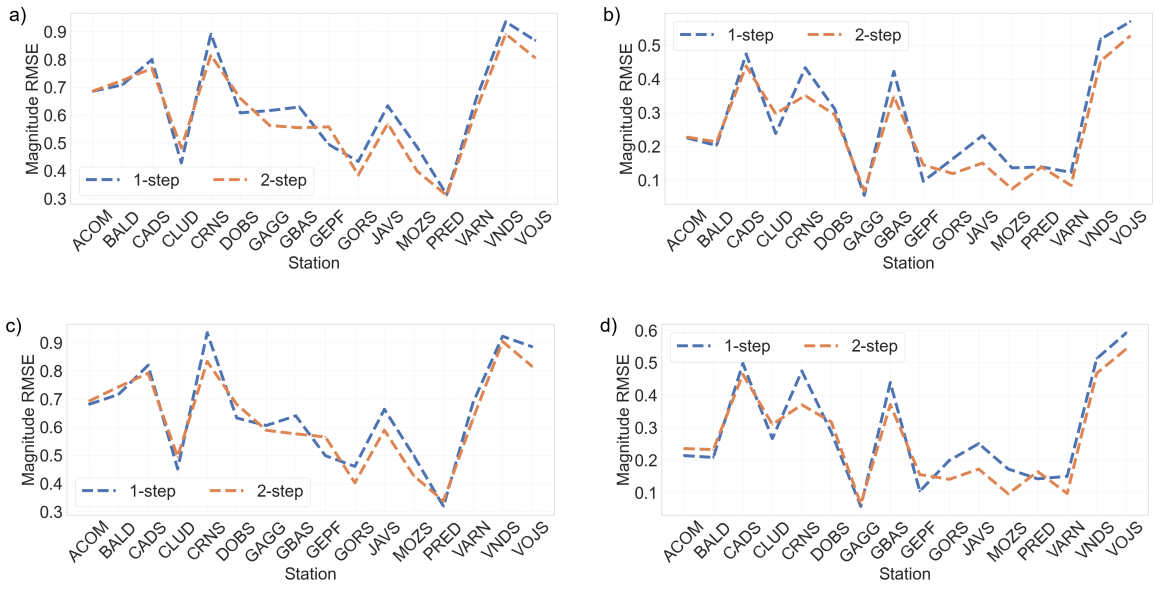

Figure 19: Similar to Figure 16 but only for 1-step and 2-step methods. a) Magnitude RMSE results for different reference stations without using weights and without using H/V. b) Magnitude RMSE results for different reference stations without using weights and with using H/V. c) Magnitude RMSE results for different reference stations with using weights and without using H/V. d) Magnitude RMSE results for different reference stations with using weights and with using H/V.

Focusing specifically on the two-step GIT, Figure 20 demonstrates that incorporating the H/V spectral ratio into Equation 23 yields improved results across both ED and magnitude RMSE metrics. In the figure, the blue and green curves which do not use H/V are usually overlapping. Similarly, the red and orange curves which use H/V are mostly overlapping. The inclusion of H/V enhances the model's sensitivity to site-specific amplification effects, resulting in more consistent and lower error values across the evaluated stations. Regarding the use of weighting factors, the observed differences are relatively minor. This can be due to the fact that used waveforms of this study were filtered prior to GIT calculations which means that the signal to noise ratio is already applied to the recordings. However, the analysis suggests that omitting weights leads to slightly more favorable outcomes, especially when H/V is present in the data vector. This could also be attributed to the relatively high quality of the data used in this study, which appears to be largely free from significant noise. Overall, utilizing H/V proves to be the most effective configuration for stable and accurate magnitude estimation.

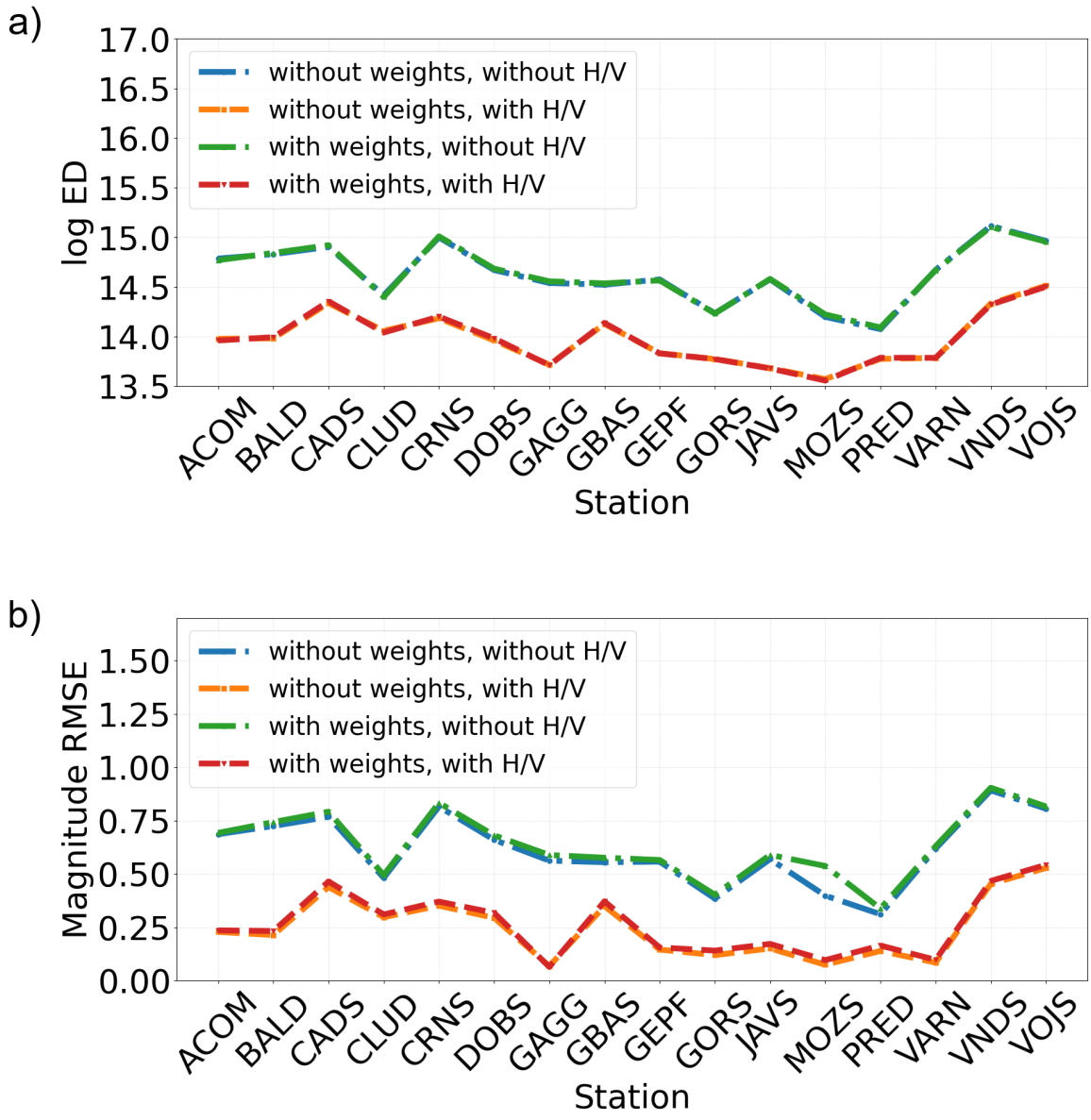

Figure 20: a) ED results of the 2-step GIT for selected stations. b) Magnitude RMSE results of the 2-step GIT for selected stations.

To identify the most suitable reference station, a combined evaluation based on both ED values and Magnitude RMSE was conducted on the 2-step GIT which is using H/V in Equation 23. Here, in order to make a suitable comparison between ED and RMSE values, all values were normalized using the following equation [Han and Kamber, 2001]:

$$X' = \frac{X - X_{min}}{X_{max} - X_{min}}(\max_{\text{new}} - \min_{\text{new}}) + \min_{\text{new}} \tag{40}$$

in which X' is the normalized value of X, and since the normalized values should be between 0 and 1, $\max_{\text{new}}$ is 1 and $\min_{\text{new}}$ is 0. As shown in Figure 21, the station *MOZS* emerged as the optimal choice. Figure 21 presents two complementary visualizations to assess the performance of selected reference stations based on spectral and magnitude criteria. Panel (a) ranks the stations by a combined score derived from normalized spectral Euclidean distance and normalized magnitude RMS error, facilitating direct comparison and selection. Panel (b) offers a two-dimensional view of the same metrics, revealing the relative trade-offs between spectral and magnitude errors for each station. Including both plots enables a more detailed interpretation: while the combined score supports ranking, the scatter plot exposes stations with asymmetric performance, guiding informed decisions in station prioritization.

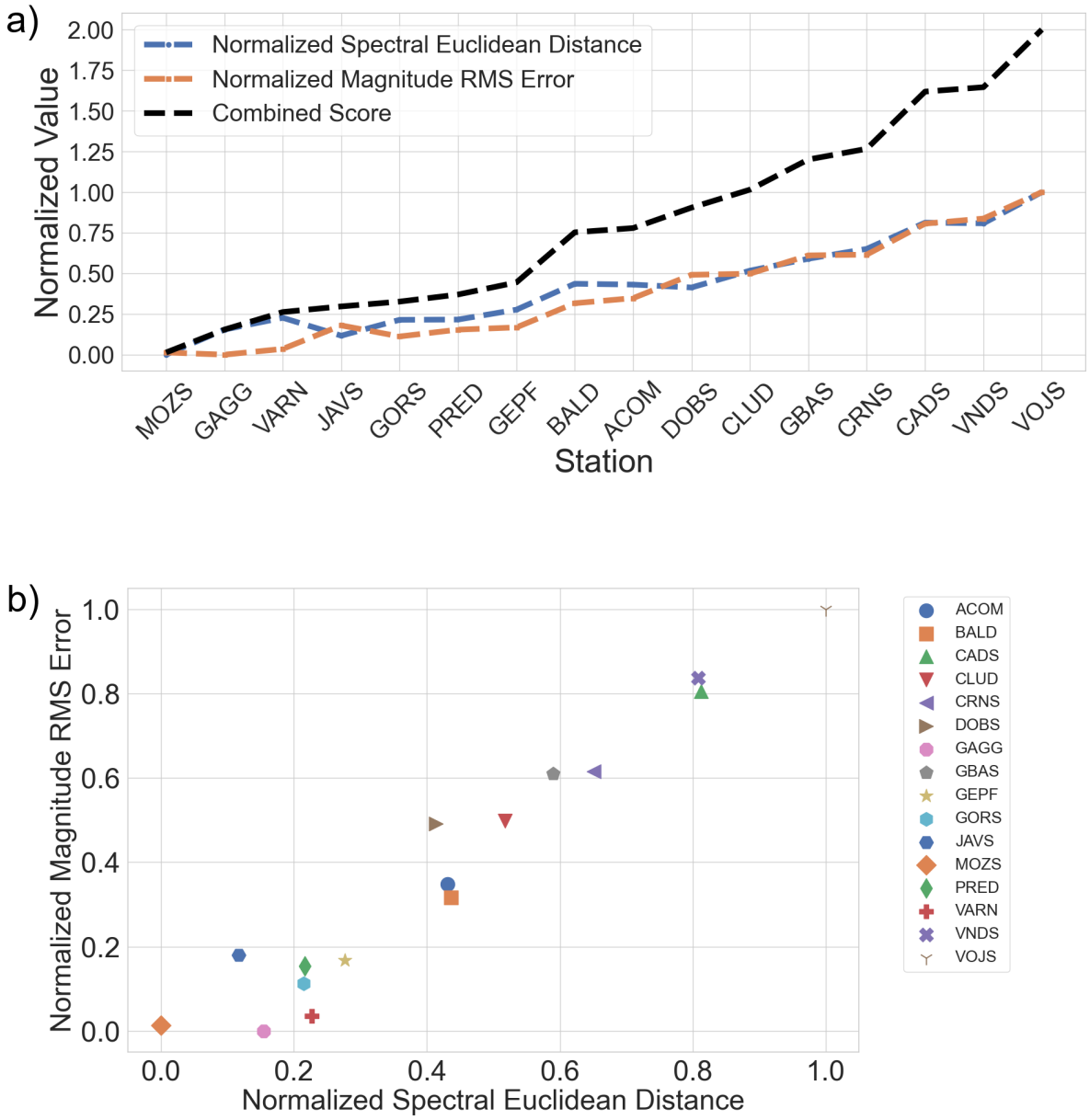

Figure 21: a) Ordering combined score of ED and Magnitude RMS Errors for the selected stations. b) Magnitude RMSE versus ED results for selected stations.

4.1.1 Source Spectra and Magnitude

The objective here is to present both the achieved events' source spectra and moment magnitudes. Figure 22 displays some of the source results obtained through the two-step GIT analysis, alongside a comparative visualization of the source spectra derived by Cataldi et al. [2025].

Each panel displays four curves: the blue line represents the source spectrum obtained in this study through spectral inversion; the orange line shows the Brune model [Brune, 1970] fitted to the blue

curve, through which the seismic moment and corner frequency obtained and the corner frequency marked by blue dot and arrow; the red line corresponds to the source spectrum reported by Cataldi et al. [2025]; and the green line depicts the theoretical Brune spectrum computed from Cataldi et al. [2025]'s published M_0 and f_c values and their corner frequency marked by black dot and arrow. These visualizations allow for direct comparison between the spectral characteristics derived in this study and those reported in prior work.

In all events, the fitted Brune model (orange) closely follows the observed source spectrum (blue), indicating that the Brune formulation provides a robust approximation of the spectral shape and energy distribution. The red curve from Cataldi et al. [2025] generally aligns with the trends observed in this study but exhibits slight deviations in amplitude and curvature, particularly before and near the corner frequency. These differences may reflect variations in data processing, attenuation correction, or inversion methodology. The green curve, being a theoretical Brune spectrum based onCataldi et al. [2025]'s parameters, serves as a benchmark for evaluating the consistency of their model. Where the red and green curves diverge, it suggests that Cataldi et al. [2025]'s spectrum may incorporate additional effects not captured by the idealized Brune formulation.

Overall, these comparisons validate the spectral inversion approach adopted in this study and demonstrate good agreement with previously published results. The close match between the fitted Brune models and the observed spectra supports the reliability of the estimated source parameters. Minor discrepancies with Cataldi et al. [2025] are expected and highlight the sensitivity of spectral modeling to methodological choices.

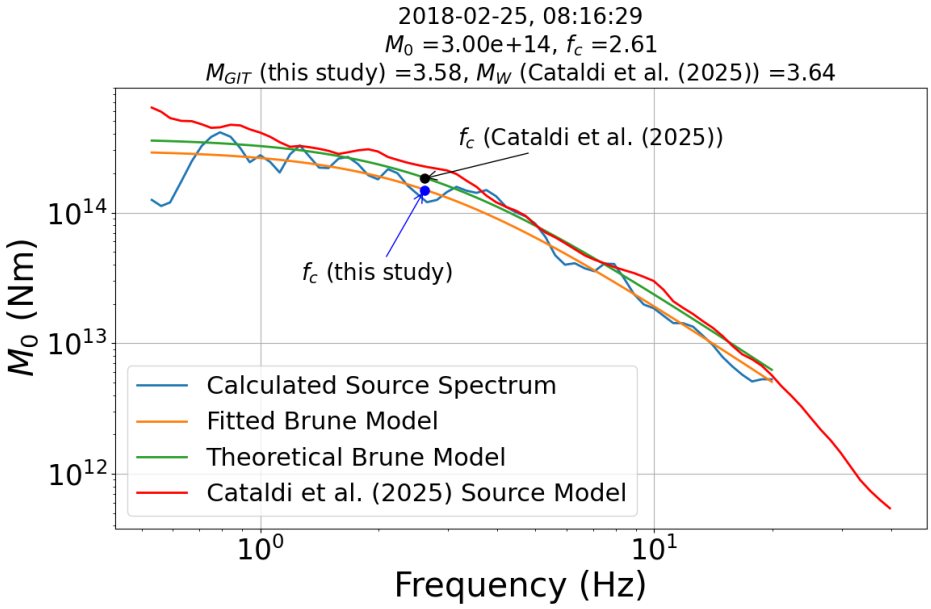
2018-02-25, 08:16:29
M_0 =3.00e+14, f_c =2.61
M_{GIT} (this study) =3.58, M_W (Cataldi et al. (2025)) =3.64
f_c (Cataldi et al. (2025))
f_c (this study)
Calculated Source Spectrum
Fitted Brune Model
Theoretical Brune Model
Cataldi et al. (2025) Source Model
M_0 (Nm)
Frequency (Hz)

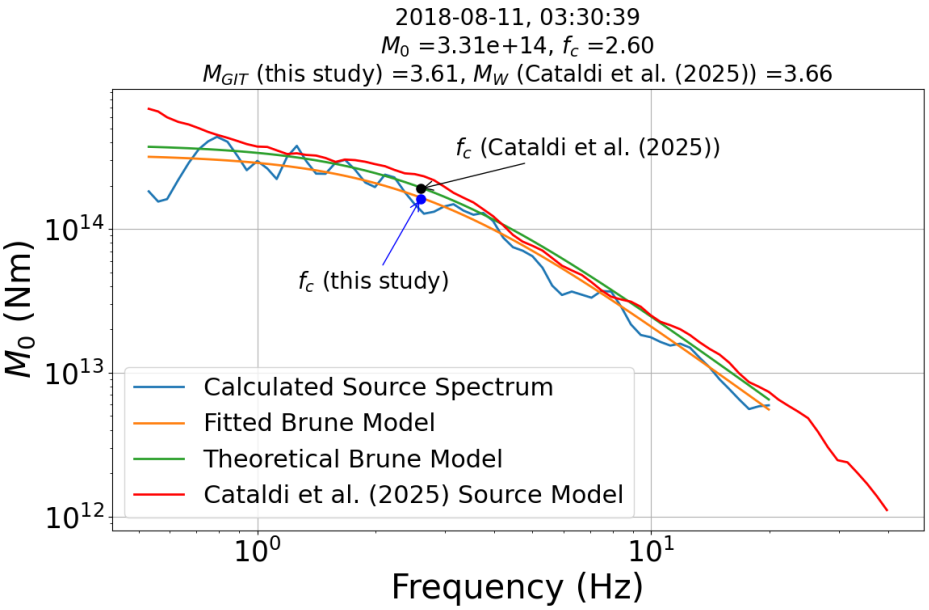
2018-08-11, 03:30:39
M_0 =3.31e+14, f_c =2.60
M_{GIT} (this study) =3.61, M_W (Cataldi et al. (2025)) =3.66
f_c (Cataldi et al. (2025))
f_c (this study)
Calculated Source Spectrum
Fitted Brune Model
Theoretical Brune Model
Cataldi et al. (2025) Source Model
M_0 (Nm)
Frequency (Hz)

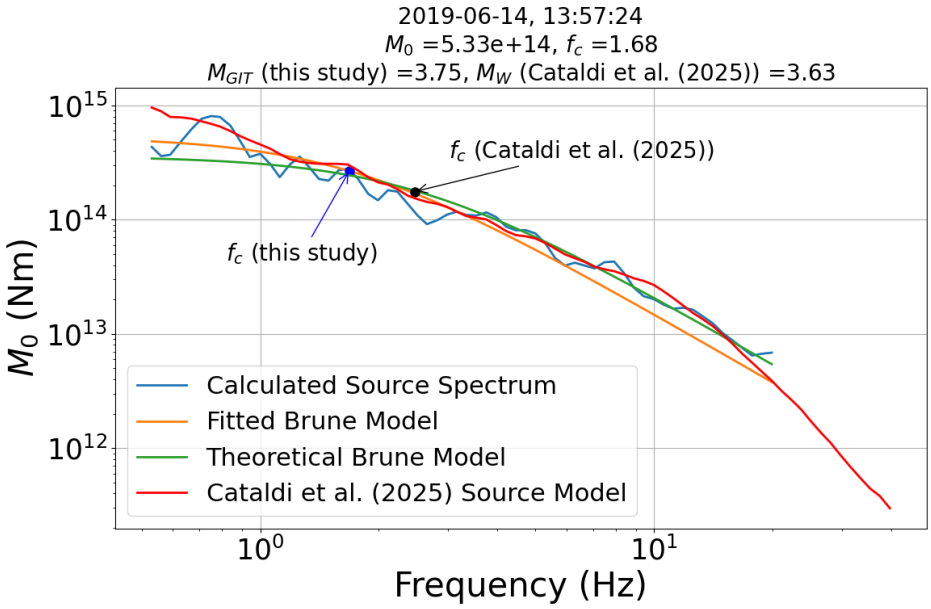
2019-06-14, 13:57:24
M_0 =5.33e+14, f_c =1.68
M_{GIT} (this study) =3.75, M_W (Cataldi et al. (2025)) =3.63
f_c (Cataldi et al. (2025))
f_c (this study)
Calculated Source Spectrum
Fitted Brune Model
Theoretical Brune Model
Cataldi et al. (2025) Source Model
M_0 (Nm)
Frequency (Hz)

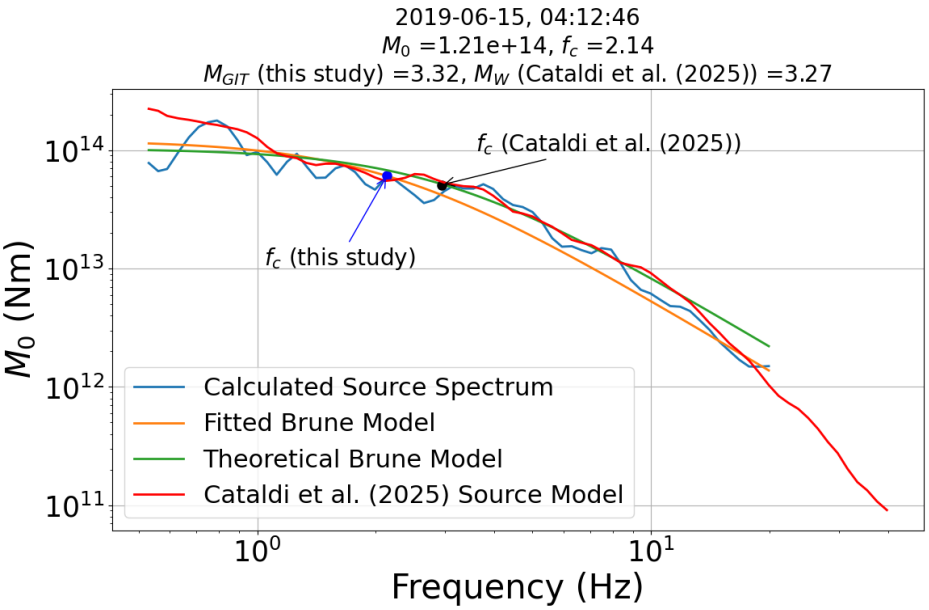
2019-06-15, 04:12:46
M_0 =1.21e+14, f_c =2.14
M_{GIT} (this study) =3.32, M_W (Cataldi et al. (2025)) =3.27
f_c (Cataldi et al. (2025))
f_c (this study)
Calculated Source Spectrum
Fitted Brune Model
Theoretical Brune Model
Cataldi et al. (2025) Source Model
M_0 (Nm)
Frequency (Hz)

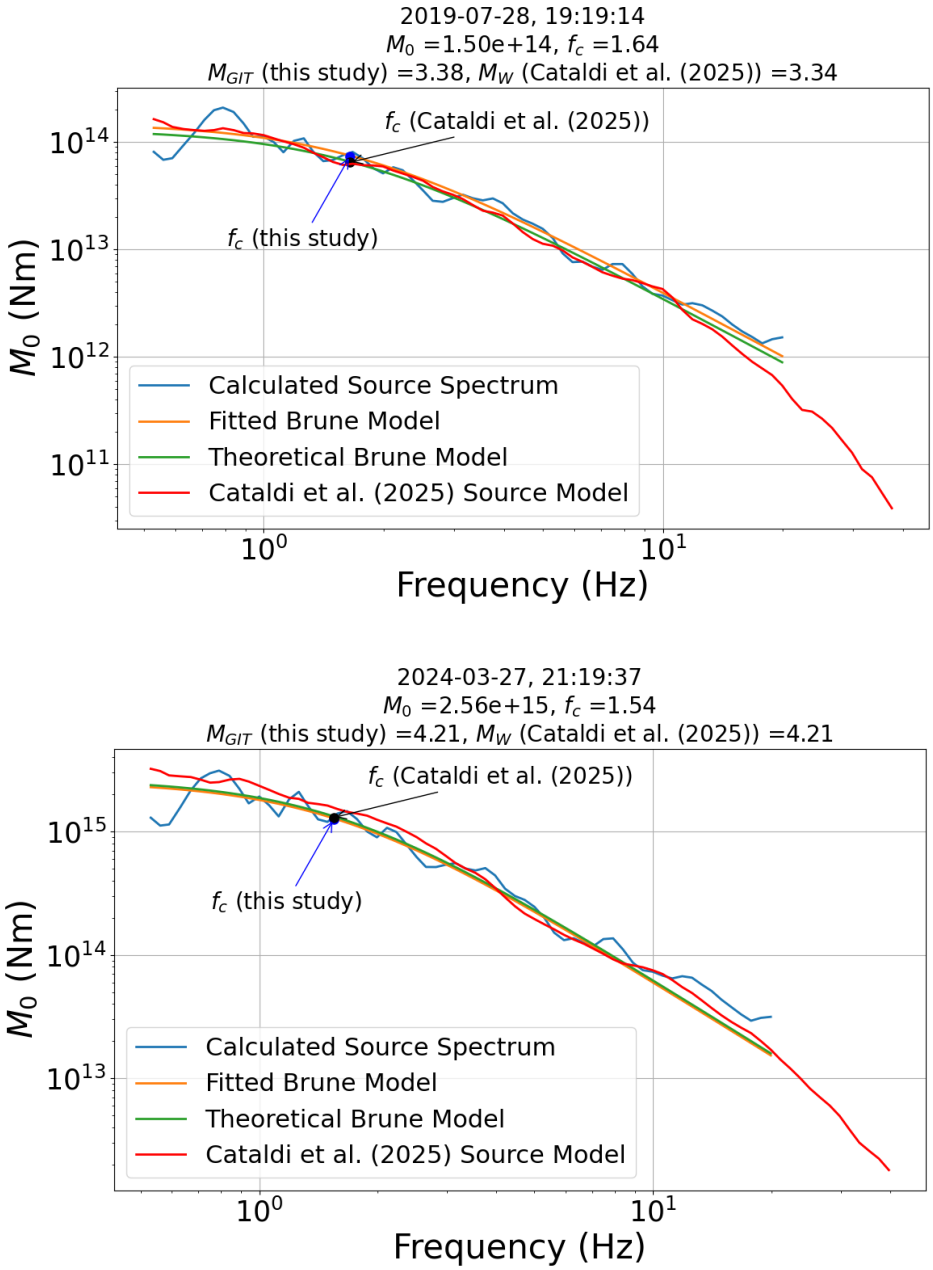

Figure 22: Some of the source models obtained by GIT.

Based on the event magnitudes, a comparative analysis with the values reported by Cataldi et al. [2025] is provided in Figure 23, while Figure 24 presents the residuals of the magnitude estimates. For this comparison, the Mean Absolute Error (MAE) is calculated as 0.05 magnitude unit, and the RMSE is 0.07 magnitude unit (with respect to to the results of Cataldi et al. [2025]). As discussed earlier, the magnitudes derived from the GIT procedure correspond to moment magnitude. These comparisons suggest that the magnitude estimates are broadly consistent with previous work, with acceptable levels of deviation. The scatter distribution and proximity to the bisector line further support the reliability of the method, while the standard deviation bands highlight the range of variability across events.

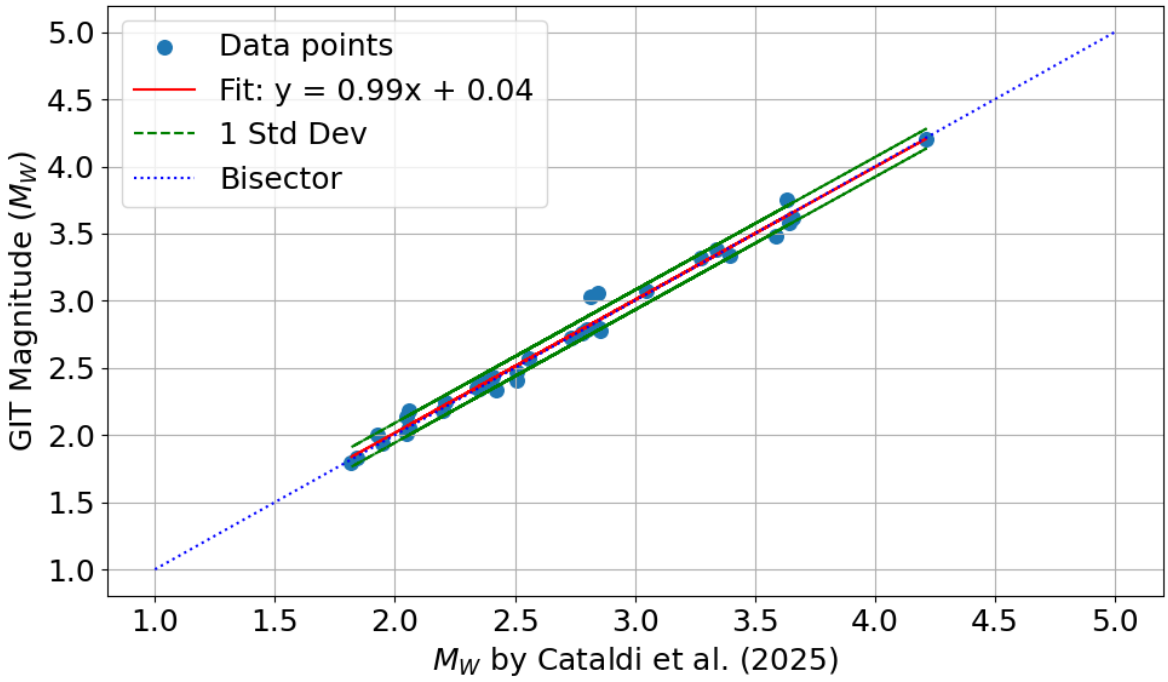

Figure 23: Comparison of the magnitudes obtained in this study with the magnitudes achieved by Cataldi et al. [2025].

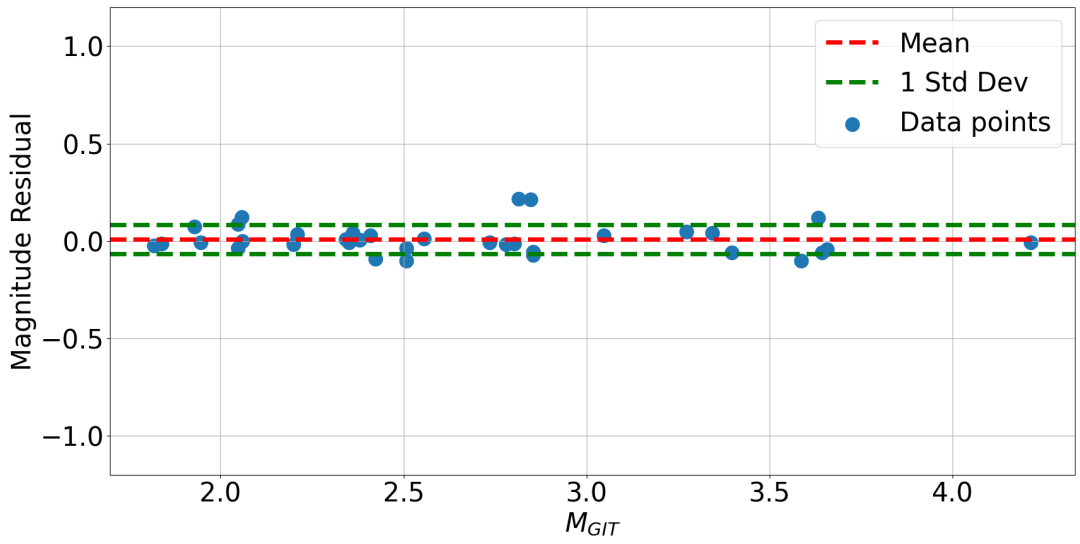

Figure 24: Magnitude residuals comparing to the results of Cataldi et al. [2025].

Although the studies by Tarchini et al. [2025] and Moratto et al. [2026] do not contain the events in 2024, they can be used to verify the results obtained in the present study. Therefore, the comparison of the moment magnitude results for the events up to the end of 2023 with the rsults of the mentioned studies are shown in Figures 25 and 26. Based on these comparisons, the RMSE with respect to the results of Tarchini et al. [2025] is 0.16 magnitude unit and with respect to the results of Moratto et al. [2026] is 0.18 magnitude unit.

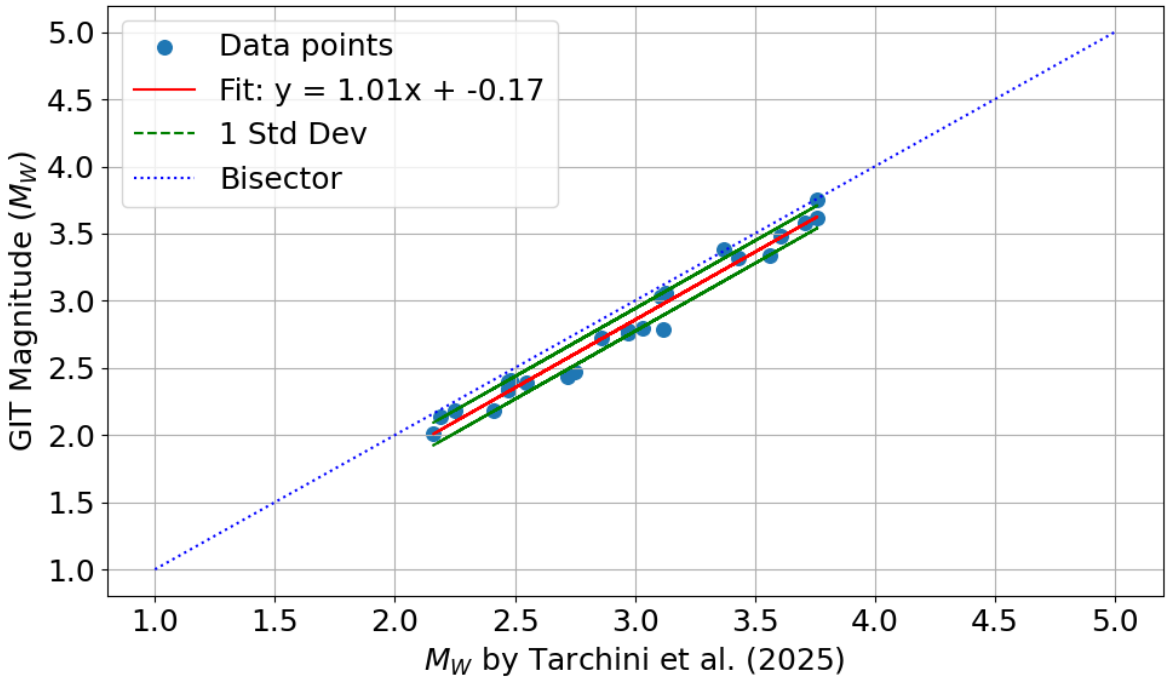

Figure 25: Comparison of the magnitudes obtained in this study with the magnitudes achieved by Tarchini et al. [2025].

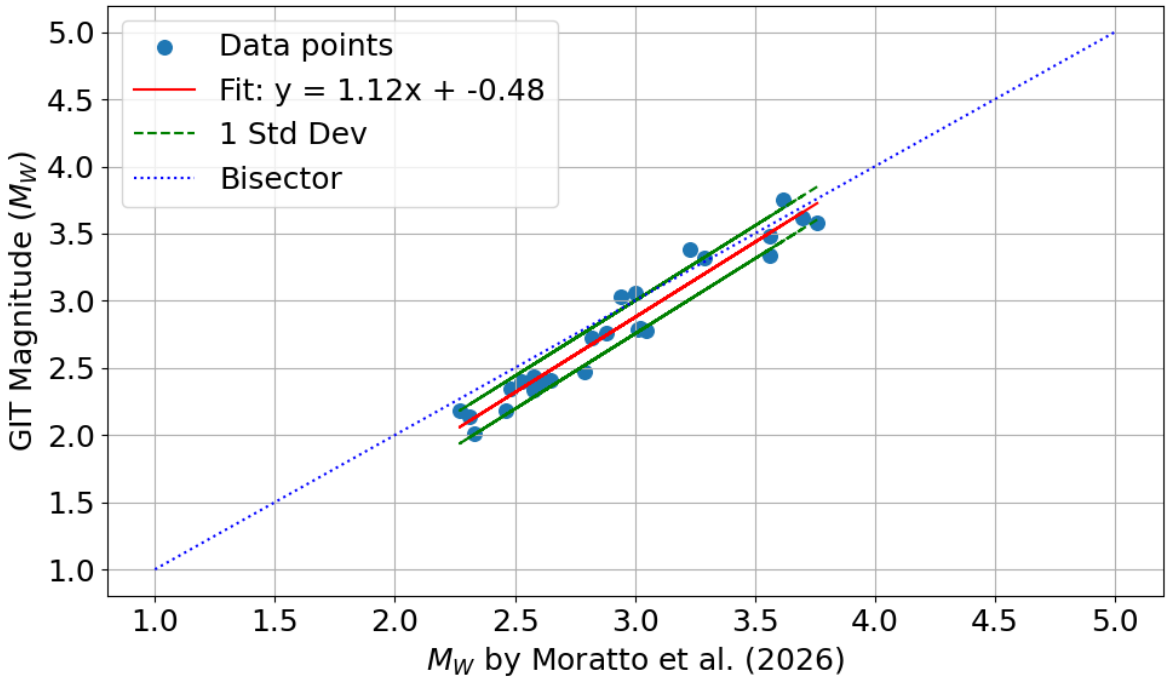

Figure 26: Comparison of the magnitudes obtained in this study with the magnitudes achieved by Moratto et al. [2026].

4.1.2 Site Amplifications

As previously discussed, one of the key outcomes of the GIT is the estimation of site amplification functions, which characterize the frequency-dependent modification of seismic waves due to local geological and geotechnical conditions. Figure 27 presents some of the site response results derived from the GIT method, offering a quantitative assessment of amplification across the studied frequency range. These results are compared against available site amplification data reported by Cataldi et al. [2025], Klin et al. [2021], University of Genoa [1967] (denoted as RSNI), Felicetta et al. [2023], Luzi et al. [2008] (denoted as ITACA), and Cultrera et al. [2022] (denoted as CRISP), providing a benchmark for validation and regional consistency. Additionally, the figure includes H/V spectral ratio curves computed using the data collected in this study.

To estimate the H/V in this study, a time window of 30 seconds was extracted which is starting from the onset of the S-wave arrival. This window was selected to ensure the inclusion of stable shear-wave energy while minimizing contamination from preceding P-wave arrivals. The two horizontal components of ground motion were transformed into the frequency domain using the Fourier transform [Fourier, 1822]. To obtain a representative horizontal amplitude spectrum, the spectral amplitudes of these components were combined via vectorial summation, as defined in Equation 8, which preserves the energy content and accounts for directional variability. The resulting composite horizontal spectrum was then divided by the vertical component's amplitude spectrum, yielding the H/V ratio as a function of frequency. This approach facilitates the identification of site-specific resonance frequencies and amplification characteristics.

Figure 27 is comparing results obtained in this study with those from previous investigations. The blue curve in each panel represents the site response derived using the GIT, while the remaining curves correspond to various estimates from other studies as mentioned before.

Overall, the GIT-derived site response shows good agreement with the general trends observed across the other studies. For all site results, the GIT curve captures the dominant amplification peaks and frequency-dependent behavior, aligning well with the H/V S-phase and noise-based estimates. Minor discrepancies in amplitude and peak frequency are expected due to differences in data type, processing techniques, and reference site assumptions. Notably, the consistency between GIT and independent studies reinforces the reliability of the inversion results and supports the use of GIT-based site corrections in subsequent spectral modeling.

These comparisons highlight the robustness of the GIT approach in capturing site-specific amplification

effects, while also demonstrating coherence with established methodologies. The inclusion of multiple reference curves provides a comprehensive validation framework, ensuring that the adopted site response functions are both physically acceptable and empirically supported.

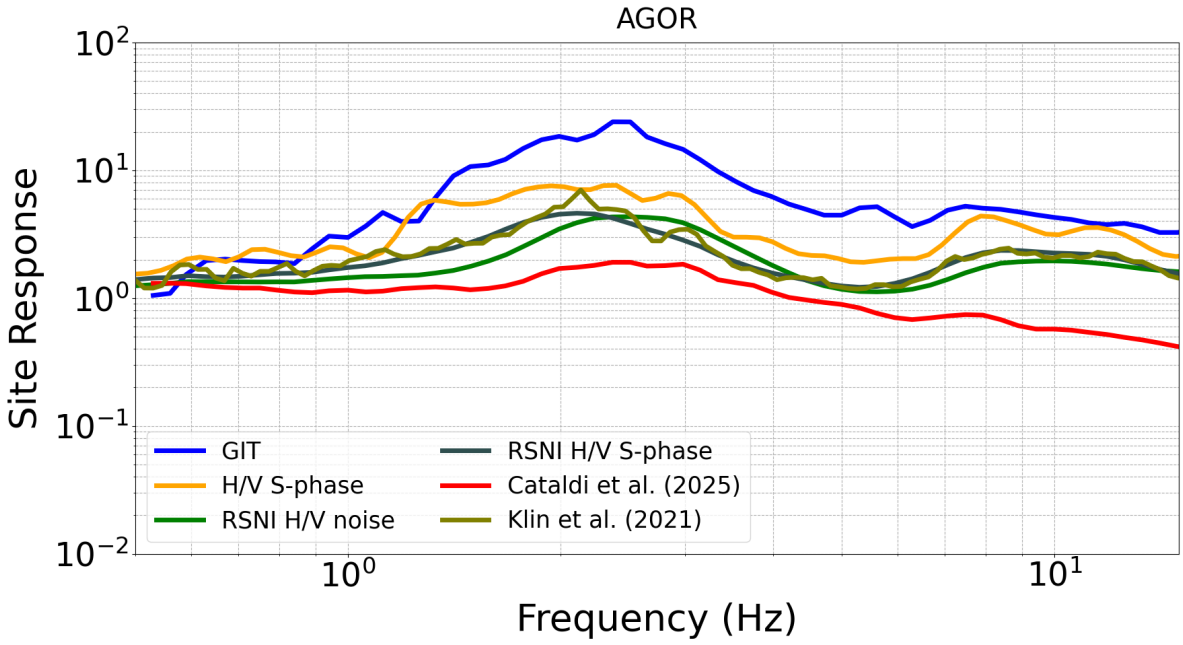

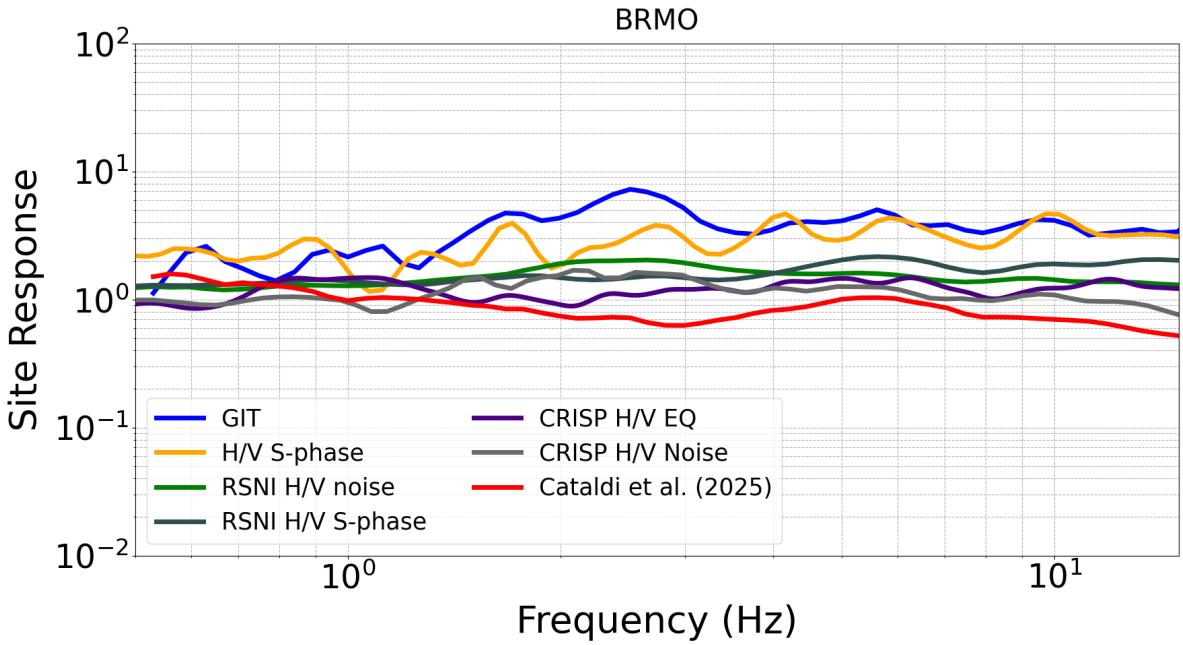

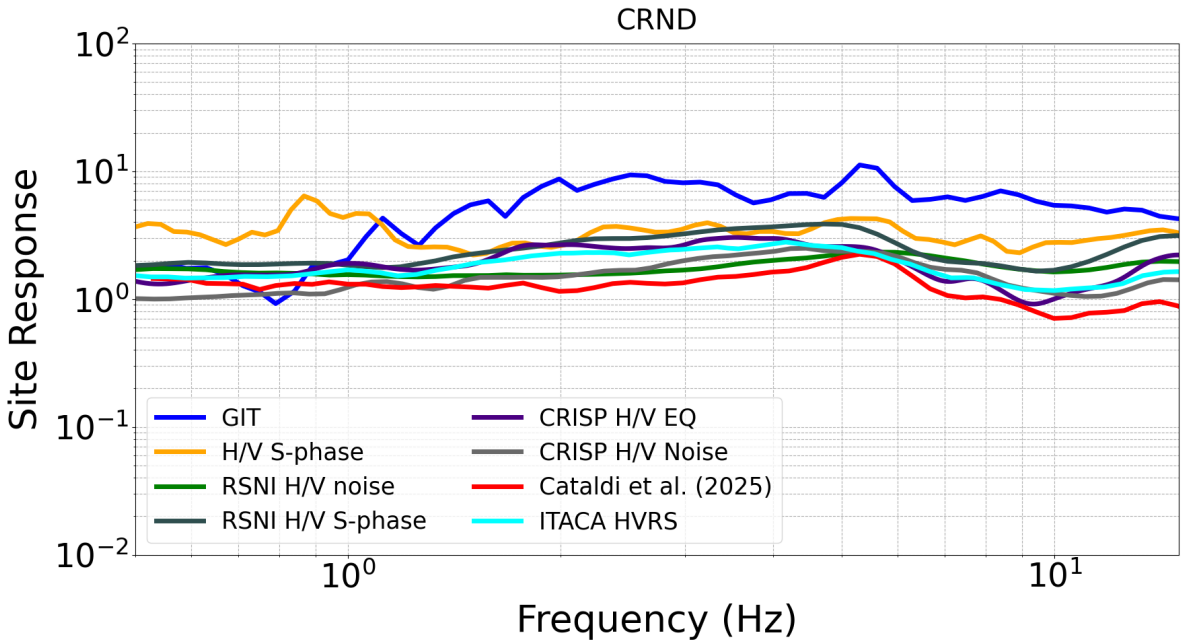
CRND
Site Response
Frequency (Hz)
GIT
H/V S-phase
RSNI H/V noise
RSNI H/V S-phase
CRISP H/V EQ
CRISP H/V Noise
Cataldi et al. (2025)
ITACA HVRS

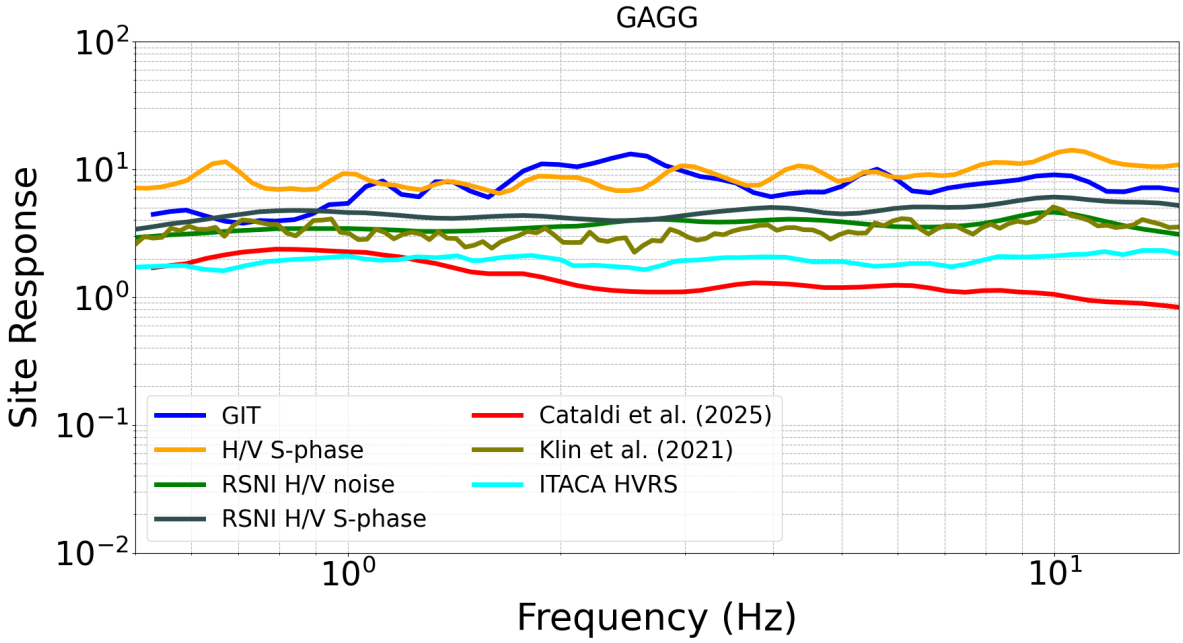
GAGG
Site Response
Frequency (Hz)
GIT
H/V S-phase
RSNI H/V noise
RSNI H/V S-phase
Cataldi et al. (2025)
Klin et al. (2021)
ITACA HVRS

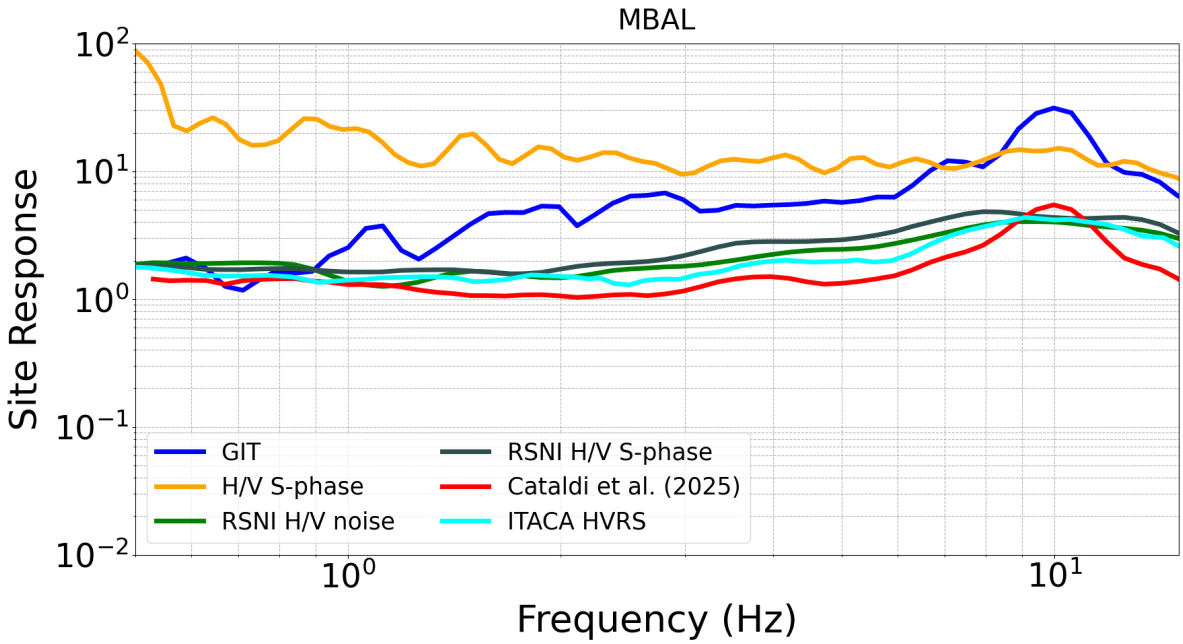
MBAL
Site Response
Frequency (Hz)
GIT
H/V S-phase
RSNI H/V noise
RSNI H/V S-phase
Cataldi et al. (2025)
ITACA HVRS

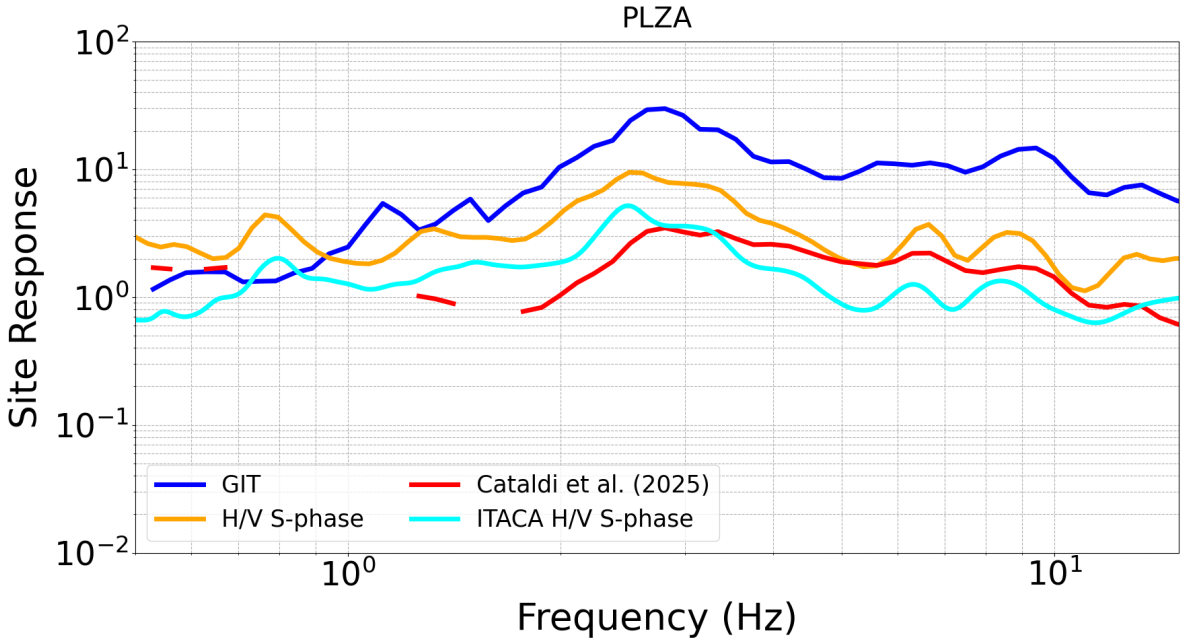
PLZA
Site Response
Frequency (Hz)
GIT
H/V S-phase
Cataldi et al. (2025)
ITACA H/V S-phase

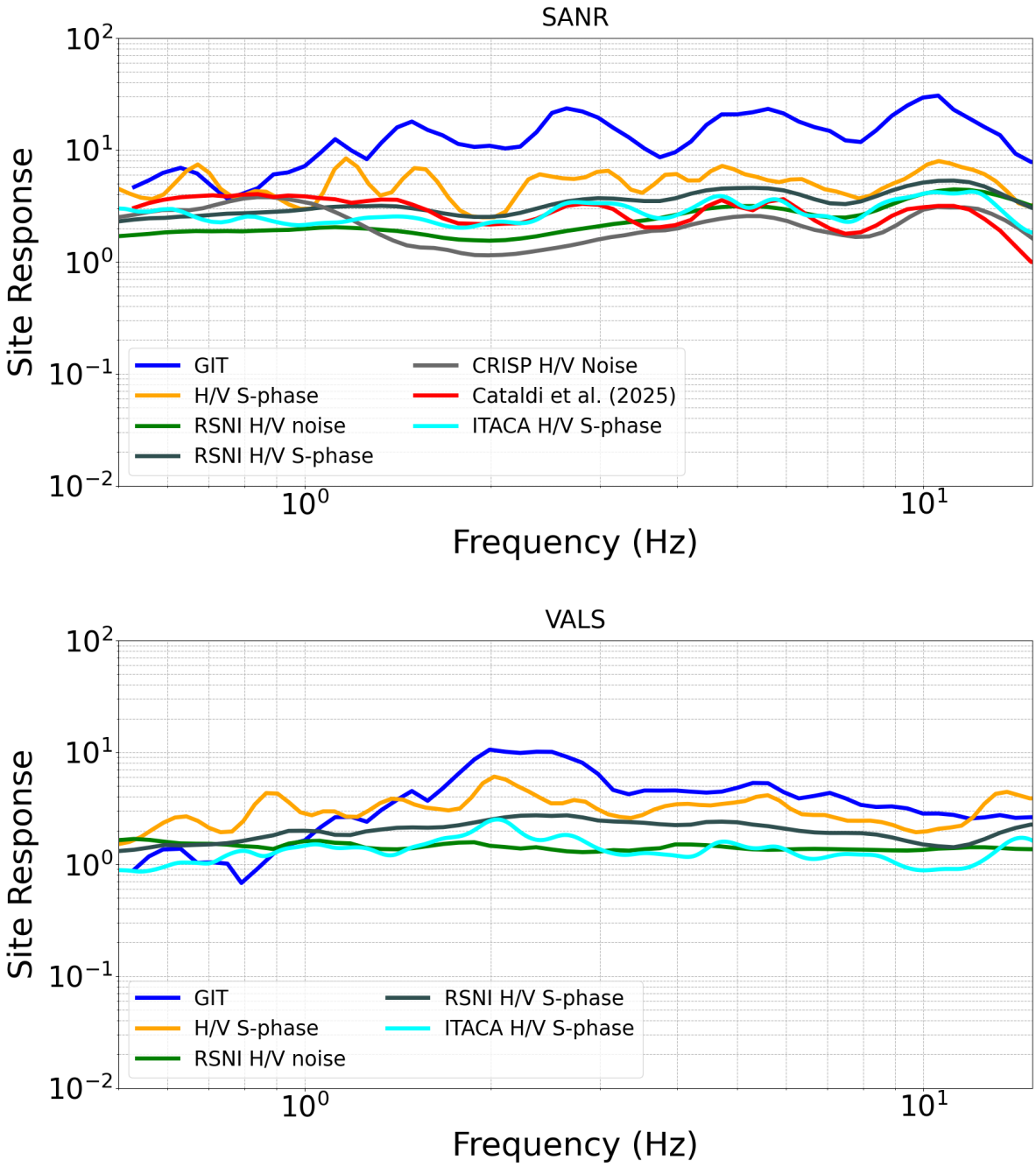

Figure 27: Some of the site amplifications obtained by GIT.

4.1.3 Attenuation

As previously declared, attenuation and path effect can be obtained through GIT as well. Figures 28 and 29 illustrate the attenuation profiles extracted through GIT in two-dimensional and three-dimensional spatial representations, respectively. These visualizations shows the spatial variability and frequency-

dependent behavior of seismic wave attenuation across the study area.

In the 2D plot, each gray line represents the attenuation curve for a specific frequency, showing how spectral amplitude decays with distance. To highlight representative frequencies, the curves for 1 Hz, 5 Hz, and 10 Hz are shown in black. A blue dashed line is included to illustrate the theoretical decay proportional to the inverse of distance, serving as a reference for geometrical spreading.

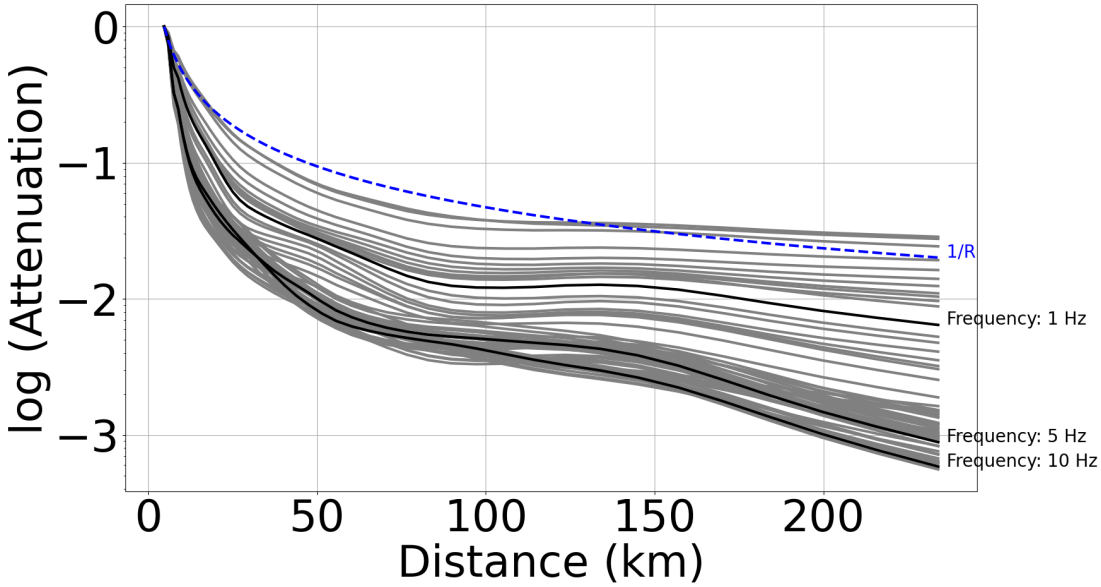

Figure 28: Attenuation curves obtained by GIT. Each grey line represents the attenuation curve for each frequency. To be distinct, the curves for frequencies 1, 5 and 10 Hz are shown by black lines. The blue dashed line is showing the decay proportional to the inverse of the distance.

The 3D surface plot provides a comprehensive view of attenuation behavior across both frequency and distance dimensions. This visualization reveals the frequency-dependent nature of attenuation, with higher frequencies exhibiting steeper decay rates over distance, consistent with expectations from anelastic attenuation and scattering effects. The surface topology can intensify attenuation with increasing frequency, reinforcing the need for frequency-specific correction in spectral modeling.

Together, these plots validate the attenuation model obtained through GIT and demonstrate its physical consistency. The alignment of the obtained curves with the theoretical decay trend supports the robustness of the inversion, while the frequency-dependent structure captured in the 3D plot highlights the importance of incorporating attenuation corrections based on spectral content. These results form a critical component of the overall source parameter estimation framework, ensuring that distance-related amplitude decay is accurately accounted for in magnitude and stress drop calculations.

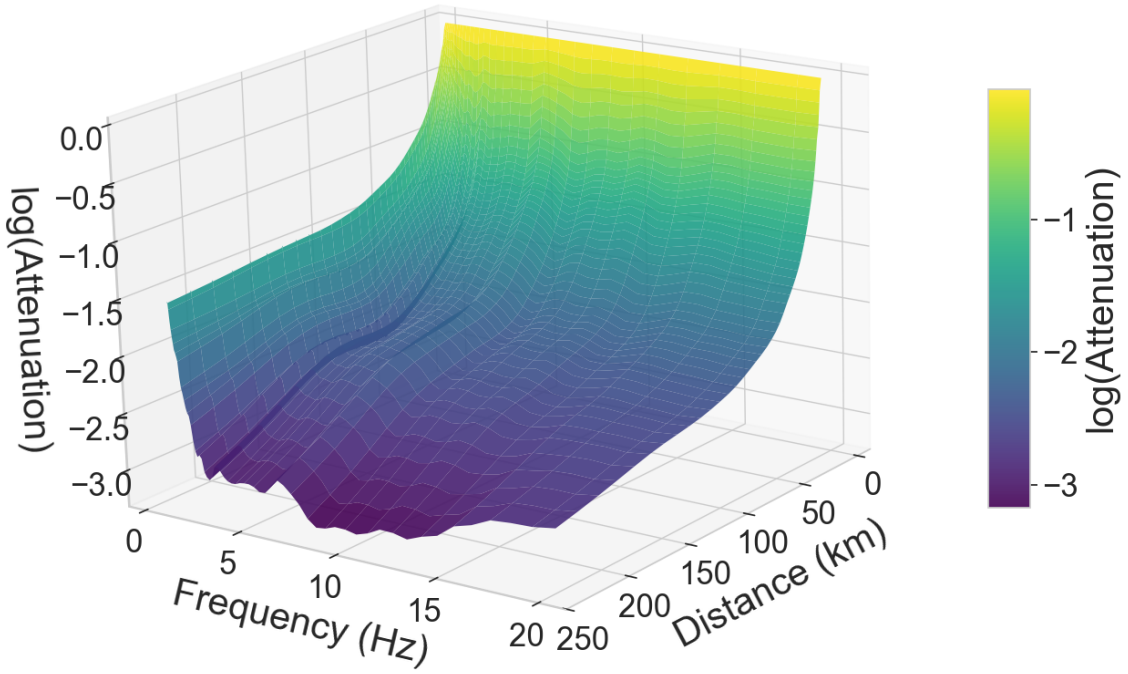

Figure 29: Attenuation curves obtained by GIT in 3D view showing the variations in attenuation along with distance and frequency.

In addition, Figure 30 provides a comparative assessment between the obtained attenuation curves in this study and those reported by Cataldi et al. [2025]. The figure builds upon the presentation in Figure 28, with the addition of attenuation curves from Cataldi et al. [2025], shown as pink lines. To enhance visual distinction, the attenuation curves corresponding to 1 Hz, 5 Hz, and 10 Hz are highlighted in red. This comparison allows for a direct evaluation of frequency-dependent attenuation behavior across studies, and helps validate the consistency of the inversion results with previously published models.

The comparison reveals strong consistency between the two studies, particularly at lower frequencies and shorter distances, where both sets of curves closely follow the expected $1/R$ decay trend. At higher frequencies and longer distances, the attenuation becomes more noticeable, reflecting the influence of anelastic effects and scattering. While differences in amplitude and slope are observed between the two results, these are likely attributable to variations in data selection, inversion parameters, and site corrections.

Overall, the agreement between the attenuation curves supports the robustness of the GIT-derived model and confirms its compatibility with previously published results. This validation is essential for ensuring reliable amplitude correction in spectral modeling.

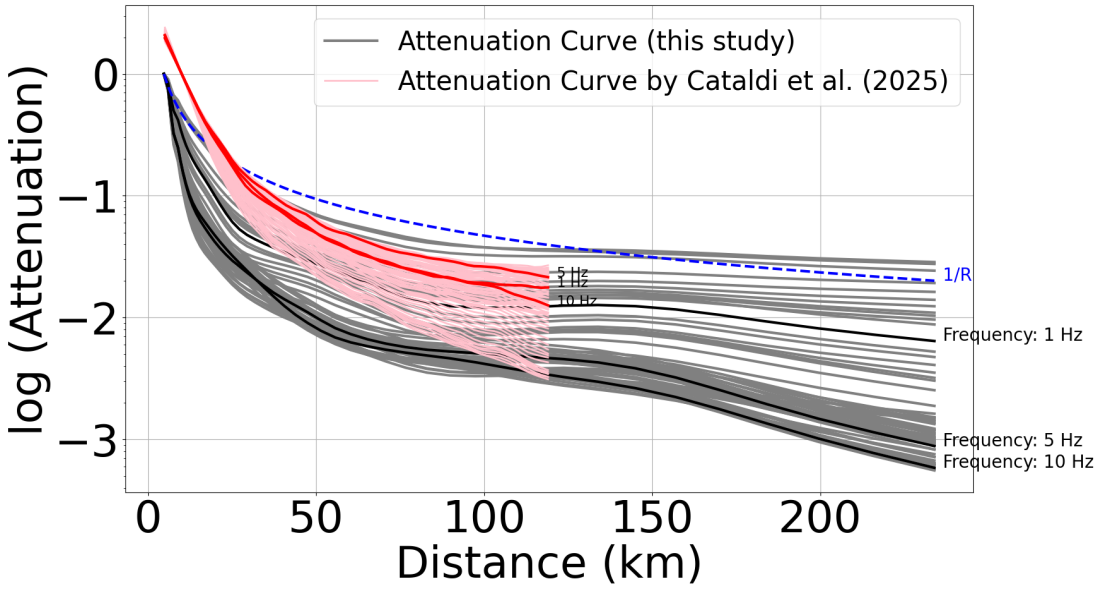

Figure 30: Same as Figure 28 with addition of the attenuation curves by Cataldi et al. [2025] as pink lines and distinguishing frequencies 1, 5 and 10 Hz with red lines.

4.1.4 Attenuation Smoothness

As previously delineated in Equations 17 and 21, Castro et al. [1990] claimed that the weighting coefficient w_2 governs the attenuation smoothness, serving as a regularization parameter within the inversion framework. To empirically determine the most appropriate value for w_2, a series of analyses were conducted. Figure 31 demonstrates that progressive increase of w_2 yields increasingly smoother attenuation profiles, indicative of enhanced regularization effects.

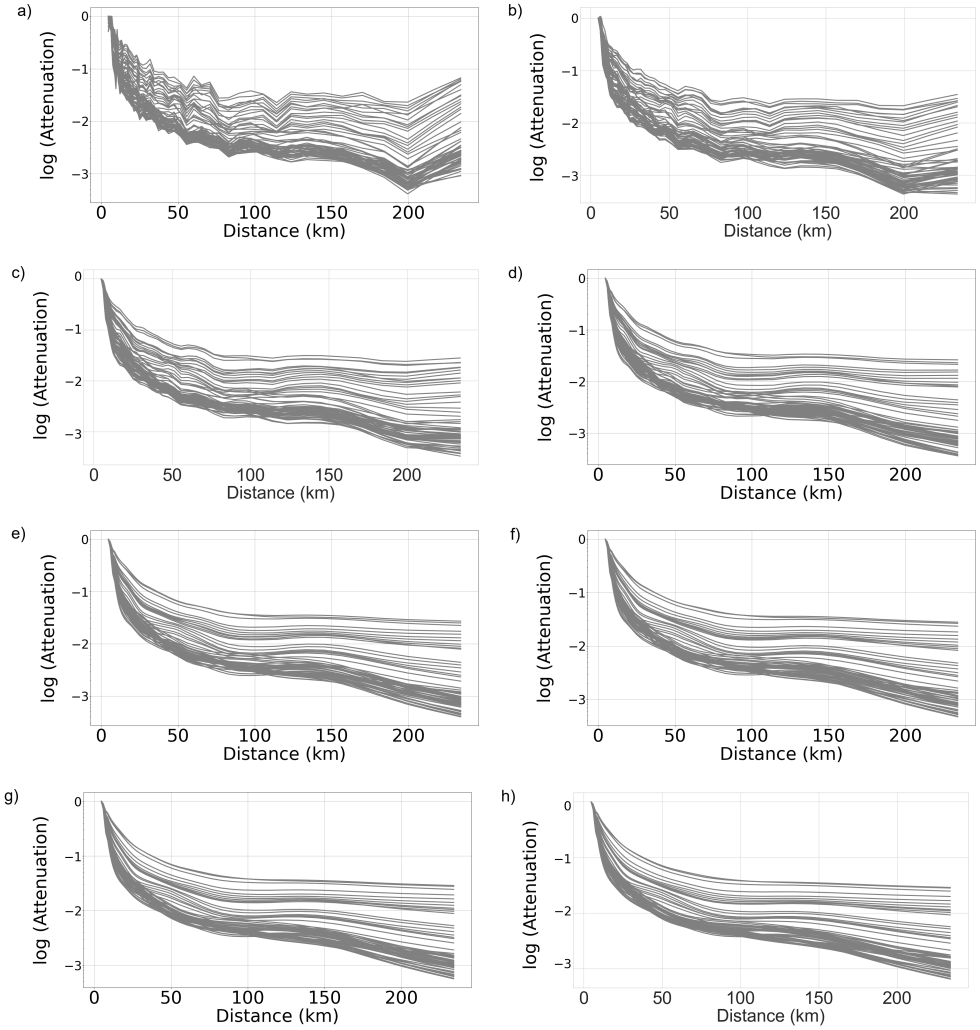

Figure 31: Achieved attenuation curves by changing w_2 in Equations 17 and 21. a) $w_2 = 1$. b) $w_2 = 5$. c) $w_2 = 10$. d) $w_2 = 20$. e) $w_2 = 30$. f) $w_2 = 40$. g) $w_2 = 50$. h) $w_2 = 60$.

Moreover, Figure 32 evaluates the trade-off between smoothness and accuracy by examining the RMSE of the magnitudes. The analysis reveals that a value of 50 optimally balances the two objectives of minimizing magnitude misfit while preserving smoothness, thereby ensuring robust and interpretable inversion outcomes (the same is true for the MAE of magnitudes).

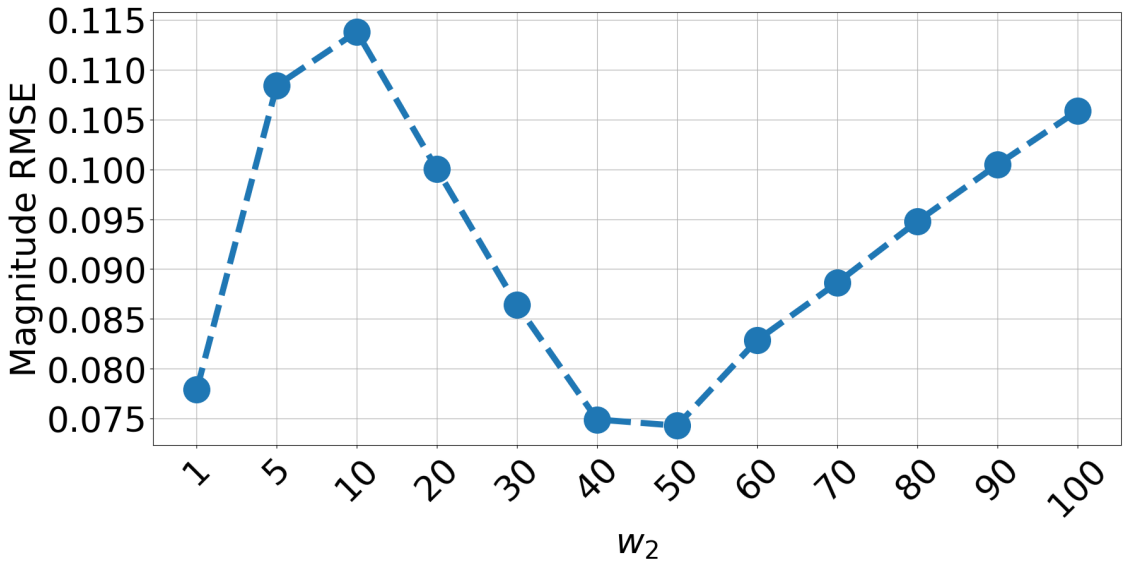

Figure 32: RMSE of magnitude results by changing w_2 in Equations 17 and 21.

4.1.5 Corner Frequency and Stress Drop

As explained earlier, from Equation 30, the corner frequency is estimated for each event, enabling direct comparison with the corner frequencies reported by Cataldi et al. [2025], as illustrated in Figure 33. The figure highlights the consistency between the two datasets across a broad frequency range, particularly for moderate-to-large events. However, at higher frequencies, typically associated with smaller magnitude events, noticeable discrepancies emerge between the results of this study and those of Cataldi et al. [2025]. These differences may stem from variations in spectral fitting procedures, attenuation corrections, or site response assumptions, which tend to have a more pronounced impact on high-frequency content. Despite these deviations, the overall agreement supports the reliability of the inversion method used in this study and underscores the sensitivity of corner frequency estimation to methodological choices, especially for the small events.

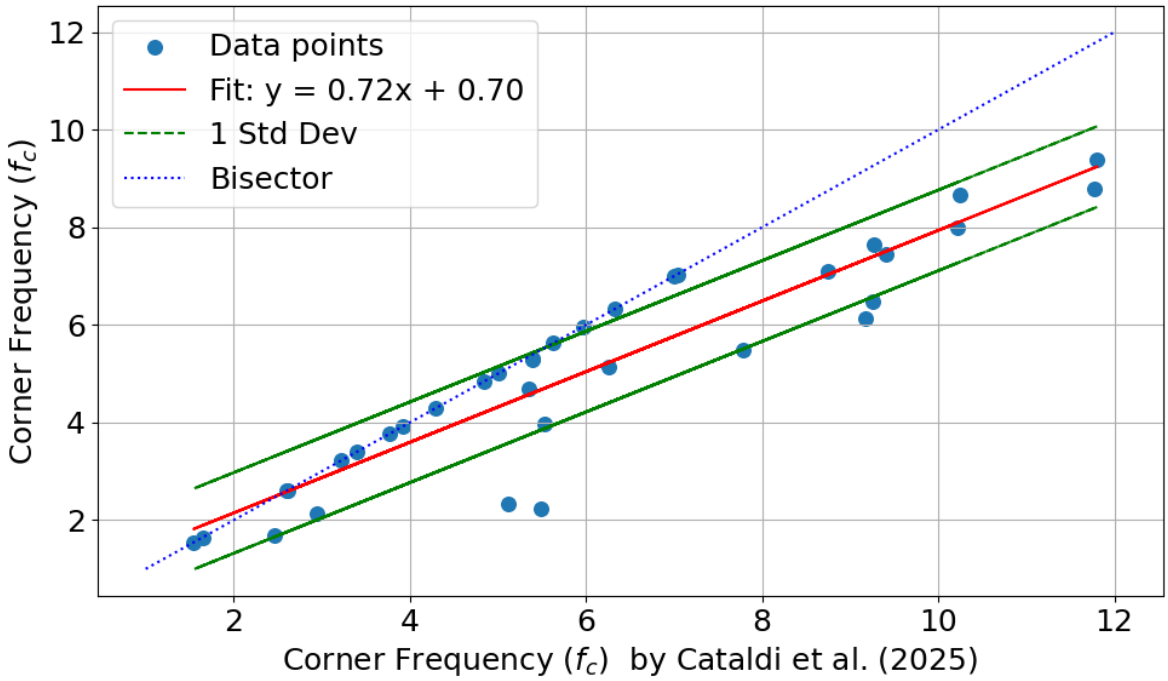

Figure 33: Comparison of the corner frequencies obtained in this study with the results achieved by Cataldi et al. [2025].

Taking Equation 41 into account [Brune, 1970], the relationship between M_0 and f_c obtained in this study follows the expected trend, as shown in Figure 34. The data points align well with the theoretical stress drop ($\Delta\sigma$) contours, represented by black lines corresponding to constant Brune stress drop values (e.g., 0.1 MPa, 1 MPa, 10 MPa). This consistency confirms the physical plausibility of the inversion results and supports the reliability of the estimated source parameters.

$$\Delta\sigma = \frac{7}{16} M_0 \left(\frac{f_c}{0.37 v_s}\right)^3 \tag{41}$$

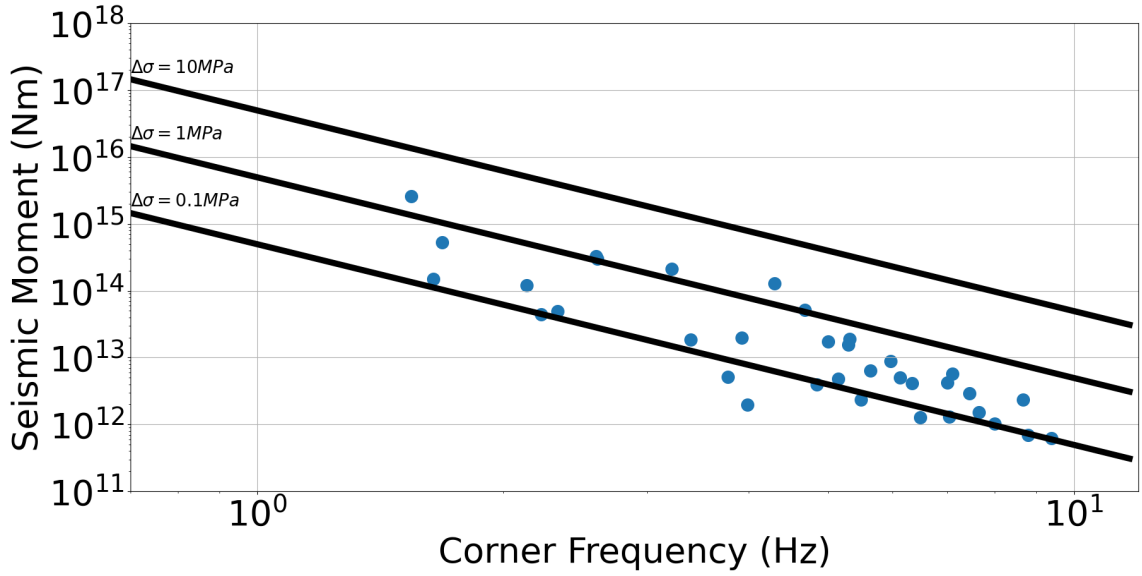

Figure 34: Seismic Moment derived from GIT versus its corresponding corner frequency (Blue dots). Black lines are showing the constant Brune stress drop.

Figure 35 further explores the relationship between M_0 and $\Delta\sigma$ providing a comparative view of the average stress drop obtained in this study (black dashed line) alongside those reported by Franceschina et al. [2006] (blue dashed line) and Cataldi et al. [2022] (red dashed line) for the same region. Notably, the stress drops derived in this study are closer to the results of Franceschina et al. [2006], suggesting methodological or regional consistency. Slight differences with respect to Cataldi et al. [2022] may reflect variations in dataset composition, inversion procedures, or correction strategies. These comparisons reinforce the robustness of the spectral inversion approach and offer regional context for interpreting stress drop variability across events.

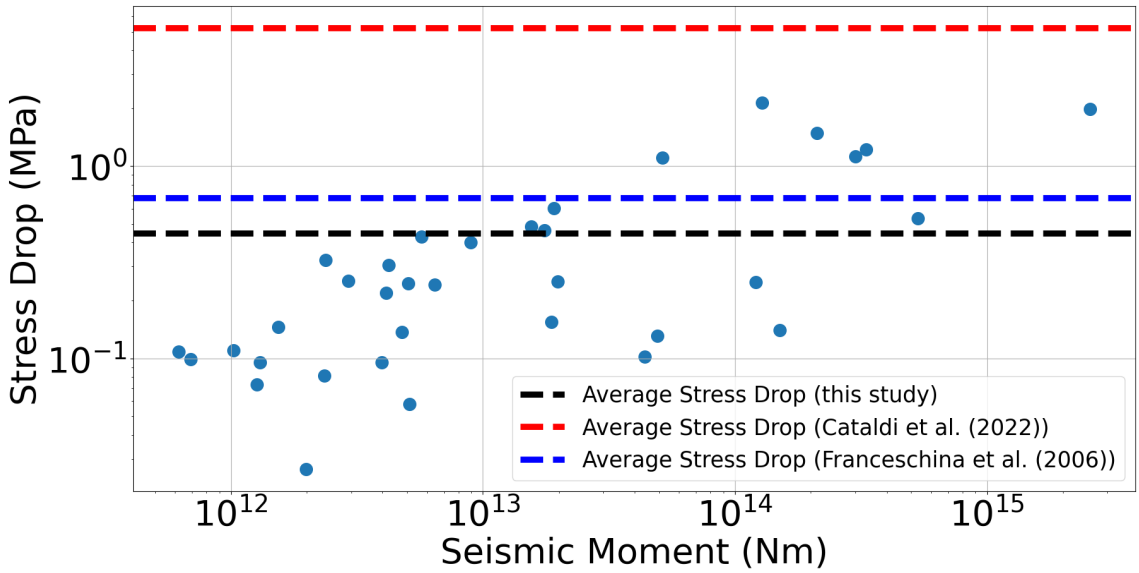

Figure 35: Seismic Moment derived from GIT versus its corresponding Stress Drop (Blue dots). Black dashed-line is showing the average Stress Drop. Blue dashed-line is showing the average Stress Drop obtained by Franceschina et al. [2006]. Red dashed-line is showing the average Stress Drop obtained by Cataldi et al. [2022].

Furthermore, the scaling relationship between M_0 and f_c proposed by Franceschina et al. [2006] for the Friuli Venezia Giulia region (Northeastern Italy) takes the form $M_0 \propto f_c^{-(3+\epsilon)}$, with an empirically derived exponent $\epsilon = 0.43$. This formulation reflects a generalized source spectral model in which the decay of M_0 with increasing f_c is affected by the parameter ϵ. In the present study, a comparable inverse power-law dependence was observed, as illustrated in Figure 36, yielding a best-fit exponent of $\epsilon = 0.59$. This result, while comparing to the result of Franceschina et al. [2006], reinforces the robustness of the M_0 and f_c scaling in the region while suggesting a slightly steeper decay trend, potentially attributable to differences in dataset composition, inversion methodology, or regional stress conditions. However, the value of 0.59 of the present study is completely consistent with the value of 0.5 obtained by Moratto et al. [2026].

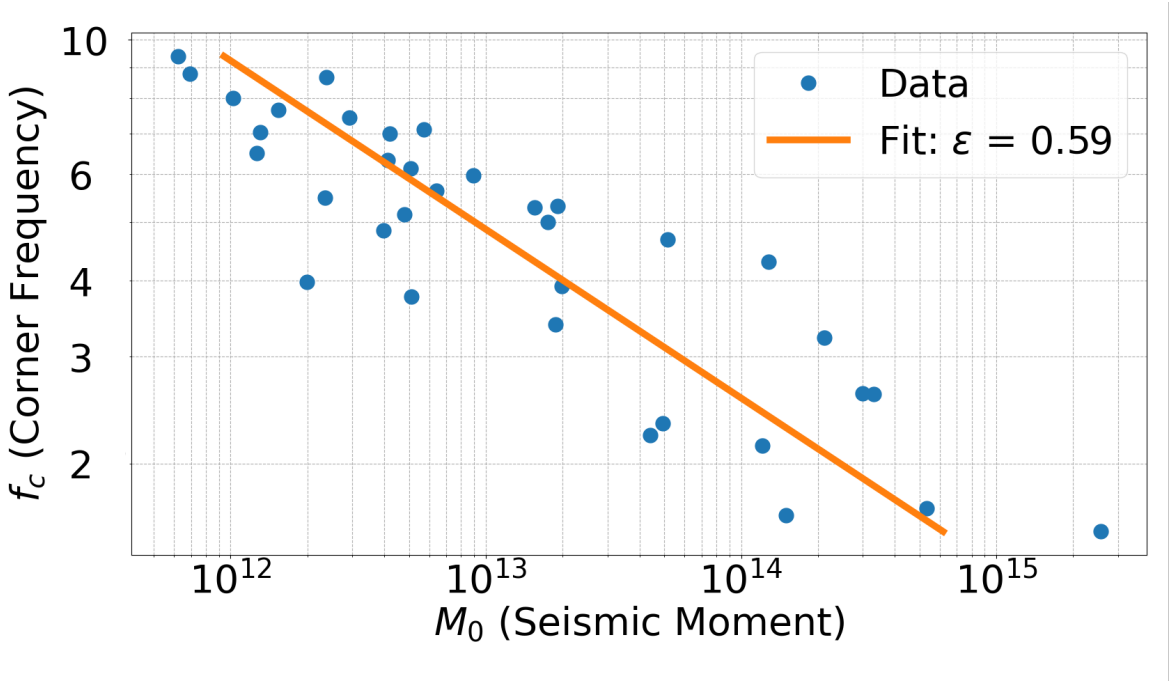

Figure 36: Obtained relation between f_c and M_0. The green line is the scaling relation $M_0 \propto f_c^{-(3+\epsilon)}$ with $\epsilon = 0.59$.

4.1.6 Residuals

To perform a comparison between the finalized source model and each corresponding Fourier amplitude spectrum, corrected for site amplification and attenuation, the residual ratio and its logarithmic average are calculated according to Equations 42 and 43 [Cataldi et al., 2022].

$$R_{ij}(f_k) = \frac{FAS^o_{ijk}}{FAS^m_{ijk}} \tag{42}$$

$$\ln(a_j(f_k)) = \frac{1}{N_i}\sum_{i=1}^{N_i} \ln(R_{ij}(f_k)) \tag{43}$$

where i is the event, j is the station, k is the frequency point, o shows the observed data and m is the modeled spectrum. The resulting metrics are evaluated across individual frequency bins, event magnitudes, focal depths, and hypocentral distances, as illustrated in Figures 37 through 40, respectively.

The results of this study demonstrate that the computed residual ratios consistently converge toward

unity across all examined parameters, including frequency points, magnitude ranges, hypocentral depths, and hypocentral distances. This uniformity suggests that the final model outputs exhibit a high degree of statistical neutrality, with no significant systematic bias present in any of the evaluated domains. In particular, the residuals, defined as the ratio between the observed and calculated values, remaining centered around 1 imply that the model neither systematically overestimates nor underestimates the spectral amplitudes and derived source parameters across all of the considered seismic events.

Such behavior is indicative of a well-calibrated inversion framework, wherein the empirical and theoretical components are yielding physically consistent and unbiased calculations. The absence of frequency-dependent or magnitude-dependent deviations further reinforces the robustness of the model, suggesting that it maintains predictive ability across varying source sizes and propagation conditions. Similarly, the stability of residuals with respect to hypocentral depths and distances confirms that the attenuation and geometrical spreading corrections embedded in the model are appropriately tuned for the regional crustal structure.

Overall, these findings show the reliability of the adopted modeling approach and support its applicability for regional seismic hazard assessment, magnitude scaling studies, and other waveform-based estimations without introducing systematic biases across key seismological parameters.

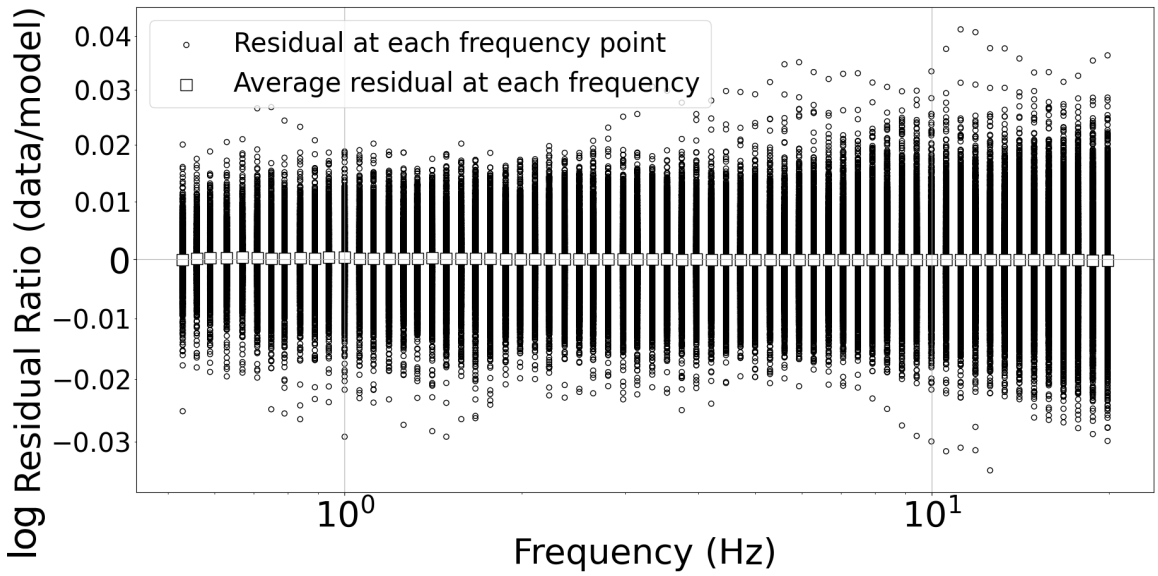

Figure 37: Residual ratios (circles) and log-average of them (squares) for each observed FAS and final modeled FAS regarding each frequency point.

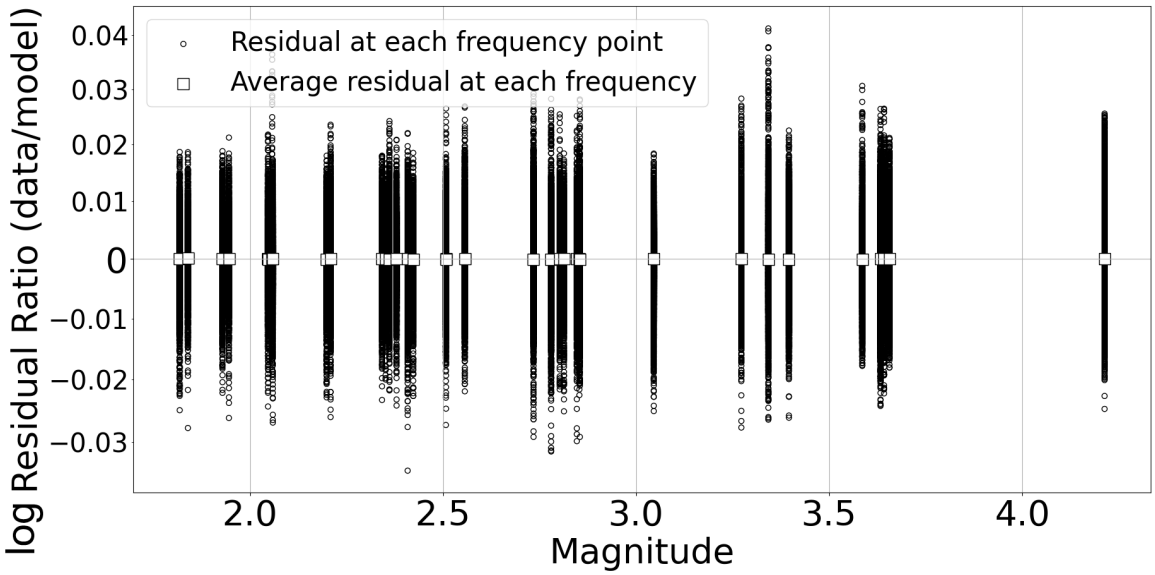

Figure 38: Residual ratios (circles) and log-average of them (squares) for each observed FAS and final modeled FAS regarding each magnitude.

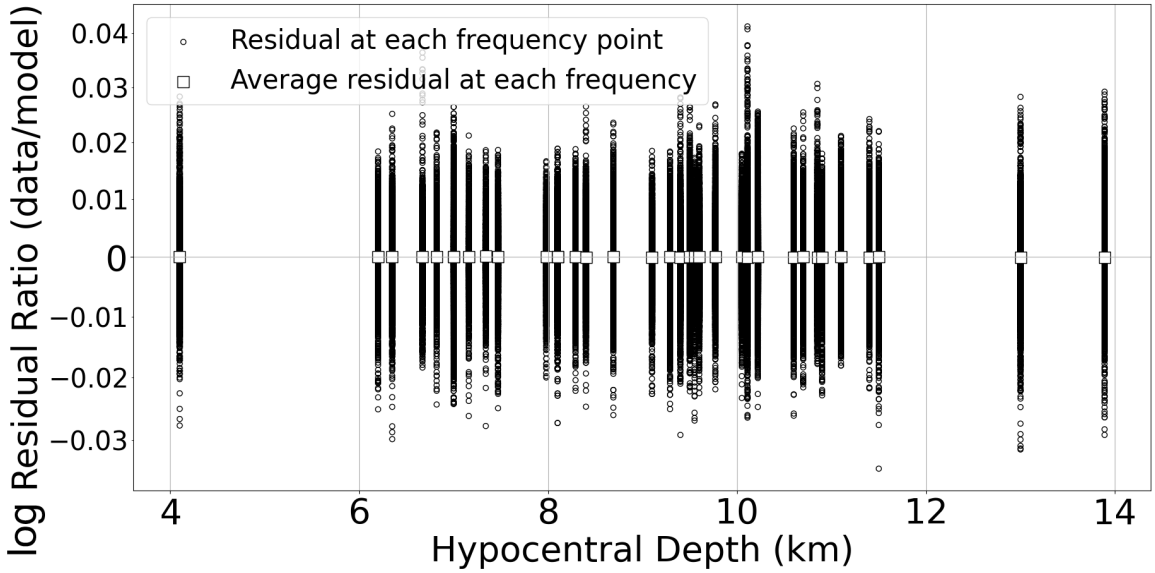

Figure 39: Residual ratios (circles) and log-average of them (squares) for each observed FAS and final modeled FAS regarding each depth.

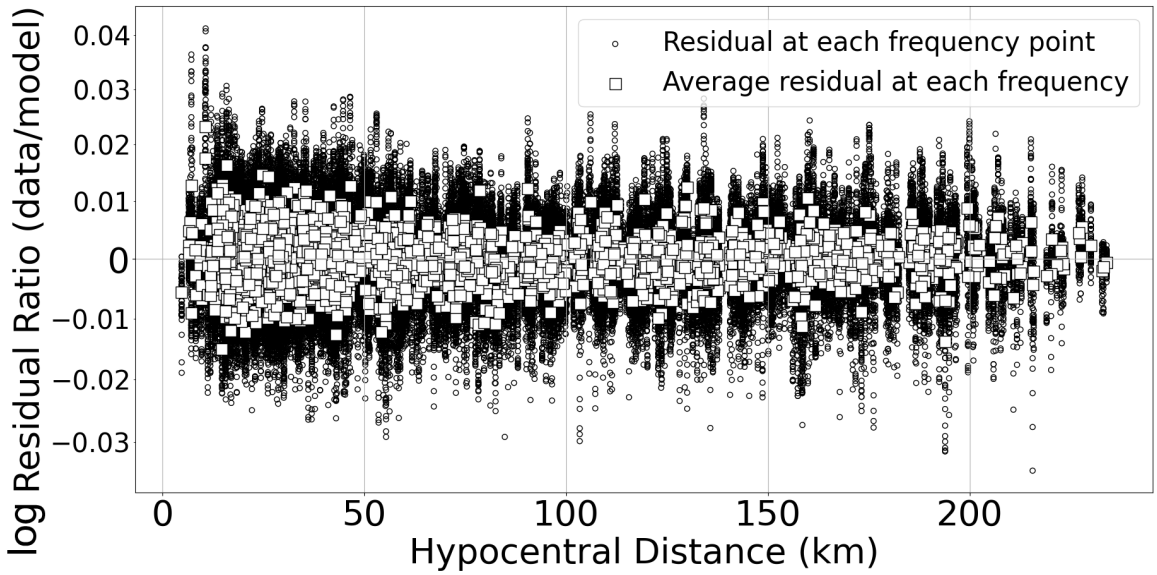

Figure 40: Residual ratios (circles) and log-average of them (squares) for each observed FAS and final modeled FAS regarding each hypocentral distance.

A closer view of the average values are presented in Figure 41 (derived from Figure 37), which is revealing that residuals tend to be higher at lower frequencies (although the values are really small i.e. on the order of about 0.001). This observation is further supported by the individual event analysis which is shown in Figure 42.

This frequency-dependent behavior may be attributed to the limited availability of reliable spectral data in the low-frequency domain, particularly for smaller-magnitude events. Due to their inherently higher corner frequencies and reduced energy content at long periods, such events often fall outside the sensitivity range required to constrain spectral amplitudes below dim 1 Hz. As a result, the inversion process may become dependent on extrapolated or noisy data in this frequency range, which can introduce minor deviations in the residual structure.

The observed pattern underscores the importance of magnitude-dependent spectral completeness in inversion workflows and suggests that future refinements to the model may benefit from enhanced low-frequency coverage, either through the inclusion of larger events or improved preprocessing techniques that extend the usable bandwidth of smaller events.

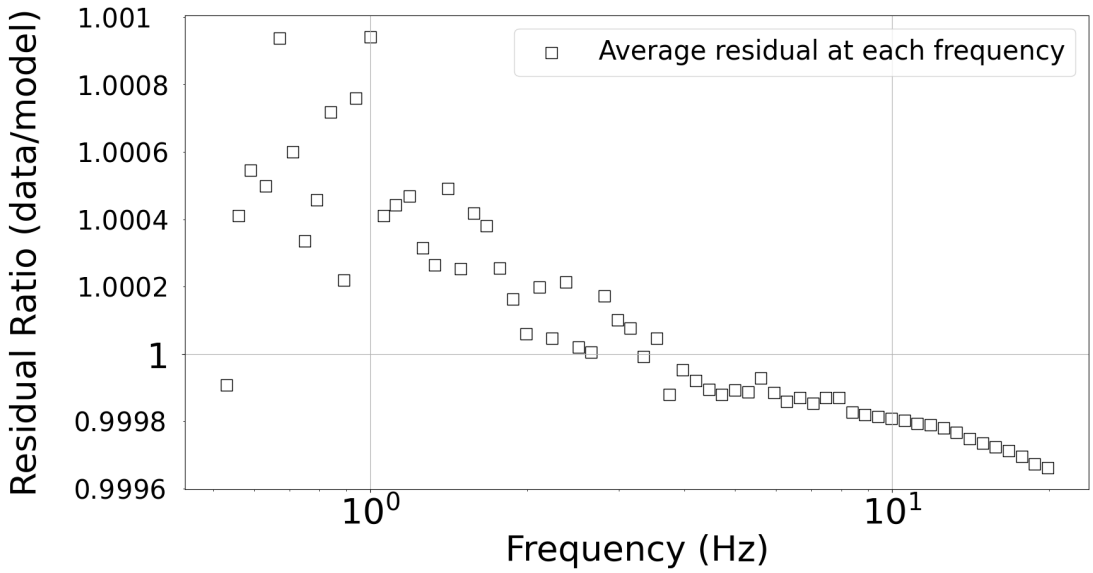

Figure 41: log-average of residual ratios for each frequency for all events.

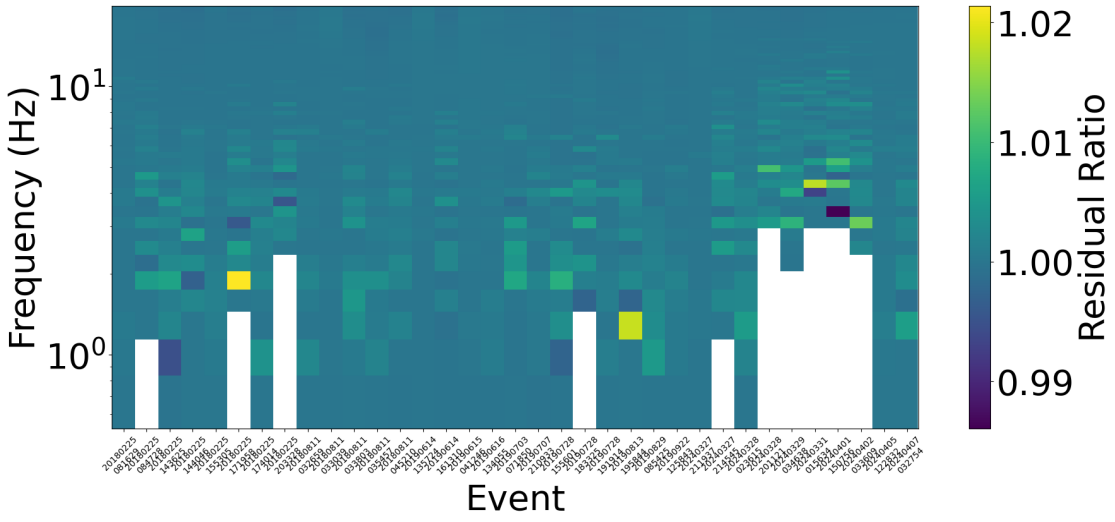

Figure 42: log-average of residual ratios for each frequency, color coded for each event (the white parts showing there is no data for that frequency).

4.2 Energy Results

In this part, the outcomes of the energy computations are presented. Figures 43 and 44 present the energy estimates calculated for seismic events using Equations 31 and 33, respectively. These results are compared with the corresponding energy values reported by Cataldi et al. [2025].

The analysis reveals that when applying Equation 31, the energy estimation yields MAE of 0.44 and RMSE of 0.47 (with respect to the results of Cataldi et al. 2025). Alternatively, using Equation 33 results in an MAE of 0.81 and an RMSE of 0.83 (with respect to the results of Cataldi et al. 2025), indicating limited suitability.

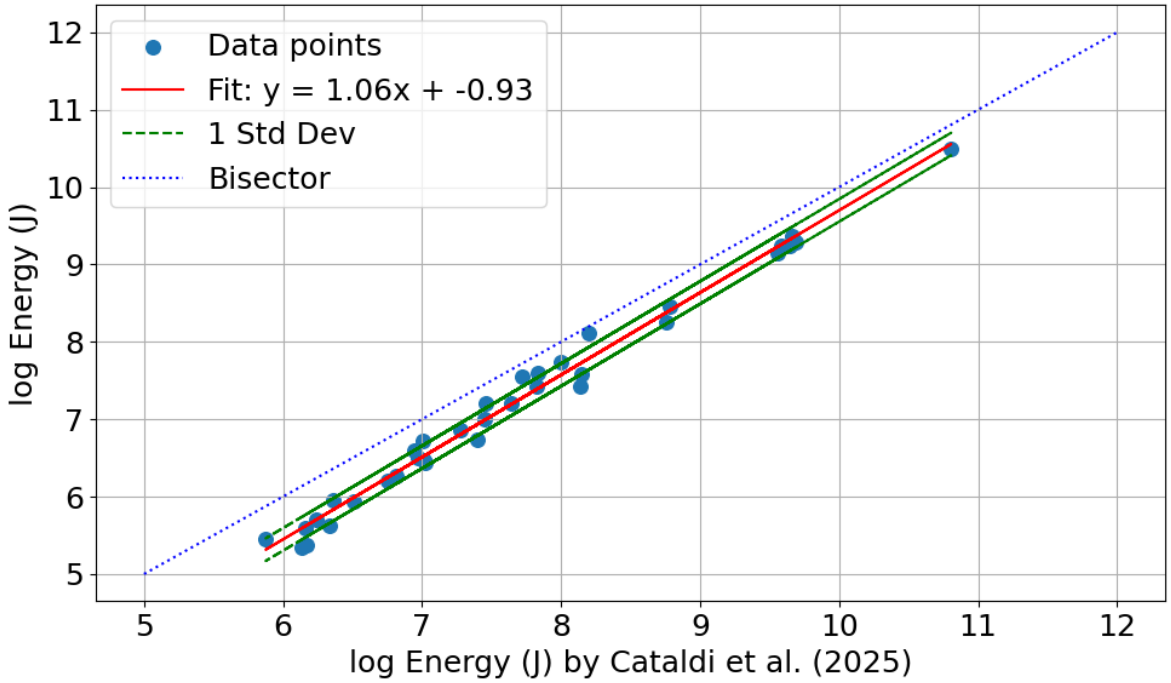

Figure 43: Comparison of the energies obtained in by using Equation 31 with the energies achieved by Cataldi et al. [2025].

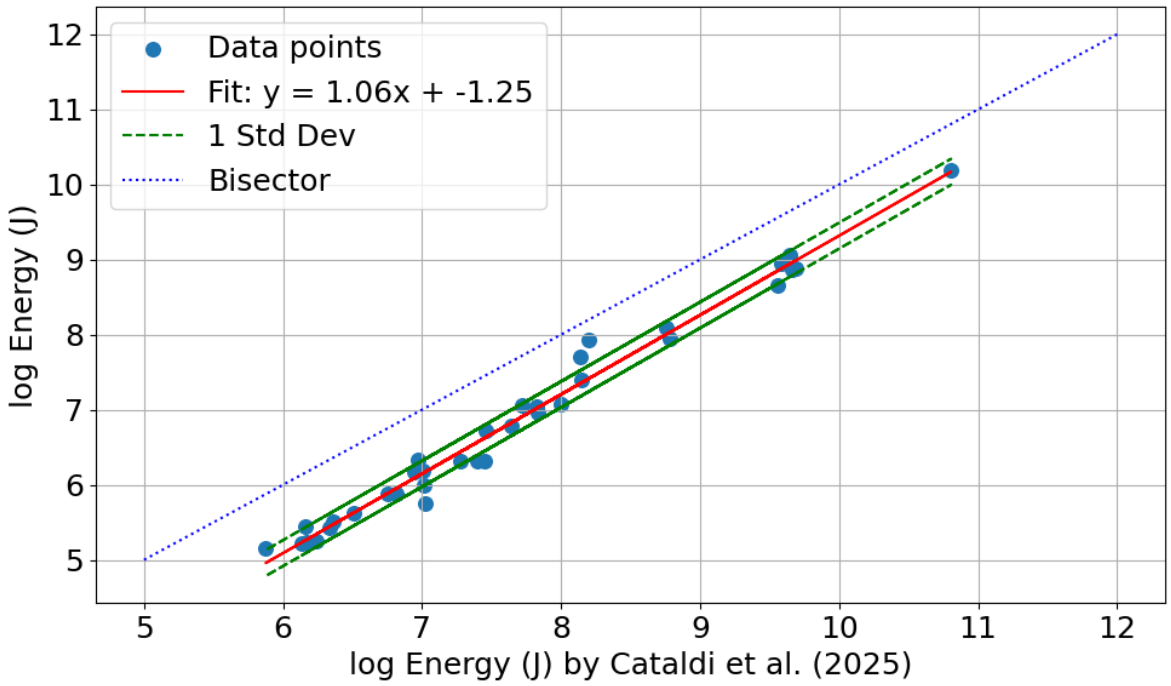

Figure 44: Comparison of the energies obtained in by using Equation 33 with the energies achieved by Cataldi et al. [2025].

As emphasized by Picozzi et al. [2018b], in the case of moderate to small seismic events ($M_W < 5$), the energy magnitude tends to be systematically lower than the corresponding moment magnitude (Figure 45).

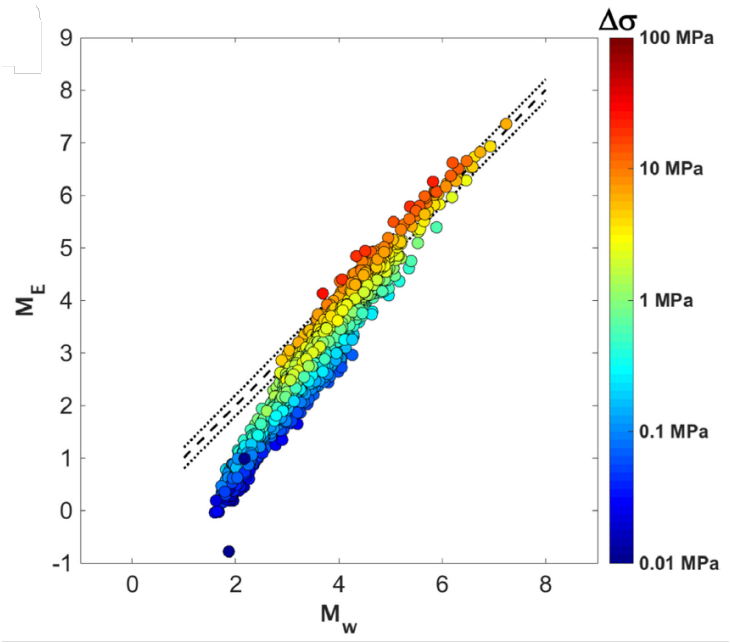

Figure 45: Relation between M_E and M_W obtained and published by Picozzi et al. [2018b].

In alignment with these findings, the M_E values derived in the present study exhibit a consistent pattern of being lower than the M_W values, reinforcing the trend reported in earlier literature. This behavior is clearly illustrated in Figures 46 and 47.

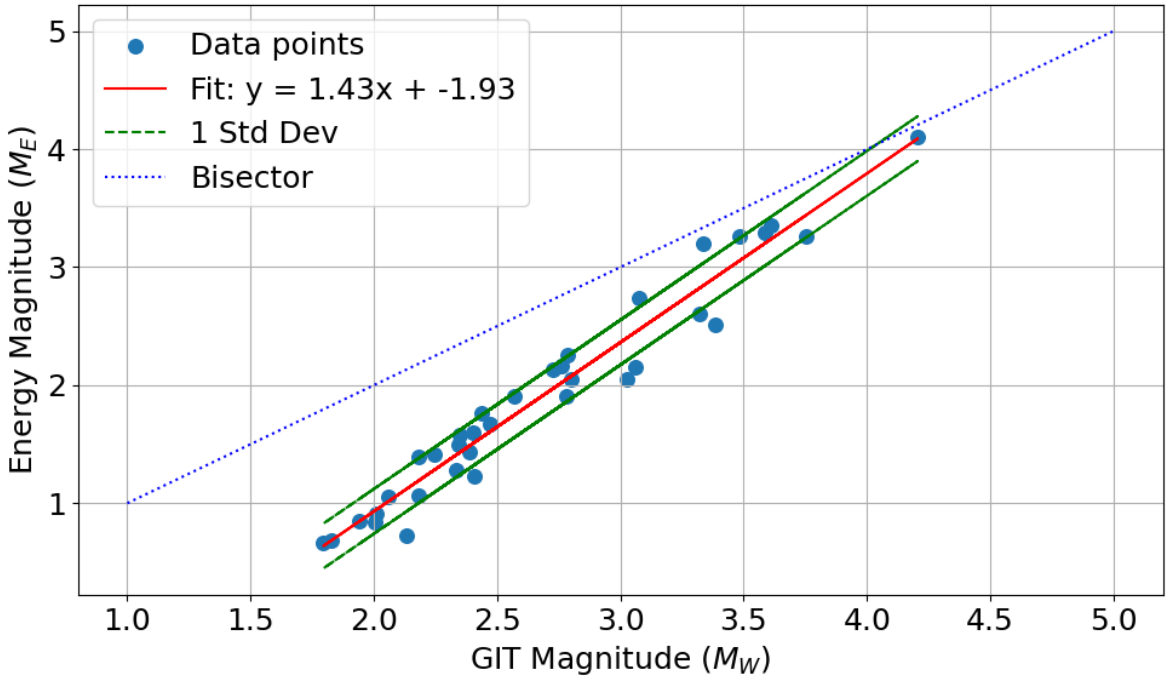

Figure 46: Relation between M_E and M_W of this study by using Equation 31.

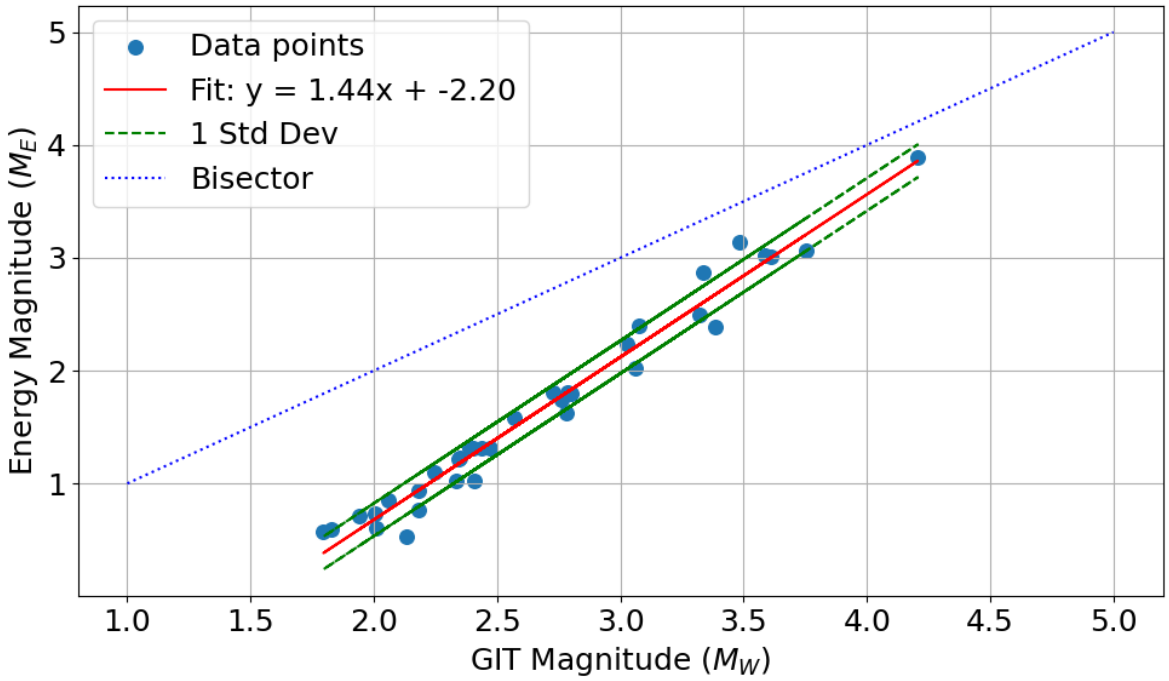

Figure 47: Relation between M_E and M_W of this study by using Equation 33.

Supporting this observation, Picozzi et al. [2018b] noted that when $\Delta\sigma$ falls below 1 MPa, the relationship between M_E and M_W tends to change. This behavior aligns with the findings presented in the *"Corner Frequency and Stress Drop"* section of this study where it is shown in the Figure 34 that most of the events used in this study have the stress drop below 1.

However, comparing the energy results of Equation 31 (which shows a bit more consistency) with the avhieved energies by Moratto et al. [2026] which is illustrated in Figure 48 shows more scattering with RMSE of 0.93 even though the general trend is consistent.

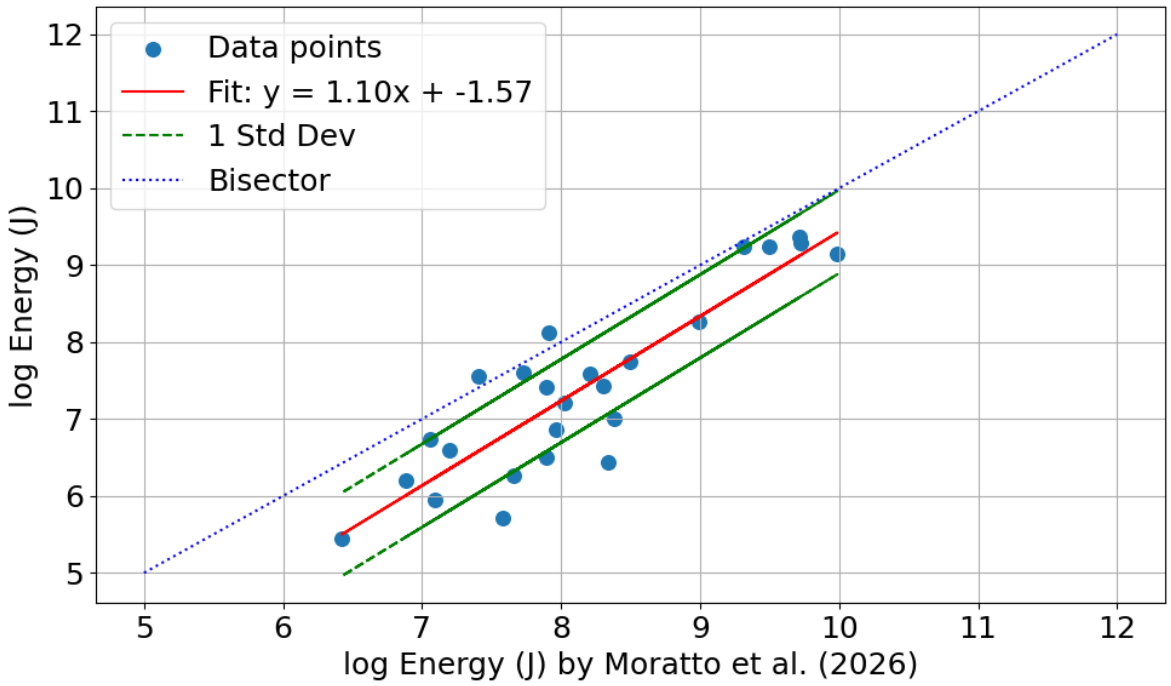

Figure 48: Comparison of the energies obtained in by using Equation 33 with the energies achieved by Moratto et al. [2026].

Additionally, to compare Energy versus Moment, Kanamori [1977] derived a condition for big events ($M_W > 5$) based on which $\log(E_R/M_0) = -4.3$. Similar to what happened for M_E and M_W, according to Picozzi et al. [2018b] (Figure 49) for moderate to small earthquakes, the trend between $\log E_R$ and $\log M_0$ is changing. The results of the present study also followed the same trend which shows their agreement to the previous observations (Figure 50).

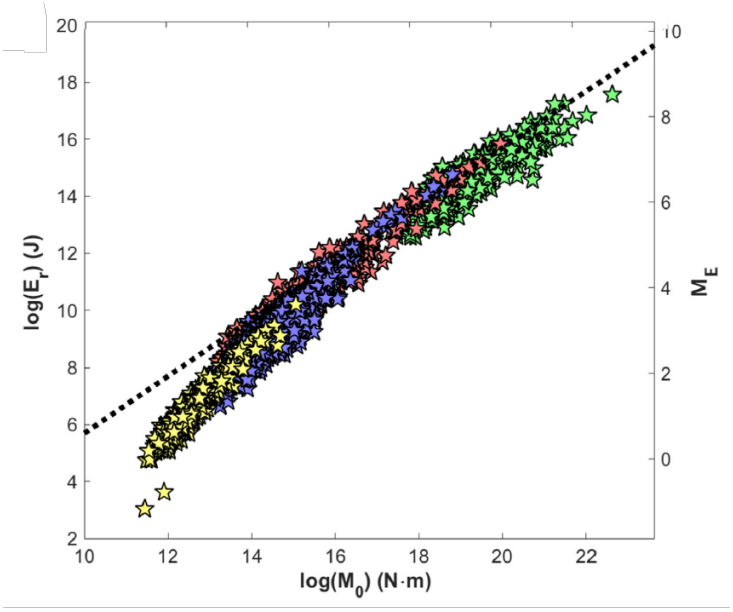

Figure 49: Relation between E_R and M_0 obtained and published by Picozzi et al. [2018b]. The black dashed line shows the condition of Kanamori [1977]

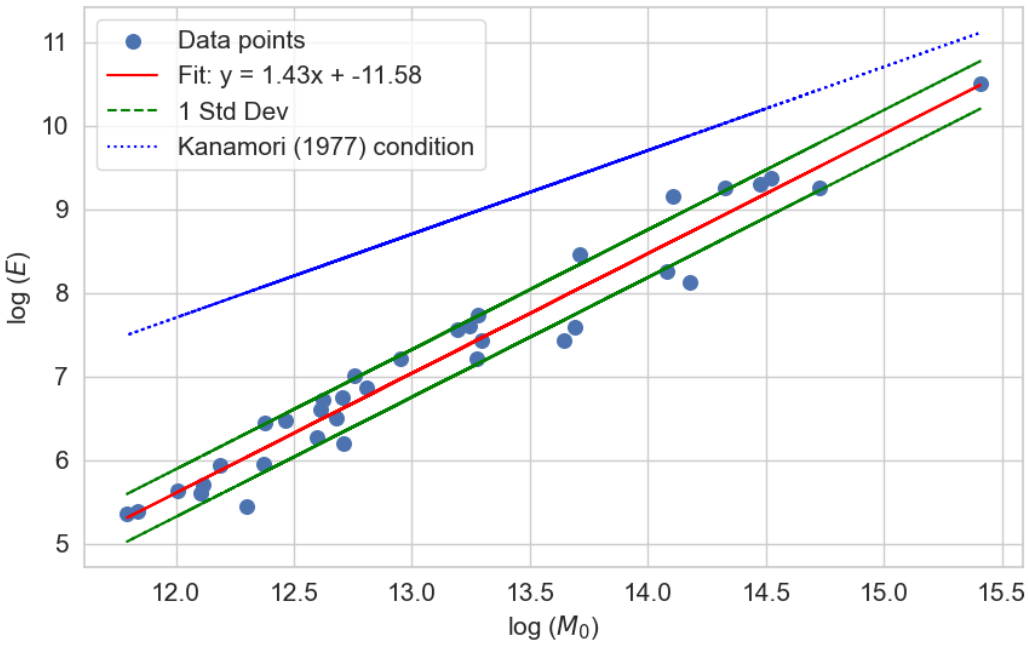

Figure 50: Achieved result of this study for the relation between E_R and M_0.

To summarize the results of this part, considering seismic energy and moment, the seismic moment exhibits a lower Root of Squared Error per observation compared to the seismic energy as shown in Figure 51. This suggests that the inversion results for M_0 are more stable and consistent with respect to the ref-

erence values reported by Cataldi et al. [2025]. The narrower distribution of errors for $\log M_0$ indicates higher reliability in moment estimation, while the broader spread of errors observed for $\log E$ reflects greater variability and uncertainty in energy determination. These findings highlight the robustness of the moment-based spectral inversion and suggest that M_0 may serve as a more dependable parameter for characterizing seismic sources in this region.

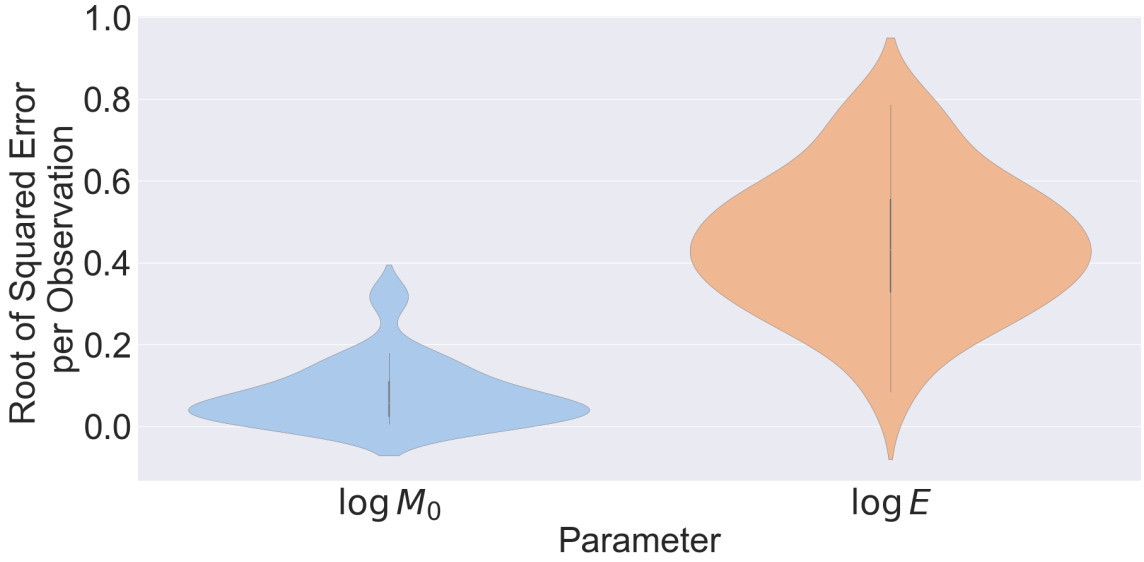

Figure 51: Achieved result of this study for the root of squared error per sample for E_R and M_0.

4.3 Results of the Model Coefficients

Utilizing the outcomes of the GIT analysis, the coefficients in Equation 35 were determined. For both Equations 34 and 35, to resolve the trade-off between coefficients A and C_j and between D and G_j, the attenuation is set to zero at the the upper limit of the first distance bin [Picozzi et al., 2018a, Spallarossa et al., 2021]. It's important to highlight that shifting the node where attenuation is constrained to zero affects both A and C_j and also D and G_j. These changes counterbalance one another, ensuring that the coefficient B in Equation 34 and coefficient F in Equation 35 remain unchanged [Picozzi et al., 2018a, Spallarossa et al., 2021]. Considering the M_0 results, the obtained coefficients are listed in Table 8.

Parameter	Value	Parameter	Value	Parameter	Value	Parameter	Value
D	-15.569	G_{12}	-0.726	G_{25}	-1.646	G_{38}	-2.396
F	0.864	G_{13}	-0.914	G_{26}	-1.646	G_{39}	-2.396
G_1	0.065	G_{14}	-1.039	G_{27}	-1.723	G_{40}	-2.396
G_2	0.000	G_{15}	-1.039	G_{28}	-1.844	G_{41}	-2.403
G_3	-0.003	G_{16}	-1.110	G_{29}	-1.883	G_{42}	-2.403
G_4	-0.006	G_{17}	-1.110	G_{30}	-1.883	G_{43}	-2.403
G_5	-0.006	G_{18}	-1.212	G_{31}	-1.883	G_{44}	-2.403
G_6	-0.173	G_{19}	-1.305	G_{32}	-2.112	G_{45}	-2.403
G_7	-0.173	G_{20}	-1.385	G_{33}	-2.170	G_{46}	-2.548
G_8	-0.657	G_{21}	-1.435	G_{34}	-2.170	G_{47}	-2.557
G_9	-0.657	G_{22}	-1.524	G_{35}	-2.245	G_{48}	-2.830
G_{10}	-0.726	G_{23}	-1.524	G_{36}	-2.332	G_{49}	-2.830
G_{11}	-0.726	G_{24}	-1.601	G_{37}	-2.396	G_{50}	-2.830

Table 8: Coefficients obtained for Equation 35.

Moreover, these coefficients compared with M_0 residuals as shown in Figure 52. This figure presents a direct evaluation of the G_j coefficients of Equation 35 with the residuals as $\Delta\log(M_0) = \log[PD_S(R_H)] - D - F\log(M_0)$ where $PD_S(R_H)$ represents the peak displacement at hypocentral distance R_H. The scatter plot shows a clear trend of decreasing residuals with increasing distance, indicating that the coefficient-based model captures the attenuation behavior effectively. The red points, representing the calculated coefficients, align well with the overall distribution of residuals, supporting the validity of the regression approach. This comparison confirms that the derived coefficients are physically consistent and capable of reproducing the observed moment-distance relationship with minimal bias.

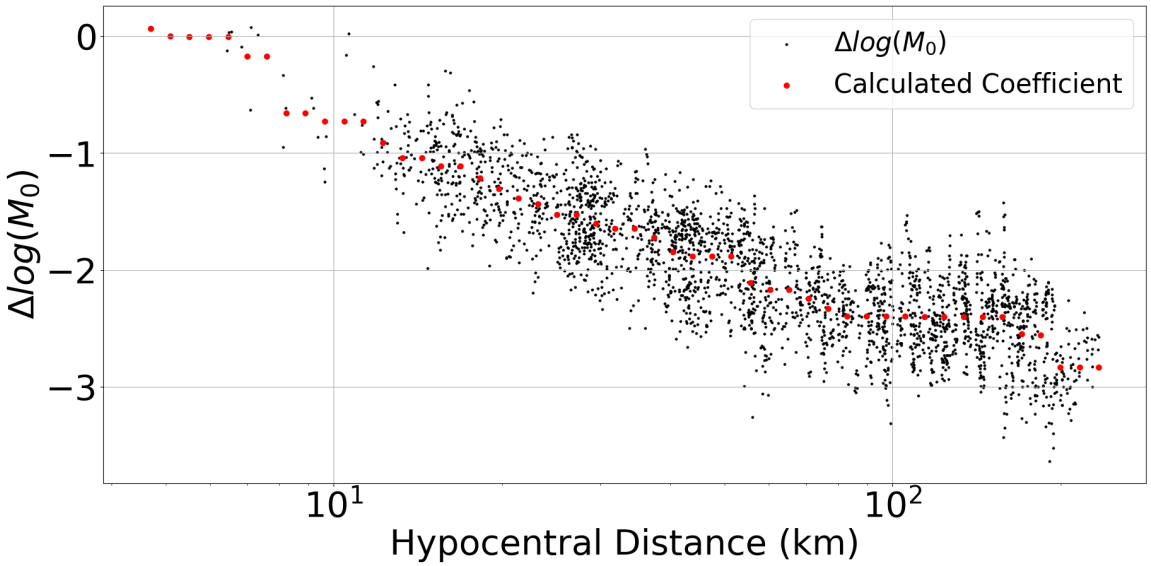

Figure 52: Comparison of the G_j coefficients of Equation 35 with the residuals as $\Delta\log(M_0) = \log[PD_S(R_H)] - D - F\log(M_0)$.

These coefficients were then validated by applying Equation 35 to compute M_0 and M_W for the second dataset provided by Presidenza del Consiglio dei Ministri, Dipartimento della Protezione Civile [2014]. A comparative assessment with the magnitudes reported by Cataldi et al. [2025] is illustrated in Figure 53. The regression fit (red line) reveals a strong linear relationship, indicating systematic agreement with a slight bias toward lower magnitude values. The mean absolute error was 0.18 and the root mean square error was 0.2 magnitude unit (with respect to the results of Cataldi et al. 2025).

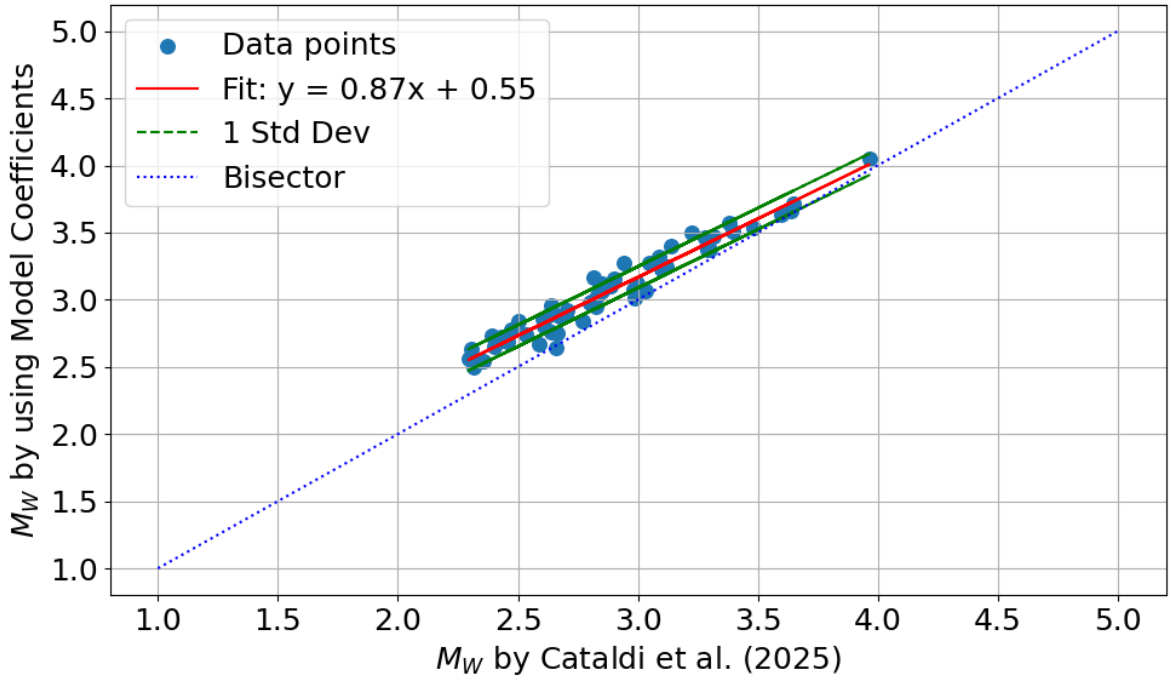

Figure 53: Comparison of the magnitudes obtained by using Equation 35 with the magnitudes achieved by Cataldi et al. [2025].

In addition to that, when comparing with the results of Tarchini et al. [2025] and Moratto et al. [2026] (although they are up to the end of 2023), the consistency is increasing, i.e. the RMSE with respect to the results of Moratto et al. [2026] is 0.12 which is shown in Figure 54 and the RMSE with respect to the results of Tarchini et al. [2025] is 0.1 which is shown in Figure 55.

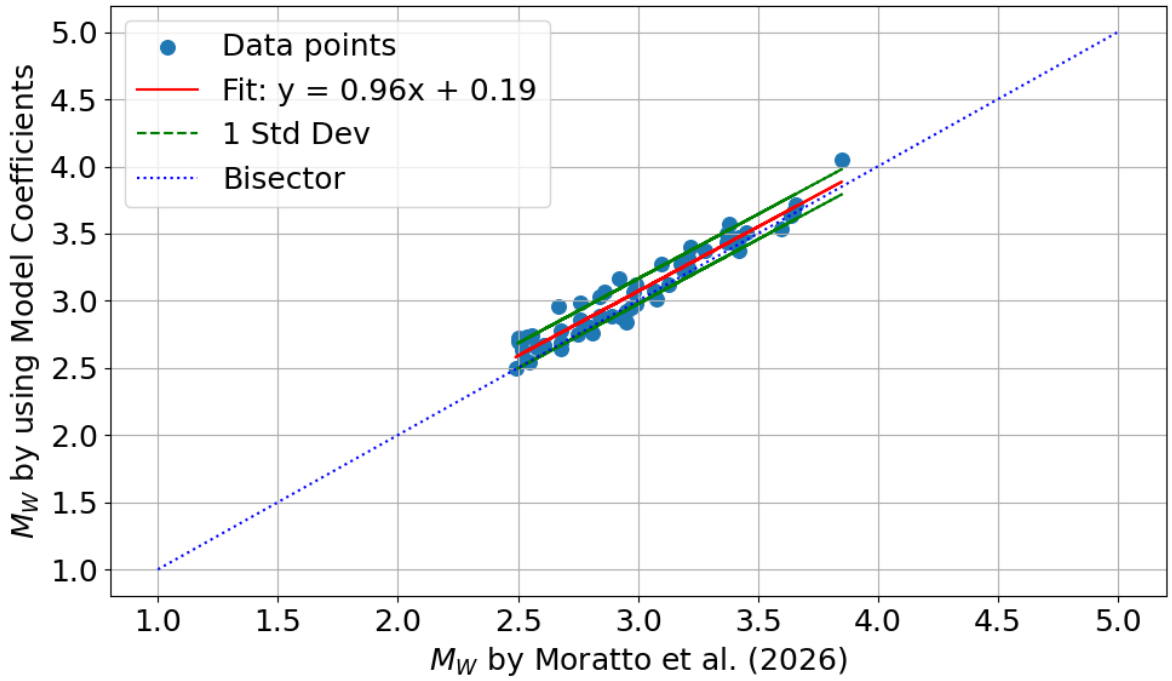

Figure 54: Comparison of the magnitudes obtained by using Equation 35 with the magnitudes achieved by Moratto et al. [2026].

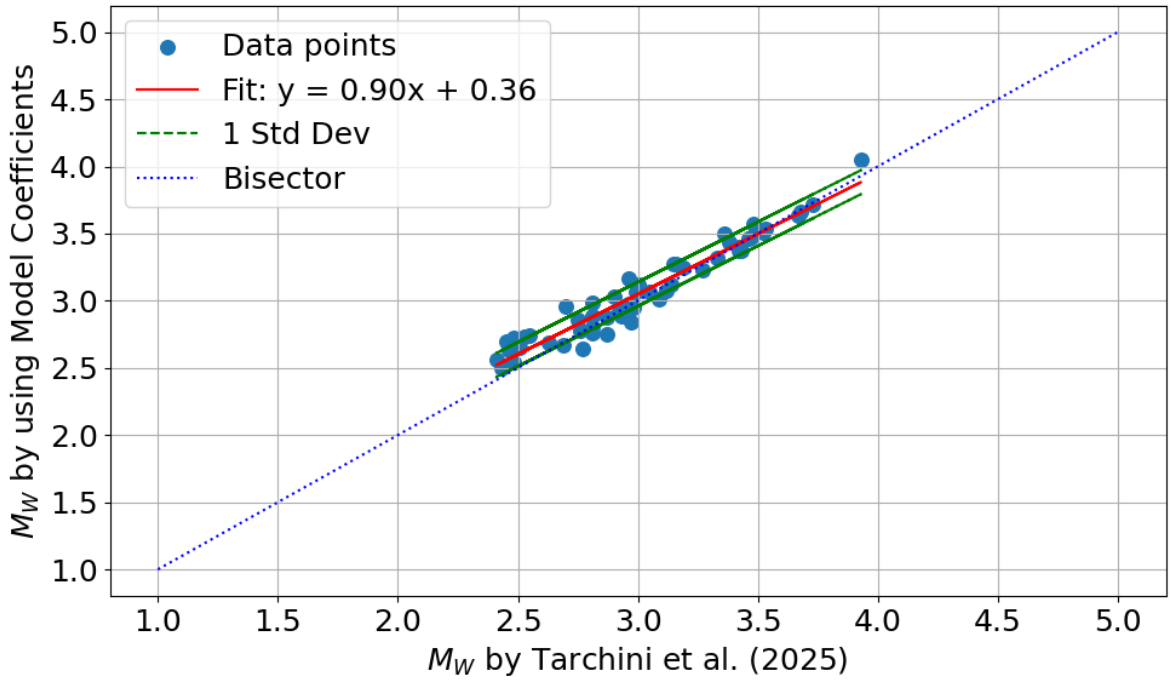

Figure 55: Comparison of the magnitudes obtained by using Equation 35 with the magnitudes achieved by Tarchini et al. [2025].

The next step is to obtain and validate the model coefficients for seismic energy. The coefficients obtained using the E_R results from Equations 31 and 33 are listed in Tables 9 and 10, respectively. Their performance is evaluated through comparison with the residuals of E_R, as illustrated in Figures 56 and 57. Specifically, these figures presents the comparison of the C_j coefficients of Equation 34 with the residuals as $\Delta\log(E_R) = \log[IV2_S(R_H)] - A - B\log(E_R)$ by using the results of Equations 31 and 33 respectively. Both scatter plots show a clear negative trend, indicating that the residuals decrease with increasing hypocentral distance, consistent with expected attenuation behavior.

The red points representing the calculated coefficients align well with the overall distribution of residuals, suggesting that the regression model effectively captures the distance-dependent decay of radiated energy. This agreement supports the physical validity of the derived coefficients and confirms their suitability for modeling energy versus attenuation in the region. The results also highlight the sensitivity of energy-based regressions to distance, reinforcing the importance of accurate coefficient calibration for reliable energy estimation.

Parameter	**Value**	**Parameter**	**Value**	**Parameter**	**Value**	**Parameter**	**Value**
A	-13.009	C_{12}	-1.937	C_{25}	-3.714	C_{38}	-5.001
B	1.035	C_{13}	-2.481	C_{26}	-3.819	C_{39}	-5.001
C_1	0.032	C_{14}	-2.562	C_{27}	-4.022	C_{40}	-5.001
C_2	0.000	C_{15}	-2.652	C_{28}	-4.057	C_{41}	-5.266
C_3	-0.007	C_{16}	-2.672	C_{29}	-4.275	C_{42}	-5.265
C_4	-0.013	C_{17}	-2.672	C_{30}	-4.275	C_{43}	-5.265
C_5	-0.013	C_{18}	-2.836	C_{31}	-4.328	C_{44}	-5.265
C_6	-0.535	C_{19}	-3.067	C_{32}	-4.581	C_{45}	-5.265
C_7	-1.117	C_{20}	-3.238	C_{33}	-4.768	C_{46}	-5.549
C_8	-1.494	C_{21}	-3.345	C_{34}	-4.768	C_{47}	-5.640
C_9	-1.494	C_{22}	-3.480	C_{35}	-4.858	C_{48}	-6.213
C_{10}	-1.494	C_{23}	-3.484	C_{36}	-4.995	C_{49}	-6.213
C_{11}	-1.494	C_{24}	-3.656	C_{37}	-4.995	C_{50}	-6.213

Table 9: Coefficients obtained for Equation 34 using the results of Equation 31.

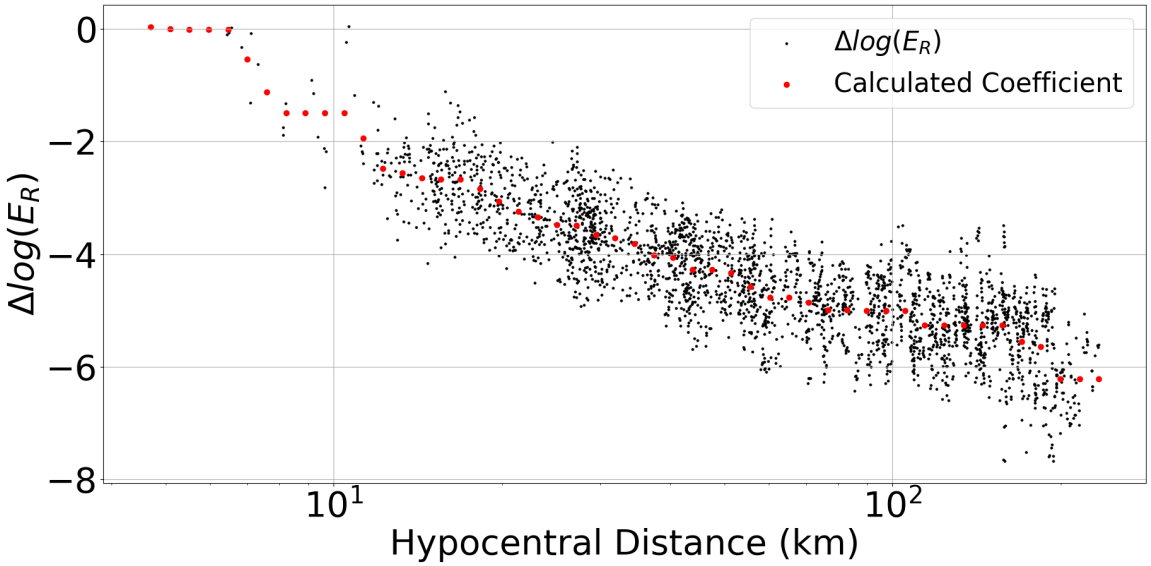

Figure 56: Comparison of the C_j coefficients of Equation 34 with the residuals as $\Delta\log(E_R) = \log[IV2_S(R_H)] - A - B\log(E_R)$ by using the results of Equation 31.

Parameter	Value	Parameter	Value	Parameter	Value	Parameter	Value
A	-12.828	C_{12}	-1.493	C_{25}	-3.184	C_{38}	-4.433
B	1.032	C_{13}	-1.916	C_{26}	-3.291	C_{39}	-4.433
C_1	0.360	C_{14}	-2.069	C_{27}	-3.450	C_{40}	-4.433
C_2	0.000	C_{15}	-2.122	C_{28}	-3.540	C_{41}	-4.673
C_3	-0.005	C_{16}	-2.145	C_{29}	-3.742	C_{42}	-4.673
C_4	-0.011	C_{17}	-2.145	C_{30}	-3.742	C_{43}	-4.673
C_5	-0.011	C_{18}	-2.325	C_{31}	-3.797	C_{44}	-4.673
C_6	-0.011	C_{19}	-2.572	C_{32}	-4.051	C_{45}	-4.673
C_7	-0.856	C_{20}	-2.742	C_{33}	-4.240	C_{46}	-4.951
C_8	-1.213	C_{21}	-2.810	C_{34}	-4.240	C_{47}	-5.018
C_9	-1.213	C_{22}	-2.968	C_{35}	-4.272	C_{48}	-5.601
C_{10}	-1.213	C_{23}	-2.968	C_{36}	-4.433	C_{49}	-5.601
C_{11}	-1.213	C_{24}	-3.153	C_{37}	-4.433	C_{50}	-5.601

Table 10: Coefficients obtained for Equation 34 using the results of Equation 33.

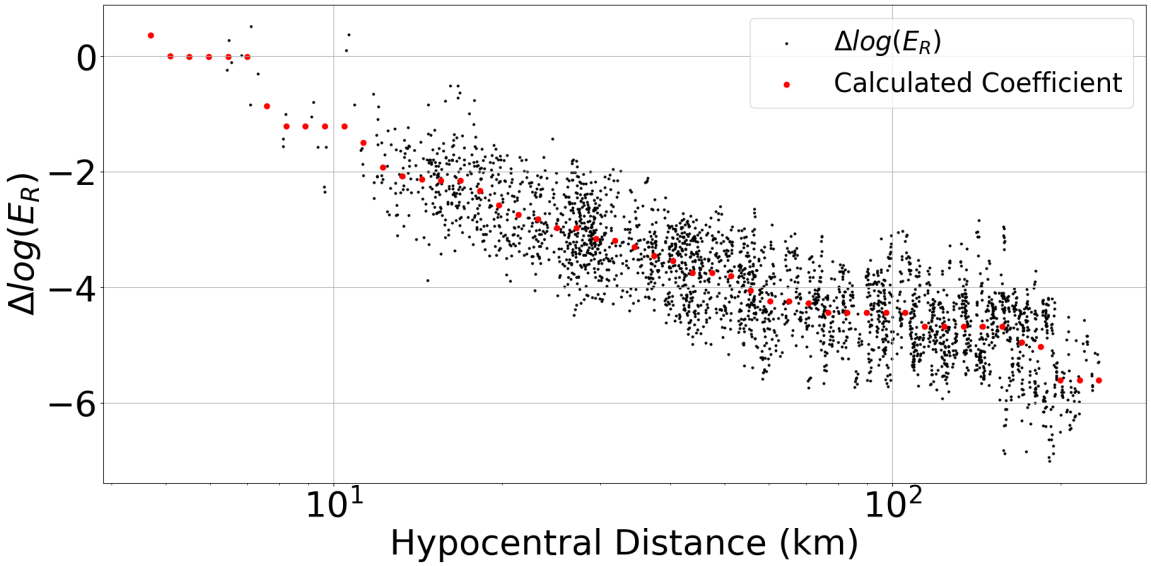

Figure 57: Comparison of the C_j coefficients of Equation 34 with the residuals as $\Delta\log(E_R) = \log[IV2_S(R_H)] - A - B\log(E_R)$ by using the results of Equation 33.

Subsequently, to validate these coefficients, Equation 34 was applied to derive energy values for the second dataset provided by Presidenza del Consiglio dei Ministri, Dipartimento della Protezione Civile [2014]. The resulting estimates were compared against the energy values reported by Cataldi et al. [2025], as shown in Figures 58 and 59.

The analysis indicates that using Equation 31 yields MAE of 0.18 and RMSE of 0.25 (with respect to the results of Cataldi et al. 2025), on the other hand, Equation 33 results are showing less reliable results with an MAE of 0.34 and RMSE of 0.39 (relative to the results of Cataldi et al. 2025). Consistent with the outcomes obtained through direct energy computation, Equation 31 produced comparatively more reliable results, reinforcing its effectiveness in this context.

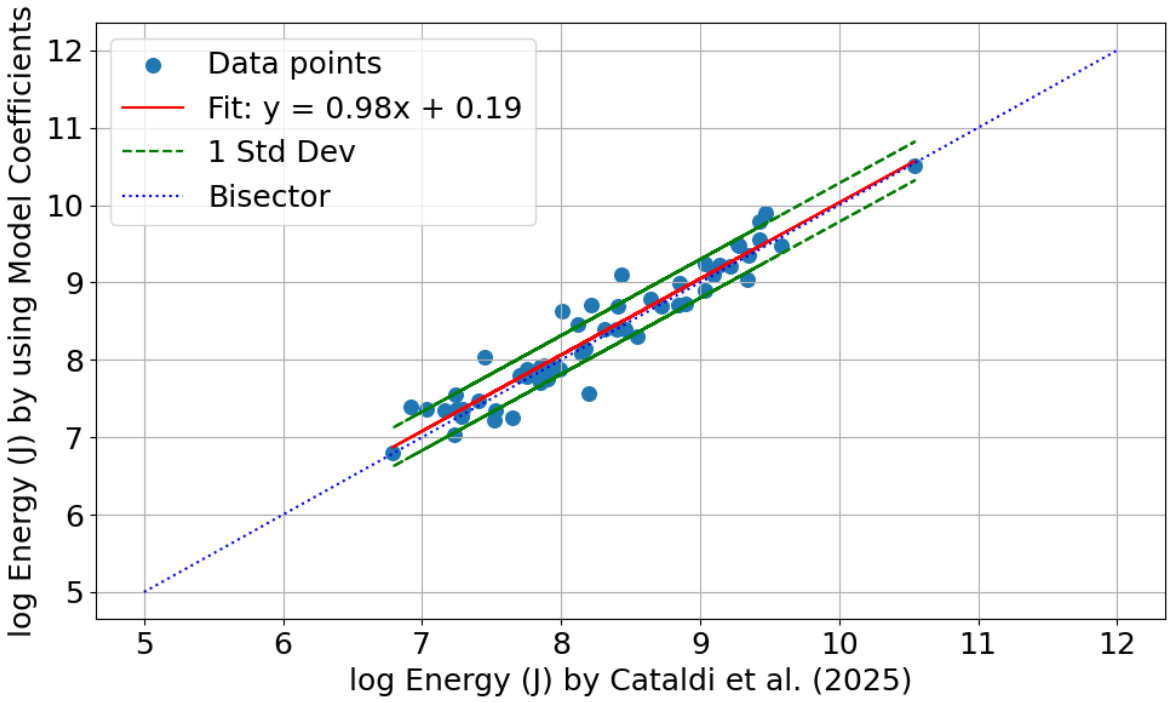

Figure 58: Comparison of the energies obtained by the Equation 34 using the results of Equation 31 with the energies achieved by Cataldi et al. [2025].

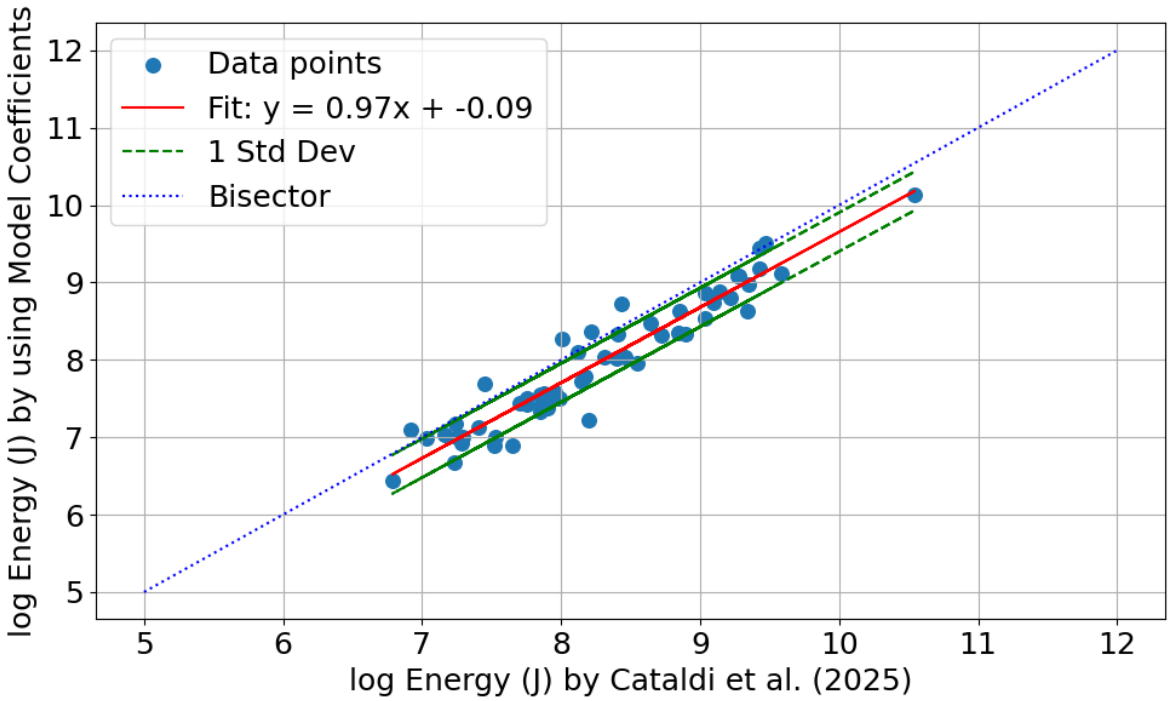

Figure 59: Comparison of the energies obtained by the Equation 34 using the results of Equation 33 with the energies achieved by Cataldi et al. [2025].

Similar to Figure 48, the energies obtained using model coefficients by taking advantage of Equation 31, when compared to results of Moratto et al. [2026], show scattering (Figure 60), however, the RMSE improved to 0.59.

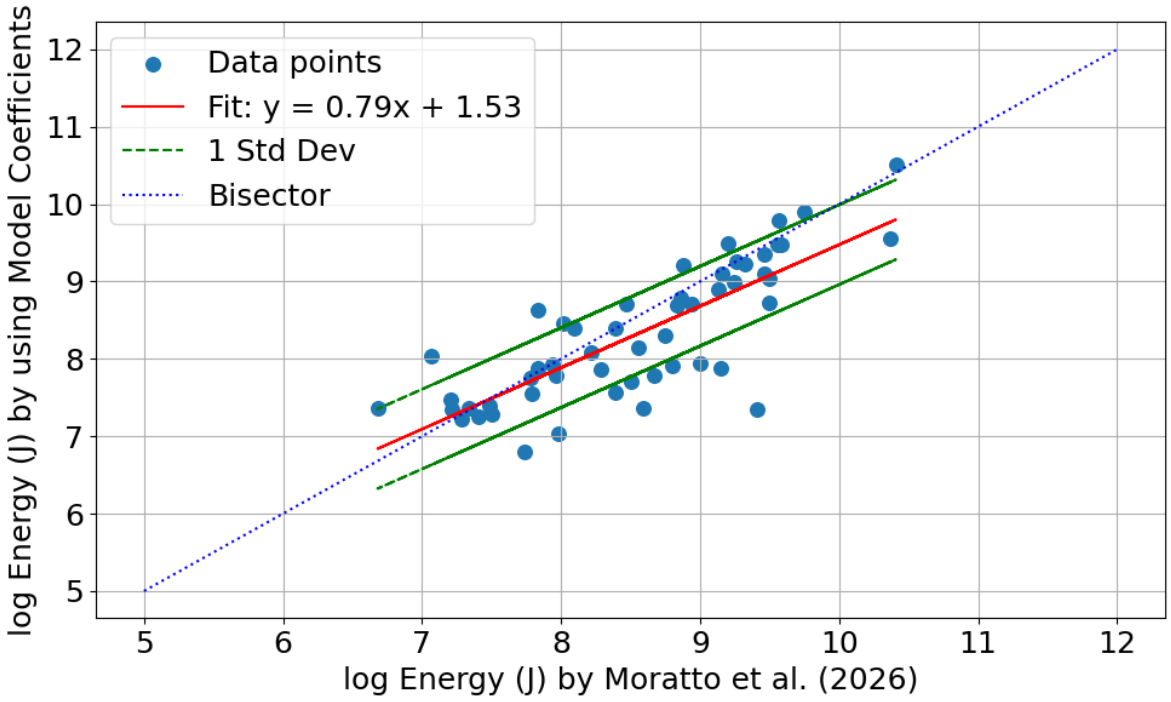

Figure 60: Comparison of the energies obtained by the Equation 34 using the results of Equation 31 with the energies achieved by Moratto et al. [2026].

Interestingly, when the regression coefficients were applied, the energy-based outcomes showed a slight advantage over the moment-based results, as illustrated in Figure 61. The distribution of root squared error per observation for $\log E_R$ appears marginally narrower and more concentrated than that of $\log M_0$ suggesting that the energy parameter may offer slightly improved predictive performance under the applied model. This small difference highlights the potential of energy-based formulations in capturing source characteristics, especially when calibrated with appropriate distance-dependent coefficients.

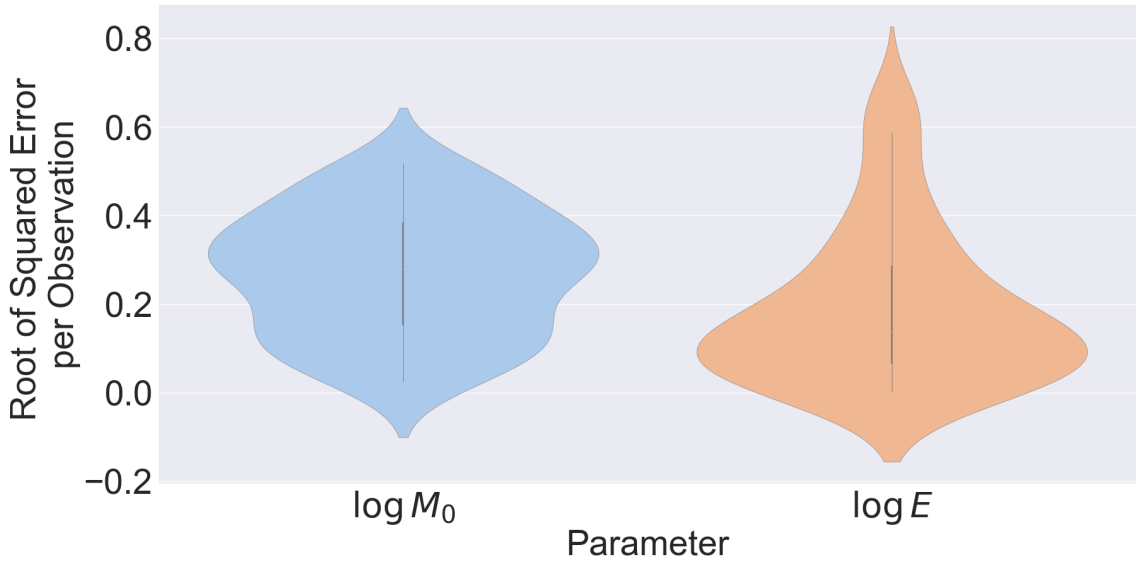

Figure 61: Root of squared error per sample for E_R and M_0 using model coefficients.

Upon observing the discrepancy between moment and energy estimates, one potential explanation that initially emerged was the difference in component usage during source parameter computation. As previously noted, radiated energy is derived using all three components of ground motion, two horizontal and one vertical, whereas seismic moment is estimated using only the horizontal components. This raised the question of whether incorporating the vertical component into moment estimation might explain the observed divergence.

To evaluate this hypothesis, a targeted test was conducted wherein seismic moment was recalculated using all three components. However, the results revealed that this modification led to an increase in the RMSE of magnitude estimates, rising from 0.2 to 0.3. This degradation in performance suggests that the inclusion of the vertical component does not enhance the accuracy of moment estimation and may introduce additional noise or instability. For further investigation, a test was done over energy by reducing the components into the two horizontal components, and again the RMSE for energy results increased from 0.25 to 0.29. Consequently, the assumption that component selection is the primary driver of the discrepancy appears to have low explanatory power, and other factors such as inversion constraints, or sensitivity of model parameters are likely to play a more significant role.

4.4 Issues about the Results

This section is to discuss about some issues about various methodological approaches adopted in this study, along with the corresponding results they produced. It aims to critically evaluate the strengths

and limitations of each technique, highlighting areas of agreement and divergence among the outcomes. By examining these aspects in detail, the section provides deeper insight into the experience behind the chosen methods, the implications of the observed results, and the broader relevance of these findings within the context of seismic moment and energy analyses.

4.4.1 Quality Factor in Equation 15

In order to resolve Equation 14, which incorporates a predefined attenuation model as expressed in Equation 15, it is necessary to adopt an appropriate frequency-dependent or frequency-independent quality factor (Q) representative of the seismic attenuation characteristics of the study region. The selection of a suitable Q model is critical, as it directly influences the accuracy of the attenuation correction and, consequently, the reliability of the derived source parameters.

Several formulations of the quality factor have been proposed in the literature for the study region. For instance, Console and Rovelli [1981] derived a frequency-dependent attenuation law of the form $Q(f) = 80f^{1.1}$ which has been widely employed in subsequent studies, including Gallo et al. [2014]. In contrast, Castro et al. [1996] proposed two distinct models based on different datasets: $Q(f) = 20.4f$ for strong motion recordings and $Q(f) = 16.1f^{0.92}$ for digital seismographic data, highlighting the variability of attenuation behavior with respect to instrumentation and signal amplitude. Furthermore, Malagnini et al. [2002] introduced a model characterized by a relatively high reference value and a gentler frequency dependence, expressed as $Q(f) = 260f^{0.55}$, which was calibrated for northern Italy using broadband waveforms.

More recently, Cataldi et al. [2022] proposed a whole path anelastic attenuation operator (t^*) which relies on a frequency-independent quality factor $Q_0 = 1145$, distance (r), shear-wave velocity (v_s) and site-related attenuation ($\kappa_0 = 0.025$). The final relation is as $t^* = \frac{r}{v_s Q_0} + \kappa_0$. In another study, Jozi Najafabadi et al. [2023] performed an analysis about Q_P in Eastern and eastern Southern Alps, and their background model was a frequency independent quality factor $Q_P = 550$ which is perturbed by high and low anomalies. Since Equation 15 needs the value for Q_S, and according to Lay and Wallace [1995], the relation between quality factors of P wave and S wave is as $Q_P \simeq \frac{9}{4}Q_S$, in this study, the value of $Q_S \simeq 244$ was chosen.

In the present study, all mentioned formulations were evaluated in their best case. As illustrated in Figure 62, apart from the models proposed by Castro et al. [1996] which showed inconsistency regarding both magnitude results and achieved spectra, other models showed better results considering magnitude estimations.

However, the models by Malagnini et al. [2002] and Jozi Najafabadi et al. [2023], showed inconsistency in high frequency part of the spectra. Moreover, the model by Console and Rovelli [1981] showed a bit more consistency in both magnitude results and obtained spectra than model by Cataldi et al. [2022]. Consequently, in this study, the model of Console and Rovelli [1981] was chosen to be used in Equation 15.

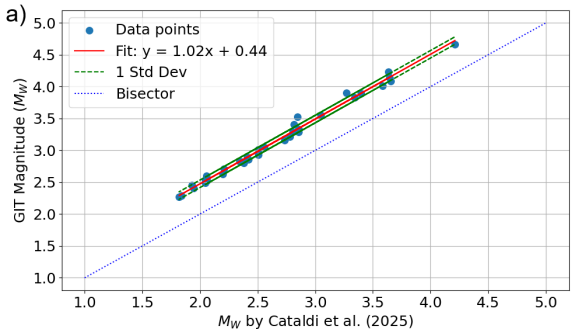
a)
Data points
Fit: y = 1.02x + 0.44
1 Std Dev
Bisector
GIT Magnitude (M_W)
M_W by Cataldi et al. (2025)

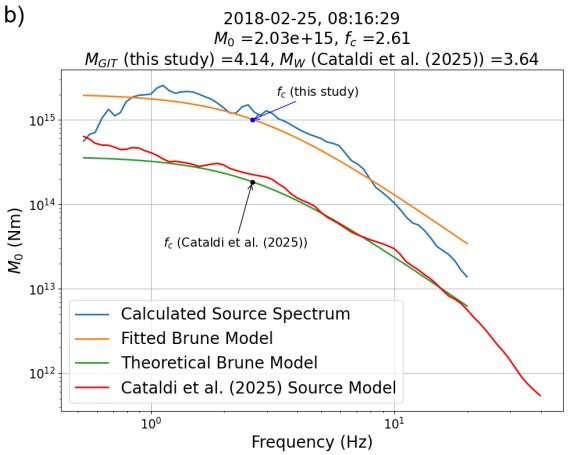
b)
2018-02-25, 08:16:29
M_0 =2.03e+15, f_c =2.61
M_{GIT} (this study) =4.14, M_W (Cataldi et al. (2025)) =3.64
f_c (this study)
f_c (Cataldi et al. (2025))
Calculated Source Spectrum
Fitted Brune Model
Theoretical Brune Model
Cataldi et al. (2025) Source Model
M_0 (Nm)
Frequency (Hz)

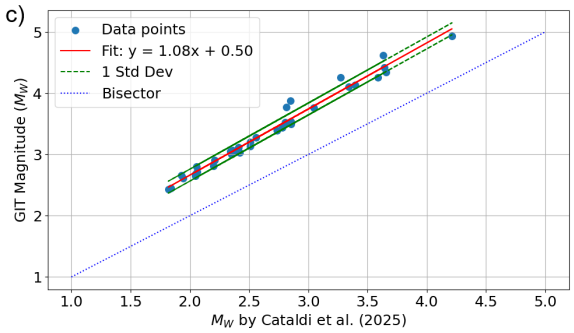
c)
Data points
Fit: y = 1.08x + 0.50
1 Std Dev
Bisector
GIT Magnitude (M_W)
M_W by Cataldi et al. (2025)

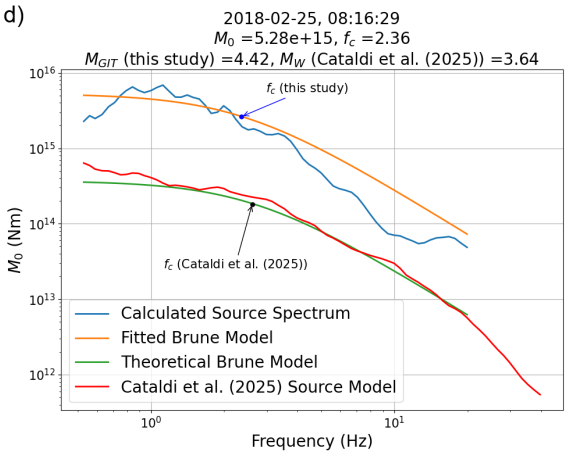
d)
2018-02-25, 08:16:29
M_0 =5.28e+15, f_c =2.36
M_{GIT} (this study) =4.42, M_W (Cataldi et al. (2025)) =3.64
f_c (this study)
f_c (Cataldi et al. (2025))
Calculated Source Spectrum
Fitted Brune Model
Theoretical Brune Model
Cataldi et al. (2025) Source Model
M_0 (Nm)
Frequency (Hz)

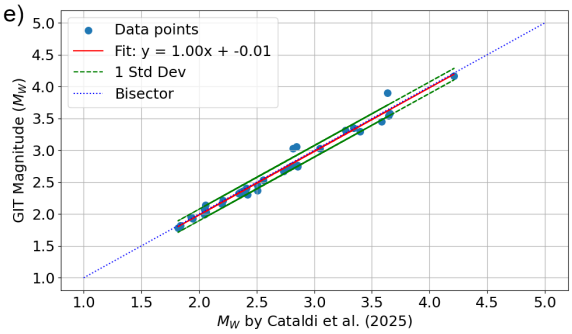
e)
Data points
Fit: y = 1.00x + -0.01
1 Std Dev
Bisector
GIT Magnitude (M_W)
M_W by Cataldi et al. (2025)

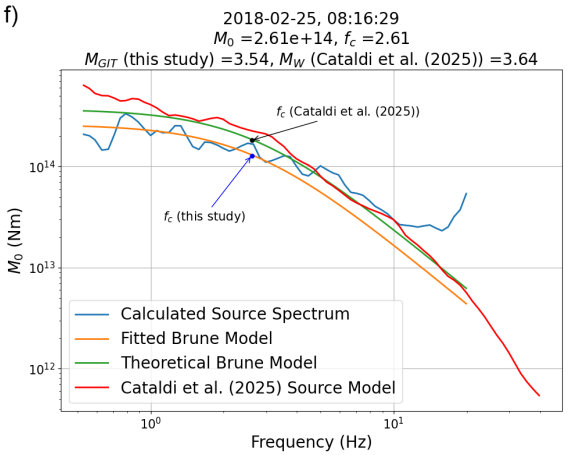
f)
2018-02-25, 08:16:29
M_0 =2.61e+14, f_c =2.61
M_{GIT} (this study) =3.54, M_W (Cataldi et al. (2025)) =3.64
f_c (Cataldi et al. (2025))
f_c (this study)
Calculated Source Spectrum
Fitted Brune Model
Theoretical Brune Model
Cataldi et al. (2025) Source Model
M_0 (Nm)
Frequency (Hz)

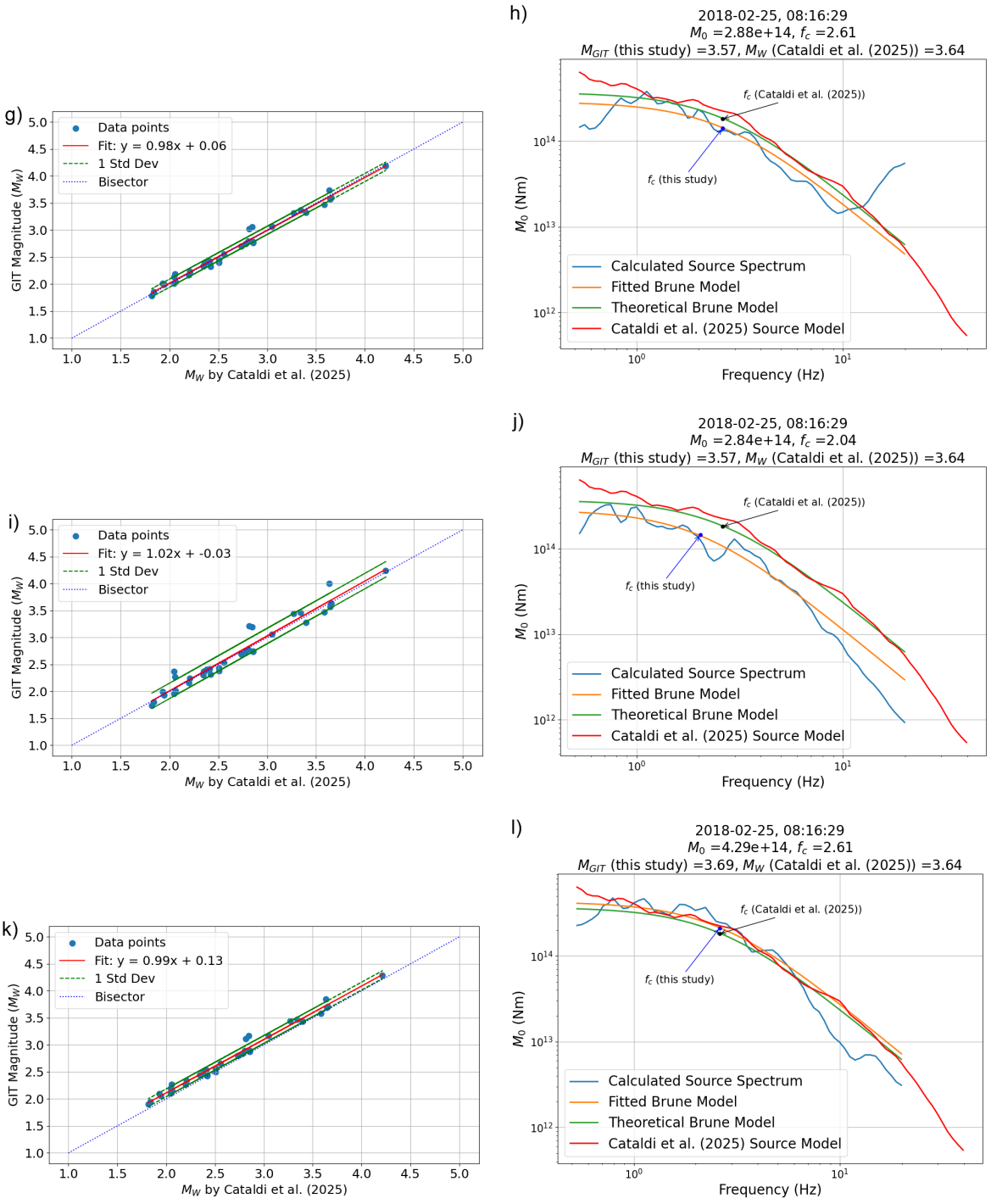

Figure 62: Left: Magnitude results comparing to the results of Cataldi et al. [2022] when using Equation 14 by taking advantage of a predefined attenuation function (Equation 15) with different quality factor models. Right: Sample of obtained source spectra when using Equation 14 by taking advantage of a predefined attenuation function (Equation 15) with different quality factor models. The Q models are: a, b) $Q(f) = 20.4f$ [Castro et al., 1996]. c, d) $Q(f) = 16.1f^{0.92}$ [Castro et al., 1996]. e, f) $Q(f) = 260f^{0.55}$ [Malagnini et al., 2002]. g, h) $Q_S \simeq 244$ [Jozi Najafabadi et al., 2023]. i, j) $t^* = \frac{r}{v_s Q_0} + \kappa_0$ with $Q_0 = 1145$ and $\kappa_0 = 0.025$ [Cataldi et al., 2022]. k, l) $Q(f) = 80f^{1.1}$ [Console and Rovelli, 1981].

4.4.2 Non-Parametric?

Given that none of the GITs employed in this study use priori structural or functional models for the output parameters, these methodologies are not being categorized in the framework of parametric inversion. Nonetheless, the integration of a predefined attenuation formulation, as explained in Equation 16, introduces a degree of model dependency that complicates the classification of the approach as strictly non-parametric. A similar ambiguity arises from the systematic inclusion of the horizontal-to-vertical spectral ratio across the implementation of all types of GITs. The incorporation of H/V into the data vector inherently influences the inversion outcome, introducing bias that deviates from the principles of pure data-driven estimation. Consequently, considering the methodology, while the GITs are fundamentally non-parametric in design, the presence of these model assumptions and data transformations makes challenges for the characterization as purely non-parametric.

Assuming the H/V is excluded from the data vector, and by referring to the comparative analysis presented in Figures 15 through 20, it indicates that the most effective inversion strategy remains the two-step GIT. In this scenario, as evidenced in Figure 63, the station named as *PRED* emerges as the optimal candidate for serving as the reference site (while the *MOZS* station becomes the second). The figure illustrates two distinct yet complementary approaches for evaluating the performance of selected reference stations based on spectral and magnitude error metrics. Panel (a) displays a ranked list of stations using a combined score that integrates normalized spectral Euclidean distance and magnitude RMSE, which is enabling straightforward comparison and selection. In contrast, panel (b) shows the same metrics in a two-dimensional scatter plot, highlighting the trade-off between spectral and magnitude performance across stations. Presenting both visualizations allows for a deeper analysis: the ranking plot simplifies selection, while the scatter plot reveals the trade-offs that inform more strategic station prioritization.

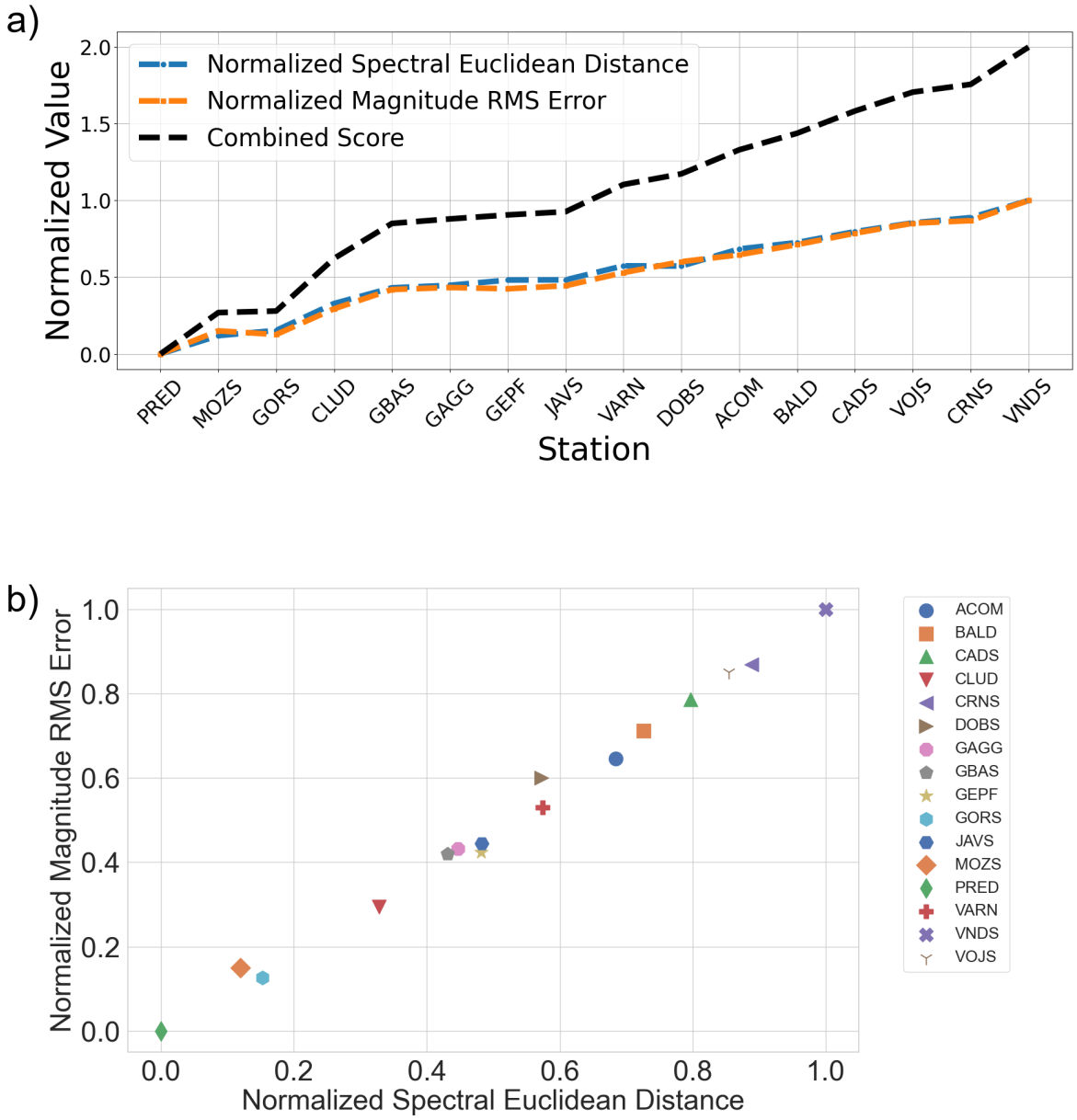

Figure 63: a) Ordering combined score of ED and Magnitude RMS Errors for the selected stations. b) Magnitude RMSE versus ED results for selected stations.

It is noteworthy that among the selected stations to evaluate being as the reference station, *PRED* exhibits the lowest median amplification, as depicted in Figure 64, underscoring its relative stability and minimal site amplification effects.

The figure presents the HVSR distributions for selected stations, with black dots indicating the 50th percentile (median) amplification, and blue and red dots representing the 5th and 95th percentiles, respectively. The wide spread observed at some stations reflects significant variability in site response,

while the narrow percentile range at *PRED* further confirms its stable amplification behavior. This characterization is essential for selecting reference stations and for applying reliable site corrections in spectral inversion.

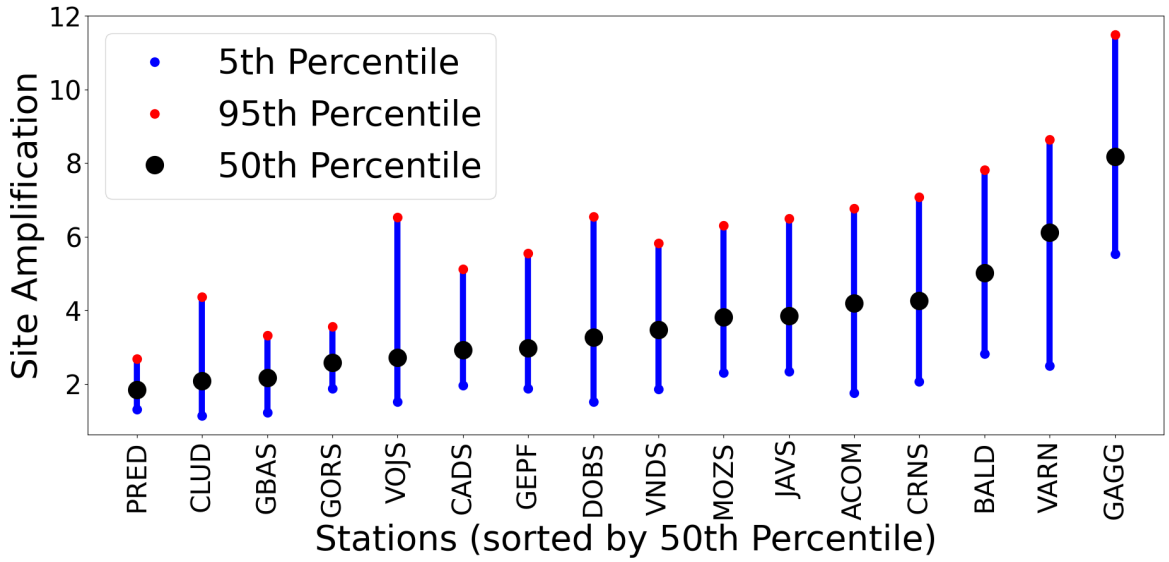

Figure 64: Horizontal to Vertical Spectral Ratio of selected stations. Black dots are showing median of site amplification while blue dots and red dots are corresponding to 5th and 95th percentile of site amplification.

Utilizing *PRED* as the reference station, the resulting source spectra corresponding to the seismic events of the first (training) dataset are depicted in Figure 65, reflecting the spectral characteristics derived under this calibration framework.

The figure presents a comparative analysis of seismic source spectra for some of the events in which each panel displays four curves: the blue line represents the calculated source spectrum obtained in this study; the orange line shows the Brune model fitted to the observed spectrum; the red line corresponds to the source spectrum reported by Cataldi et al. [2025]; and the green line depicts the theoretical Brune spectrum computed using Cataldi et al. [2025]'s published seismic moment and corner frequency.

Although in all cases the fitted Brune model (orange curve) closely follows the observed spectrum (blue curve), indicating a reliable match between theory and data, the red curve from Cataldi et al. [2025] generally shows deviations in amplitude and curvature from the obtained spectral shape. These deviations are higher with respect to the condition of using H/V in the data vector.

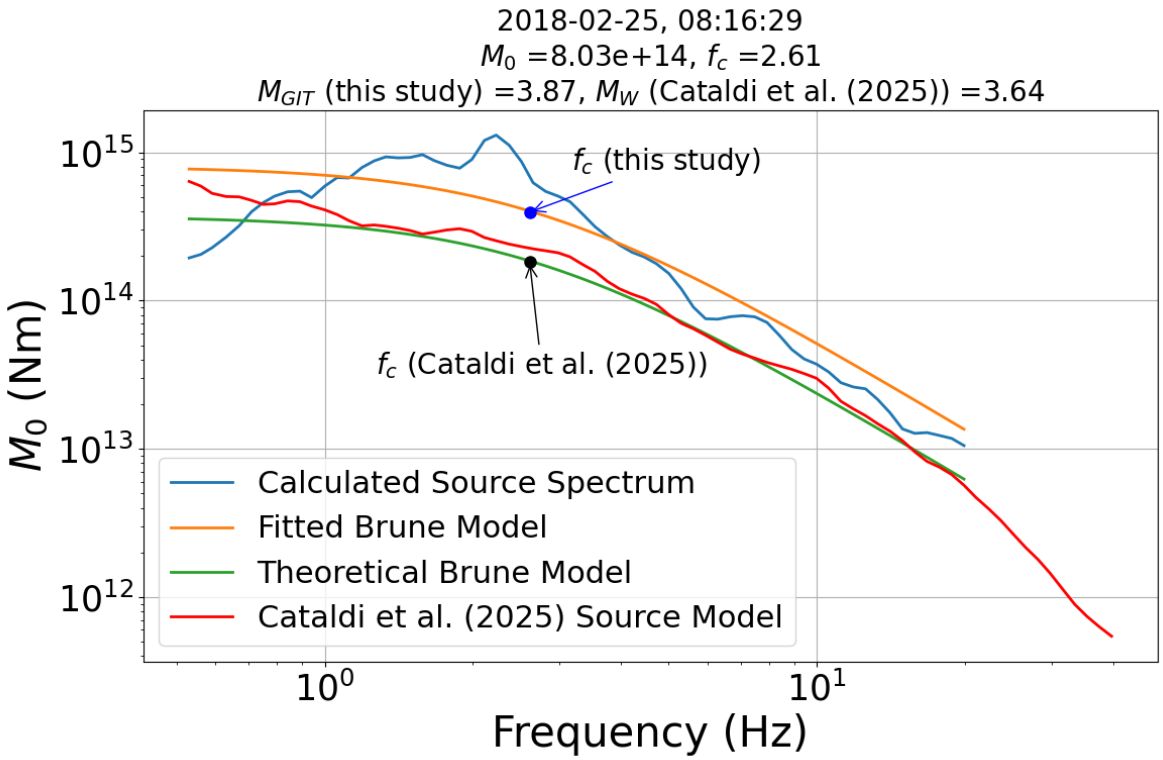

Figure 65: Source model obtained by GIT when the reference station is *PRED*.

Under this configuration, the computed MAE and RMSE of the estimated magnitudes, with respect to the findings of Cataldi et al. [2025], are 0.30 and 0.31, respectively which shows more error in comparison to the situation of using H/V in the data vector. A detailed comparative visualization of these results is provided in Figure 66, highlighting the degree of consistency between the two datasets which is less than the consistency when using H/V.

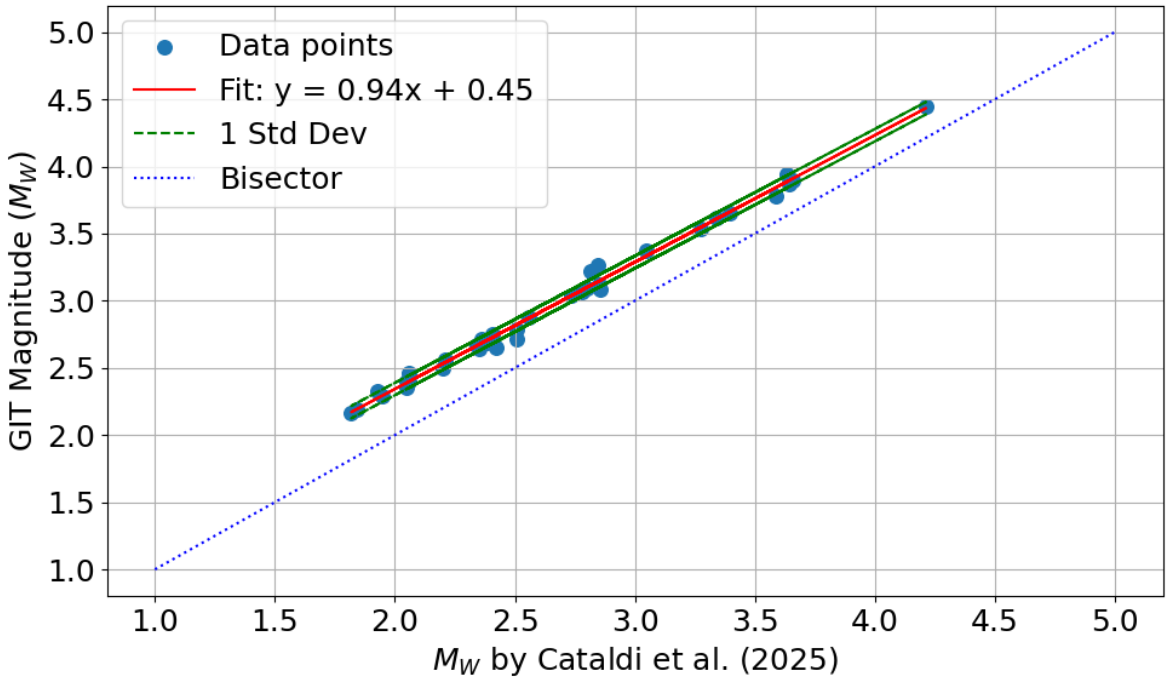

Figure 66: Comparison of the magnitude results when the reference station is *PRED* with the magnitudes of Cataldi et al. [2025].

Consequently, the magnitude results obtained by applying regression coefficients to the second dataset show a noticeable decline in performance compared to those derived using the H/V spectral ratio in the data vector, as illustrated in Figure 67. This degradation suggests that incorporating H/V contributes positively to the stability and accuracy of magnitude estimation, likely due to its ability to account for site-specific amplification effects. The comparison, furthermore, highlights the sensitivity of coefficient-based magnitude calibration to the structure of the input data vector.

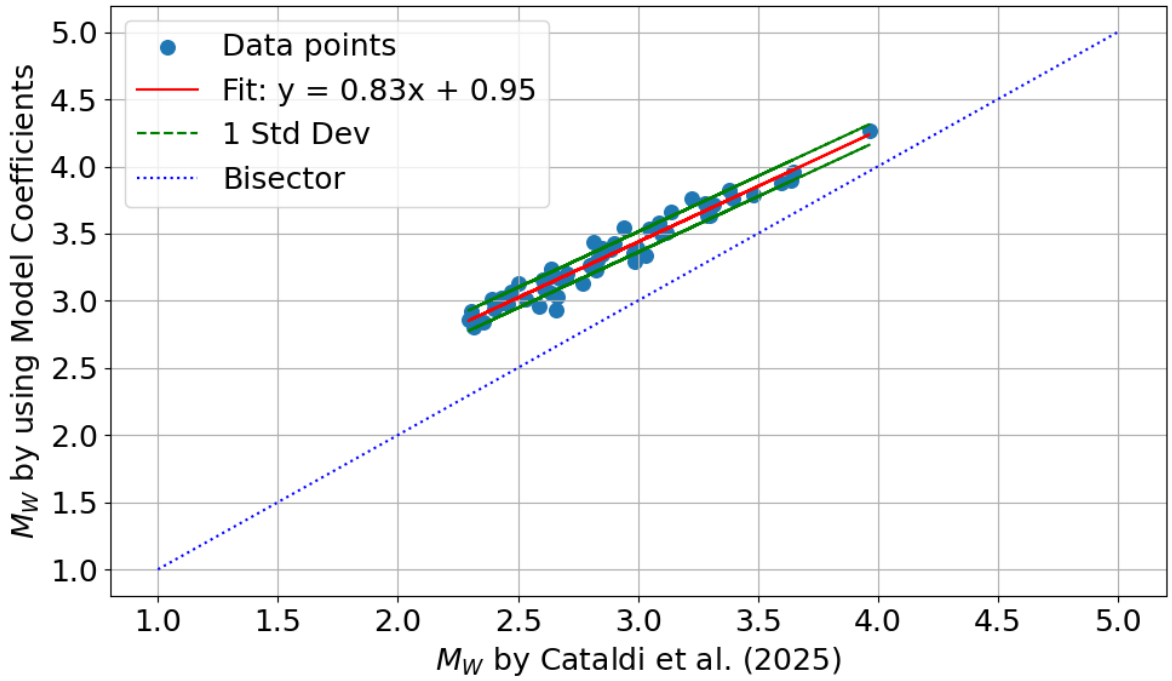

Figure 67: Comparison of the magnitudes achieved by coefficients (under the condition that the reference station is *PRED*) with the magnitudes of Cataldi et al. [2025].

4.4.3 No Reference Station

In the present study, the adopted methodology involved identifying and utilizing a single station as the reference site for inversion calibration. However, Castro et al. [1990] introduced an alternative strategy, in which, instead of anchoring the analysis to a specific station, a global constraint is imposed on the site amplification parameters, expressed as:

$$\Sigma \log Z_j = 0 \tag{44}$$

where Z denotes the site amplification factor for each station j. When this constraint is applied, the resulting source spectra is as illustrated in Figure 68. Each panel displays four spectral curves plotted against frequency: the blue line represents the calculated source spectrum obtained in this study using average site effect of all stations in the GIT; the orange line shows the fitted Brune model on the blue line; the red line depicts the source spectrum reported by Cataldi et al. [2025] and the green line corresponds to the theoretical Brune spectrum using their inversion-derived parameters.

As illustrated in the figure, the magnitude results obtained using average site effect of all stations shows

a noticeable decline in accuracy when compared to those derived using a single reference station. This degradation highlights the stabilizing effect of station-specific calibration, particularly when site amplification is well-characterized. The use of one reference station, typically selected for its minimal site effects and consistent spectral behavior, appears to reduce variability and improve the reliability of magnitude estimates. In contrast, applying generalized site effect across multiple stations introduces greater uncertainty, especially when site conditions vary significantly. These findings underscore the importance of careful reference station selection.

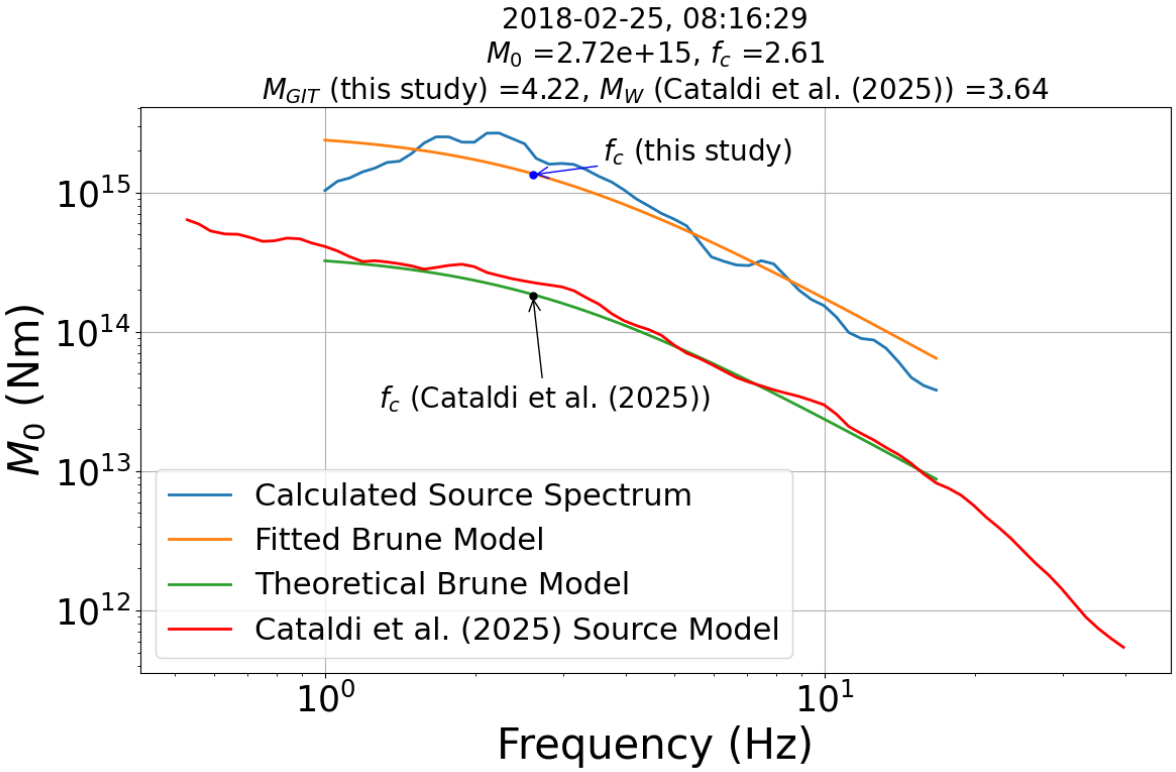

Figure 68: Source model obtained by GIT when the log average of stations sets to zero.

The corresponding magnitude estimates, with respect to the results of Cataldi et al. [2025], which is shown in Figure 69, showing that the inversion performance under this conditions which is not using one reference station resulted in moments and magnitudes which do not seem suitable.

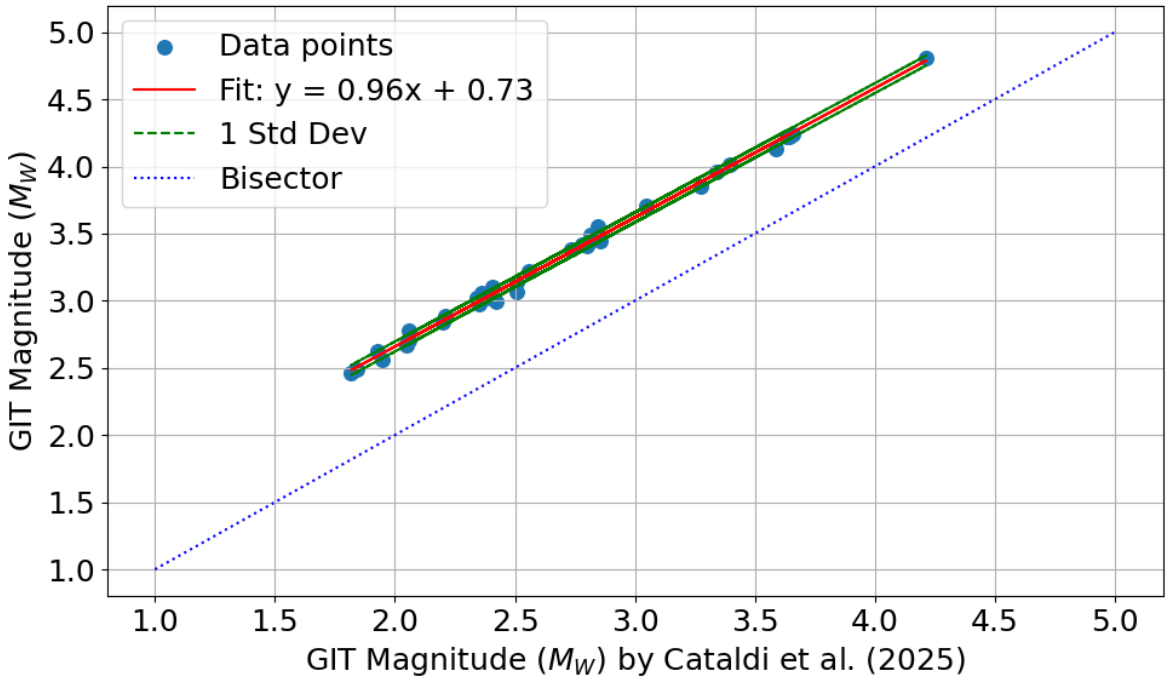

Figure 69: Comparison of the magnitude results when the log average of stations sets to zero with the magnitudes of Cataldi et al. [2025].

Moreover, Figure 70 is showing the magnitude results when using the model coefficients for the second dataset under this condition which again shows less suitable outcomes.

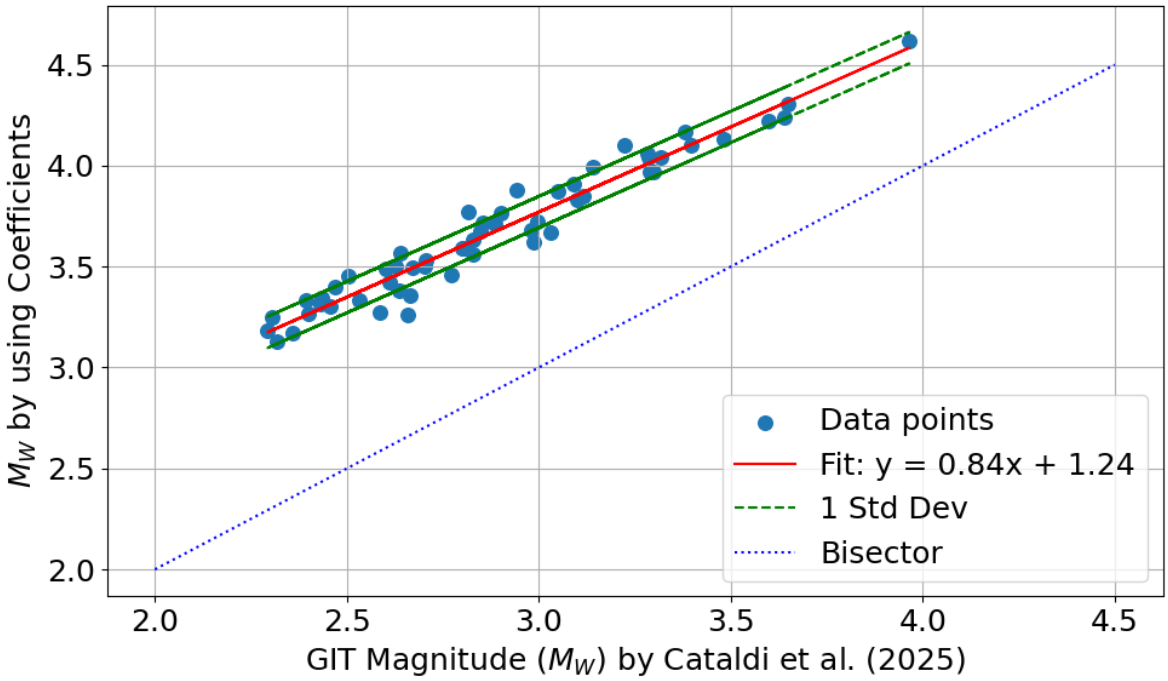

Figure 70: Comparison of the magnitude results by using coefficients when the log average of stations sets to zero with the magnitudes of Cataldi et al. [2025].

4.4.4 Extra Method to Calculate Energy

In addition to the introduced methodologies employed for estimating seismic radiated energy, an alternative formulation, originally proposed by Kanamori et al. [1993] and subsequently implemented by Bindi et al. [2018], was evaluated. This approach offers another framework for quantifying the energy released during seismic events, leveraging empirical observations and nonparametric attenuation modeling. The radiated energy E_i associated with a given seismic event i is expressed as:

$$E_i = \frac{4\pi\rho v_s}{A^2} D_{ref}^2 10^{H_i} \tag{45}$$

where ρ denotes the medium density, v_s is the shear-wave velocity, $A = 2$ accounts for the amplification effects at the free surface, D_{ref} is the reference hypocentral distance, and H_i shows the event-specific logarithmic energy scaling parameter. The latter is derived through an inversion of integrated squared velocity amplitudes, as formulated in the following expression:

$$\log IV_{kl}(R) = b_n \log F_0(R_n) + b_{n+1} log F_0(R_{n+1}) + \Sigma_{i=1}^{N_{ev}} \delta_{ik} H_i + \Sigma_{j=1}^{N_{sta}} \delta_{jl} Z_j \tag{46}$$

In this equation, IV_{kl} represents the time-integrated squared velocity over the S-wave window, summed across all three components for the kth seismic event recorded at the lth station. The term F_0 corresponds to a nonparametric attenuation function, constrained to be 0 at a given reference distance D_{ref}; and Z_j denotes the station-specific correction factor for the jth station. The hypocentral distances (R) are discretized into N_d bins with $n = 0,...,N_d$; $b_n = (R_{n+1} - \Delta R)/\Delta R$; $\Delta R = (R_{n+1} - R_n)$; $b_{n+1} = 1 - b_n$; and δ is the Kronecker delta which allows the use of the related variable. The total number of seismic events and stations are denoted by N_{ev} and N_{sta} respectively. An additional constraint, as claimed by Bindi et al. [2018], ensures that the sum of all station corrections satisfies $\Sigma_j Z_j = 0$ thereby preserving the stability of the inversion.

The above formulation could be rewritten as a matrix representation (Equation 46), enabling efficient implementation within a linear inversion framework and facilitating the joint estimation of energy scaling parameters and station corrections across large seismic datasets.

$$\begin{pmatrix} \log(IV)_{11} \\ \log(IV)_{12} \\ \vdots \\ \log(IV)_{kl} \end{pmatrix} = \begin{pmatrix} \underbrace{\begin{matrix} b_1 & b_2 & 0 & . & \dots \\ 0 & b_2 & b_3 & . & \dots \\ . & . & . & . & \dots \\ 0 & 0 & b_n & b_{n+1} & \dots \\ \vdots & \vdots & \vdots & \vdots & \vdots \end{matrix}}_{\text{attenuation parameters}} & \underbrace{\begin{matrix} 1 & 0 & 0 & . & \dots \\ 0 & 1 & 0 & . & \dots \\ . & . & . & . & \dots \\ 1 & 0 & 0 & . & \dots \\ \vdots & \vdots & \vdots & \vdots & \vdots \end{matrix}}_{\text{stations}} & \underbrace{\begin{matrix} 1 & 0 & 0 & . & \dots \\ 0 & 1 & 0 & . & \dots \\ . & . & . & . & \dots \\ 0 & 1 & 0 & . & \dots \\ \vdots & \vdots & \vdots & \vdots & \vdots \end{matrix}}_{\text{sources}} \end{pmatrix} \begin{pmatrix} \log F_0(R_1) \\ \log F_0(R_2) \\ \vdots \\ \log F_0(R_{N_d}) \\ Z_1 \\ Z_2 \\ \vdots \\ Z_{N_{sta}} \\ H_1 \\ H_2 \\ \vdots \\ H_{N_{ev}} \end{pmatrix} \tag{47}$$

The matrix formulation of the inversion system is divided into three distinct segments, each belonging to a specific class of parameters. The left block of the system matrix is related to the attenuation, specifically the nonparametric distance-dependent decay functions. The central block is reserved for site corrections, reflecting local amplification effects at individual recording stations. The right block corresponds to source-related terms, capturing the energy scaling factors for each seismic event.

Each row of the matrix represents a unique waveform, and the columns are receiving values according to the spatial and observational relationships between events and stations. For the attenuation segment, the column corresponding to the distance bin between the hypocenter and the station is assigned the interpolation weight b_n while the adjacent column receives the complementary weight b_{n+1}, ensuring smooth transitions across distance intervals. In the site correction segment, the column corresponding to the recording station is set to unity, indicating the presence of a station-specific term. Similarly, in the source segment, the column associated with the seismic event is marked with a value of one, showing its contribution to the observed amplitude.

Figure 71 illustrates the initial energy estimates derived from this inversion framework. As it is shown in the figure, the difference between the observed and calculated values is very significant.

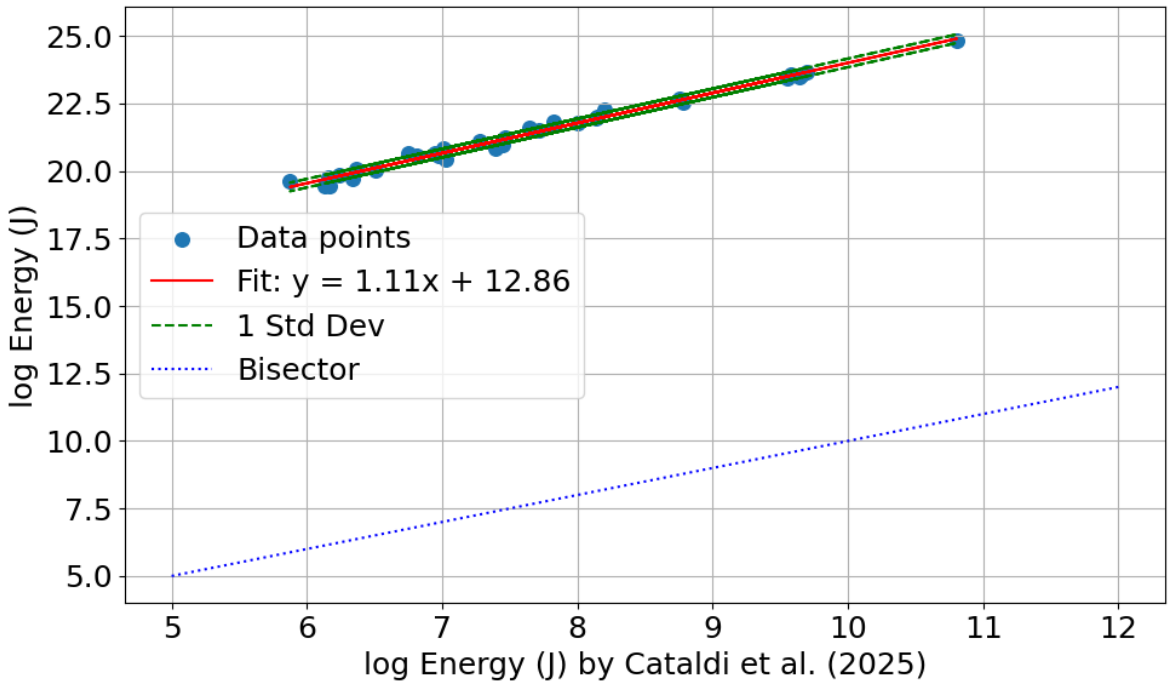

Figure 71: Comparison of the energy results by using Equation 45 with the energy results of Cataldi et al. [2025].

Moreover, when the coefficients are recalculated using Equation 34, the updated energy distribution is presented in Figure 72. However, similar to previous figure, it is revealing that the resulting energy trend shows lack of consistency and exhibit considerable scatter, suggesting limitations in the current approach.

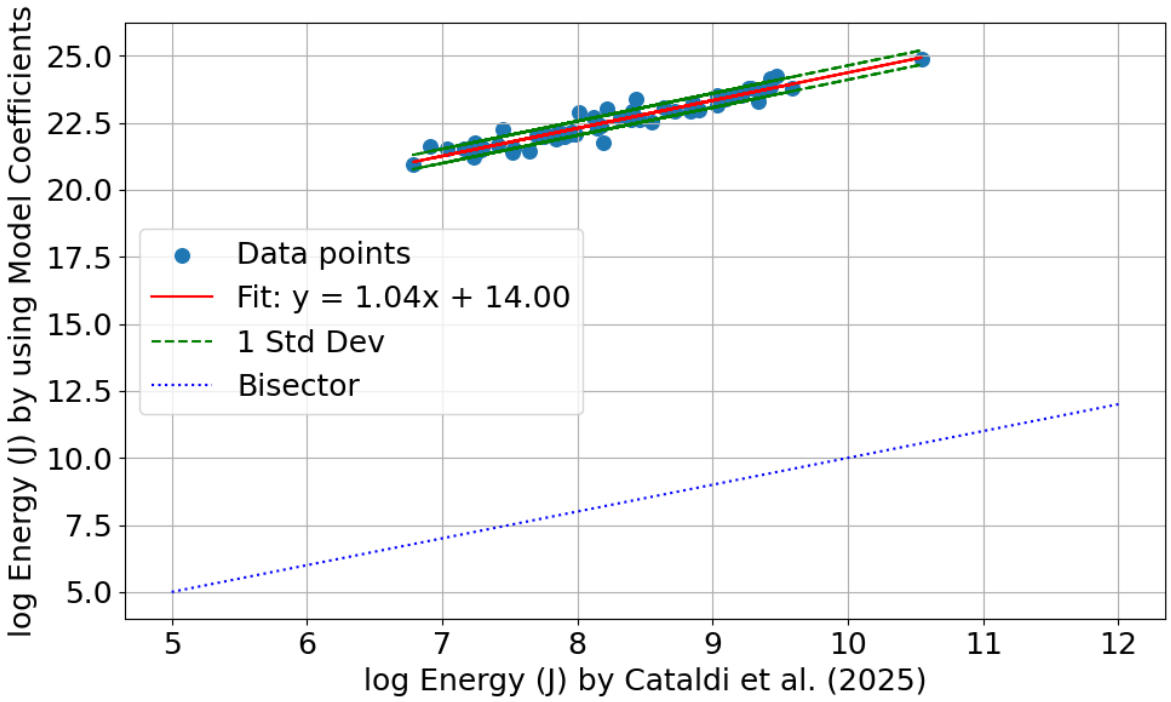

Figure 72: Comparison of the energy results by using coefficients produced based on the Equation 45 with the energie results of Cataldi et al. [2025].

A further methodological point arises in the definition of the distance bins difference ΔR. While Bindi et al. [2018] adopt the formulation $\Delta R = (R_{n+1} - R_n)$, Spallarossa et al. [2021] used an alternative expression $\Delta R = (R_{n+1} - R)$ in similar situation where R is the actual hypocentral distance. Implementing this latter definition within the same inversion framework yields more degraded results, as evidenced in Figure 73, underscoring the sensitivity of the energy estimates to the discretizations strategy employed in the attenuation modeling.

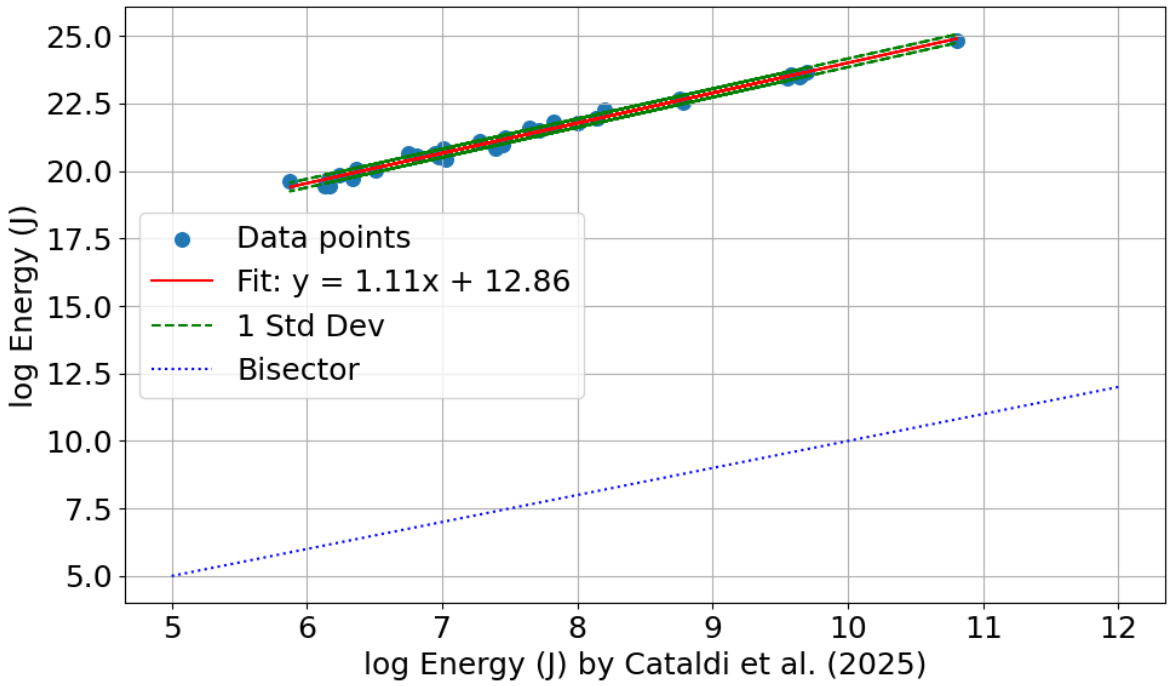

Figure 73: Comparison of the energy results by using Equation 45 while using $\Delta R = (R_{n+1} - R)$, with the energy results of Cataldi et al. [2025].

4.4.5 Station Correction

As detailed in the section *Empirical Attenuation Characteristics*, [Picozzi et al., 2018a] established empirical formulations for estimating the E_R and M_0 which are presented in Equations 34 and 35. These expressions are based on observed ground motion metrics and attenuation behavior, offering an easier and time-saving approach for source parameter estimation across regional networks.

Building upon this framework, Spallarossa et al. [2021] proposed a refinement by incorporating an additional term, referred to as the *Station Correction*, to account for site amplification effects and systematic biases inherent to individual recording stations as shown in Equations 48 and 49.

$$\log[IV2_s(R_H)]_{kl} = A + B\log(E_R)_k + w_j C_j + (1 - w_j)C_{j+1} + \Sigma_{i=1}^{N_{sta}} \delta_{il} S_i \tag{48}$$

$$\log[PD_s(R_H)]_{kl} = D + F\log(M_0)_k + w_j G_j + (1 - w_j)G_{j+1} + \Sigma_{i=1}^{N_{sta}} \delta_{il} Z_i \tag{49}$$

This modification introduces two corrective parameters S_i and Z_i associated with each station i, where N_{sta} denotes the total number of stations involved in the analysis. The inclusion of these terms necessitates a revision of the previously defined system matrices in Equations 37 and 38, which is effectively expanding the inversion framework to accommodate station-dependent changes as shown in Equations 50 and 51.

$$\begin{pmatrix} \log(IV2_s)_{11} \\ \log(IV2_s)_{12} \\ \vdots \\ \log(IV2_s)_{kl} \end{pmatrix} = \begin{pmatrix} \underbrace{1 & \log(E_R)_1 & \log(E_R)_k}_{\text{source}} & \underbrace{w_1 & 1-w_1 & 0 & \dots & \dots}_{\text{attenuation}} & \underbrace{\delta_{11} & 0 & \dots \\ 0 & w_2 & 1-w_2 & \dots & 0 & \delta_{12} & \dots \\ \vdots & \vdots & \dots & \dots & \vdots & \vdots & \dots \\ . & . & \dots & \dots & \dots & \delta_{kl} & \dots}_{\text{stations}} \end{pmatrix} \begin{pmatrix} A \\ B \\ C_1 \\ C_2 \\ \vdots \\ C_j \\ S_1 \\ S_2 \\ \vdots \\ S_{N_{sta}} \end{pmatrix} \tag{50}$$

$$\begin{pmatrix} \log(PD_s)_{11} \\ \log(PD_s)_{12} \\ \vdots \\ \log(PD_s)_{kl} \end{pmatrix} = \begin{pmatrix} \underbrace{1 & \log(M_0)_1 & w_1 & 1-w_1}_{\text{source}} & \underbrace{0 & \dots & \dots}_{\text{attenuation}} & \underbrace{\delta_{11} & 0 & \dots}_{\text{stations}} \\ 1 & \log(M_0)_1 & 0 & w_2 & 1-w_2 & \dots & 0 & \delta_{12} & \dots \\ \vdots & \vdots & \vdots & \vdots & \dots & \dots & \vdots & \vdots & \dots \\ 1 & \log(M_0)_k & . & . & \dots & \dots & \dots & \delta_{kl} & \dots \end{pmatrix} \begin{pmatrix} D \\ F \\ G_1 \\ G_2 \\ \vdots \\ G_j \\ Z_1 \\ Z_2 \\ \vdots \\ Z_{N_{sta}} \end{pmatrix} \tag{51}$$

The resulting station correction coefficients, derived from the updated inversion scheme, are visualized in Figure 74. The coefficients S_i exhibit a range from –1.5 to 1.5, while the coefficients Z_i vary between –0.8 and 0.7. These value ranges are consistent with the findings reported by Spallarossa et al. [2021], confirming the physical plausibility and regional compatibility of the derived parameters. The agreement reinforces the reliability of the regression framework adopted in this study and supports its applicability.

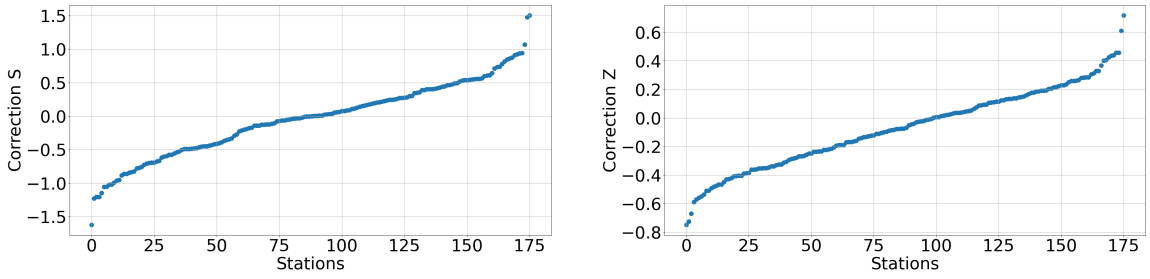

Figure 74: a) Station Correction coefficients S_i (Equation 48). b) Station Correction coefficients Z_i (Equation 49).

However, this methodological adjustment, while theoretically motivated to enhance model fidelity, led

to a slight differences in the overall performance of the regression. Specifically, the recalculated energy estimates (Equation 31) exhibit slight reduced coherence, as illustrated in Figure 75 by showing MAE of 0.28 and RMSE of 0.34.

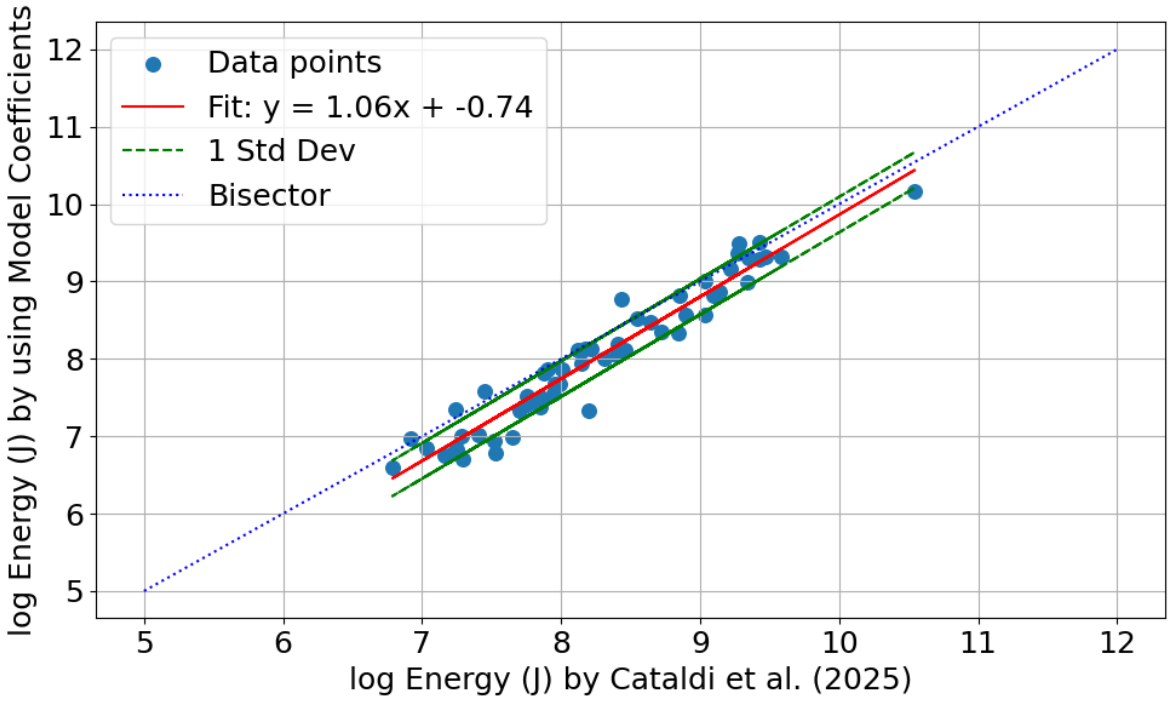

Figure 75: Comparison of the energy results by using coefficients of Equation 48 with the energy results of Cataldi et al. [2025].

The same happened when comparing to the results of Moratto et al. [2026] (Figure 76) in which the RMSE showed an increase to the value of 0.76.

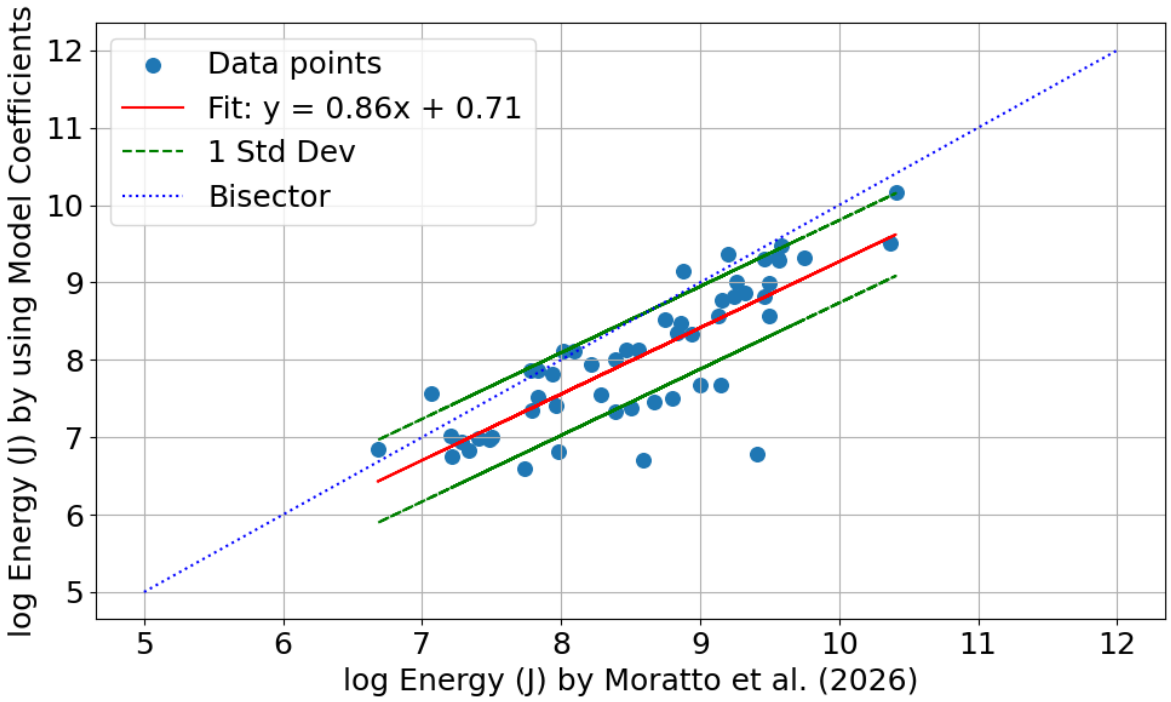

Figure 76: Comparison of the energy results by using coefficients of Equation 48 with the energy results of Moratto et al. [2026].

Nonetheless, seismic moment and moment magnitude values exhibit slightly improved consistency, specially the moment magnitude, (Figure 77) by showing MAE of 0.12 and RMSE of 0.15.

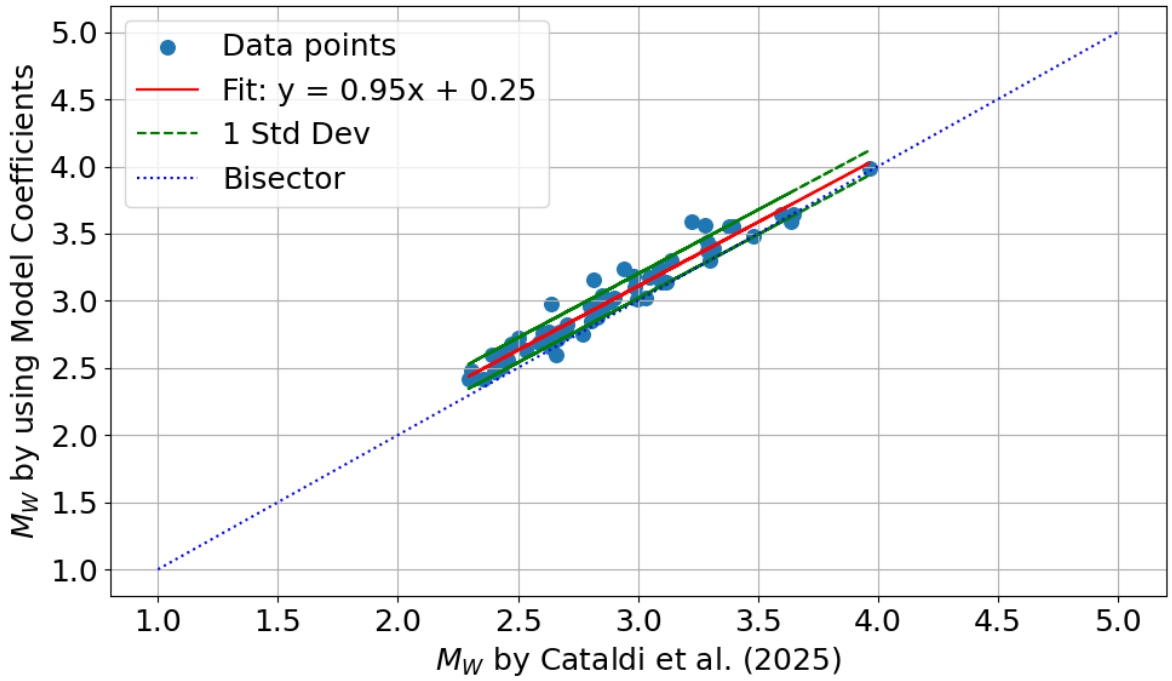

Figure 77: Comparison of the moment magnitude results by using coefficients of Equation 49 with the moment magnitude results of Cataldi et al. [2025].

This improvement can also be seen while comparing to the results of Tarchini et al. [2025] (Figure 78) and Moratto et al. [2026] (Figure 79). In both of which, the RMSE is showing the value of 0.1.

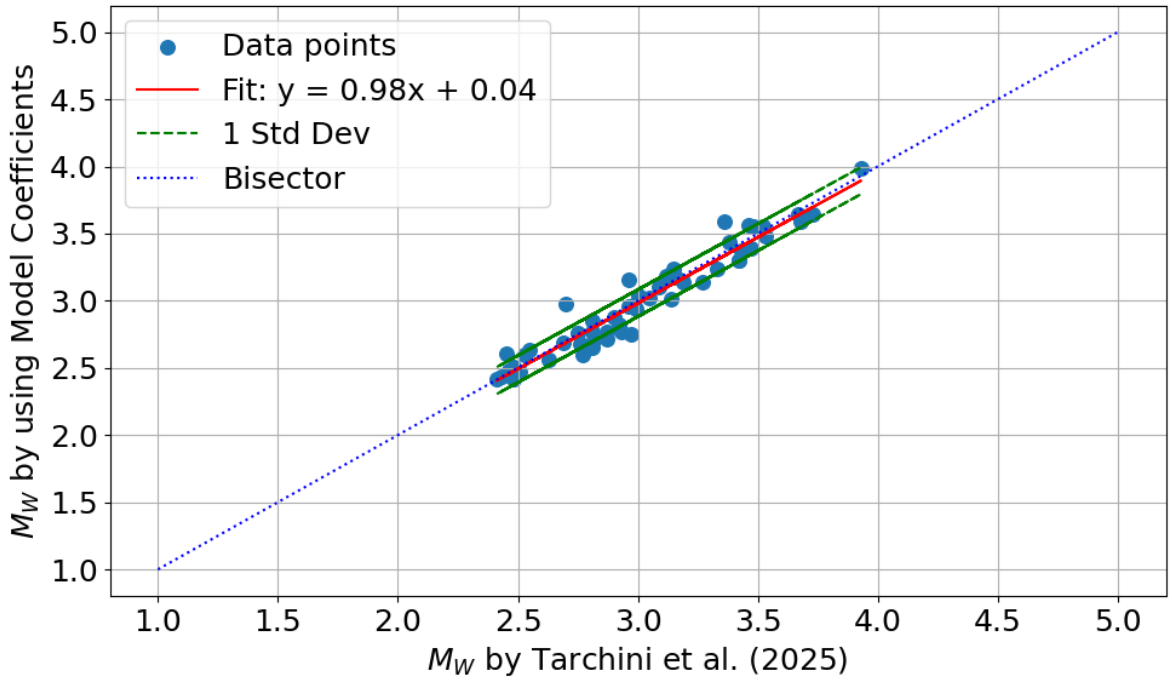

Figure 78: Comparison of the moment magnitude results by using coefficients of Equation 49 with the moment magnitude results of Tarchini et al. [2025].

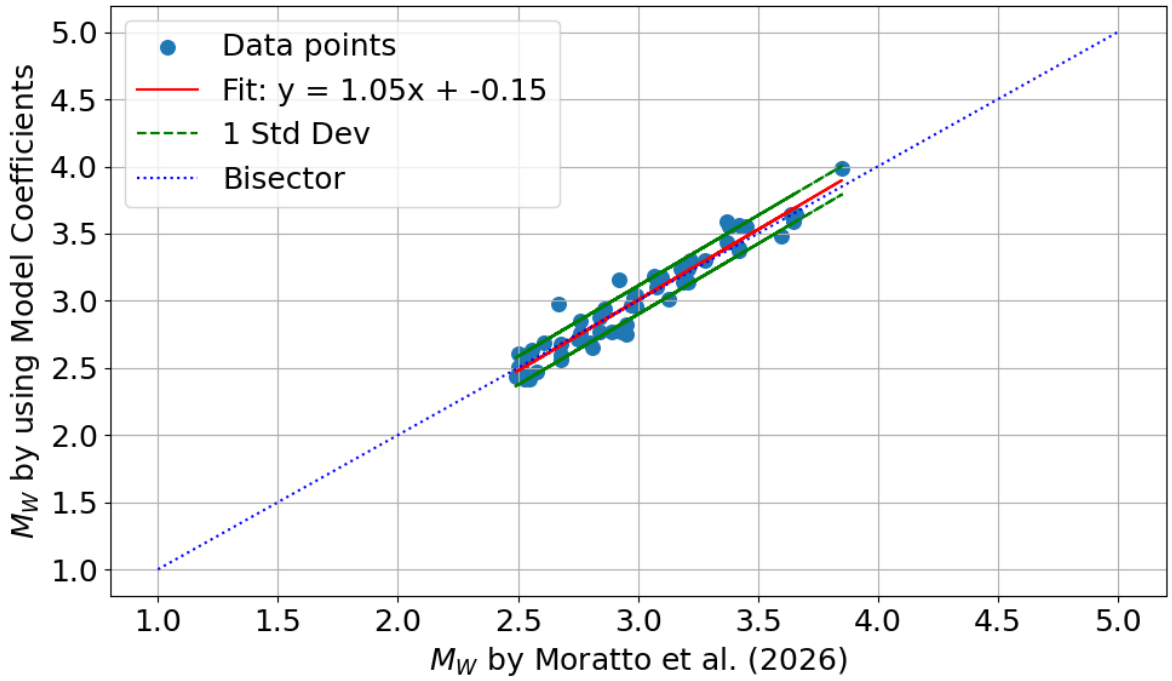

Figure 79: Comparison of the moment magnitude results by using coefficients of Equation 49 with the moment magnitude results of Moratto et al. [2026].

Root of squared error per sample for both E_R and M_0 while using Equations 48 and 49 are shown in Figure 80. The root of squared error per observation for $\log M_0$ becomes narrower and more symmetric, indicating reduced variability and better consistency in moment estimation in comparison to the condition of not using station correction. This suggests that the correction term effectively accounts for site effects that influence moment calculations. However, for $\log E$, the root of squared error per sample appears wider and more irregular than the condition without station correction implying increased scatter and less stable energy estimates.

Figure 80: Root of squared error per sample for E_R and M_0 using coefficients by taking advantage of station correction term.

5 Discussion

In this chapter, the main findings of the study are interpreted. The goal is to understand what the results mean, how they compare with previous research, and what they suggest about the methods used. Different topics are reviewed, and their strengths and weaknesses are discussed. This section also talks about some unexpected outcomes and considers possible reasons behind them.

5.1 Overview of Methodological Framework

This study has demonstrated the efficiency of GIT in decomposing and quantifying the individual contributions of seismic source characteristics, propagation path effects, and local site responses from recorded ground motions. By applying GIT to a regional dataset, the research underscores its robustness in extracting meaningful physical parameters from seismic waveforms and their spectra. The ability of GIT to isolate source, path and site terms is particularly valuable in regions with heterogeneous geological conditions, where traditional parametric models may fail in capturing localized anomalies.

A key methodological insight from this work is the comparative performance of different GIT configurations. According to Figures 15, 16, the results of 1-step GIT with predefined attenuation model were not fully consistent with previous studies which shows that careful attention must be paid to define attenuation and Q models. On the other hand, the results of 1-step and 2-step methods were really similar that could be due to the fact that their data, parameters, constraints and resolving problems are the same. Consequently, slight differences in their performance could be addressed to the performances of the methods, which shows a really small relative preference of the 2-step method (Figures 18 and 19).

5.2 Magnitude Estimation for Small Events

Estimating seismic moment and moment magnitude for low-magnitude events remains a challenging topic. Edwards et al. [2010] suggest that the lower threshold for reliable moment magnitude estimation is approximately $M = 3.5$, primarily due to limitations in signal-to-noise ratio and spectral resolution at long periods. Gallo et al. [2014] proposes a slightly more optimistic threshold of $M = 3.0$ which is the same opinion as Yen et al. [2024]. However, the current study demonstrates that even for events

with $M < 3$, the inversion framework, whether through direct low-frequency spectral amplitude or coefficient-based estimation, which is from the model, achieves RMS errors below 0.2. This finding is significant, as it suggests that with careful preprocessing and inversion design, meaningful source parameters can be extracted from seismic events with small magnitudes.

Kaneko and Shearer [2014] concerned about systematic biases in spectral methods, particularly the overestimation of seismic moment by approximately 18% for S-waves due to Brune's spectral function exaggerating long-period amplitudes. Despite this claim, the results of this study show good agreement with earlier literature.

Considering the percentage change [Törnqvist et al., 1985] as:

$$\text{Percentage Change} = \frac{\text{Calculated Value - Reference Value}}{\text{Reference Value}} \times 100 \tag{52}$$

and calculating this change, value by value, and then averaging, in the case of seismic moment showed 5.7% overestimation suggesting that the adopted inversion strategy effectively implemented spectral decomposition.

5.3 Reference Station and H/V

One of the most critical methodological decisions in GIT is the selection of the reference station. This choice has important influences on the inversion results, because it affects the baseline against which all other site and path effects are measured. The complexity appears from the need to balance multiple factors, including the accuracy of magnitude estimation, local site amplification, path-dependent attenuation, soil composition, S-wave velocity profiles, and topographic features. Chen et al. [2024] emphasizes on the statement of Steidl et al. [1996] that uncertainties in reference station characteristics can significantly affect inversion outputs. This is also agreed by Shible et al. [2022] who claims that the reference site selection significantly shapes the final results.

While the ideal reference station would be located on hard rock with minimal site amplification, such conditions are not easy to achieve in every geological setting. To address this, the study explores the use of horizontal-to-vertical spectral ratios in the data vector for the reference station. Although this introduces potential bias, it also offers several advantages:

- It integrates prior site information derived from ambient noise or earthquake recordings. This integration provides a better understanding of the site's frequency-dependent amplification char-

acteristics. By using this empirical knowledge in the inversion framework, the model becomes better equipped.

- It enhances inversion stability when the reference station deviates from the ideal "flat" response. Therefore, H/V ratios help the inversion by offering a correction through which the reference site's response can be interpreted better, thereby the inversion process could be done more securely.
- It enables more realistic modeling in regions lacking suitable rock sites. In many study environments it is difficult to access the stations on hard-rock, making it impractical to have robust reference criteria. By allowing for the inclusion of H/V-derived corrections, researchers can extend the applicability of GIT to a broader range of geological settings without sacrificing model integrity. While this introduces some bias, it will provide a more robust and context-sensitive inversion design that reflects the complexities of real-world seismic environments.

These trade-offs highlight the significant role of H/V in inversion design and suggest that when it is used wisely, it can improve model robustness without having negative influence on interpretability.

5.4 Parametric vs. Non-Parametric Approaches

The study also touched upon a part of the broader methodological topic between parametric and non-parametric inversion strategies. Parametric approaches, which rely on predefined models such as Brune's source spectrum, offer stability in environments with sparse data and facilitate simpler computation. However, they have the risk of oversimplifying complex source and attenuation behaviors, especially in geologically heterogeneous regions [Shible et al., 2022, Cataldi et al., 2022].

In contrast, non-parametric methods provide greater flexibility and fewer assumptions, allowing the data to speak more directly [Shible et al., 2022, Morasca et al., 2025]. However, non-parametric approaches are more sensitive to data quality and completeness. Gaps in the dataset or irregular station coverage can introduce instability, and trade-offs at high frequencies, such as those noted by Shible et al. [2022], Saraò et al. [1998], which can affect the fidelity of the inversion. They also assume the initial value for attenuation to be unity at reference distance, which may cause inaccuracy if near-source data are sparse. Nonetheless, Baker [1988] and later, Castro et al. [1990] also claimed that the non-parametric approaches are more powerful to better achieve attenuation behavior, therefore, they are particularly more capable of revealing unmodeled features and capturing small variations in source, site and path effects.

Overall, according to the mentioned studies, the performance of all approaches is often robust when they appropriately tuned and the assumed functional forms adequately represent the underlying physics.

Therefore, specially for parametric approaches, it is advantagous to define the required models, specially the attenuation models, very carefully and accurately.

While the recommendation by Shible et al. [2022] to adopt a non-parametric approach when dense observational datasets are available will present a more reliable strategy, particularly for enhancing model flexibility and minimizing assumptions, the findings of the present study suggest a more improved approach, which is the incorporation of H/V into the data vector. This refinement introduces a form of structured constraint that, while not shifting the overall methodology to strictly parametric, forces the inversion process with certain stabilizing characteristics.

This configuration appears to build a productive balance between methodological rigidity and empirical flexibility. On one hand, the inclusion of H/V ratios serves to regularize the inversion, and mitigating instability that can appear in purely non-parametric formulations, especially when data coverage is uneven or site effects are significant. On the other hand, the framework is still taking advantage of non-parametric modeling, namely, its capacity to capture spatial and spectral heterogeneity without imposing rigid functional forms or regional assumptions.

The results of this study (Figures 15, 16, 17, 20) therefore support such a constrained modeling philosophy, in which selective use of some constraints (such as H/V ratios) enhances the robustness and interpretability of the inversion outputs, while preserving the flexibility required to find localized complexities in attenuation behavior.

5.5 Energy Calculation

In this study, Equation 31 selected as the foundational framework for energy estimation, which exhibits a significant sensitivity to the reliability of the seismic moment and corner frequency input, that is derived from the GIT. Given that seismic moment is a critical parameter in magnitude and energy formulations, any uncertainty or bias introduced during its inversion directly propagates into the final magnitude and energy estimates. Therefore, the fidelity of Equation 31 is fundamentally depend on the robustness and stability of the inversion algorithm employed.

The results obtained in this study demonstrate that when Equation 31 is used, which is supplied with source parameters, the resulting estimates are slightly more consistent across events (Figures 43, 44, 58, 59).

However, the inversion process itself is influenced by methodological choices, particularly the inclusion or exclusion of H/V spectral ratios. These ratios, which often used to enhance stability or constrain site effects, can significantly change the spectral shape and amplitude, thereby having impact on the mo-

ment estimation and, by extension, the energy output. The study confirms that variations in site effect treatment can introduce important differences in the energy estimates, highlighting the need for careful consideration of spectral preprocessing steps when applying Equation 31 in regional or comparative analyses.

5.6 Use of Empirical Attenuation Models

The findings of this study reveal a trade-off between methodological accuracy and computational efficiency in the estimation of seismic source parameters. When seismic moment and radiated energy are derived directly from waveform data, typically through spectral analysis, the moment estimates exhibit superior accuracy, characterized by lower associated uncertainties. This outcome underscores the robustness of moment retrieval when is based on spectral inversion, which inherently captures the source properties more comprehensively (Figure 51).

Conversely, when both parameters are estimated from scaling model coefficients, i.e. within empirical attenuation models, a technique which is famous for its computational efficiency and suitability for large datasets, the energy estimates demonstrate a modest advantage over moment estimates in terms of consistency and relative performance (Figure 61). This suggests that, under certain conditions, energy may be more flexible to the simplifications, i.e. in attenuation-based modeling.

Overall, the study highlights that while direct waveform-based approaches remain preferred for moment estimation, empirical-attenuation-based methods offer a pragmatic alternative for energy characterization, especially in rapid-response or large-scale applications where computational resources and data completeness may be constrained.

Initially, the observed difference between moment and energy estimates was hypothesized to stem from differences in data (i.e. waveform components) during source parameter derivation. Specifically, radiated S-wave energy is calculated using all three components of ground motion (two horizontal and one vertical) thereby capturing the seismic energy release from full vectorial components, including the vertical motion that may be significant in certain source–site configurations.

In contrast, seismic moment is conventionally estimated using only the two horizontal components, primarily due to their more direct sensitivity to shear-wave radiation in typical recordings. This methodological distinction was assumed to influence the comparative performance of the two parameters. This can mean when more components used for energy estimation, it potentially offers a more complete characterization.

However, the test conducted in this study revealed that the discrepancy may not be attributed to the

component selection. Comparative analyses using all three components (for moment estimation), in which magnitude RMSE increased from 0.2 to 0.3, explained that the divergence in performance between moment and energy estimates still exists even when both parameters are derived from all three components. This finding suggests that other factors, such as spectral fitting behavior, inversion stability, or frequency-dependent sensitivity, may play a more dominant role in shaping the observed differences, and requires further investigation about the adopted mechanisms.

5.7 Use of Station Correction

The role of station correction in empirical attenuation modeling has been investigated in section *"Station Correction"*. In the study which is done by Picozzi et al. [2018a], attenuation functions were derived without applying station corrections in regression, resulting in R^2 value of 0.84 for the energy results and 0.87 for the moment results. Conversely, Spallarossa et al. [2021] incorporated station corrections into their attenuation models, achieving improved R^2 value of 0.93 for the energy and 0.92 for the moment estimates.

In the present study, the implementation of station correction for radiated energy led to a modest increase in the R^2 value from 0.91 to 0.93, indicating a better fit between observed and predicted values. However, this improvement was accompanied by an increase in the RMS error from 0.25 to 0.34, suggesting a trade-off between regression strength and residual scattering. For the seismic moment, the application of station correction resulted in a slight decrease in R^2 value from 0.95 to 0.94, yet the RMS error improved significantly, dropping from 0.38 to 0.28. This implies that while the overall variance explained by the model slightly reduced, the prediction accuracy at individual events improved (Figures 61 and 80).

Furthermore, when moment magnitude was computed from the seismic moment estimates, a similar trend was observed: the R^2 value decreased slightly from 0.95 to 0.94, but the RMS error was reduced from 0.2 to 0.15. These results highlight the gentle impact of station correction, which may affect regression metrics depending on the source parameter considered. Overall, the findings suggest that station correction can be beneficial for reducing residual errors, even if its effect on regression strength is not uniformly positive across all parameters.

6 Conclusion

In conclusion, this study underscores the robustness and ability of the generalized inversion technique as a powerful tool for seismic source characterization. Through a series of methodological enhancements, most notably the implementation of a non-parametric inversion framework (with a very small preference of 2-step method over 1-step method also without considering predefined attenuation model) and the use of H/V in inversion procedure which improved the results (Figures 15 to 20), as well as the strategic selection of reference station (Figure 21), this work achieves improved consistency and reliability in source parameter estimation. A particularly significant outcome is the successful retrieval of seismic moment and magnitude for low-energy events (below $M_W = 3$) with minimal RMS error, thereby extending the operational threshold of spectral inversion techniques and challenging traditional magnitude cutoffs.

In order to evaluate the general performance of the GIT, the analysis revealed that under any methodological framework for the GIT, well tuning and careful design of the parameters and used models are important. Moreover, all decomposed components through GIT, namely the source contribution (Figure 22), the site response (Figure 27), and the attenuation characteristics (Figure 30), exhibited consistency which is showing the reliability of the decomposition methodology.

Furthermore, the dependency of energy calculations through Equation 31 on the GIT's outputs (i.e. M_0 and f_c) highlights a critical relationship between the seismic moment and the radiated energy. Specifically, whenever the seismic moment demonstrates stability and accuracy, the corresponding energy estimations also display coherence.

Beyond methodological improvements, this work establishes empirical relationships based on the seismotectonic context of Northeastern Italy, making the possibility of rapid estimation of seismic moment and radiated energy from waveform parameters (Tables 8 and 9). This region-specific calibration enhances the practical utility of spectral inversion, especially for small-magnitude earthquakes that often escape traditional cataloging thresholds.

Collectively, these findings contribute to a more refined and scalable framework for earthquake source analysis, with implications for both regional seismic hazard assessment and global seismotectonic stud-

ies. By bridging theoretical accuracy with empirical validation, this work suggests a basis for future research aimed at enhancing the resolution, reliability, and interpretability of seismic source parameters across diverse tectonic regimes.

In general, the study demonstrates that not all source parameters are equally stable. In analytical approaches, seismic moment is generally well constrained, whereas radiated energy and stress drop show strong sensitivity to methodological choices, particularly for small earthquakes and at higher frequencies. Conversely, while using empirical models, the energy results showed better consistency. Moreover, using station correction helped seismic moment more than radiated energy.

According to these findings, inversion configuration, attenuation modeling, station selection, and site effects can significantly influence the results. Consequently, careful optimization of these methodological decisions is therefore crucial for obtaining reliable rapid estimates.

6.1 Broader Implications and Future Directions

As Spallarossa et al. [2021] and Morasca et al. [2025] noted, the spreading of dense seismic networks has enabled the recording of hundreds of thousands of micro-earthquakes, particularly in tectonically active regions near fault zones. This explosion of data presents both an opportunity and a challenge. GIT offers a powerful tool for extracting meaningful information from these datasets, but their computational demands and sensitivity to input parameters necessitate careful design.

In this context, empirical relations, such as the models which are linking waveform parameters to magnitude or energy, can serve as efficient alternatives for rapid analyses. These relations, when calibrated against robust inversion results, enable large-scale processing of seismic catalogs and facilitate further studies.

However, the study also talks about some limitations. Noticeable among them is that, as previous studies mentioned, for small events, due to presence of noises in the waveforms, the calculations faced challenges because of the reduction in available frequency band. Moreover, some stations showed poor site characterization. Additionally, the scarcity of reference materials for benchmarking inversion results poses a challenge for validation. Future work should focus on expanding the dataset, refining reference station selection criteria, and exploring even machine learning techniques to enhance inversion stability and interpretability.

References

R. E. Abercrombie. Resolution and uncertainties in estimates of earthquake stress drop and energy release. *Philosophical Transactions of the Royal Society A: Mathematical, Physical and Engineering Sciences*, 379(2196):20200131, 2021. URL https://doi.org/10.1098/rsta.2020.0131.

R. E. Abercrombie, A. Baltay, S. Chu, T. Taira, D. Bindi, O. S. Boyd, X. Chen, E. S. Cochran, E. Devin, D. Dreger, W. Ellsworth, W. Fan, R. M. Harrington, Y. Huang, K. B. Kemna, M. Liu, A. Oth, G. A. Parker, C. Pennington, M. Picozzi, C. J. Ruhl, P. Shearer, D. Spallarossa, D. Trugman, I. Vandevert, Q. Wu, C. Yoon, E. Yu, G. C. Beroza, T. Eulenfeld, T. Knudson, K. Mayeda, P. Morasca, J. S. Neely, J. Roman-Nieves, C. Satriano, M. Supino, W. R. Walter, R. Archuleta, G. M. Atkinson, G. Calderoni, C. Ji, H. Yang, and J. Zhang. Overview of the scec/usgs community stress drop validation study using the 2019 ridgecrest earthquake sequence. *Bulletin of the Seismological Society of America*, 115(3): 734–759, 05 2025. ISSN 0037-1106. URL https://doi.org/10.1785/0120240158.

K. Aki. Generation and propagation of g waves from the niigata earthquake of june 16, 1964. : Part 2. estimation of earthquake moment, released energy, and stress-strain drop from the g wave spectrum. *Bulletin of the Earthquake Research Institute*, 44:73–88, 1966. URL https://doi.org/10.15083/0000033586.

K. Aki. Scaling law of seismic spectrum. *Journal of Geophysical Research (1896-1977)*, 72(4):1217–1231, 1967. URL https://doi.org/10.1029/JZ072i004p01217.

K. Aki and P. G. Richards. *Quantitative Seismology*. University Science Books, 2002. ISBN 0935702962.

L. Anderlini, E. Serpelloni, C. Tolomei, P. M. De Martini, G. Pezzo, A. Gualandi, and G. Spada. New insights into active tectonics and seismogenic potential of the italian southern alps from vertical geodetic velocities. *Solid Earth*, 11(5):1681–1698, 2020. URL https://doi.org/10.5194/se-11-1681-2020.

D. J. Andrews. *Objective Determination of Source Parameters and Similarity of Earthquakes of Different Size*, pages 259–267. American Geophysical Union (AGU), 1986. ISBN 9781118664865. URL https://doi.org/10.1029/GM037p0259.

A. Aoudia, A. Saraó, B. Bukchin, and P. Suhadolc. The 1976 friuli (ne italy) thrust faulting earthquake: A reappraisal 23 years later. *Geophysical Research Letters*, 27(4):573–576, 2000. URL https://doi.org/10.1029/1999GL011071.

G. M. Atkinson and D. M. Boore. Ground-motion relations for eastern north america. *Bulletin of the Seismological Society of America*, 85(1):17–30, 02 1995. ISSN 0037-1106. URL https://doi.org/10.1785/BSSA0850010017.

B. Aucun, E. Carvalho, M. Fardis, and P. Pinto, editors. *Eurocode 8 – Seismic design of buildings - Worked examples*. Publications Office, 2012. URL https://doi.org/10.2788/91658.

J. S. Baker. Wave propagation modeling of ground-motion attenuation in the northeastern united states and adjacent canada. In *Proceedings of the EPRI Conference on Earthquake Ground-Motion Estimation in Eastern North America*, 1988.

D. Bindi and S. R. Kotha. Spectral decomposition of the engineering strong motion (esm) flat file: regional attenuation, source scaling and arias stress drop. *Bulletin of Earthquake Engineering*, 18(6): 2581–2606, 2020. ISSN 1573-1456. URL https://doi.org/10.1007/s10518-020-00796-1.

D. Bindi, F. Pacor, L. Luzi, M. Massa, and G. Ameri. The mw 6.3, 2009 l'aquila earthquake: source, path and site effects from spectral analysis of strong motion data. *Geophysical Journal International*, 179(3): 1573–1579, 12 2009. ISSN 0956-540X. URL https://doi.org/10.1111/j.1365-246X.2009.04392.x.

D. Bindi, D. Spallarossa, M. Picozzi, D. Scafidi, and F. Cotton. Impact of magnitude selection on aleatory variability associated with ground-motion prediction equations: Part i—local, energy, and moment magnitude calibration and stress-drop variability in central italy. *Bulletin of the Seismological Society of America*, 108(3A):1427–1442, 05 2018. ISSN 0037-1106. URL https://doi.org/10.1785/0120170356.

D. Bindi, D. Spallarossa, M. Picozzi, A. Oth, P. Morasca, and K. Mayeda. The community stress-drop validation study-part i: Source, propagation, and site decomposition of fourier spectra. *Seismological Research Letters*, 94(4):1980–1991, 05 2023a. ISSN 0895-0695. URL https://doi.org/10.1785/0220230019.

D. Bindi, D. Spallarossa, M. Picozzi, A. Oth, P. Morasca, and K. Mayeda. T he community stress-drop validation study-part ii: Uncertainties of the source parameters and stress drop analysis. *Seismological Research Letters*, 94(4):1992–2002, 05 2023b. ISSN 0895-0695. URL https://doi.org/10.1785/0220230020.

A. G. Bluman. *Elementary Statistics: A Step by Step Approach*. McGraw-Hill Education, 10th edition, 2017.

J. Boatwright and J. B. Fletcher. The partition of radiated energy between p and s waves. *Bulletin of the Seismological Society of America*, 74(2):361–376, 04 1984. ISSN 0037-1106. URL https://doi.org/10.1785/BSSA0740020361.

J. Boatwright, J. B. Fletcher, and T. E. Fumal. A general inversion scheme for source, site, and propagation characteristics using multiply recorded sets of moderate-sized earthquakes. *Bulletin of the Seismological Society of America*, 81(5):1754–1782, 10 1991. ISSN 0037-1106. URL https://doi.org/10.1785/BSSA0810051754.

J. Boatwright, G. L. Choy, and L. C. Seekins. Regional estimates of radiated seismic energy. *Bulletin of the Seismological Society of America*, 92(4):1241–1255, 05 2002. ISSN 0037-1106. URL https://doi.org/10.1785/0120000932.

D. M. Boore. Simulation of ground motion using the stochastic method. *Pure and Applied Geophysics*, 160(3):635–676, 2003. ISSN 1420-9136. URL https://doi.org/10.1007/PL00012553.

R. D. Borcherdt. Effects of local geology on ground motion near san francisco bay*. *Bulletin of the Seismological Society of America*, 60(1):29–61, 02 1970. ISSN 0037-1106. URL https://doi.org/10.1785/BSSA0600010029.

P. Bormann, editor. *New Manual of Seismological Observatory Practice (NMSOP-2)*. Deutsches GeoForschungsZentrum GFZ; IASPEI, Potsdam, 2012. URL https://doi.org/10.2312/GFZ.NMSOP-2. also https://gfzpublic.gfz-potsdam.de/pubman/item/item_245421.

P. Bormann and D. D. Giacomo. The moment magnitude mw and the energy magnitude me: common roots and differences. *Journal of Seismology*, 15(2):411–427, 2011. ISSN 1573-157X. URL https://doi.org/10.1007/s10950-010-9219-2.

J. N. Brune. Tectonic stress and the spectra of seismic shear waves from earthquakes. *Journal of Geophysical Research (1896-1977)*, 75(26):4997–5009, 1970. URL https://doi.org/10.1029/JB075i026p04997.

E. Brückl, M. Behm, K. Decker, M. Grad, A. Guterch, G. R. Keller, and H. Thybo. Crustal structure and active tectonics in the eastern alps. *Tectonics*, 29(2), 2010. URL https://doi.org/10.1029/2009TC002491.

P. Burrato, M. E. Poli, P. Vannoli, A. Zanferrari, R. Basili, and F. Galadini. Sources of mw 5+ earthquakes in northeastern italy and western slovenia: An updated view based on geological and seismological evidence. *Tectonophysics*, 453(1):157–176, 2008. ISSN 0040-1951. URL https://doi.org/10.1016/j.tecto.2007.07.009. Earthquake Geology: Methods and Applications.

R. Camassi, C. H. Caracciolo, V. Castelli, and D. Slejko. The 1511 eastern alps earthquakes: a critical update and comparison of existing macroseismic datasets. *Journal of Seismology*, 15(2):191–213, 2011. ISSN 1573-157X. URL https://doi.org/10.1007/s10950-010-9220-9.

R. R. Castro, J. G. Anderson, and S. K. Singh. Site response, attenuation and source spectra of s waves along the guerrero, mexico, subduction zone. *Bulletin of the Seismological Society of America*, 80(6A): 1481–1503, 12 1990. ISSN 0037-1106. URL https://doi.org/10.1785/BSSA08006A1481.

R. R. Castro, F. Pacor, A. Sala, and C. Petrungaro. S wave attenuation and site effects in the region of friuli, italy. *Journal of Geophysical Research: Solid Earth*, 101:22355–22369, 1996. URL https://doi.org/10.1029/96jb02295.

L. Cataldi, V. Poggi, G. Costa, S. Parolai, and B. Edwards. Parametric spectral inversion of seismic source, path and site parameters: application to northeast italy. *Geophysical Journal International*, 232, 11 2022. URL https://doi.org/10.1093/gji/ggac431.

L. Cataldi, M. Picozzi, M. D'Amico, P. Morasca, D. Bindi, V. Poggi, G. Costa, A. Viganò, and D. Spallarossa. Supplements to "stress drop and seismic efficiency distributions over the adriatic indenter (european southeastern alps)", Mar. 2025. URL https://doi.org/10.5281/zenodo.15052354.

T. Chai and R. R. Draxler. Root mean square error (rmse) or mean absolute error (mae)? – arguments against avoiding rmse in the literature. *Geoscientific Model Development*, 7(3):1247–1250, 2014. URL https://doi.org/10.5194/gmd-7-1247-2014.

D. Cheloni, N. D'Agostino, and G. Selvaggi. Interseismic coupling, seismic potential and earthquake recurrence on the southern front of the eastern alps (ne italy). *Journal of Geophysical Research*, 119, 05 2014. URL https://doi.org/10.1002/2014JB010954.

K. Chen, X. Chen, Y. Wang, and X. Li. Source scaling, spatially variable path attenuation, and site-effect parameters via a generalized inversion technique for strong-motion data from sichuan, china. *Bulletin of the Seismological Society of America*, 114(5):2504–2523, 05 2024. ISSN 0037-1106. URL https://doi.org/10.1785/0120230268.

G. L. Choy and J. L. Boatwright. Global patterns of radiated seismic energy and apparent stress. *Journal of Geophysical Research: Solid Earth*, 100(B9):18205–18228, 1995. URL https://doi.org/10.1029/95JB01969.

G. L. Choy and J. L. Boatwright. Radiated seismic energy and energy magnitude. In P. Bormann, editor, *New Manual of Seismological Observatory Practice 2 (NMSOP-2)*, pages 1–9. Deutsches GeoForschungsZentrum GFZ, Potsdam, 2012. URL https://doi.org/10.2312/GFZ.NMSOP-2_IS_3.6.

G. L. Choy, J. Boatwright, and S. Kirby. The radiated seismic energy and apparent stress of interplate and intraplate earthquakes at subduction zone environments; implications for seismic hazard estimation. Open-File Report 2001-5, U.S. Dept. of the Interior, U.S. Geological Survey, 2001. URL https://doi.org/10.3133/ofr015.

G. L. Choy, A. McGarr, S. H. Kirby, and J. Boatwright. *An Overview of the Global Variability in Radiated Energy and Apparent Stress*, pages 43–57. American Geophysical Union (AGU), 2006. ISBN 9781118666272. URL https://doi.org/10.1029/170GM06.

Comité Européen de Normalisation. *Eurocode 8: Design of Structures for Earthquake Resistance. Part 1: General Rules, Seismic Actions and Rules for Buildings*. European Standard EN 1998-1. European Committee for Standardization, Brussels, 2004.

R. Console and A. Rovelli. Attenuation parameters for friuli region from strong-motion accelerogram spectra. *Bulletin of the Seismological Society of America*, 71(6):1981–1991, 12 1981. ISSN 0037-1106. URL https://doi.org/10.1785/BSSA0710061981.

G. Costa, A. Ammirati, R. Nardis, L. Filippi, A. Gallo, G. Lavecchia, S. Sirignano, P. Suhadolc, E. Zambonelli, and M. Nicoletti. The italian strong motion network (ran), near-real time data acquisition and data analysis: A useful tool for seismic risk mitigation. In ,, 08 2014. URL https://doi.org/10.13140/2.1.3513.4722.

G. Costa, P. Brondi, L. Cataldi, S. Cirilli, A. Cuius, D. Ertuncay, P. Falconer, L. Filippi, S. Fornasari, V. Pazzi, and P. Turpaud. Near-real-time strong motion acquisition at national scale and automatic analysis. *Sensors*, 22, 07 2022. URL https://doi.org/10.3390/s22155699.

F. Cotton, F. Scherbaum, J. J. Bommer, and H. Bungum. Criteria for selecting and adjusting ground-motion models for specific target regions: Application to central europe and rock sites. *Journal of Seismology*, 10(2):137–156, 2006. ISSN 1573-157X. URL https://doi.org/10.1007/s10950-005-9006-7.

F. Cruz Hernández and R. R. Castro. Seismic energy radiated by earthquakes in the north-central region of the gulf of california, mexico. *Bulletin of the Seismological Society of America*, 115(3):1031–1050, 01 2025. ISSN 0037-1106. URL https://doi.org/10.1785/0120240096.

M. Cuffaro, F. Riguzzi, D. Scrocca, F. Antonioli, E. Carminati, M. Livani, and C. Doglioni. On the geodynamics of the northern adriatic plate. *RENDICONTI LINCEI*, 21:253–279, 12 2010. URL https://doi.org/10.1007/s12210-010-0098-9.

G. Cultrera, P. Bordoni, A. Mercuri, M. Quintiliani, L. Minarelli, D. Famiani, P. Casale, M. Pischiutta, C. Ladina, F. Cara, G. Di Giulio, S. Pucillo, G. Monti, and C. W. Group. Database for site characterization of permanent seismic stations (crisp). Dataset, Istituto Nazionale di Geofisica e Vulcanologia (INGV), 2022. URL https://doi.org/10.13127/crisp.

F. A. Dahlen. The balance of energy in earthquake faulting. *Geophysical Journal International*, 48(2):239–261, 02 1977. ISSN 0956-540X. URL https://doi.org/10.1111/j.1365-246X.1977.tb01298.x.

M.-A. P. des Chênes. Mémoire sur les séries et sur les intégrales définies. Unpublished manuscript, 1799. Submitted to the French Academy of Sciences.

G. Di Capua, G. Lanzo, S. Peppoloni, V. Pessina, A. Rovelli, and C. Di Alessandro. *Revised seismic classification of the ITACA stations, according to the EC8 and the Italian norms site classes*. „ Jun 2010. URL https://www.earth-prints.org/handle/2122/6527.

G. Di Capua, G. Lanzo, V. Pessina, S. Peppoloni, and G. Scasserra. The recording stations of the italian strong motion network: geological information and site classification. *Bulletin of Earthquake Engineering*, 9(6):1779–1796, 2011. ISSN 1573-1456. URL https://doi.org/10.1007/s10518-011-9326-7.

Y. Dodge. *Standard Deviation*, pages 505–508. Springer New York, New York, NY, 2008. ISBN 978-0-387-32833-1. URL https://doi.org/10.1007/978-0-387-32833-1_381.

S. Drouet, S. Chevrot, F. Cotton, and A. Souriau. Simultaneous inversion of source spectra, attenuation parameters, and site responses: Application to the data of the french accelerometric network. *Bulletin of the Seismological Society of America*, 98(1):198–219, 02 2008. ISSN 0037-1106. URL https://doi.org/10.1785/0120060215.

B. Edwards, A. Rietbrock, J. J. Bommer, and B. Baptie. The acquisition of source, path, and site effects from microearthquake recordings using q tomography: Application to the united kingdom. *Bulletin of the Seismological Society of America*, 98(4):1915–1935, 08 2008. ISSN 0037-1106. URL https://doi.org/10.1785/0120070127.

B. Edwards, B. Allmann, D. Fäh, and J. Clinton. Automatic computation of moment magnitudes for small earthquakes and the scaling of local to moment magnitude. *Geophysical Journal International*, 183(1):407–420, 10 2010. ISSN 0956-540X. URL https://doi.org/10.1111/j.1365-246X.2010.04743.x.

FDSN. Seed manual version 2.4, appendix a: Channel naming, 2007. URL https://fdsn.org/pdf/SEEDManual_V2.4_Appendix-A.pdf. International Federation of Digital Seismograph Networks.

FDSN Working Group II on Data Exchange. *SEED Reference Manual Version 2.4*. Federation of Digital Seismographic Networks, 2000. Available at https://www.fdsn.org/pdf/SEEDManual_V2.4.pdf.

C. Felicetta, E. Russo, M. C. D'Amico, S. Sgobba, G. Lanzano, C. Mascandola, F. Pacor, and L. Luzi. Italian accelerometric archive v4.0. Dataset, Istituto Nazionale di Geofisica e Vulcanologia (INGV), Dipartimento della Protezione Civile Nazionale, 2023. URL https://doi.org/10.13127/itaca.4.0.

F. Fitzko, P. Suhadolc, A. Aoudia, and G. Panza. Constraints on the location and mechanism of the 1511 western-slovenia earthquake from active tectonics and modeling of macroseismic data. *Tectonophysics*, 404(1):77–90, 2005. ISSN 0040-1951. URL https://doi.org/10.1016/j.tecto.2005.05.003.

J. Fourier. *Théorie analytique de la chaleur*. Didot, Paris, 1822.

G. Franceschina, S. Kravanja, and G. Bressan. Source parameters and scaling relationships in the friuli-venezia giulia (northeastern italy) region. *Physics of the Earth and Planetary Interiors*, 154:148–167, 02 2006. URL https://doi.org/10.1016/j.pepi.2005.09.004.

F. Galadini, M. E. Poli, and A. Zanferrari. Seismogenic sources potentially responsible for earthquakes with m $\geq$ 6 in the eastern southern alps (thiene-udine sector, ne italy). *Geophysical Journal International*, 161(3):739–762, 06 2005. ISSN 0956-540X. URL https://doi.org/10.1111/j.1365-246X.2005.02571.x.

A. Gallo, G. Costa, and P. Suhadolc. Near real-time automatic moment magnitude estimation. *Bulletin of Earthquake Engineering*, 12, 02 2014. URL https://doi.org/10.1007/s10518-013-9565-x.

P. Gasperini, F. Bernardini, G. Valensise, and E. Boschi. Defining seismogenic sources from historical earthquake felt reports. *Bulletin of the Seismological Society of America*, 89(1):94–110, 02 1999. ISSN 0037-1106. URL https://doi.org/10.1785/BSSA0890010094.

Geological Survey-Provincia Autonoma di Trento. Trentino seismic network [data set], 1981. URL https://doi.org/10.7914/SN/ST.

GeoSphere (former ZAMG). Austrian seismic network [data set], 1987. URL https://doi.org/10.7914/SN/OE.

P. Goldstein, D. Dodge, M. Firpo, and L. Minner. Sac2000: Signal processing and analysis tools for seismologists and engineers. In *The IASPEI International Handbook of Earthquake and Engineering Seismology*. Academic Press, 2003.

M. Guidarelli, A. Aoudia, and G. Costa. 3-d structure of the crust and uppermost mantle at the junction between the southeastern alps and external dinarides from ambient noise tomography. *Geophysical Journal International*, 211(3):1509–1523, 09 2017. ISSN 0956-540X. URL https://doi.org/10.1093/gji/ggx379.

C. Hammerl. The earthquake of january 25th, 1348: Discussion of sources. In P. Albini and A. Moroni, editors, *Materials of the CEC Project Review of Historical Seismicity in Europe*, volume 2, pages 225–240. CNR, Milano, Italy, 1994.

J. Han and M. Kamber. *Data Mining: Concepts and Techniques*. Morgan Kaufmann, 2001. ISBN 978-1558604896.

T. C. Hanks and H. Kanamori. A moment magnitude scale. *Journal of Geophysical Research: Solid Earth*, 84(B5):2348–2350, 1979. URL https://doi.org/10.1029/JB084iB05p02348.

S. H. Hartzell. Site response estimation from earthquake data. *Bulletin of the Seismological Society of America*, 82(6):2308–2327, 12 1992. ISSN 0037-1106. URL https://doi.org/10.1785/BSSA0820062308.

N. A. Haskell. Total energy and energy spectral density of elastic wave radiation from propagating faults. *Bulletin of the Seismological Society of America*, 54(6A):1811–1841, 12 1964. ISSN 0037-1106. URL https://doi.org/10.1785/BSSA05406A1811.

Istituto Nazionale di Geofisica e Vulcanologia (INGV). Rete sismica nazionale (rsn) [data set], 2005. URL https://doi.org/10.13127/sd/x0fxnh7qfy.

Istituto Nazionale di Oceanografia e di Geofisica Sperimentale - OGS. North-east italy seismic network [data set], 2016. URL https://doi.org/10.7914/SN/OX.

Istituto Nazionale di Oceanografia e di Geofisica Sperimentale and University of Trieste. North-east italy broadband network [data set], 2002. URL https://doi.org/10.7914/SN/NI.

Y. Izutani and H. Kanamori. Scale-dependence of seismic energy-to-moment ratio for strike-slip earthquakes in japan. *Geophysical Research Letters*, 28(20):4007–4010, 2001. URL https://doi.org/10.1029/2001GL013402.

D. E. James. *The Encyclopedia of solid earth geophysics*. Encyclopedia of earth sciences series. Van Nostrand Reinhold, 1989. ISBN 0442243669.

A. Jozi Najafabadi, C. Haberland, M. R. Handy, E. Le Breton, and M. Weber. Seismic wave attenuation (1/qp) in the crust underneath the eastern and eastern southern alps (europe): imaging effects of faults, fractures, and fluids. *Earth, Planets and Space*, 75(1):187, 2023. ISSN 1880-5981. URL https://doi.org/10.1186/s40623-023-01942-0.

H. Kanamori. *Theoretical basis of some empirical relations in seismology*. California Institute of Technology, 1975.

H. Kanamori. The energy release in great earthquakes. *Journal of Geophysical Research (1896-1977)*, 82 (20):2981–2987, 1977. URL https://doi.org/10.1029/JB082i020p02981.

H. Kanamori, J. Mori, E. Hauksson, T. H. Heaton, L. K. Hutton, and L. M. Jones. Determination of earthquake energy release and ml using terrascope. *Bulletin of the Seismological Society of America*, 83 (2):330–346, 04 1993. ISSN 0037-1106. URL https://doi.org/10.1785/BSSA0830020330.

Y. Kaneko and P. M. Shearer. Seismic source spectra and estimated stress drop derived from cohesive-zone models of circular subshear rupture. *Geophysical Journal International*, 197(2):1002–1015, 03 2014. ISSN 0956-540X. URL https://doi.org/10.1093/gji/ggu030.

P. Klin, G. Laurenzano, and E. Priolo. Gitanes: A matlab package for estimation of site spectral amplification with the generalized inversion technique. *Seismological Research Letters*, 89, 12 2017. URL https://doi.org/10.1785/0220170080.

P. Klin, G. Laurenzano, C. Barnaba, E. Priolo, and S. Parolai. Site amplification at permanent stations in northeastern italy. *Bulletin of the Seismological Society of America*, 111(4):1885–1904, 06 2021. ISSN 0037-1106. URL https://doi.org/10.1785/0120200361.

B. V. Kostrov. Seismic moment and energy of earthquakes, and seismic flow of rock. *Izv. Earth Phys.*, 1: 23–40, 1974. [Engl. transl.].

C. A. Langston. Corvallis, oregon, crustal and upper mantle receiver structure from teleseismic p and s waves. *Bulletin of the Seismological Society of America*, 67(3):713–724, 06 1977. ISSN 0037-1106. URL https://doi.org/10.1785/BSSA0670030713.

T. Lay and T. Wallace. *Modern global seismology*. Academic Press, 1995. ISBN 012732870X.

J. Lermo and F. J. Chávez-García. Site effect evaluation using spectral ratios with only one station. *Bulletin of the Seismological Society of America*, 83(5):1574–1594, 10 1993. ISSN 0037-1106. URL https://doi.org/10.1785/BSSA0830051574.

L. Luzi, S. Hailemikael, D. Bindi, F. Pacor, F. Mele, and F. Sabetta. Itaca (italian accelerometric archive): A web portal for the dissemination of italian strong-motion data. *Seismological Research Letters*, 79(5): 716–722, 09 2008. ISSN 0895-0695. URL https://doi.org/10.1785/gssrl.79.5.716.

R. Madariaga. Earthquakes, source theory. In H. K. Gupta, editor, *Encyclopedia of Solid Earth Geophysics*, pages 248–252. Springer, 2011.

A. Magrin and G. Rossi. Deriving a new crustal model of northern adria: The northern adria crust (nac) model. *Frontiers in Earth Science*, Volume 8 - 2020, 2020a. ISSN 2296-6463. URL https://doi.org/10.3389/feart.2020.00089.

A. Magrin and G. Rossi. the northern adria crust (nac) model, Feb. 2020b. URL https://doi.org/10.5281/zenodo.3666708.

L. Malagnini, A. Akinci, R. B. Herrmann, N. A. Pino, and L. Scognamiglio. Characteristics of the ground motion in northeastern italy. *Bulletin of the Seismological Society of America*, 92(6):2186–2204, 08 2002. ISSN 0037-1106. URL https://doi.org/10.1785/0120010219.

M. Massa, A. L. Rizzo, A. Lorenzetti, S. Lovati, E. D'Alema, R. Puglia, S. Carannante, and L. Luzi. Rete di monitoraggio multiparametrico del garda (nord italia) - pdnet, 2021. URL https://doi.org/10.13127/SD/YHCFOMCBO_.

MedNet Project Partner Institutions. Mediterranean very broadband seismographic network (mednet) [data set], 1990. URL https://doi.org/10.13127/sd/fbbbtdtd6q.

W. Menke. *Geophysical data analysis discrete inverse theory*. Academic Press, 1984. ISBN 978-0-12-490920-5.

W. Menke. *Geophysical Data Analysis: Discrete Inverse Theory*. International Geophysics. Academic Press, 1989. ISBN 9780080507323.

P. Morasca, M. D'Amico, D. Spallarossa, D. Bindi, M. Picozzi, A. Oth, and F. Pacor. Gitpy: A python implementation of the generalized inversion technique. *Seismological Research Letters*, 07 2025. ISSN 0895-0695. URL https://doi.org/10.1785/0220250042.

L. Moratto, F. Abdi, and A. Saraò. Seismic source parameters analysis in southeastern alps and associated tectonic implications. *Tectonophysics*, 923:231069, 2026. ISSN 0040-1951. doi: https://doi.org/10.1016/j.tecto.2026.231069. URL https://www.sciencedirect.com/science/article/pii/S0040195126000028.

Y. Nakamura. A method for dynamic characteristics estimation of subsurface using microtremor on the ground surface. *Quarterly Report of RTRI*, 30(1):25–33, 1989. URL https://trid.trb.org/view/294184.

A. Oth, D. Bindi, S. Parolai, and F. Wenzel. S-Wave Attenuation Characteristics beneath the Vrancea Region in Romania: New Insights from the Inversion of Ground-Motion Spectra. *Bulletin of the Seismological Society of America*, 98(5):2482–2497, 10 2008. ISSN 0037-1106. URL https://doi.org/10.1785/0120080106.

A. Oth, S. Parolai, D. Bindi, and F. Wenzel. Source spectra and site response from s waves of intermediate-depth vrancea, romania, earthquakes. *Bulletin of the Seismological Society of America*, 99(1):235–254, 02 2009. ISSN 0037-1106. URL https://doi.org/10.1785/0120080059.

A. Oth, D. Bindi, S. Parolai, and D. Di Giacomo. Spectral analysis of k-net and kik-net data in japan, part ii: On attenuation characteristics, source spectra, and site response of borehole and surface stations. *Bulletin of the Seismological Society of America*, 101(2):667–687, 04 2011. ISSN 0037-1106. URL https://doi.org/10.1785/0120100135.

S. Parolai, D. Bindi, and P. Augliera. Application of the generalized inversion technique (git) to a microzonation study: Numerical simulations and comparison with different site-estimation techniques. *Bulletin of the Seismological Society of America*, 90(2):286–297, 04 2000. ISSN 0037-1106. URL https://doi.org/10.1785/0119990041.

R. Penrose. A generalized inverse for matrices. *Mathematical Proceedings of the Cambridge Philosophical Society*, 51(3):406–413, 1955. URL https://doi.org/10.1017/S0305004100030401.

M. Picozzi, D. Bindi, P. Brondi, D. Di Giacomo, S. Parolai, and A. Zollo. Rapid determination of p wave-based energy magnitude: Insights on source parameter scaling of the 2016 central italy earthquake sequence. *Geophysical Research Letters*, 44(9):4036–4045, 2017. URL https://doi.org/10.1002/2017GL073228.

M. Picozzi, D. Bindi, D. Spallarossa, D. Di Giacomo, and A. Zollo. A rapid response magnitude scale for timely assessment of the high frequency seismic radiation. *Scientific Reports*, 8, 06 2018a. URL https://doi.org/10.1038/s41598-018-26938-9.

M. Picozzi, D. Bindi, D. Spallarossa, A. Oth, D. Di Giacomo, and A. Zollo. Moment and energy magnitudes: diversity of views on earthquake shaking potential and earthquake statistics. *Geophysical Journal International*, 216(2):1245–1259, 11 2018b. ISSN 0956-540X. URL https://doi.org/10.1093/gji/ggy488.

M. Picozzi, G. Festa, A. Zollo, D. Bindi, and D. Spallarossa. Detecting long-lasting transients of earthquake activity on a fault system by monitoring apparent stress, ground motion and clustering. *Scientific Reports*, 9, 11 2019. URL https://doi.org/10.1038/s41598-019-52756-8.

Presidency of Council of Ministers - Civil Protection Department. Italian strong motion network [data set], 1972. URL https://doi.org/10.7914/SN/IT.

Presidenza del Consiglio dei Ministri, Dipartimento della Protezione Civile. Ran - rete accelerometrica nazionale, 2014. URL https://ran.protezionecivile.it. also https://doi.org/10.7914/SN/IT.

W. H. Press, S. A. Teukolsky, W. T. Vetterling, and B. P. Flannery. *Numerical recipes in C: the art of scientific computing*. Cambridge University Press, New York, 1994.

Province Südtirol. Province südtirol seismic network [data set], 2006. URL http://www.fdsn.org/networks/detail/SI. also https://eida.ingv.it/en/network/SI.

L. Rivera and H. Kanamori. Representations of the radiated energy in earthquakes. *Geophysical Journal International*, 162(1):148–155, 07 2005. ISSN 0956-540X. URL https://doi.org/10.1111/j.1365-246X.2005.02648.x.

A. Rovida, R. Camassi, P. Gasperini, and M. Stucchi. Catalogo parametrico dei terremoti italiani (cpti11), 2011. URL https://doi.org/10.6092/INGV.IT-CPTI11.

A. Rovida, M. Locati, A. Antonucci, and R. Camassi. Archivio storico macrosismico italiano (asmi). https://doi.org/10.13127/asmi, 2017. (a cura di).

A. K. Samantaray, P. A. Mooney, and C. A. Vivacqua. Bergen metrics: composite error metrics for assessing performance of climate models using euro-cordex simulations. *Geoscientific Model Development*, 17(8):3321–3339, 2024. URL https://doi.org/10.5194/gmd-17-3321-2024.

A. Saraò, S. Das, and P. Suhadolc. Effect of non-uniform station coverage on the inversion for earthquake rupture history for a haskell-type source model. *Journal of Seismology*, 2(1):1–25, 1998. ISSN 1573-157X. URL https://doi.org/10.1023/A:1009795916726.

A. Saraò, P. L. Bragato, and P. Bernardi. Real time seismology of the ogs seismological research centre, 2009. URL https://rts.crs.inogs.it.

C. Satriano. Sourcespec – earthquake source parameters from p- or s-wave displacement spectra (version 1.8), 2024. URL https://doi.org/10.5281/zenodo.3688587. Zenodo software release.

F. Scherbaum, J. J. Bommer, H. Bungum, F. Cotton, and N. A. Abrahamson. Composite ground-motion models and logic trees: Methodology, sensitivities, and uncertainties. *Bulletin of the Seismological Society of America*, 95(5):1575–1593, 10 2005. ISSN 0037-1106. URL https://doi.org/10.1785/0120040229.

C. Scholz. *The Mechanics of Earthquake Faulting*. „ 05 2002. ISBN 9780521652230. URL https://doi.org/10.1017/CBO9780511818516.

P. M. Shearer. *Introduction to Seismology*. Cambridge University Press, 2 edition, 2009.

H. Shible, F. Hollender, D. Bindi, P. Traversa, A. Oth, B. Edwards, P. Klin, H. Kawase, I. Grendas, R. R. Castro, N. Theodoulidis, and P. Gueguen. Gitec: A generalized inversion technique benchmark. *Bulletin of the Seismological Society of America*, 112(2):850–877, 02 2022. ISSN 0037-1106. URL https://doi.org/10.1785/0120210242.

L. Sirovich and F. Pettenati. Source inversion of intensity patterns of earthquakes: A destructive shock in 1936 in northeast italy. *Journal of Geophysical Research*, 109, 10 2004. URL https://doi.org/10.1029/2003JB002919.

Slovenian Environment Agency. Seismic network of the republic of slovenia [data set], 1990. URL https://doi.org/10.7914/SN/SL.

D. Spallarossa, M. Picozzi, D. Scafidi, P. Morasca, C. Turino, and D. Bindi. The ramones service for rapid assessment of seismic moment and radiated energy in central italy: Concepts, capabilities, and future perspectives. *Seismological Research Letters*, 92, 03 2021. URL https://doi.org/10.1785/0220200348.

J. H. Steidl, A. G. Tumarkin, and R. J. Archuleta. What is a reference site? *Bulletin of the Seismological Society of America*, 86(6):1733–1748, 12 1996. ISSN 0037-1106. URL https://doi.org/10.1785/BSSA0860061733.

S. Stein and M. Wysession. *Introduction to Seismology, Earthquakes, and Earth Structure*. Blackwell Publishing, 2003.

G. Tarchini, L. Moratto, and A. Saraò. A comprehensive moment magnitude catalog for the northeastern italy region. *Seismological Research Letters*, 96(4):2714–2723, 03 2025. ISSN 0895-0695. URL https://doi.org/10.1785/0220240303.

L. Törnqvist, P. Vartia, and Y. O. Vartia. How should relative changes be measured? *The American Statistician*, 39(1):43–46, 1985. URL https://doi.org/10.1080/00031305.1985.10479385.

A. Udías and E. Buforn. *Principles of Seismology*. Cambridge University Press, 2 edition, 2017.

University of Genoa. Regional seismic network of north western italy, 1967. URL http://www.distav.unige.it/rsni.

University of Trieste. Friuli venezia giulia accelerometric network [data set], 1993. URL https://doi.org/10.7914/SN/RF.

A. van der Sluis and H. A. van der Vorst. *Numerical solution of large, sparse linear algebraic systems arising from tomographic problems, In: Nolet, G. (eds) Seismic Tomography. Seismology and Exploration Geophysics*, pages 49–83. Springer Netherlands, Dordrecht, 1987. ISBN 978-94-009-3899-1. URL https://doi.org/10.1007/978-94-009-3899-1_3.

M.-H. Yen, D. Bindi, A. Oth, B. Edwards, R. Zaccarelli, and F. Cotton. Source parameters and scaling relationships of stress drop for shallow crustal seismic events in western europe. *Journal of Seismology*, 28(1):63–79, 2024. ISSN 1573-157X. URL https://doi.org/10.1007/s10950-023-10188-y.

V. Zhelezniak, A. Savkov, A. Shen, and N. Hammerla. Correlation coefficients and semantic textual similarity. In J. Burstein, C. Doran, and T. Solorio, editors, *Proceedings of the 2019 Conference of the North American Chapter of the Association for Computational Linguistics: Human Language Technologies, Volume 1 (Long and Short Papers)*, pages 951–962, Minneapolis, Minnesota, June 2019. Association for Computational Linguistics. URL https://doi.org/10.18653/v1/N19-1100.

C. Zhu, S. Bora, B. A. Bradley, and D. Bindi. Spectral decomposition of ground motions in new zealand using the generalized inversion technique. *Geophysical Journal International*, 238(1):364–381, 05 2024. ISSN 1365-246X. URL https://doi.org/10.1093/gji/ggae163.

M. Zivcic, A. Govoni, and G. Costa. The 1998 krn mountains earthquake sequence. the combined data set of the ursg, ogs and dst temporary and permanent seismic networks. CD-ROM, 2000. Data coverage: April 12–December 31.

A. Zollo, A. Orefice, and V. Convertito. Source parameter scaling and radiation efficiency of microearthquakes along the irpinia fault zone in southern apennines, italy. *Journal of Geophysical Research: Solid Earth*, 119(4):3256–3275, 2014. URL https://doi.org/10.1002/2013JB010116.

La borsa di dottorato è cofinanziata con risorse dell'Unione europea, NextGeneration EU - Piano Nazionale di Ripresa e Resilienza, Missione 4 – Componente 2 – Investimento 3.1 – NexGenerationEU – Codice Progetto IR0000025, Programma "MEET - Monitoring Earth's Evolution and Tectonics" – CUP J93C22001510006